Temperature Dependence and Touch Sensitivity of Electrical Transport in Novel Nanocomposite Printable Inks

WEBB, ALEXANDER,JAMES

Temperature Dependence and Touch Sensitivity of Electrical Transport in Novel Nanocomposite Printable Inks

Alexander James Webb

A thesis submitted in partial fulfilment of the requirements for the degree of Doctor of Philosophy

Durham University, Department of Physics, 2014

Abstract

Printed electronics is an established industry allowing the production of electronic components such as resistors, and more complex structures such as solar cells, from functional inks. Composites, a mixture of two or more materials with different physical and/or chemical properties that combine to create a new material with properties differing from its constituent parts, have been important in areas such as the textile and automotive industries, and are significant in printed electronics as inks for printed circuit components, touch and vapour sensors. Here, the functional performance and physical behaviour of two screen printable multi-component nanocomposite inks, formulated for touch-pressure sensing applications, are investigated. They each comprise a proprietary mixture of electrically conducting and insulating nanoparticles dispersed in an insulating polymer binder, where one is opaque and the other transparent. The opaque ink has a complex surface structure consisting of a homogeneous dispersion of nanoparticles. The transparent inks structure is characterised by large aggregates of nanoparticles distributed through the printed layer. Temperature dependent electrical transport measurements under a range of compressive loadings reveal similar non-linear behaviour in both inks, with some hysteresis observed, and this behaviour is linked to the inks structures. A physical model comprising a combination of linear and non-linear conduction contributions, with the linear term attributed to direct connections between conductive particles and the non-linear term attributed to field-assisted quantum tunnelling, has been developed and used successfully to describe the underpinning physical processes behind the unique electrical functionality of the opaque ink and, to a lesser extent, the transparent ink.

Declaration

Unless explicitly stated otherwise, the work presented in this thesis is solely that of the author and has not been submitted for examination for any other degree at any University.

Thermogravimetric analysis and differential scanning calorimetry experiments were coordinated by the author but performed by Doug Carswell at the Department of Chemistry at Durham University. The analysis of the resulting data was undertaken by the author.

Acknowledgements

There are numerous people whom I would like to thank for their support and friendship. Firstly, I wish to thank Dr. Del Atkinson and Dr. Marek Szablewski for their invaluable guidance and supervision which has been critical to the completion of this work.

The majority of the measurements in this thesis were obtained in the Peratech laboratory and the microscopy facility, so I would like to thank Duncan McCallum for his hard work in maintaining the laboratories and Leon Bowen for his training and assistance in the use of the scanning electron microscope and focussed ion beam facilities. Many thanks must also go to all the past and present staff at Peratech: Dr. Adam Graham, Prof. David Bloor, Dr. Paul Laughlin, and David Lussey. This research would not have been possible without all of their hard work. Special thanks go to Dr. Adam Graham, who was my point of contact at the company, and Prof. David Bloor, with whom I had several useful discussions.

Thanks also go Dr. Richard Thompson and Doug Carswell in the Department of Chemistry for their time and assistance in the thermogravimetric and differential scanning calorimetry experiments. Additionally I wish to thank all those in room 12: Dr. Erhan Arac, Dr. David Burn, Dr. Mussab Sultan, Sarah Dempsey, Mustafa Tokac, and Richard Rowan-Robinson.

Finally, I wish to extend my sincere gratitude to my family and friends, in particular my parents David and Isa, who have always supported me in all of my endeavours through thick and thin, and Sharihan Al-Akhras, for her undying encouragement and kinship.

List of Publications

A Multi-Component Nanocomposite Screen-Printed Ink with Non-Linear Touch Sensitive Electrical Conductivity

A. J. Webb, M. Szablewski, D. Bloor, D. Atkinson, A. Graham, P. Laughlin, and D. Lussey

Nanotechnology **24**, 165501 (2013)

A Novel Screen-Printed Multi-Component Nanocomposite Ink with a Pressure Sensitive Electrical Resistance Functionality

A. J. Webb, S. J. Dempsey, D. Bloor, A. Graham, P. Laughlin, D. Lussey, M. Szablewski, and D. Atkinson

13th IEEE Conference on Nanotechnology, 671-674 (2013)

Temperature Dependence of Non-Linear Electrical Conduction Behaviour in a Screen-Printed Multi-Component Nanocomposite

A. J. Webb, D. Bloor, M. Szablewski, and D. Atkinson

13th IEEE Conference on Nanotechnology, 1115-1118 (2013)

Vapor Sensing Properties of a Conductive Polymer Composite Containing Nickel Particles with Nano-Scale Surface Features

S. J. Dempsey, A. J. Webb, A. Graham, D. Bloor, D. Atkinson, and M. Szablewski

13th IEEE Conference on Nanotechnology, 665-670 (2013)

Temperature Dependence of Electrical Transport in a Pressure-Sensitive Nanocomposite

A. J. Webb, D. Bloor, M. Szablewski, and D. Atkinson

ACS Appl. Mater. Interfaces, **6**, 12573-12580 (2014)

List of Conferences

ICN+t 2012

European Physical Society

Paris Sorbonne, France

—

Annual Student Conference 2012

IOP Printing and Graphics Science Group

Institute of Physics, London

(Awarded Student Presentation Prize 2012)

—

13th IEEE Conference on Nanotechnology 2013

IEEE

Shangri-La Hotel, Beijing, China

Contents

1. Introduction

1.1 Background

Printed electronics is a term that encompasses any and all electronic devices that can be produced using a conventional industrial printing process, such as screen, inkjet, or gravure printing, onto a variety of substrates. The printing of conducting tracks, connects and resistors has been common in the printed circuit board industry for some decades now but, as the ability to customise materials and processes has progressed, so has the diversity of potential applications.

One particular area that has seen significant research and growth is that of sensor applications, such as those for touch and vapour detection. While thin film vapour sensors are common, they are produced using relatively costly techniques such as chemical vapour deposition. The use of printed vapour sensing inks, such as those containing titanium dioxide and tin dioxide nanoparticles, allows vapour sensors to be produced quickly and on a wider range of substrates than before, even on textiles.

Touch sensors have become ubiquitous in a variety of consumer electrical products and devices, finding use as track pads and touch screens. Like vapour sensors, these devices are commonly made using traditional deposition techniques, and often require additional lithographic patterning to facilitate or enhance the touch sensitive characteristic. Printing processes can eliminate the need for these additional patterning steps, for example through the use of direct write techniques such as inkjet printing, and thus have the potential to speed up and lower the cost of the production of these sensors.

Composite materials, defined as a mixture of two or more materials with different physical and/or chemical properties that, when combined, produce a material with properties that differ from the individual constituents, are of great interest in printed electronics. Traditionally, composites have been produced in bulk form by dispersing filler or reinforcement particles within materials (known as matrices) such as cement [1] and silicone rubber [2]. These have found use in structural applications, for example reinforced concrete in architecture, advanced carbon fibre/resin composites in sporting equipment and aircraft [3] [4], and brake discs [5] (a composite of metal particles and ceramic: it's properties, such as the thermal conductivity, can be tailored by varying the ratio of metal particles to ceramic).

As mentioned above, touch sensitive inputs have become increasingly important in consumer electronics but these are limited by complex manufacturing and, even in the case of printed inks, the necessity for patterning and additional structures to create functional touch sensitive devices. By mixing electrically conducting nanoparticles with insulating polymer binders/resins, printable functional electronic components such as resistors, touch-pressure and vapour sensors and electronic switches can be readily produced. The touch sensitivity arises by compressing the pliable polymer matrix: while connected in an electrical circuit and in an uncompressed state, the composite is insulating. As compression increases, the conducting filler particles are pushed into close proximity and ultimately into direct contact, creating conducting pathways through the composite. This switches the composite from an electrically insulating to a conductive state. In some composite systems, the particles need not touch to form a percolative conducting network, utilising quantum tunnelling effects to transport charge along the pathways

formed by the filler particles. Touch-pressure sensitivity in composite systems is a highly attractive feature for applications touch sensors. As the composite material is intrinsically touch sensitive, no additional structures or patterning are required to create a touch input device.

Peratech Ltd has produced bulk conductive composites for a number of years, developing both bulk and, recently, printable inks. The company has a track record of publications with the Department of Physics at Durham University [6] [7]. The original composite produced by Peratech was QTC™, or quantum tunnelling composite. QTC™ comprises microscale nickel particles with nanoscale surface spikes dispersed and wetted in silicone rubber. This bulk composite exhibits unique and highly sensitive deformation dependent electrical behaviour; its resistance falls under compression, torsion and, to a lesser extent, stretching (through the Poisson effect). Early research in collaboration with Durham University established that quantum mechanical tunnelling processes significantly contribute to the electrical conductivity of QTC™. In a circuit, QTC™ is an insulator. If the composite is compressed however, the conducting particles are pushed into closer proximity, as described above. Large electric fields develop at the ends of the surface spikes on the nickel particles and, when the separation between the tips of adjacent particles has been reduced sufficiently, charge transfers between the tips by field-assisted quantum tunnelling.

The efficiency of quantum tunnelling is highly sensitive to conductor separation and this makes this composite well suited to touch-pressure sensing applications, such as track pads and switches. QTC™ is particularly useful in this regard as the particles within the composite don't come into direct contact to conduct charge. This

increases the longevity of the material due to insignificant physical wearing of the nickel surface spikes.

Peratech Ltd has gone on to develop nanocomposite inks which exhibit similar touch sensitive electrical behaviour [7]. While the touch sensitivity of these new inks is macroscopically similar to that of QTC™, the physical basis for their electrical behaviour may be different and this is the focus of this study.

1.2 Aim of this thesis

Two touch-pressure sensitive nanocomposite inks, developed empirically by Peratech Ltd, have been studied as the focus of this thesis. The first is named QTC™ Ink, henceforth referred to as opaque ink. It comprises acicular (needle-like) titanium dioxide needles with a conductive antimony-doped tin oxide surface coating, (referred to as needles) and insulating near-spherical titanium dioxide nanoparticles (referred to as TiO_2 particles), dispersed in an insulating polymer binder. The second nanocomposite ink is QTC™ Clear ink, referred to as transparent ink from here on in. This ink variant comprises conductive antimony-doped tin oxide needles (Sb-needles) and conductive near-spherical antimony-doped tin oxide nanoparticles (Sb-particles) dispersed in a polymer binder. These inks display unique non-linear touch-sensitive electrical behaviour and can be compressed from electrically insulating to a conductive state with the application of 2 N [7]. They have been designed as part of a long iterative process and have proprietary particle/polymer ratios selected for optimal touch sensitivity.

They have been developed for applications in printed touch sensors, such as track pads, pressure sensors and touch screens in devices such as laptops; games

console controllers; mobile phones; and interactive electronic whiteboards. While composite materials, such as these inks, have always had their conductivity modelled with percolation and effective medium theories, these are both phenomenological and only describe composite conductivity with regard to filler particle concentration.

The aim of this research is to develop a deeper understanding of the physical processes that underpin the pressure sensitive electrical functionality of these inks. This has involved a detailed analysis of the physical structure and thermal properties of the inks and the individual constituents using scanning electron microscopy, thermogravimetric analysis and differential scanning calorimetry. The pressure sensitive electrical behaviour was studied as a function of both compression and temperature. The pressure range studied was appropriate for touch input and the temperature range was constrained by what was deemed to be academically suitable and by temperature limits in potential applications. Much of the data accumulated in this thesis is not only interesting in an academic sense but is also significant from an industrial perspective: the data can and has been used to determine operating voltage and temperature limits of the inks, and has lead to informed improvements to the inks, such as choice of filler particle size, shape, material etc. Ultimately, the aim is to construct a simple physical model that can accurately reproduce and describe the observed electrical behaviour.

1.3 Outline

In order to present a detailed insight into these materials it is necessary to understand something of the applications technology background, the various printing methods and their limitations, and the physics of conduction in composite systems. Therefore, Chapter 2 presents a detailed review of printed electronics,

covering the development and types of printable functional inks, common applications, bulk composite materials and composite inks, and the printing techniques used most widely in the printed electronics industry which are relevant to this study. A detailed understanding of conduction in composites is needed and Chapter 3 presents the relevant background knowledge of electrical conduction in metals, semiconductors (as these materials are commonly used as filler powders in composites, including the inks studied here) and insulators, as well as discussions on quantum mechanical effects, such as tunnelling, and the temperature dependence of various conduction mechanisms. In Chapter 4 the experimental techniques utilised in this study are described along with the underlying physical principles upon which their operation is based. The results of this research are divided into three chapters: Chapter 5 details the structural and thermal properties analysis from electron microscopy, thermogravimetric analysis, and differential scanning calorimetry. The assembly of the nanoparticles in the inks, how these nanoparticles are wetted by the insulating polymer, and how the inks respond to changes in temperature, such as physical or chemical transitions, may significantly influence the electrical behaviour. Chapters 6 and 7 present the compression and temperature dependent electrical transport measurements for the opaque and transparent inks, respectively. With reference to Chapter 3, conduction mechanisms exhibit specific dependencies on compression and temperature, and the electrical transport measurements were undertaken to analyse these relations and to develop an informative physical model of the conduction in these composite inks. Chapter 8 further discusses and summarises the key findings of this thesis, linking the structure and thermal properties of the inks with their touch sensitive electrical behaviour, as well as commenting on possible areas for further study.

2. Printed electronics and printing techniques

2.1 Introduction

Printed electronics is the manufacturing of electrical devices from electrically functional organic and inorganic inks using conventional printing technologies such as screen printing, inkjet and gravure printing. A critical feature of printed electronics is the capability to manufacture devices on a diverse range of substrate materials; the substrates can be rigid, or flexible and stretchable. Printed electronics has made the transition from the laboratory to the consumer market and is predicted to grow in market share value from $16.04 billion to approximately $76.79 billion by 2023 [8], largely due to its potential to facilitate the production of electronic devices on a wide range of substrate materials at a much lower cost per unit area than traditional silicon-based electronics that involves vacuum deposition and lithographic technologies.

This chapter provides an overview of the printed electronics sector as a whole, detailing the development of functional inks, common applications, printing techniques, and the links between these three key aspects of printed electronics.

2.2 Electrically functional inks and their applications

The oldest and most basic application of printed electronics is the production of conducting tracks/connects and electrodes. These structures typically comprise of a single active layer which must be uniform and unbroken, adhere well to the substrate and have a sufficiently high electrical conductivity. The first uses of printing,

particularly screen printing, for making electrical connects and electrodes were in the manufacturing of printed circuit boards (*PCBs*) circa 50 years ago [9], and the screen printing method remains an important tool in PCB production today [10].

Originally, screen printing was used to print a negative mask on an insulating substrate, such as FR-2 (paper/resin composite) or FR-4 (fibreglass/resin composite – more common), plated with a uniform layer of copper. The ink used for the mask was designed to be resistant to an etching process, typically chemical etching. The unmasked copper was etched away and the ink resist washed off with a solvent, leaving the desired conducting tracks and structures in place [11]. The development of electrically conducting inks allowed the direct printing of the required conducting tracks and electrodes. The simplest of such inks are particulate suspensions. These are defined as particles of conducting material, typically metals such as nickel, gold or silver, suspended in a solvent, or a mixture of solvents and polymer binders (to tailor the viscosity of the resulting ink) [12]. This type of ink is well suited to screen printing and gravure printing, both of which are techniques that can process inks of a wide range of viscosities and are less prone to blockages than inkjet printing [13]. These methods are discussed later.

Particulate suspensions are difficult to use with inkjet systems, even with nanoscale particles, as the presence of the particles and the viscosity of the ink tend to cause the inkjet nozzles to become clogged. Once printed, the ink typically has a higher electrical resistance than the bulk conducting component [14]. This is due to the fact that the layer may not be uniform: it comprises a rough, broken layer of particles. The electrical resistance can be reduced by first curing (heating to remove solvent and other organic components), and then sintering the printed ink layer [15]. Sintering

involves exposing the printed ink to high temperatures for a given amount of time (depending on the size of the particles and the thickness of the printed layer), for example 260° C for 3 minutes is suitable in the case of 50 nm silver colloids in a water-based ink printed to a thickness of approximately 1 μm [16]. This causes the particles to neck and join into a single, uniform layer [16], see figure 2.1.

While this is not a problem for PCBs on FR-4, the need for a high temperature sintering step presents a serious issue for printing good quality conducting layers on to flexible substrates, such as plastics [17]. This issue has been addressed by reducing the size of the conducting particles, as the melting point for nanoparticles can be lower than that of the corresponding bulk material (known as melting point depression), and by developing inks which do not require a sintering step; using materials like carbon nanotubes [18], organometallic inks [19], or by the use of

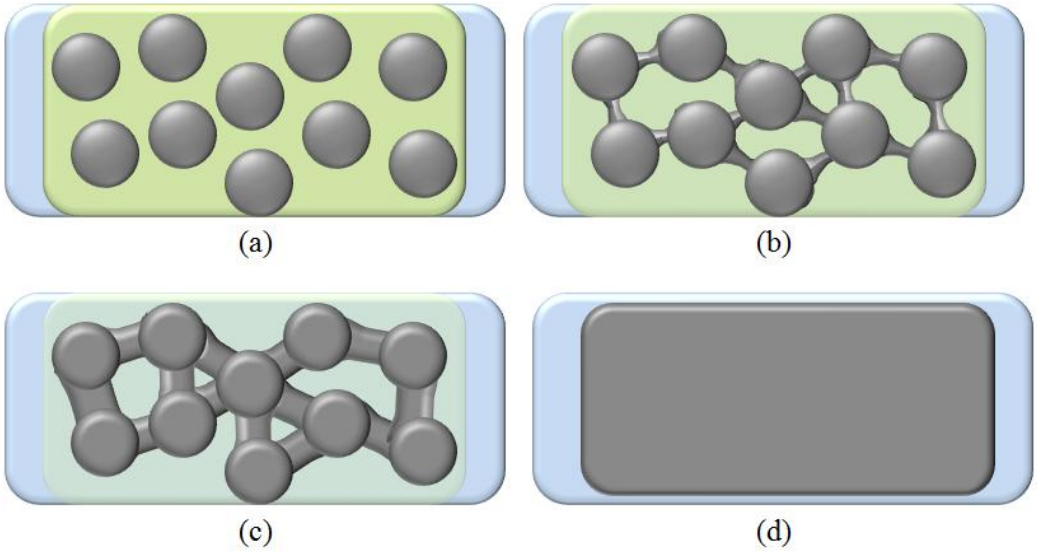

Figure 2.1. A series of schematic diagrams depicting the necking of printed metal nanoparticles into a single uniform layer during a sintering process. (a) The as-printed nanoparticles before sintering. Here, the blue tile is the substrate, the green layer is the printed solvent/polymer binder and the grey dots are the printed nanoparticles; (b) The solvent starts to be driven off by the increased temperature at the beginning of the sintering step. Small necks begin to form between the nanoparticles; (c) Most of the solvent has now evaporated and the necks continue to grow in size as the sintering process progresses; (d) At the end of the sintering step a single uniform layer has formed from the printed metal nanoparticles.

electrical [20], localised laser [21], and photonic [22] sintering techniques described in more detail below.

Organometallic inks utilise metallic/organic compounds in solution, which can be decomposed to precipitate a single conducting layer [23]. This decomposition occurs at a typically lower temperature than that of traditional sintering processes, and much of the literature focuses on carrying out the technique using laser irradiation, further reducing temperature induced stress on the substrate as the printed ink may be heated very quickly and in a localised manner. For example, Nie, Wang and Zou (2012) produced an inkjet printed silver film on PET using a post printing thermal treatment at 150 °C [23]. As organometallic inks contain no solid materials until heat treatment drives off the solvents, they tend to have low viscosity, and are widely applicable to inkjet printed electronics. Recently new nanomaterials such as carbon nanotubes, which are of particular interest due to their high as-printed electrical conductivity [24] and crucially their flexibility [25], have been considered for use in conducting inks.

In addition to conducting tracks and electrodes, resistors and capacitors are further essential applications of printed electronics, each consisting of a minimum of three printed layers: where two layers form electrodes and the intermediate layer is a resistive or dielectric layer. Embedded, printed resistors are now commonplace in the PCB industry [26]. They are commonly made from conducting printable ceramic materials known as cermets [27], or printable carbon [28]. Both of these materials are conducting composites, made from a mixture of electrically conducting particles and electrically insulating materials. Cermets are composed of metallic particles blended with insulating ceramic powder in a viscous solvent, which allows the material to be

screen printed. The conductive powders used include various metals [29], such as ruthenium [30] and nickel [31]. The liquid cermet material is screen printed [32], air dried, and then sintered at high temperature to form an electrical component. Printed carbon electrodes are similar in that they comprise carbon, often carbon black powder, mixed with a viscous polymer solvent; this flowing composite is screen printed to form electrical components, as with cermet materials [33]. Typically, proprietary blends of specific ratios of metal oxide, ceramic powder, carbon powder, and viscous carrier solvent are used, but the resistance value of the printed component is tailored either by varying the area of the final printed resistor, or through the variation of the thickness of the thick film. This has been achieved through mechanical, chemical, and laser trimming [34] [35].

Alternatively, changing the volume fraction of conducting powder in the composite also affects the final electrical resistance, but this is more difficult to accomplish due to the manner with which the conductivity rises dramatically with very small increases in the conducting components of composites. Many composite systems can have their conductivity described well by percolation theory [36] [37]. At low conducting filler content fractions, the conductivity of the composite takes a value close to that of the bulk insulating material.

An increase in the filler content fraction will initially have little effect on the conductivity, until the content fraction reaches a critical value known as the percolation threshold [38]. Here, the filler content fraction is great enough for direct contacts to form between the filler particles, creating a conducting pathway throughout the insulating material. The transition from an insulating to a conducting

state is typically very sharp, as shown in Figure 2.2; these characteristics of typical composite materials are discussed later in Chapter 3 in more detail.

Printable functional inks, including nanoparticle suspensions, organometallic inks and conductive polymer inks, are also being applied to create more complex device structures and functionalities such as thin film transistors [39], photovoltaic cells [40], batteries [41] and OLEDs [42], but many of these are still very much in the research stage and not highly commercialised.

As well as printed resistors and capacitors, an established area of printed electronics is in sensor applications. In particular, printed functional inks are being used widely for low cost vapour sensors and touch pressure sensors. Many printed vapour sensors comprise either a metal oxide film [43] [44], a polymer layer [45], or a layer of nanocomposite material [46]. Tin oxide is a very common vapour sensing

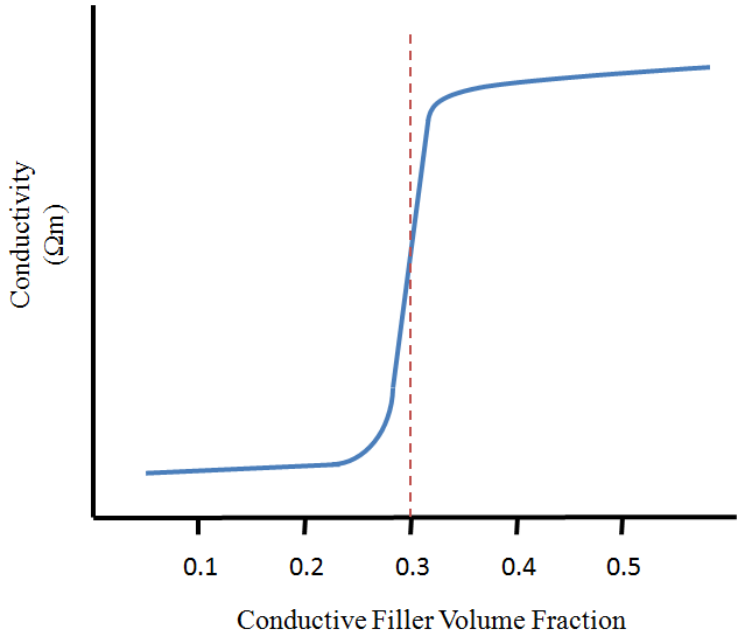

Figure 2.2. An example of how the electrical conductivity of a composite material, σ, varies as a function of the conductive filler volume fraction. At the *percolation threshold*, signified by the dashed red line, the conductivity of the composite rises dramatically as conducting pathways form through the body of the composite material.

material, as is titanium dioxide [47] [48]. Tin oxide sensors operate by undergoing an increase in electrical conductivity when in the presence of reducing agents, such as carbon monoxide, which donate electrons to the tin-oxide, called an n-type semiconductor [49]. Conversely, the conductivity of the tin oxide decreases when exposed to an oxidizing agent, such as oxygen.

Conducting polymer vapour sensors are thought to interact with vapours in a similar way, with different vapours affecting the how charge is transported across the polymer chains [50]. Printed composites, consisting of a homogeneous mixture of electrically conducting or semiconducting particles in a viscous insulating matrix, may operate in an electrochemical way, as described above, or through swelling of the insulating matrix resulting from exposure to vapour, which lowers the conductivity of the composite.

Composite systems which utilise polymer swelling to detect vapours are usually made in a conductive state to begin with: the conducting filler content fraction must be just above the percolation threshold. In this state, many of the filler particles are in direct contact and conductive pathways span the whole body of the material. When the composite is exposed to a vapour, the polymer swells and this acts to increase the distance between the filler particles, akin to how two dots drawn on a balloon will become further separated as the balloon is inflated. This process breaks up the conductive pathways in the composite, increasing the electrical resistance, illustrated in Figure 2.3.

Touch-pressure sensitive sensors have become an important component in consumer electronics, popularised by products such as track pads, smart phones and tablet computers. In these current devices the touch sensors used are typically

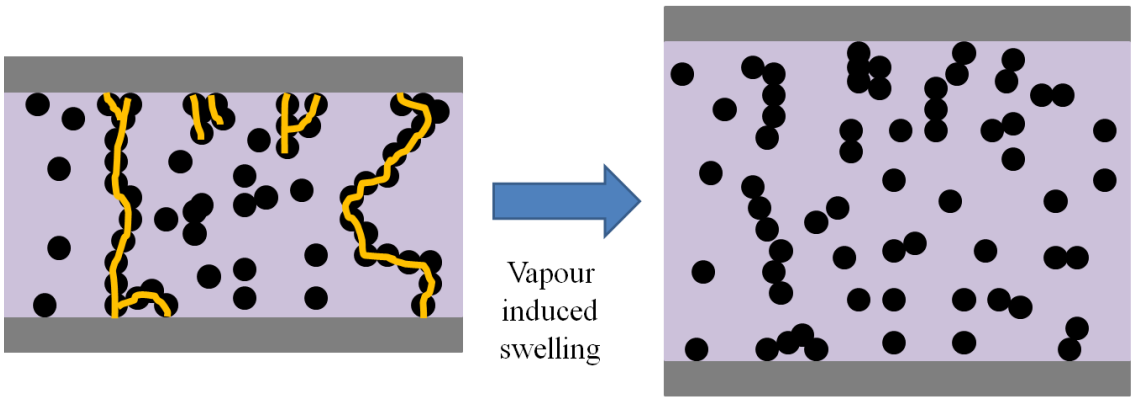

Figure 2.3. A schematic diagram showing the effect of vapour induced polymer swelling on a composite initially loaded to be in a conducting state. The grey bars are the electrodes, the lilac shaded area the insulating matrix, the black dots the conducting filler particles and the yellow lines represent conducting pathways.

capacitive and usually comprise of indium tin oxide (ITO) transparent electrodes and a dielectric material, which can be a printable ink [51]. Touch-pressure input is detected by sensing a change in capacitance when a conductor, or a material with a dielectric constant different to that of air, comes into close proximity or touches the surface of the sensor device. Capacitive sensors do not require hard presses to operate and are capable of detecting very light touches.

This contrasts with older resistive touch sensors, which comprise a flexible top electrode and rigid bottom electrode, separated by air or microdots or some other spacer layer or structure [52]. The application of pressure causes the electrodes to flex and make contact, changing the electrical resistance at the point of contact. These older sensors have become less popular as they generally require harder pressure and can become damaged more easily.

Conducting composite materials are, however, emerging as an important new class of material for use in a new generation of resistive touch sensors. If a composite material is loaded with a conductive filler content just below the percolation

threshold, then the resistance of the material may become highly sensitive to compressive force [53]. As well as being able to detect the x-y location of a touch in the plane of the screen or touchpad, resistive based touch interfaces may also detect/sense the touch force, which adds a third dimension of user control for electronic devices with touch interfaces. When subjected to compressive force, the conducting particles in the composite are forced closer together, pushing the composite through the percolation threshold. The electrical resistance is reduced by the formation of direct electrical contacts between the filler particles, and/or through more efficient quantum tunnelling conduction through thinner potential barriers between the filler particles.

Composites which utilise the latter conduction mechanism have distinct touch sensitivity, effectively rivalling the light touch detection of capacitive technology, and are more durable than the older type of resistive touch sensor due to the fact the filler particles do not have to physically contact each other in order to form conduction pathways, which significantly reduces wear [6].

Resistive touch sensitive interfaces have been developed with conducting composite materials before [54] [55], but they required the utilisation of bumps, posts and other such structures to enable touch location sensing capability. Most recently, conducting composite touch sensors of this type have been used in making the Microsoft Surface Touch Cover keypads. Ideally a single layer of intrinsically pressure sensitive resistive material, printed directly onto a matrix electrode architecture, is desired. Such an ink material is studied in this thesis.

2.3 Printing techniques

There are many printing methods available for use in printed electronics, each with their own benefits and drawbacks. The most common, both in industry and academic research, are discussed here in turn.

2.3.1 Screen printing

The most common method of printing functional inks for printed electronics is screen printing. This is a well established technique for the production of electrical components, for example thick film resistors for PCBs, mentioned earlier [56]. The screen printing technique utilises a masked screen, commonly made from a metal wire, polymer or silk mesh, to transfer an image or pattern of the ink onto a substrate. It is a so called push-through technique; the ink is pushed through the screen on to the substrate by a squeegee or doctor blade [57]. Below, the specific constituents and characteristics of screen printers and the screen printing process are discussed in turn.

2.3.1.1 Frames and screens

The frame, which holds the screen, can be made out of wood, plastic or metal. For use in printed electronics, where tolerances in final printed resolution are small, metal frames are most commonly used, often an aluminium alloy [58]. During the printing process, the frame may experience loads of the order of 50 kg; wood and plastic frames are often not stable enough and the strength of a metal frame is required.

The screen, affixed to the frame, is made from a woven mesh of fabric. Traditionally, this fabric was silk, hence the name “silk screen printing”, but it is more

common for the screen material to be either a polymer or metal wire, such as stainless steel. Common polymers include nylon and polyester, the latter being used more frequently due to its greater stability in the presence of humidity and temperature. Metal screens are less susceptible to wear than polymer screens but are more easily dented [59]. After weaving, polymer screens must be passed through heated rollers to "weld" the threads together, preserving the woven pattern. This step is not necessary for metal threads as they naturally bend and lock together during the weaving process [59].

The degree of open area in the screen is determined by the thread count and the thread diameter and is a variable which affects the amount of ink deposited in the final image. Screens come in a range of thread counts, from 10 to 200 per cm, but are typically made from threads of one of 4 standard thicknesses. These are denoted by the suffixes S, T, HD and HD Super [59]. These suffixes date from when silk screens were commonly used, where threads of thickness "S" were used for serigraphic (fine art) prints, whereas "T" thickness threads were utilised in screens for textiles. HD and HD Super are both for heavy duty applications. Using the values for thread diameter and thread count, one can calculate the open screen area A, as a percentage of the total surface area, using the following relation [58]:

$$A(\%) = \frac{w^2}{a^2} \times 100 \qquad (2.1)$$

where w is the width of open mesh space and a is the thread spacing.

The geometry is shown in Figure 2.4. Screens are fixed under tension to the frame. This tension is tailored to stretch the screen by a sufficient amount to allow it to peel away from the substrate after printing but not stretch it so much as to

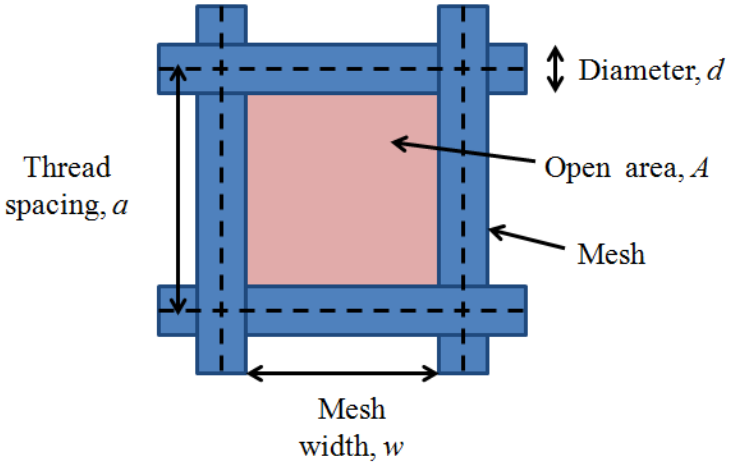

Figure 2.4. Screen-printing: a diagram of the mesh geometry showing the open area, *A*; the mesh width, *w*; the thread spacing, *a*; and the thread diameter, *d*.

cause damage to the mesh. This is dependent on the yield point of the mesh material. During printing the screen is pressed by a squeegee which stretches the screen into contact with the substrate. This acts to increase the size of the printed image as compared to the original size of the stencil. This stretching is depicted in Figure 2.5.

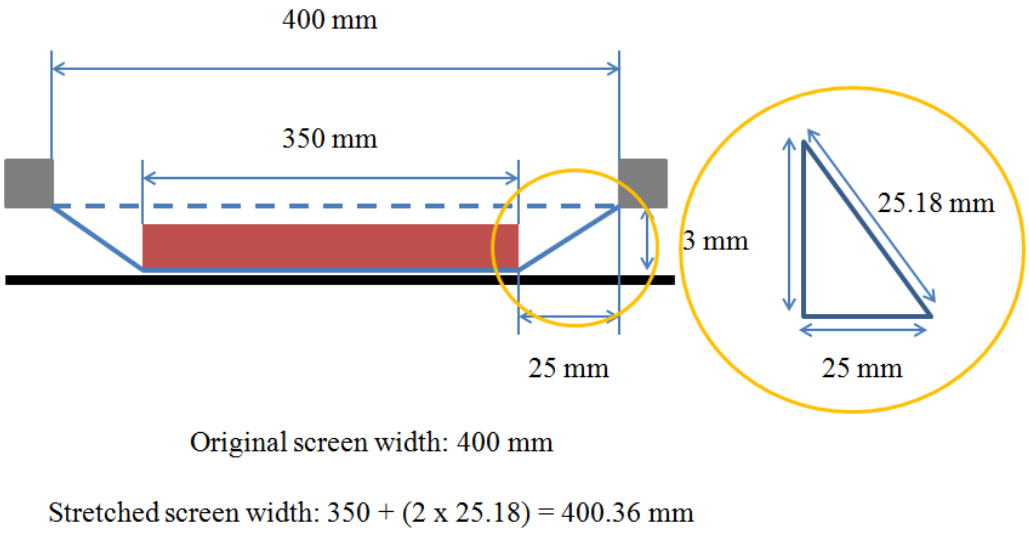

Figure 2.5. Screen printing: a cross-sectional schematic diagram showing how the screen mesh is stretched when pressed onto the substrate by the squeegee. Here, the grey squares are the frame, the red block is the squeegee, the black line is the substrate, the thick blue dashed line is the original screen position and the thick solid blue line is the stretched screen. A simple calculation shows that, in this case, the screen mesh is stretched by 0.36 mm.

Screens held at a higher tension may be held closer to the substrate during printing, which reduces image distortion.

2.3.1.2 Stencils

The stencil is the carrier of pattern information on the screen. A good stencil must permeate the entire mesh structure and extend out of the plane of the surface of the screen. This ensures the screen mesh structure does not cause image defects during the printing process and thus increases the image resolution and accuracy. There are several ways to manufacture stencils for use in screen printing. The methods can be separated into two broad classifications: manual and photochemical stencils.

Manual techniques for producing stencils are generally used for small scale arts, crafts and serigraphy work, and include: cutting, masking, and washing off. The cutting technique involves producing the stencil by hand, cutting material to produce a negative mask and sticking it to the screen with adhesive. Masking is where a negative mask stencil is painted directly onto the screen with an impermeable varnish. Washing off, a more complex procedure, entails painting a positive image mask onto the screen using a varnish soluble in a particular solvent. After this step, the entire screen is painted over with varnish soluble in a different solvent. The screen is then washed in the solvent for the first varnish layer, removing the positive image pattern and leaving the negative image mask in place on the screen.

Photochemical techniques are the most common group of stencil production techniques used in the screen printing industry. They all involve the application of photosensitive resists to manufacture stencil masks. There are three main types of photochemical mask, based on whether the stencil mask is produced on the screen or

separately from the screen and then affixed to the mesh, or a combination of both. They are termed direct, indirect, and direct/indirect, respectively. These techniques are discussed in turn.

Direct stencils are made by applying a photosensitive film to the screen and then developing the stencil on the screen. The stencil layer can either be coated on to the screen with a squeegee or scoop coater, and may be applied on both the print side and the squeegee side of the screen to ensure a thick, even coating. The stencil film material is designed to be soluble in a specific solvent, such as water or acetone, but insoluble after exposure to UV light, which facilitates cross linking of the polymer that makes up the film. Once the stencil film is attached, it is exposed to a film positive image of the stencil pattern with UV light. The areas of the stencil film not protected by the film positive cross-link and become insoluble under exposure to UV light, while the shaded areas remain soluble. The unexposed areas are then washed off with solvent to leave a completed stencil. This method is used frequently due to its simplicity and low cost, and produces stencils precise enough for most applications [58].

Indirect stencils are prepared away from the screen and adhered to the mesh after the UV exposure and washing off steps have been completed. Indirect stencils come as a sheet of sensitised emulsion on a plastic support sheet. This sheet of emulsion is developed using a film positive, in much the same way as direct stencils. After this step the stencil film is placed on a flat surface, emulsion side up. A clean, degreased screen, wetted slightly with a solvent such as water to soften the stencil emulsion, is lowered onto the stencil film and is gently pressed onto the film so that the emulsion permeates the screen mesh by capillary action. Once dry, the plastic

support can be removed and screen is ready for printing. This method is used when there are more stringent controls on the thickness of the final print layer [58].

Direct/Indirect stencils combine the above two methods. A photosensitive film, similar to that used for indirect stencils, is fixed onto the screen through capillary action of the film emulsion into the screen mesh. The film is then patterned on-screen through exposure to UV with a film positive and then washed with solvent to fully develop the stencil [58]. There are other methods of creating stencils for screen printing but they are not commonplace. These methods include laser etching of films and using inkjet printers to deposit UV impermeable masks: here, the stencil pattern film positive, made with UV impermeable ink, is printed on a photosensitive film. Exposure to UV light hardens the film not covered by the printed film positive. The washing off process then removes the printed film positive and underlying undeveloped film, leaving the final stencil.

In industrial printed electronics applications, the resolution of the final printed patterns is of great importance, far more than in graphic arts applications. In figure 2.5, it was shown how the screen is stretched slightly when pressed onto the substrate. If the stencil image covers an area too close to the screen edge, the printed image will be distorted. Additionally, it is more difficult for the squeegee to press the mesh into contact with the substrate close to the edge of the frame, which will negatively impact on the precision of the final print thickness.

To combat these issues, the sizes of the screen and image stencil are made in a ratio of 1.5 to 1 or 2 to 1, so that the image is sufficiently far away from the screen edge [59]. The quality of the final print is thus dependent on the frame material, the

thread count of the mesh material (the number of mesh threads per cm), the thread thickness (diameter), the thickness of the screen and the degree of open area.

2.3.1.3 Types of screen printer

The most basic form of screen printing process is *flat-bed screen printing*. In this process, both the printing plate, which is the combination of the screen mesh and the frame, and the substrate, are flat and lie parallel to each other. The ink is applied to the screen on the squeegee side and is spread across the entire printing plate area, either by hand or with the print squeegee or a second squeegee known as a flood bar, at a very low contact force. During this process, called pre-loading or flooding, the ink fills the screen mesh through capillary action. Figure 2.6, below, schematically represents the printing process [58]. The squeegee is then pressed into the printing plate, bringing the screen and the substrate into direct contact, and is moved along

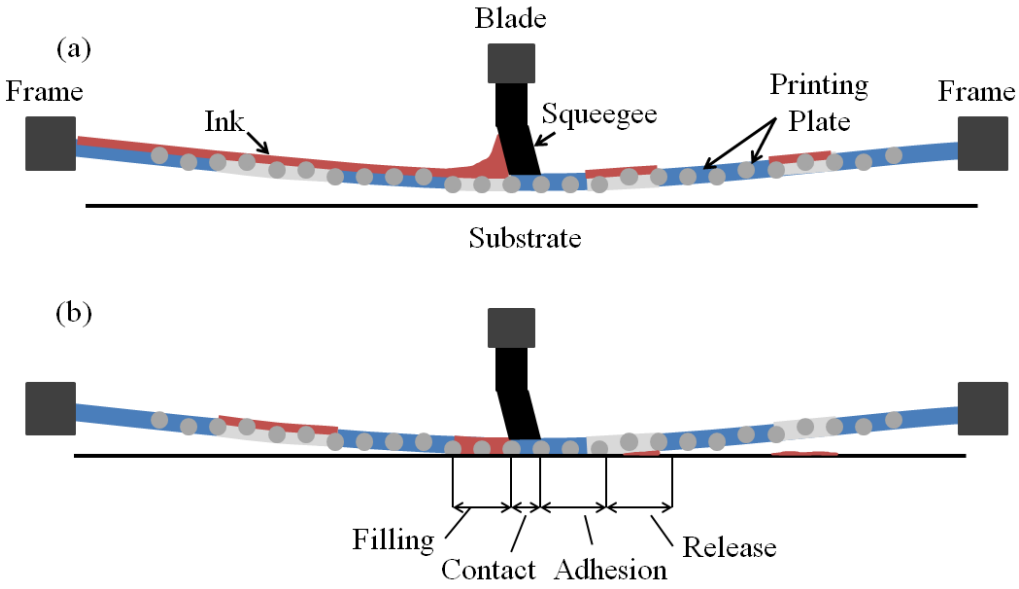

Figure 2.6. Screen printing: a schematic diagram showing (a) the optional pre-flood step, and (b) the screen-print process; as the squeegee progresses along the printing plate (the combination of the screen and stencil), the ink is pushed into the mesh in the filling zone. The mesh comes into contact with the substrate in the contact region. The ink adheres to the substrate here and in the adhesion area. The mesh peels away from the substrate surface in the release area, leaving a printed ink layer on the substrate.

the length of the printing plate at constant velocity. The region beneath the squeegee is the contact region. It is here that the screen comes into contact with the substrate. Immediately behind the squeegee is the adhesion region. Here, the ink adheres to the substrate. Behind this region is the release or peel region, also known as the snap-off region. The screen peels away from the substrate here, leaving the ink firmly in place.

It is also possible to print on curved surfaces such as cylinders and conical surfaces using flat bed printing frames; the substrate is rotated at the same velocity as the squeegee, and the frame is guided over the surface of the substrate at a tangent. The final dry thickness of the printed film, *t*, is dependent on several variables but can be estimated using the following relationship [60]:

$$t = t_{sc} k_p \frac{c}{\rho} \tag{2.2}$$

where t_{sc} is the printed wet thickness and is equal to the thread diameter plus the thickness of the stencil layer; k_p is the pickout ratio, defined as the amount of ink which remains in the mesh and does not get printed; c is the concentration or density of solid particles in the wet ink; ρ is the density of the dry printed ink layer. The pickout ratio k_p is difficult to measure, as it is dependent on the ink viscosity, the force with which the squeegee is applied, the speed of the squeegee and the distance between the mesh and the substrate.

Rotary screen printers allow continuous printing, without seams. A cylindrical printing plate is used with a flat substrate and the squeegee is housed inside the printing plate. Ink is fed directly into the mesh via a feeding system attached to the squeegee mount. This setup is shown schematically in figure 2.7 [60].

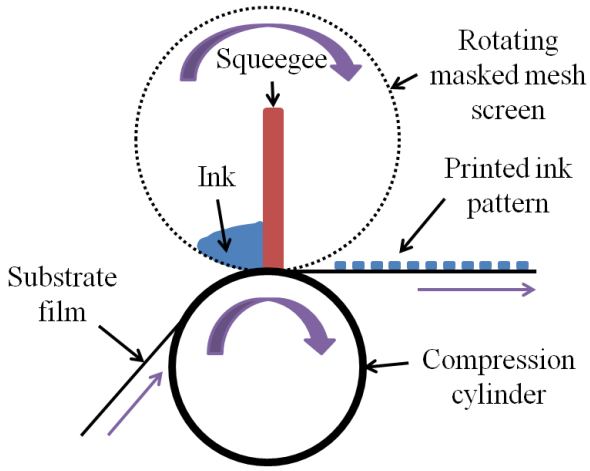

Figure 2.7. Screen printing: a schematic diagram of a *rotary screen-printing* setup. The printing plate is not flat, as in *flat bed screen printing*, but is in the form of a cylinder. The squeegee and ink feeding system is housed inside the cylindrical screen which transfers the printed image to a flat substrate sheet with the aid of a compression cylinder.

After the printing stage the inks must be dried. This can take place in an oven at a temperature high enough to quicken the drying process but not to cause any damage to either the ink or the substrate. This is particularly crucial when printing on textiles and flexible polymer substrates with low glass transition, melting and/or decomposition temperatures.

Screen printers come with varying degrees of automation. Small scale graphic arts projects typically utilise manual screen printers whereas large scale industrial print runs utilise either semi-automatic or fully automatic screen printers. Semi-automatic printers have a fully automated squeegees/flood bars and the lowering of the printing plate is also computer controlled. Only the placement of the substrate is performed manually. In fully automated screen printers everything is computer controlled with substrate sheets fed mechanically, either one by one for flat bed systems or as a roll in rotary systems. These systems may or may not have an automated drying system attached [58].

The screen printing technique is well suited for producing thick films (> 1μm) with inks that can have a wide range of viscosities. Generally, however, inks with higher viscosities, often called paste rather than ink, are used as the inks are left freestanding during the drying process and must not spread out. However, the print speed is not as fast as well established roll-to-roll techniques such as gravure and offset printing (squeegee speeds can be anything between approximately 30 [61] to 550 [62] mm s^{-1}, and web speeds of around 1 m^{-1} [62]), so screen print runs are often batch operated. While this is a very versatile technique, the print resolution is limited by the thread count of the mesh so the smallest features printable are typically in the order of 50 to 100 μm [63].

2.3.2 Inkjet printing

Screen printing is already a well established technique in the printed electronics sector but the inkjet process is the target for most current research in printed electronic architectures. Inkjet printing is also desirable because it is a mask-less, or direct write, printing process; the required image or pattern is directly printed onto the substrate without the need for a stencil. This drastically improves the efficiency of the print as there is the opportunity to waste very little ink and enhance and quicken image/pattern manufacture through computer aided design (CAD). Ink is transferred directly onto the substrate via a print nozzle, or print head, and the print head and ink supply are generally combined into a single unit. There are two basic variants of this technique: continuous inkjet and drop-on-demand (DOD) inkjet. In continuous inkjet systems a constant stream of ink droplets is created where only some of the drops are utilised for printing. In contrast, DOD systems only produce droplets when they are required. Both of these overarching techniques can be further

subdivided into process variants, described in more detail below. Continuous inkjet can be split into two subdivisions: binary deflection and multi deflection [58].

2.3.2.1 Continuous inkjet

In binary deflection, the ink drops are given one of two possible electrical charge values and this determines their deflection through the nozzle: the drop is either deposited on the substrate, or is directed into a gutter and recycled. Pressurised ink is ejected from the nozzle with the aid of an oscillating piezoelectric crystal, which pushes the ink. The size of the drops produced is dependent on the frequency of the oscillation, the diameter of the nozzle, and the viscosity and surface tension of the ink. Once out of the nozzle the drops pass through a charging electrode. Here the drops are, depending on the image signal, given a specific charge state or remain neutral. The jet proceeds past the deflector electrodes, which deflects the charged drops into a gutter, while the electrically neutral drops strike the substrate [58]. This process is shown in Figure 2.8 below.

Multi deflection inkjet printing is more complex but has the same basic setup as binary deflection printing. In this process, each drop is given its own unique charge state so that each drop can independently deflected to the desired position on the substrate. This allows the printer to image a short line. The scale of the line can be determined by the distance between the tip of the nozzle and the substrate. If this distance is increased, the scale of the line increases but the resolution of the printed image is decreased. Either the nozzle or the substrate may be moved in a lateral direction to create a two dimensional (2D) print image. The resolution in the lateral axis is decided by the velocity of the nozzle or substrate and the rate of ink drop

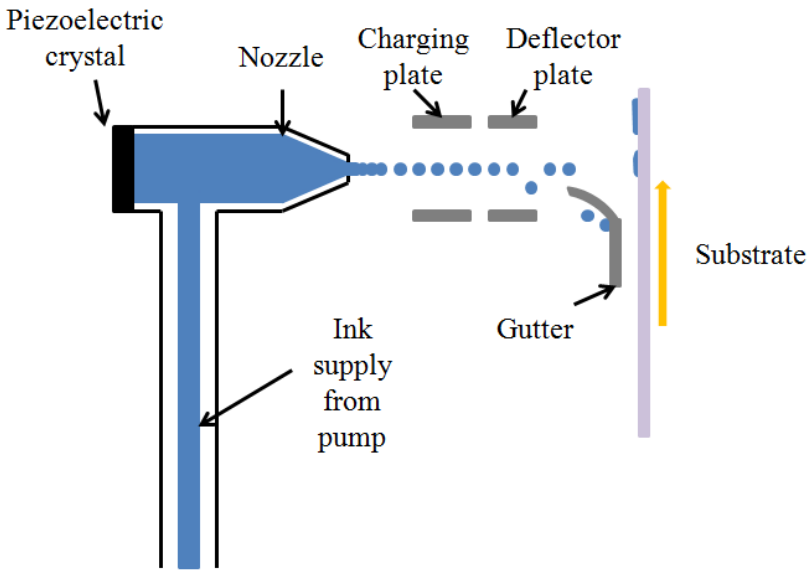

Figure 2.8. Inkjet printing: a diagram of a binary deflection continuous inkjet nozzle. The image signal to the charging plate gives drops one of two electrical states, either charged or neutral. The charged droplets are deflected into a gutter to be recycled while the neutral drops are directed towards the substrate for printing.

production. Alternatively, 2D deflection jets may be used so 2D images may be printed while the nozzle/substrate is stationary [58].

2.3.2.2 Drop-on-demand inkjet

The classification of DOD systems is based on how the ink drops are created. Ink drops may be created via any one of three routes: the thermal inkjet, the piezo inkjet and the electrostatic inkjet.

Thermal inkjet, see Figure 2.9, is the most widely used DOD system, being commonplace in most consumer desktop inkjet printers due to the ease of implementation and relative cost [58]. As the name suggests, a change in the ink temperature within the print nozzle is responsible for the production of the drop. Within the nozzle cavity there is a heating element which, upon receiving the electrical image signal, is momentarily activated. The element rapidly heats the ink

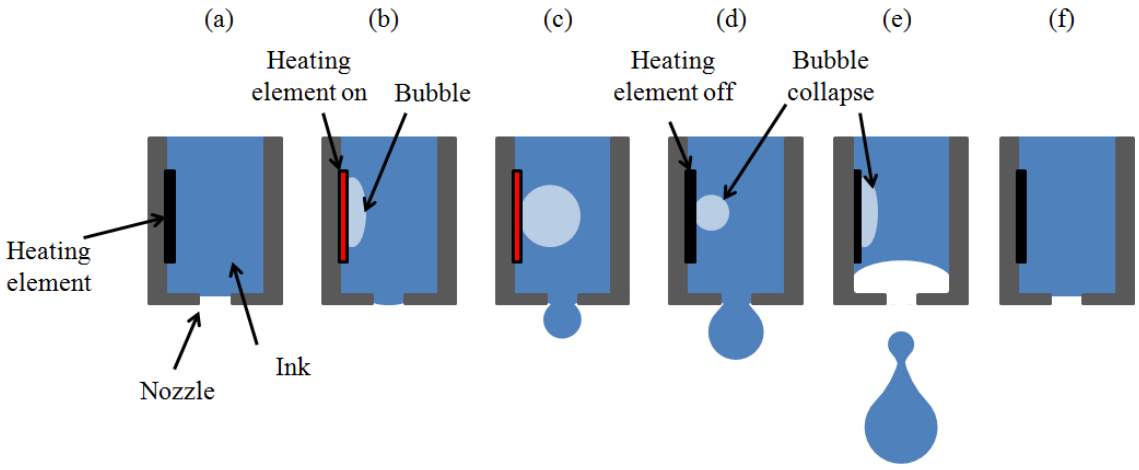

Figure 2.9. Inkjet printing: a series of schematic diagrams showing the production of an ink drop in a *thermal DOD inkjet* printer. (a) ink floods the nozzle cavity; (b) the image signal turns on the heating element which vaporises some of the ink, creating a bubble; (c) the bubble expands and begins to push liquid ink out of the nozzle; (d) the heating element cools and the bubble begins to collapse, ceasing to add liquid to the forming drop; (e) *break-off* occurs and the drop is ejected from the nozzle; (f) The cavity refills with fresh ink.

within the cavity, causing it to vaporise and form a bubble. The bubble displaces the remaining liquid phase ink and forces a drop out of the print nozzle. As the temperature drops the bubble collapses. As this occurs, capillary action draws fresh ink into the cavity and the drop is fully ejected from the nozzle [64]. This technique is also sometimes referred to as bubble jet [58]. Due to the small volume of ink held in the cavity, heating and cooling times are very quick and the drop frequency can be as high as 8 kHz. The drop diameter is of the order of around 35 µm [58]. Thermal inkjet printers tend to suffer from a build up of ink residue within the cavity from successive heating and cooling cycles. Practically this issue can be resolved simply by constructing the cavities within a disposable ink cartridge.

The *piezo inkjet* technique uses mechanical displacement of the cavity walls, through the action of a piezoelectric ceramic material, to produce ink drops [64]. There are two types of displacement modes used: extension or shear mode. The former changes the volume of the cavity whereas the latter changes the cavity geometry and is more widely used [64]. When the cavity receives the image signal, the piezoelectric

ceramic material responds by shearing the cavity, changing its shape and creating a pressure pulse. It is this pressure pulse that ejects the drop from the nozzle. This process is shown in Figure 2.10, below [58]. Piezo inkjet printers can produce drops at higher frequency than thermal inkjet printers and are able to use a wider variety of ink formulations, including hot melt inks which must be heated before being injected into the nozzle cavity [58]. Inks used in thermal inkjet must be made with a volatile component to allow the rapid vaporisation and bubble formation necessary for the creation of the ink drops. Piezo inkjet printers are, however, considerably more expensive due to the inclusion of piezoelectric ceramics and have previously been reserved for commercial and industrial applications [58], with the exception of Epson which uses piezoelectric print-heads on all of its products.

The final technique is electrostatic inkjet. This is a DOD variant that relies on the creation of an electrostatic field formed between the nozzle head and the substrate, modulated by the image signal [58]. Electrostatic inkjet is an umbrella term, and encompasses three further subdivisions: electrostatic inkjet

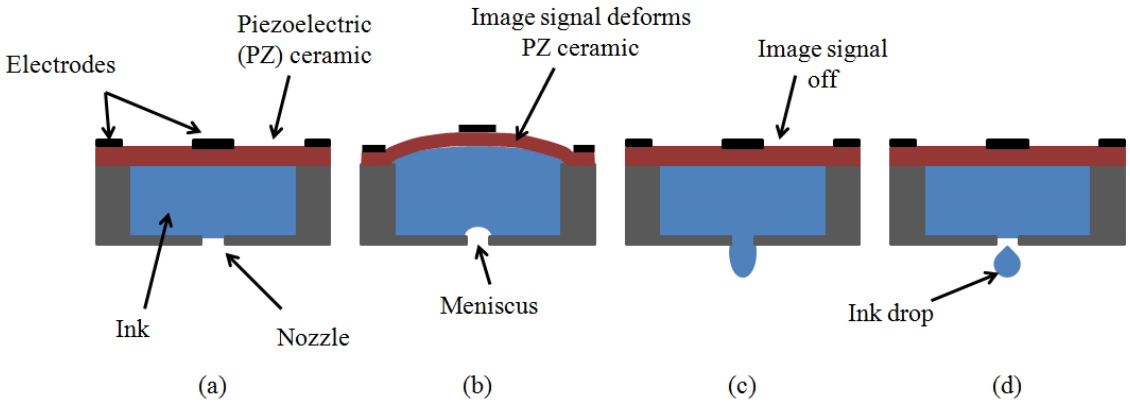

Figure 2.10. Inkjet printing: a series of schematic diagrams showing the production of an ink drop from a *piezo inkjet* system in shear mode; (a) ink fills the cavity; (b) the image signal is sent to electrodes on the piezoelectric (PZ) ceramic cavity wall. This deforms the ceramic, changing the shape of the cavity, and creates a meniscus at the nozzle; (c) the image signal ends and the PZ ceramic cavity wall returns to its original shape. Ink is pushed out of the nozzle by the resulting pressure pulse; (d) an ink drop is formed, and fresh ink refills the cavity.

by the Taylor effect, electrostatic inkjet with thermal effect control and electrostatic ink mist jet.

Electrostatic inkjet by the Taylor effect utilises an electrostatic field between the nozzle and the substrate. The force on the ink, which acts to draw it out of the nozzle, is in balance with the surface tension and viscosity of the ink in its rest state. The electrostatic field is modulated by the image signal in the form of a voltage pulse and this modulation momentarily increases the force on ink, forming a Taylor cone. From this cone a filament of ink may be drawn onto the substrate, forming a printed drop. The volume of the drop is determined by the duration of the image signal [65]. The benefit of this technique is that the filaments, and resultant ink drop diameters, are far smaller than the nozzle diameter, relaxing an otherwise important design constraint. In fact, there need be no complicated nozzle/cavity structure, simply a hole from which to draw the ink [58] [66].

Electrostatic inkjet with thermal effect control is a combination of the above method and the thermal inkjet technique. Here, a ring shaped heating element at the edge of the nozzle, controlled by image signal current pulses, is used to change the viscosity and thus the surface tension of the ink. A filament and subsequent ink drop is drawn via the electrostatic force between the nozzle and substrate [58].

Electrostatic Ink Mist Jet uses ultrasonic waves, focussed at the nozzle aperture, to produce a mist of very fine ink droplets which are directed to the substrate by an electrostatic field. A single printed pixel comprises a multitude of ink droplets.

In general, inkjets allow a more rapid progression from image/pattern design to printing as there is no time needed to create a stencil or master mask. The print

speed is, however, a limiting factor unless multiple print heads are used, with hundreds of nozzles per printing head. One drawback is that the nozzles do tend to become clogged over time, either from the drying of residual ink within the nozzle or from aggregation blockages from the use of nanoparticle suspensions [67] [68]. Either way, nozzle failures are critical in printed electronics where unbroken, uniform printed layers are often required. This can be combated by frequently cleaning the nozzles, either with water or specialised solvents or through the use of disposable print heads.

Another problem is how the ink dries on the substrate. If the ink is slow to dry then the printed ink drop undergoes the coffee ring, or coffee drop, effect [17]. This is a natural phenomenon that occurs when a drop, containing suspended particles of a solid, evaporates. As the drop dries, rings of deposited solid particles form on the substrate resembling a coffee ring stain. How the rings form is related to the speed of evaporation, the movement of the suspended particles and internal flows of fluid during evaporation [69] [70]. This effect is widely studied as it is completely undesirable not only in graphic arts but more critically in printed electronics applications, where uniform printed layers are necessary for many device structures.

A further contentious issue is that of satellite drops [71] [72]. During the ejection of a drop from the nozzle of an inkjet printer, the ink is forced into a thin, pole-like shape called a ligament. The drop forms from this ligament due to surface tension but smaller drops may form behind it as the ligament collapses. These satellite drops, far smaller than the primary drop, result in a decrease in printing precision and accuracy.

2.3.3 *Gravure printing*

Screen printing and inkjet printing can be readily adapted to batch production scale manufacturing and into a roll-to-roll production line for longer manufacturing runs. Both of these printing techniques, however, suffer from limited printing speed. As printed electronics become ubiquitous in both commercial and consumer technology, printed devices will need to be produced in greater numbers and at far increased speeds.

A printing technique, best suited for long and very large scale production runs, now being studied and applied for printed electronics applications is gravure printing [73] [74]. In this technique, illustrated schematically in figure 2.11, the substrate is fed in between two rollers: the compression roller and the gravure cylinder. It is the gravure cylinder that carries the image and transfers it to the substrate. This cylinder is constructed from steel, with a copper surface coating, deposited by electroplating. The image or pattern to be printed is chemically

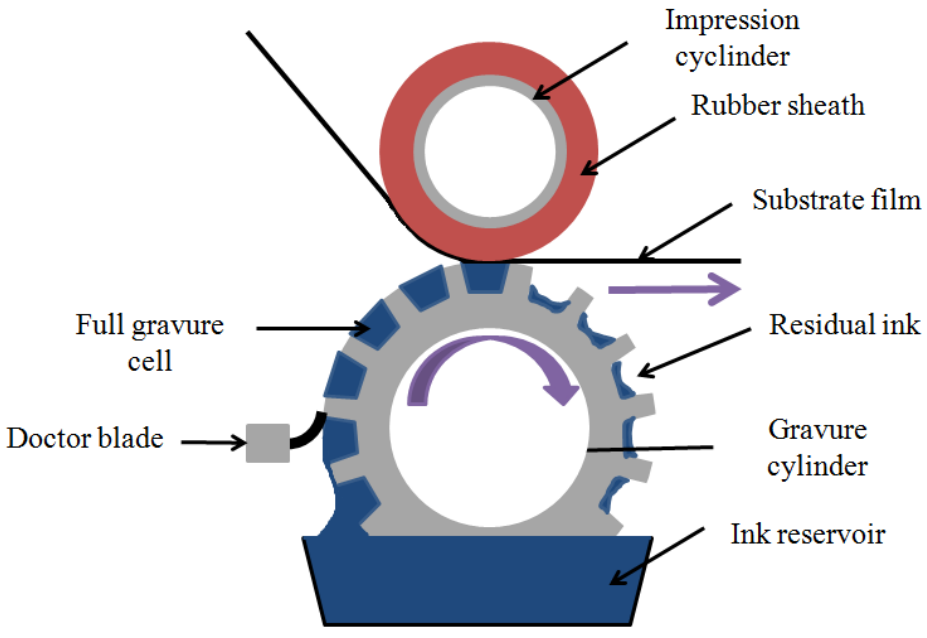

Figure 2.11. A schematic illustration of the gravure printing method.

etched or mechanically engraved (using a diamond scribe) onto the copper, with the image comprising gravure cells. The gravure cells in the surface of the copper act as wells which hold the ink to be deposited on the substrate as pixels, and the size and shape of the gravure cells determines how much ink is printed onto the substrate [75] [76]. Printing speeds of up to several metres per second are easily attainable using this technique but the high cost of producing the gravure cylinder creates a financial constraint, limiting its use to only very large print runs.

2.4 Summary

Printed electronics are now an established area of technology with printed components, such as resistors and capacitors, already common in many devices in the form of PCBs. Research is now gearing towards creating more complex printed structures such as transistors, solar cells and touch sensors. Conducting composite materials, important for printed cermet, and carbon resistors are now being recognised as being ideal for use in sensor applications, in particular vapour and touch pressure sensing.

While early printed composite touch sensors have needed additional structuring and patterning of bumps/posts to enable the touch location sensing characteristic, a single layer of intrinsically touch sensitive composite ink which may be directly printed over device electronics is desired. Such a material is described and studied in this research. Screen printing remains the most widely spread form of printing used in the printed electronics industry due to its ease of use and its flexibility with regards to ink's physical properties, such as viscosity. Inkjet printing, however, is the target of most current research in printable electronic technologies.

3. Physical principles and mechanisms for electrical transport in composites

3.1 Introduction

This chapter presents the background physical knowledge relevant to a study of electrically conducting behaviour of composites and how this is linked to their physical structure. The chapter begins by first considering the physical behaviour of typical conducting composite systems; this will identify the main topics that need to be considered in the context of composite behaviour. Next, percolation theory and effective medium theory will be discussed as these theories underpin the understanding of conduction in composite materials. The chapter will then progress to cover electrical conduction in conductors, semi-conductors and insulators, before delving into quantum tunnelling, field emission and thermionic emission. A brief summary of core concepts will bring this chapter to a close.

3.2 Physical characteristics and behaviour of typical composite materials

A typical conducting composite comprises electrically conducting filler particles dispersed in an electrically insulating matrix material. This class of material has been a focus of academic and industrial research for over half a century [77]. A wide variety of conducting filler materials have been used for the manufacture of conducting composites; these range from simple metal powders, such as nickel [78] and silver, [79] to carbon black (a paracrystalline, or semi-amorphous, form of carbon which is

produced as a high surface-area-to-volume ratio powder) [80], and to more recent nano-materials such as carbon nanotubes [81] and graphene [82]. The size and geometry of the filler particles can be tailored; particles can range in size from tens of nanometres to tens of micrometres [83] and can be either amorphous or a more ordered polyhedral [84], for example spherical or high aspect ratio acicular [85] and flake shaped [86]. The choice of insulating matrix material depends on the desired application: conducting composites have been fashioned with insulating matrices made from rigid bulk materials such as cement [87], more flexible polymeric materials including polyethylene [88], polyethylene terephthalate [89] and epoxy resins [90], and more recently, printable insulating solutions [91].

Conducting composites have an electrical conductivity that is highly dependent on the fraction of conducting filler particle material used in their manufacture. Increasing the filler volume fraction up to a critical concentration, called the percolation threshold, causes a dramatic onset of direct connections between filler particles creating electrically conducting pathways through the body of the composite. Classically the critical volume fraction has been approximated to be circa 16 % in 3D composite systems and about 45% in 2D composite systems [92] [93], in the case of spherical filler particles. Many composite systems using small (micro- and nano-scale filler particles), however, exhibit critical volume fractions below this theoretical limit and this effect can be linked to the filler particle size [94]. The inter-particle distance tends to decrease as the diameter of the filler particle is reduced, so the percolation threshold becomes dependent on the particle size in composites made with small filler particles [94]. This dependence has been described using percolation and effective medium theories, explained in the following section 3.3.

As well as being dependent on the filler fraction, conducting composite electrical conductivity can be sensitive to applied compressive force. Applied force pushes the filler particles together, simulating the effect of increasing the filler fraction and leading to the creation of conducting pathways through the composite, as depicted in figure 3.1. The mechanisms by which charge is transported through composite materials is of great interest and research has shown that composite materials conductivity can be complex, involving percolative conduction as well as quantum tunnelling conduction and hopping mechanisms, which are explained further on in this chapter. Additionally, the electrical transport behaviour may involve charge trapping and space charge limited currents (SCLC) within the insulating matrix. These are described in more detail in sections 3.4 and 3.5. When a composite system with a conducting filler particle volume fraction close to the percolation threshold is compressed it can switch from an insulating to a conducting state; the conduction mechanisms responsible for electrical transport through the composite can vary during this transition, and this is the focus of this study.

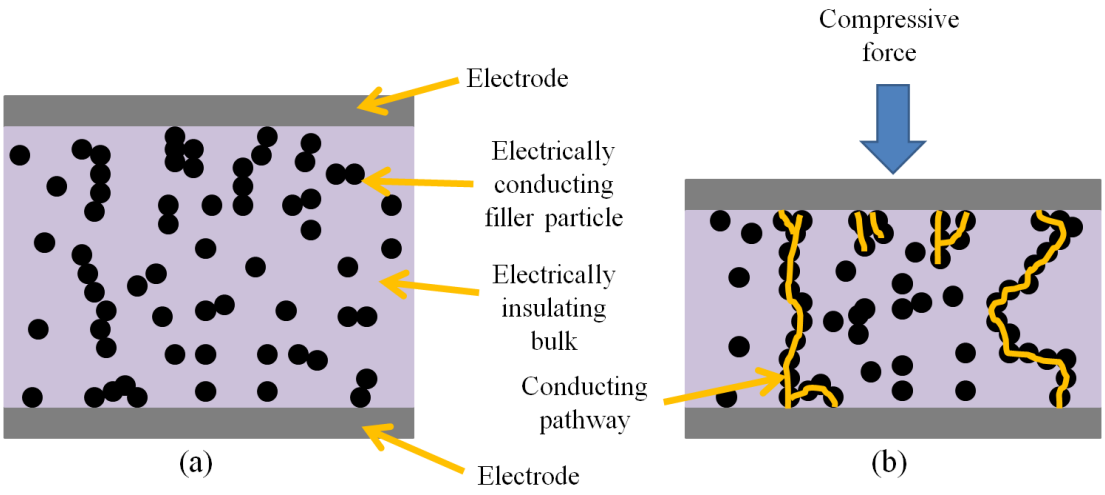

Figure 3.1. A composite system in (a) an uncompressed state. Solid circles represent the conducting filler particles; (b) under compression.

3.3 Percolation theory and effective medium theory

3.3.1 Percolation theory

Percolation theory was first developed by Broadbent and Hammersley in 1957 [95]. The original work was intended to describe how water flows through a porous material: the material was envisaged as a three dimensional (3D) array of randomly dispersed independent points. These points represent solid areas of the material, where water cannot flow. Connections between the points represent holes or channels in the material and it is through these channels that water may flow. In essence, the water would flow along the connections and around the points. A probability, *p*, is assigned to the existence of a connection and therefore the probability of there being no connection between any two points is *1-p*.

In the case of composite materials, this model is applicable in describing the flow of charge along electrically conducting pathways through an otherwise insulating medium by making the analogy that the electrically insulating bulk of the composite is the porous material (the points of the array), the direct electrical connections between filler particles are the akin to holes in the porous material and that the electrical charge is equivalent to the flow of water through the porous material. With this model, the electrical conductivity, σ, of a composite can be described as a function of the volume fraction of conducting filler particles in the relation [96]:

$$\sigma \propto \left(\varphi - \varphi_C\right)^t \qquad (3.1)$$

where φ is the volume fraction of conducting filler particles, φ_C is the volume fraction of the percolation threshold and t is an exponent which has a value between 1 and 6.27 for 3D systems and varies depending on what type of percolation model is used [97].

Initial increases in the filler volume fraction do not significantly increase the electrical conductivity of the composite until the percolation threshold is reached. Conducting pathways form through the body of the composite material when the filler volume fraction equals that of the percolation threshold. A dramatic rise in the electrical conductivity occurs as the filler volume fraction is increased above the percolation threshold and more conducting pathways form through the composite. A physical representation of percolation is shown in figure 3.2, while the generalised behaviour of the electrical conductivity as a function of filler volume fraction is shown in figure 3.3. The percolation model is limited in that it realistically

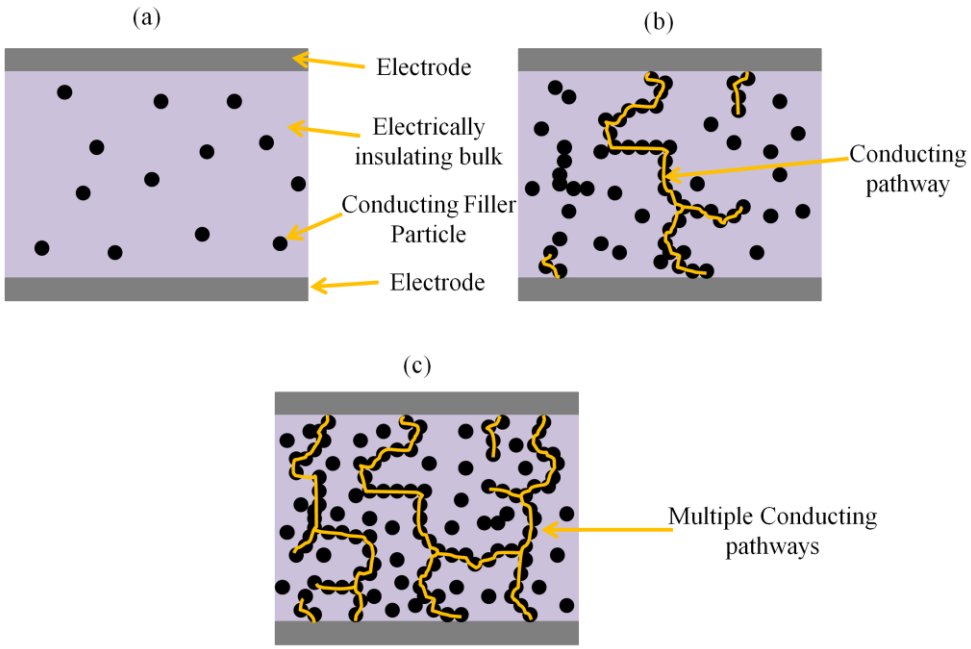

Figure 3.2. A composite system with (a) a low conducting filler content fraction; (b) a filler content fraction equal to the percolation threshold; (c) a filler content fraction larger than the percolation threshold.

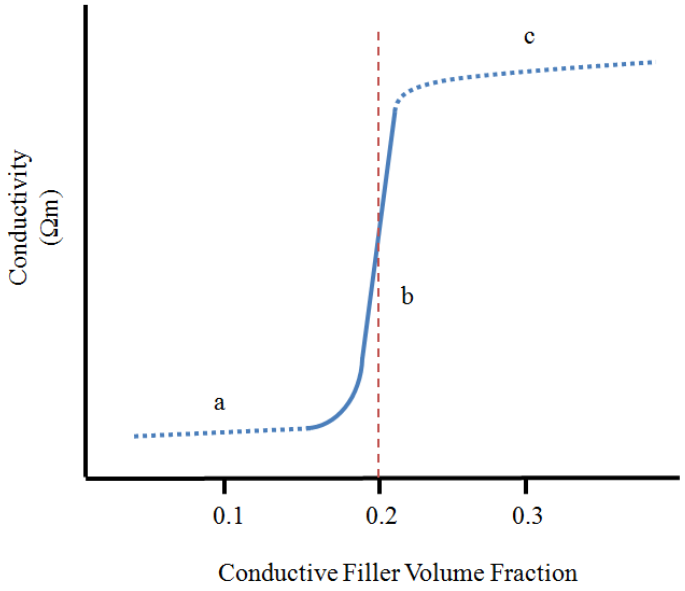

Figure 3.3. The general behaviour of composite electrical conductivity (solid curve) as a function of conductive filler volume fraction: (a) the composite has a conductivity close to that of the bulk insulating matrix material; (b) the percolation threshold. In this example the percolation threshold is at the volume fraction 0.2, signified by the dashed red line; (c) The maximum conductivity is reached. Percolation theory cannot predict regions (a) and (c).

describes the conductivity only above the percolation threshold and it does not describe the ohmic behaviour of conductivity below the percolation threshold. Nor is it capable of describing how the conductivity tends to a maximum value at high filler volume fractions. The model typically describes the transition from electrically insulating to a conducting state as very sharp, as only small changes in the filler volume fraction can lead to a dramatic change in the electrical conductivity. In real composite systems this is not always the case [98]. Particle geometry or alignment is not considered as the model is only concerned with whether or not a connection exists between points in the composite. A final but crucial limitation is that percolation theory is phenomenological, so it does not provide insight into the physical processes responsible for charge transport in the composite system.

3.3.2 Effective medium theory

Effective medium theory (EMT) [99] [100] is built upon identical fundamental principles as for percolation theory. Here, a conducting composite system is modelled as a 3D array of randomly distributed independent points. In percolation theory, the points represented the insulating bulk material of the composite but in EMT, they are representative of the conductive filler particles. Each independent point is given an electrical resistance between each of its nearest neighbouring points. An average resistance value is then calculated from these and assigned to each of the connections between the points. This process creates a single effective medium that is symmetric, homogeneous and retains the macroscopic properties of the percolation model [101], i.e., it exhibits the same generalised conduction behaviour. EMT, by averaging the material properties, provides a more accurate approximation of the conductivity at φ_C by removing the very sharp transition from insulating to a conducting state which is a typical feature of percolation theory [97].

General Effective Medium theory (GMT), developed by McLachlan [102], adds further detail by taking into account the conductivity contribution from the conducting filler particle shape, size and orientation. Figure 3.4 compares the percolation theory and GMT model curves. The GMT relation is given below [103]:

$$\frac{f\left(\sigma_l^{1/t}-\sigma_m^{1/t}\right)}{\sigma_l^{1/t}+A\sigma_m^{1/t}}+\frac{\varphi\left(\sigma_h^{1/t}-\sigma_m^{1/t}\right)}{\sigma_h^{1/t}+A\sigma_m^{1/t}}=0 \qquad (3.2)$$

where σ_l and σ_h are the electrical conductivities of the low and high conductivity components (the insulating material and conducting filler particles, respectively) of the composite; σ_m is the average electrical conductivity of the

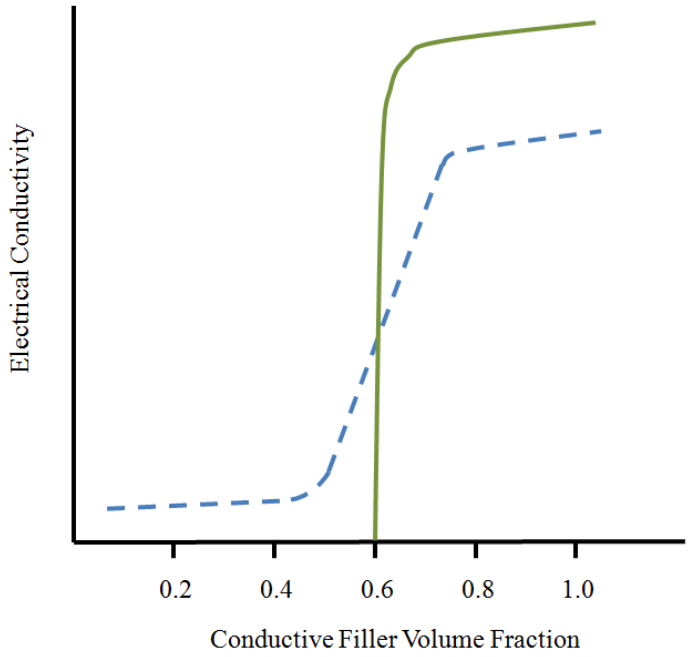

Figure 3.4. An illustrative comparison of the predictions of electrical conductivity from percolation theory (green solid line) and effective medium theory (blue dashed line). The percolation threshold in this example is at 0.6 volume fraction.

effective medium; f and ψ are volume fractions of the low and high conductivity components; t is an exponent; A is a ratio of the low conductivity component critical volume fraction and the high conductivity component critical volume fraction, or f_c $/\Psi_c$. The exponent, t, is defined by the following relations for orientated and randomly orientated particles:

$$t = {}^{1}\!\Big/\!_{\left(1 - L_f + L_\varphi\right)} \text{ Orientated ellipsoids} \tag{3.3}$$

$$t = {}^{\left(m_f \times m_\varphi\right)}\!\Big/\!_{\left(m_f + m_\varphi\right)} \text{ Random ellipsoids} \tag{3.4}$$

where L_f, L_ψ, m_f, and m_ψ are phenomenological constants of the low and high conductivity components. The value of these constants is dependent on the shape of the particles. For example, t = 1/3 for spherical filler particles.

The ratio A is defined as follows:

$$A = {(1 - \varphi_C)}/{\varphi_C} = {f_C}/{(1 - f_C)} \tag{3.5}$$

where ψ_C and f_C are the critical volume fractions for the high conductivity and low conductivity components respectively. These critical volume fractions can in turn be related to the orientation and shape of the low and high conductivity components as a function of the phenomenological constants introduced above:

$$\varphi_C = {L_\varphi}/{(1 - L_f + L_\varphi)} \tag{3.6}$$

$$\varphi_C = {m_f}/{(m_f + m_\varphi)} \tag{3.7}$$

While providing a better description of percolative behaviour, GMT is still limited as a phenomenological model.

3.4 Electrical conduction in metals, semiconductors, and insulators

It is important to reflect on electrical conduction in metals, semiconductors and insulators when considering conduction behaviour in composite materials as the former two are often used as conducting filler material, whereas the bulk matrix of a composite is usually an insulator. These considerations allow a quantitative model of electrical conduction in composite materials to be constructed. Electrical conductivity is defined as a measure of a material's ability to pass an electric current, and is the reciprocal of electrical resistivity (a measure of a material's tendency to

oppose the flow of an electric current with the S.I unit ohm metres, Ωm). It has S.I units of siemens per metre (Sm^{-1}). When an electric field exists within a material an electric current will flow. A material's resistivity is the ratio of the electric field magnitude, E (Vm^{-1}), and the subsequent current density, J (Am^{-2}):

$$\rho = {}^{E}/_{J} \tag{3.8}$$

The conductivity is the reciprocal of this expression. In the case of a uniform material, with constant cross-sectional area, the resistivity relates to the resistance and dimension l;

$$\rho = {}^{RA}/_{l} \tag{3.9}$$

where R is the electrical resistance, A is the cross-sectional area and l is the length of the material.

Conductivity in metals, semiconductors and insulators, or the lack thereof, may be explained with band theory. Whilst in classical physics particles may take on any arbitrary energy value, in quantum mechanics energy is quantised; in an atom there are energy levels which electrons can occupy and values which lie in between these fixed energy levels are forbidden. An energy band can be understood as a group of energy levels closely spaced together, i.e. they have similar energy values. Energy bands arise from the nearly free electron model, which is discussed in section 3.4.2. A material may contain several energy bands but, when discussing conductivity, two specific energy bands are considered: the valence band (VB) and the conduction band (CB). Electrons in the CB may move freely as part of an electric current. Metals, semiconductors and insulators all have differently filled energy bands and this changes their electrical conductivity behaviour. The band structure, and hence the

conductivity behaviour of metals, semiconductors, and insulators will be discussed in turn.

3.4.1 Metals

Metals are well described using the free electron model [104]. A metal is comprised of a lattice of atoms which have outer electrons that are able to dissociate from their parent atoms and move freely through the lattice structure, known as a positive ionic lattice. This "sea" of electrons allows the metal to conduct electricity in the presence of an electric field. In the free electron model, it is assumed that the electrons do not interact strongly with the ionic lattice, or with each other: essentially they can be treated as independent particles.

The free electrons do not interact with the lattice due to the screening effect, which reduces the Coulomb interactions between the electrons and the ions. Interactions between the conduction electrons are rare and may be ignored due to the Pauli exclusion principle, which states that no two electrons may occupy the same quantum state. As such, each orbital may hold 2 electrons, one in a spin-up orientation and the other in a spin-down orientation.

Electrons fill these orbitals according to the Fermi-Dirac distribution, which gives the probability that an electron orbital at an energy ϵ will be occupied [104]:

$$f(\epsilon) = \frac{1}{\exp[(\epsilon-\mu)/k_B T]+1} \tag{3.10}$$

where k_B is the Boltzmann constant, T is the temperature in Kelvin, and μ is the Fermi level, or total chemical potential for electrons (this corresponds to the amount of energy required to add one more electron to a system, or a theoretical energy level

which has a 50% probability of being occupied). At $T = 0$, the total chemical potential is equal to the Fermi energy.

Electron wavefunctions may be calculated using the time independent free particle Schrödinger equation in three dimensions [104]:

$$-\frac{\hbar^2}{2\mathrm{m}}\left(\frac{\partial^2}{\partial \mathrm{x}^2}+\frac{\partial^2}{\partial \mathrm{y}^2}+\frac{\partial^2}{\partial \mathrm{z}^2}\right)\psi_{\mathbf{k}}(\mathrm{r})=\epsilon_{\mathbf{k}}\psi_{\mathbf{k}}(\mathbf{r}) \tag{3.11}$$

where $\hbar$ is the reduced Planck constant, m is the electron mass, ψ_K is the wavefunction of the electron, ε_K is the electron energy, and $\boldsymbol{r}$ is a vector of coordinates in space. The solution to this equation is a travelling plane wave:

$$\psi_{\mathbf{k}}(\mathbf{r})=\exp(\mathrm{i}\mathbf{k}\cdot\mathbf{r}) \tag{3.12}$$

$$\text{For wavevector components } \mathrm{k}_{\mathrm{x,y,z}}=\pm\frac{2\mathrm{n}\pi}{\mathrm{L}}$$

where the electrons are confined to a cube of sides L in length. The Fermi energy in such a case is:

$$\epsilon_{\mathrm{F}}=\frac{\hbar^2}{2\mathrm{m}}\left(\frac{3\pi^2\mathrm{N}}{\mathrm{V}}\right)^{2/3} \tag{3.13}$$

where N is the total number of electrons in the system and V is the volume of the system.

In metallic materials, the Fermi energy lies inside the conduction band, so the dissociated outer electrons may contribute freely to an electric current. With increasing temperature, the Fermi level increases as thermal electrons are excited to higher energy levels. This may be represented using the density of states $D(\epsilon)$, in equation 3.14 (using eq. 3.13 rearranged for N) and figure 3.5, which shows the

density of occupied orbitals per unit energy. In figure 3.5, as the temperature of the system is increased, electrons are promoted to higher orbitals and move from region *a* to region *b* in the figure [104].

$$D(\epsilon) = \frac{dN}{d\epsilon} = \frac{V}{2\pi^2} \cdot \left(\frac{2m}{\hbar^2}\right)^{3/2} \cdot \epsilon^{1/2} = \frac{3N}{2\epsilon} \qquad (3.14)$$

Electrical resistance in metals is caused by interactions between the electrons and lattice imperfections and interactions with phonons. Phonons are quantised lattice vibrations which increase with temperature. Generally, a metal will have a finite electrical resistance at zero temperature due to imperfections in the crystal lattice. As the temperature of the metal is increased thermal phonons are generated and these further scatter the conduction electrons. Over the temperature range used in this study (room temperature to 150 °C), the temperature dependence of

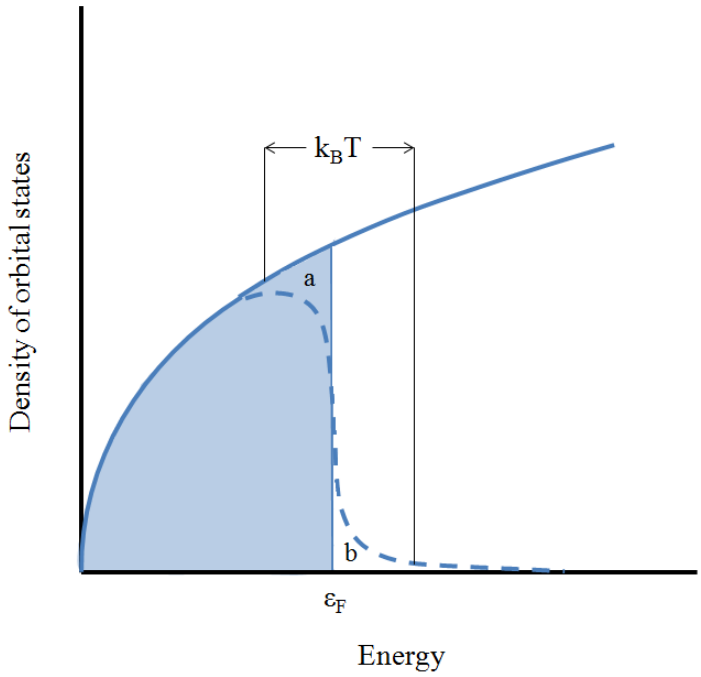

Figure 3.5. Illustration of how the occupied orbital density varies with energy. The solid line is the density of states, the shaded area represents the filled states at zero temperature. The dashed line is the density of filled orbitals at a finite temperature.

the electrical resistivity of metals can be regarded as linear, following the relation given below:

$$\rho(T) = \rho_0[1 + \alpha(T - T_0)] \quad (3.15)$$

where α is an empirically calculated constant called the temperature coefficient of resistivity (for example, α_{copper} = 3.9 x 10^{-3} K^{-1} α_{silver} = 3.8 x 10^{-3} K^{-1}), T is the temperature and ρ_0 is the electrical resistivity at the reference temperature, T_0. As the temperature is increased, the resistance of a metal will also increase.

Over larger temperature ranges, the resistivity of a metal follows the Bloch-Gruneisen function [105] and Matthiessen's rule, shown in equation 3.16 [104]:

$$\frac{1}{\mu} = \frac{1}{\mu_L} + \frac{1}{\mu_i} + \cdots \quad (3.16)$$

where μ is the overall electron mobility, and μ_L and μ_i are the electron mobilities due to phonon and impurity scattering respectively. The rule may be extended to accommodate scattering due to lattice imperfections or any other source of electron scattering.

Matthiessen's rule states that the average mobility of an electron in a metal can be a series summation of electron mobility due to various scattering sources, such as impurity (lattice defects from impurity atoms) and phonon scattering. The different scattering mechanisms, if simultaneously present in a metal, may each be described using the Bloch-Gruneissen function and then added in series to calculate the actual resistivity.

3.4.2 Semiconductors

Semiconducting materials require a more detailed model because of the importance of band structure to their electrical behaviour. In semiconducting materials the Fermi energy is found in between the valence band and the conduction band, in an aforementioned energy gap. In the nearly free electron model, the band electrons are treated as being weakly perturbed by the positive ionic lattice [104] [106]. The energy gaps originate because of Bragg reflection. Bragg's Law gives the angles for coherent and incoherent scattering within a lattice, and is shown below [107].

$$2d \sin \theta = n\lambda \tag{3.17}$$

where *d* is the interplanar distance (the size of the gap between lattice planes), θ is the scattering angle, *n* is an integer and λ is the wavelength. Figure 3.6 shows a plot of energy against wavevector *k* for nearly free electrons in a lattice with lattice vector *a*. An energy gap exists at $k = +/- \pi/a$. The Bragg condition for diffraction is defined as $(k + G)^2 = k^2$ and, in one dimension, becomes:

$$k = \pm\frac{1}{2}G = \pm n\,{}^{\pi}/_{a} \tag{3.18}$$

The region in reciprocal space between $k = \pi/a$ and $k = - \pi/a$ is known as the first Brillouin zone. Energy gaps occur at other values of *n* in equation 3.18. At the edges of the Brillouin zone, the electron wavefunctions comprise of equal parts moving to the left and to the right, that is, they are standing waves. These standing waves have different energies and so an energy gap of width E_g exists if the standing waves differ in energy by E_g [104]. The filling of orbitals in semiconductors is shown in figure 3.7. While the Fermi level is often in the forbidden energy gap, the VB and CB

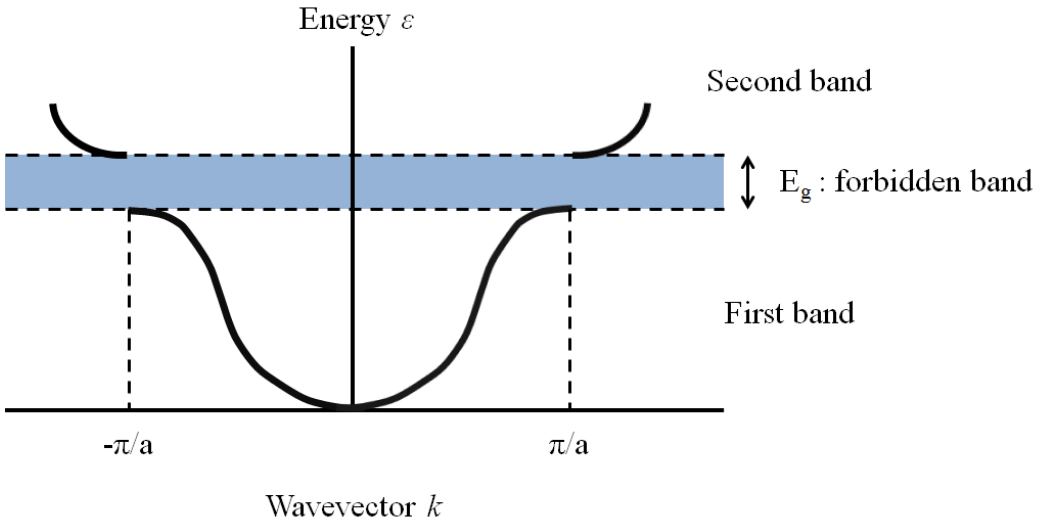

Figure 3.6. A schematic diagram of the first Brillouin Zone showing the first and second energy bands, separated by the energy gap (the shaded region). The vertical dashed lines indicate the edges of the Brillouin zone.

of semiconductors are close enough together for electrons to thermally populate the CB, leaving positive "holes" in the VB. At zero temperature, intrinsic (un-doped) semiconductors are perfect insulators but, as the temperature increases, electrons are thermally excited into the CB (the Fermi level rises), increasing the conductivity of the semiconductor. The temperature dependence of electrical resistivity for intrinsic semiconductors can be expressed in the relation on the following page [108].

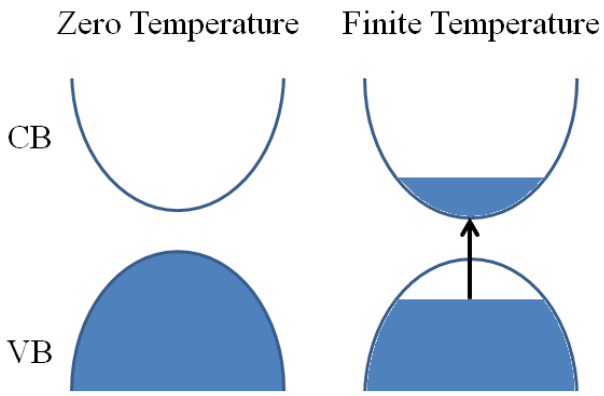

Figure 3.7. A schematic illustration of the filling of energy bands in semiconductors at zero and finite temperature.

$$\rho = \rho_0 \exp(\alpha/T) \quad (3.19)$$

where ρ_0 is the extrapolated initial, intrinsic resistivity, α is a constant equivalent to $E_g/2k_B$ (where E_g is the energy required to promote charge carriers to the conduction band and is equal to the energy gap if no impurity states are present, and k_B is the Boltzmann constant), and T is the temperature.

Extrinsic (doped) semiconductors have an electrical conductivity with a more complicated temperature dependence. With temperature increasing from 0 K, the electrical resistance will initially drop as majority charge carriers are released from either the donors or acceptors. Further increases in temperature will cause the resistance to then increase, due to the mobility of the carriers decreasing, as would happen in a metallic material, before the thermal charge carriers overcome the dopant charge carrier population and the semiconductor behaves as though it were intrinsic. The higher the dopant concentration, the lower the electrical resistance and the more these temperature dependent effects will be seen [109].

In non-crystalline semiconducting materials, charge may move via a quantum tunnelling effect between localised sites, termed variable-range hopping. This is explained further in the next subsection.

3.4.3 Insulators

Like semiconductors the Fermi energy or Fermi level, in electrically insulating materials, lies in a forbidden energy gap. The difference between semiconductors and insulators is that while the conduction band in a semiconductor can be easily populated with thermally excited charge carriers, allowing electrical current to flow, the valence band and conduction band of insulators are typically too far away from

the Fermi level for this to happen. That said, charge may be injected into insulating materials much in the way charge is injected into a vacuum from a metal object by thermionic emission. The emitted charge forms a cloud, or space, within the material hence the name space charge limited current. In solids, space charge limited current occurs only when the injected carrier density overcomes the thermal-free carriers (which is a small number in insulating materials). When this occurs, the current follows what is known as Child's law, which states that the current between two plane parallel electrodes varies as a power of anode voltage. This relation holds for insulators with no charge traps or scattering [110]:

$$I = JS = \alpha \frac{SV^{3/2}}{d^2} \tag{3.20}$$

where *J* is the current density, *S* is the anode area, α is a constant, *V* is the anode voltage and *d* is the separation between the cathode and anode. In the case of strong scattering of charge carriers the Mott-Gurney square law is applicable [111] [112]:

$$J = \frac{9}{8} \varepsilon \mu \left(\frac{V^2}{L^3}\right) \tag{3.21}$$

where ε is the dielectric constant of the insulating material, μ is the carrier mobility (indicating how quickly a charge carrier moves through a material under an electric field; the ratio of drift velocity to electric field), and *L* is the length of the plane parallel sample. Trapping sites may exist in the forbidden energy gap, which can be described as shallow traps or deep traps. Shallow traps are close to the conduction band above the Fermi level whereas deep traps are closer to the valence band below the Fermi level. The voltage dependence of the current in insulating materials is illustrated in figure 3.8. Traps are created by chemical impurities and

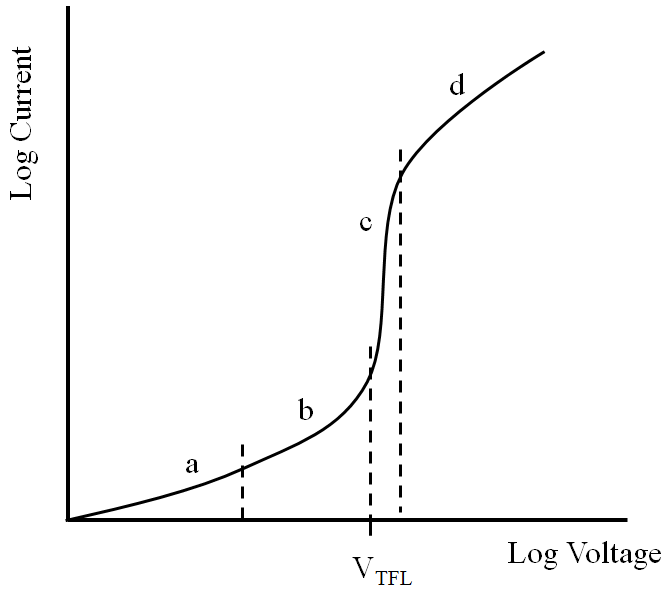

Figure 3.8. The space charge limited current (SCLC) observed in an insulator may exhibit up to four characteristics, all shown here: (a) ohmic behaviour seen at low current and voltage; (b) shallow trap behaviour; (c) deep traps become full and no longer inhibit current flow; (d) trap-free behaviour following either Child's Law or the Mott-Gurney square law.

physical deformations within the insulating structure. Chemical impurity traps operate by having a different electron (or hole) affinity to the surrounding atoms of the insulator. When the electron affinity is greater than that of the surrounding lattice, a trap for electrons is created. The "depth" of the trap is dependent on the difference in affinities. Physical deformations act to modify the energy levels of the insulator, creating empty energy states within the energy gap, which may become filled and trap charge. Initially, charge injected into an insulator will obey Ohm's law, but charge will begin to fall into traps as the current increases.

Current behaviour in an insulating material with shallow traps is very similar to the case of trap-free insulators. In the case of deep traps, however, a significant number of charge carriers fill the trap site and do not contribute further to the electrical current. When the trap site becomes filled, a discontinuous rise in the current is observed before the current increases according to Child's law [111] [113].

This pattern of behaviour can be observed multiple times as traps can exist at higher voltages.

Charge may exit traps either through thermal excitation or with the assistance of an external electric field. Given enough thermal energy, trapped charge may gain enough kinetic energy to exit a trap and contribute to electrical conduction in a material. In a process known as Variable Range Hopping [114], trapped charges absorb phonons and use the acquired energy to "hop" from one localised site to another. Charge will attempt to move to another site of similar energy, no matter the distance to that site, hence the "variable range" term. The ability of charge to hop into higher energy trap sites is largely dependent on the amount of energy acquired from the absorbed phonon. This thermally activated mechanism is important in both semiconducting and insulating materials, and is illustrated in figure 3.9 [101].

Alternatively, an electric field may modify or even destroy a trap in what is known as the Poole-Frenkel Effect [115]. Here, an electric field lowers the trapping potential in one dimension, allowing trapped charge to either flow out of the trap

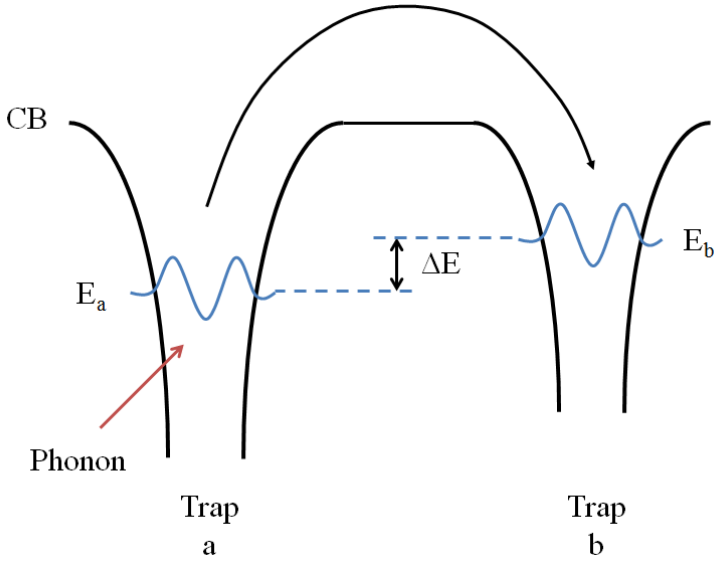

Figure 3.9. A schematic illustration of the variable range hopping mechanism.

or tunnel through the potential barrier and escape the trap, see figure 3.10 [101]. This modification of the trapping potential is analogous to the Schottky effect, which is explained in greater detail in the following section.

3.5 Thermionic emission

Thermionic emission is the process by which charge may be emitted from a surface, or escape a potential barrier, using acquired thermal energy. The minimum energy required to escape the surface of a material is called the work function, denoted as φ.

In a material, such as a metal, the conduction electrons will be distributed in energy levels up to the Fermi energy, E_f. Therefore, the energy required to escape the surface of the metal is $E_f + \varphi$. If the temperature of the metal is increased above absolute zero, electrons may acquire thermal energy and use this energy to overcome the potential barrier, or work function, and escape the surface of the metal: thermionic emission. Richardson calculated that thermionic emission current density

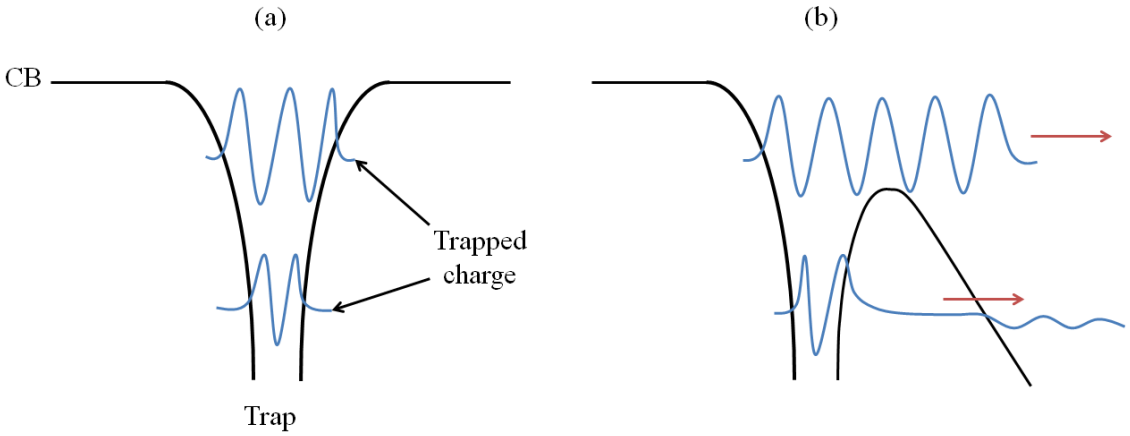

Figure 3.10. A schematic illustration of (a) a trap site, with no external field present, containing trapped charge; (b) a trap site in the presence of an external electric field: the Poole-Frenkel Effect.

is dependent on the square of temperature, and the relation is as follows [116] [101]:

$$J = A_0(1-\sigma)(k_B T)^2 \exp\left(-\varphi/k_B T\right) \quad (3.22)$$

where A_0 (A m^{-2} K^{-2}) is a universal constant, σ is the reflection coefficient (number of electrons reflected at the conductor/insulator interface, taking a value between 0, full transmission and 1, full reflection), k_B (eV K^{-1}) is the Boltzmann constant, φ (eV) is the workfunction of the conductor, and T (K) is the temperature. The relation for thermionic emission is modified by two phenomena: the image potential and the Schottky effect. These are discussed in turn.

3.5.1 Image potential

When a point charge leaves a conducting surface, it experiences an electrostatic force with that surface that may be modelled by replacing the surface with a mirror point charge an equal distance from the surface in the opposite direction [117]. This setup is shown schematically in figure 3.11. The attractive force experienced by the charge may be calculated using:

$$F = \frac{e^2}{4\pi\varepsilon}\frac{1}{(2x)^2} \quad (3.23)$$

where x is the distance separating the charges from the surface and e is the charge of an electron. Integrating equation 3.23 from zero to infinity gives the potential of the point charge.

$$V(x) = -\frac{e^2}{16\pi\varepsilon x} \quad (3.24)$$

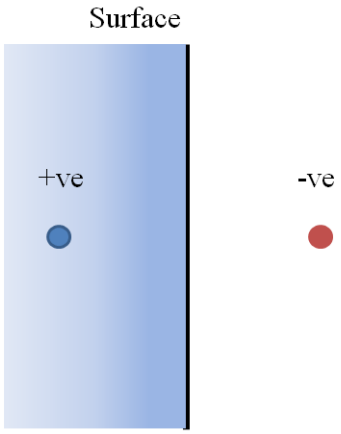

Figure 3.11. A schematic illustration of the theory of mirrored charge.

To escape the surface, the charge must overcome both the work function and the image potential.

3.5.2 Schottky effect

An external electric field, given in 3.24, can have a significant effect on a potential barrier and, consequently, on the conduction mechanisms associated with it.

$$V(x) = -eEx \tag{3.25}$$

The external electric field acts to lower the potential barrier, rounding its edges and causing it to slope, as shown in figure 3.12 [101]. In extreme situations, a very large electric field will triangulate the potential barrier, which is the basis for field assisted tunnelling; this is explained further in the following subsection. This lowering of the potential barrier is known as the Schottky effect [118] [119]. It is deliberately utilised in electron emitting devices, such as field emission tips in scanning electron microscopes, to help facilitate the generation of intense electron beams. The combined diminutive effect of the image potential and Schottky effect on the potential barrier may be found by summing the two, and then differentiating (and

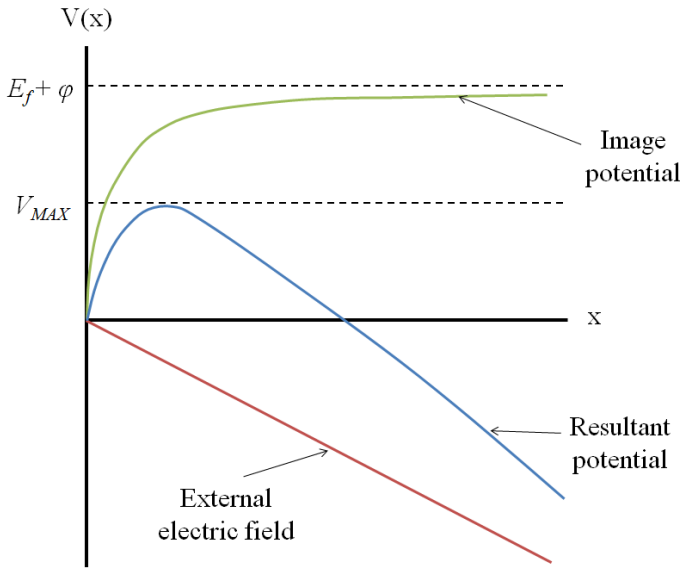

Figure 3.12. An illustration of the effect of the image potential and the Schottky effect on a potential energy barrier.

setting equal to zero) to find a maximum barrier reduction quantity, V_{MAX}.

$$V(x) = -\frac{e^2}{16\pi\varepsilon_0 x} - eEx \tag{3.26}$$

$$V_{MAX} = -e\left(\frac{eE}{4\pi\varepsilon_0}\right)^{1/2} \tag{3.27}$$

The lowering of the work function increases the efficacy of thermionic emission, leading to the following current density relation:

$$J = A_0(1-\sigma)(k_B T)^2 \exp\left(\frac{-\varphi - V_{MAX}}{k_B T}\right) \tag{3.28}$$

This equation is applicable in situations where the electric field is below approximately 10^8 Vm^{-1} in strength. Above this field strength, field emission contributes more and more greatly to the emission current, eventually becoming the dominant mechanism at very high field strengths.

3.6 Quantum tunnelling and field emission

3.6.1 Quantum tunnelling in one dimension

Quantum tunnelling is a quantum mechanical phenomenon. It describes how a particle may pass, or "tunnel", through an energy barrier that it would otherwise not be able to according to classical physics. Understanding how particles are able to accomplish this feat can be accomplished by considering the particles as behaving as waves with a wavefunction described by the Schrödinger equation. A simple illustrative example is that of a particle tunnelling through a one dimensional (1D) barrier. Figure 3.13 shows such a scenario. The wavefunction of the free particle may be found as the solution to the time independent Schrödinger equation, given below in equation 3.28 [107]:

$$-\frac{\hbar}{2m}\frac{d^2\psi(x)}{dx^2} + V(x)\psi(x) = E\psi(x) \qquad (3.29)$$

where $\psi(x)$ is the particle's wavefunction, a complex number defined as the

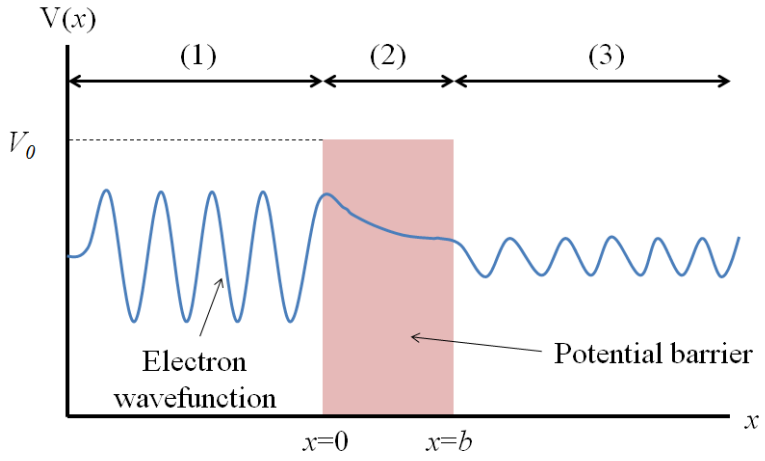

Figure 3.13. Schematic illustration of an electron tunnelling through a rectangular potential barrier of height V_0 and width b.

probability amplitude of the particles position; *E* is the energy of the particle; *m* is the particle mass; *ħ* is the reduced Planck constant (*h/2π*).

In classical physics, the particle position in figure 3.13 would be fully bound by the barrier at *x = 0*. In quantum mechanics, however, there is a finite probability that the particle will be able to pass through the barrier, (region 2 in figure 3.13) hence the term "tunnelling". In practice, some of the incoming wave tunnels through the barrier, while some is reflected back to the left in region 1. The wave would then propagate as normal in region 3. Solutions to equation 3.28 may be derived for the three regions signified in figure 3.13 [120].

$$\psi_1(x) = Ae^{ikx} + Be^{-ikx} \tag{3.30}$$

$$\psi_2(x) = Ce^{\mu x} + De^{-\mu x} \tag{3.31}$$

$$\psi_3(x) = Fe^{ikx} + Ge^{-ikx} \tag{3.32}$$

where $k = \sqrt{2mE_x}/\hbar$

$\mu = \sqrt{2m(V_0 - E_x)}/\hbar$

V_0 is the barrier height, and E_x is the energy of the free electron wave.

In a barrier of finite width, the wavefunction inside the barrier (section 2 of figure 3.13) contains exponential terms that both increase and decrease with increasing distance, due to the fact that there may be electrons transmitted or reflected at both sides of the barrier. To simplify this scenario, however, one can assume there will be no reflections from the interface between region 2 and region 3

(right side barrier/conductor interface), and the coefficient *C* will be equal to zero. Similarly, *G* is equal to zero as only transmitted electron waves, travelling to the right, exist on this side of the barrier.

A transmission coefficient, τ, which is the probability of the particle passing through the barrier, may then be calculated from these solutions by imposing wavefunction matching boundary conditions at the start and end of the barrier. This process results in the following definition [101] [120]:

$$\tau = {|F|^2}\Big/{|A|^2} = \frac{16\mu^2 k^2 \exp(-2\mu b)}{(k^2+\mu^2)^2} = 16\left(\frac{E_x}{V_0}\right)\left(1-\frac{E_x}{V_0}\right)\exp(-2\mu b) \quad (3.33)$$

where *b* is the barrier width.

As the barrier width increases, *exp(-2μb)* tends to 0, meaning that quantum tunnelling is only observed over very short distances: the thinner the barrier, the more quantum tunnelling current there is.

3.6.2 Field-assisted quantum tunnelling

The presence of an electric field has a distinct effect on the transmission coefficient. In what is known as field assisted quantum tunnelling, as mentioned earlier, an external electric field distorts the potential barrier into a rounded triangular shape, as depicted in figure 3.14. This is the aforementioned Schottky Effect. The distortion acts to effectively narrow the barrier and this leads to particles being able to tunnel more efficiently, as stated by the quantum tunnelling transmission coefficient in section 3.6.1. There are several types of field assisted tunnelling and these are

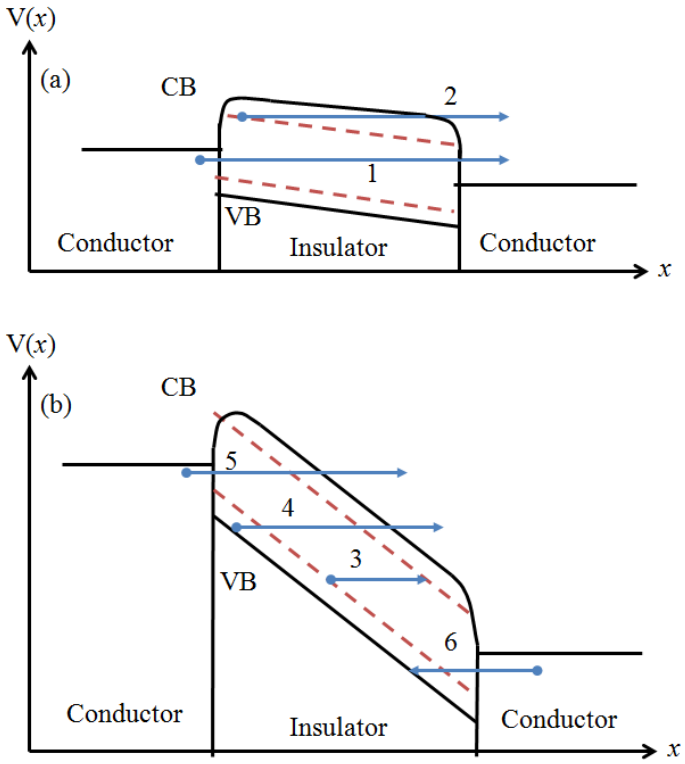

Figure 3.14. A schematic illustration of field assisted quantum tunnelling mechanisms in (a) the low field limit: (1) direct tunnelling, and (2) the ionization of impurity states, and (b) the high field limit: (3) Zener tunnelling, (4) intra-impurity tunnelling, (5) electron tunnelling, and (6) hole tunnelling.

summarised below and in figure 3.14 [121]. The type of field emission present across a tunnelling barrier is dependent on the strength of the external applied electric field strength.

In the low electric field limit the bias field is lower than the height of the tunnel barrier. In this case, charge may tunnel through the barrier via two routes: direct tunnelling, or ionization of impurity states. Direct tunnelling is the normal mode of tunnelling as described above, labelled (1) in figure 3.14(a). Charge tunnels from one conductor through the insulating barrier to the conductor on the other side. Field ionisation of impurity states, labelled (2) in figure 3.14(a), involves the movement of charge from the conduction band of the insulating material into the barrier before

moving to the conductor on the other side of the barrier. This process may also occur at high bias.

In the high electric field limit tunnelling may occur via Zener tunnelling (3), intra-impurity tunnelling (4), electron injection (5), or hole injection (6). These are shown schematically in figure 3.14 (b). In Zener tunnelling, charge tunnels from the valence band of the insulating material to the conductor, while in intra-impurity tunnelling, charge tunnels through multiple impurity states in the barrier to the conductor. Electron and hole injection are both analogous to a process known as Fowler-Nordheim (FN) tunnelling [121] [122]. This special form of tunnelling is ascribed to the movement of charge through exact and/or rounded triangular potential barriers at metal/vacuum interfaces under very high bias.

Current through a triangulated barrier may be calculated using the Wentzel-Kramers-Brillouin (WKB) approximation, giving the following result:

$$J = A_0 \exp\left(-\frac{4}{3}\left(\frac{2m}{\hbar^2}\right)^{1/2} \cdot \frac{(V_0 - E_x)^{3/2}}{eE} \cdot b\right) \tag{3.34}$$

In the case of FN tunnelling, charge tunnels and flows in the CB of the insulating material making up the barrier so the above current density relation must be modified, taking Child's law into account; current flow in the CB of the insulator adds a quadratic dependence of the electric field. The relation becomes [101]:

$$J = \frac{A_0 E^2}{\varphi} \exp\left(-\frac{4}{3}\left(\frac{2m}{\hbar^2}\right)^{1/2} \cdot \frac{(V_0 - E_x)^{3/2}}{eE} \cdot b\right) \tag{3.35}$$

Internal field emission follows a distinct temperature dependence, as calculated by Murphy and Good [123]. The temperature dependence takes the form of a pre-exponential coefficient, highlighted in the box:

$$J = \frac{A_0 E^2}{\varphi}\boxed{\left(\frac{\pi\zeta T}{\sin \pi\zeta T}\right)}\exp\left(-\frac{4}{3}\left(\frac{2m}{\hbar^2}\right)^{1/2} \cdot \frac{(V_0 - E_x)^{3/2}}{eE} \cdot b\right) \qquad (3.36)$$

where ζ is a constant which includes numerous factors such as the work function. This temperature dependence is of particular importance to this thesis, which utilises electrical transport measurements at various compressive loadings and temperatures to investigate and describe the electrical behaviour of nanocomposite ink.

3.7 Summary

The electrical behaviour of conducting composites may be described by percolation theory and effective medium theory, which detail how changes in the conducting filler content affect variation of the electrical conductivity of a composite system. These models are phenomenological, however, and do not provide much insight into the conduction mechanisms responsible for the electrical behaviour.

If composites are tailored to have a conductive filler particle content close to the percolation threshold, they may become highly sensitive to compressive force and changes in temperature; applied force may compress the composite into a conducting state by pushing conductive particles into direct contact or altering barrier widths at quantum tunnelling junctions, while temperature may cause the composite material to expand (reducing conductivity by expanding and breaking

percolation networks) and may change the number of intrinsic charge carriers through thermal activation.

Charge carriers may be transported through electrically conducting, semiconducting, or insulating materials in a composite, therefore a detailed understanding of charge transport in these types of materials is required before beginning to unravel electrical transport phenomena in composite systems. The nature by which the conductivity of field-assisted quantum tunnelling junctions and semiconducting materials increase with temperature is of particular importance to this specific study.

4. Experimental techniques: background and methodologies

4.1 Introduction

This chapter details the relevant theory and techniques utilised in the production of the ink samples and their structural analysis with scanning electron microscopy and focussed ion beam milling, and temperature dependent electrical transport measurements. The chapter also describes the chemical analysis, using energy dispersive x-ray (EDX) analysis, and the thermal behaviour of the inks with thermogravimetric analysis and differential scanning calorimetry. The chapter concludes with a description of the electrical measurement setup.

4.2 Sample preparation

4.2.1 Ink production

Two formulations of touch-pressure sensitive conductive ink, formulated at Peratech, were investigated in this study: opaque ink and transparent ink. While they comprise different components, their overall method of manufacture is the same. This process is summarised in the flow chart figure 4.1. The screen printing process is described in detail in Chapter 2.

The opaque ink comprised a proprietary blend [124] of Ishihara FT-2000 titanium dioxide needles with a semiconducting antimony-doped tin oxide surface coating, and Kronos Type 1080 electrically insulating, approximately spherical titanium dioxide nanoparticles, all dispersed in a flowing polyvinyl resin base ink,

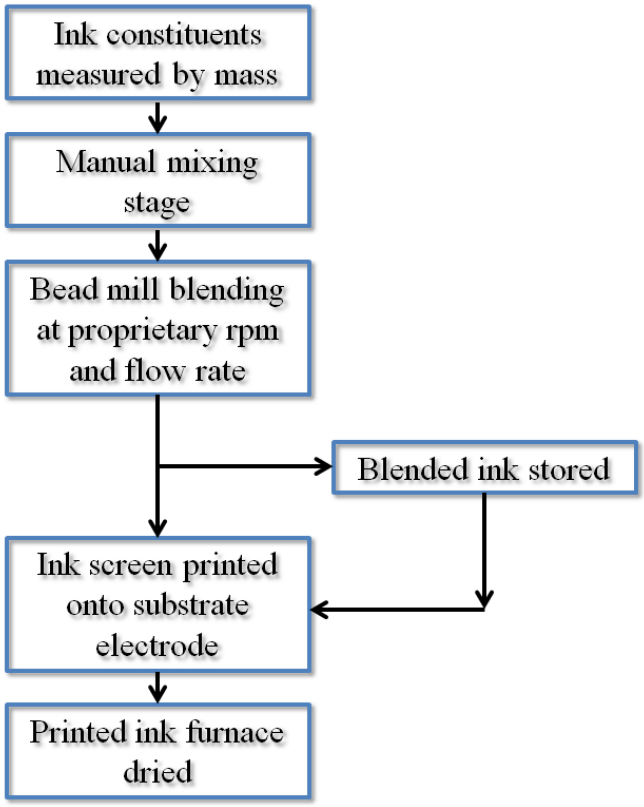

Figure 4.1. The step-by-step process of blending and printing the functional inks used in this study.

Sericol VA401 APR Varnish. All the ingredients were commercially obtained and the filler particles were produced via chemical synthesis methods [125] [126] [127]. The components were blended by a bead mill at 4000 rpm.

The transparent ink comprised a proprietary mix [128] of Ishihara antimony-doped needles (FS10P) and near-spherical (SN100P) nanoparticles, and Microbeads CA-6 PMMA spherical beads (used as a spacer material to prevent false touches in sensor devices), dispersed in Sericol VA401 APR Varnish. As with the opaque ink, all the components were commercially obtained and the filler particles were manufactured via chemical synthesis methods [129]. The transparent ink components were blended in a bead mill at 3500 rpm.

4.2.2 Fabrication of test device structures

Test structures were prepared on *macor* machinable ceramic tile substrates. This material was chosen primarily for its low coefficient of thermal expansion (9.3×10^{-8} $°C^{-1}$ between 25 and 300 °C) [130], which was beneficial for the temperature and touch-pressure dependent electrical transport measurements presented in Chapters 6 and 7. The as-printed inks are highly sensitive to compression and flexion. A substrate that is stable over a wide range of compressive loads and invariant with temperature (i.e. does not flex under compression easily and does not significantly expand or contract in response to changes in temperature) was required to ensure the properties of the ink were being measured, not the properties of the substrate. Additionally, the machinable nature of *macor* ceramic allowed the time efficient manufacture, in a mechanical workshop, of tiles in the required geometry for the experiment.

The tiles were machined and polished to have a large flat area for the ink to be printed and a tab for making electrical connections. The tile and electrode schematic is shown in figure 4.2. Electrodes were formed on the tiles by thermally evaporating a 2 nm chromium layer and a 150 nm copper electrical conduction layer, capped with a 50 nm gold layer. The chromium was used as an intermediate layer to facilitate good adhesion of the conducting copper electrode layer to the ceramic. The electrode layer needed a high conductivity as this experiment utilised a two-probe method, with the whole electrode surface, apart from the tab seen in figure 4.2 (b), being used as the contact area.

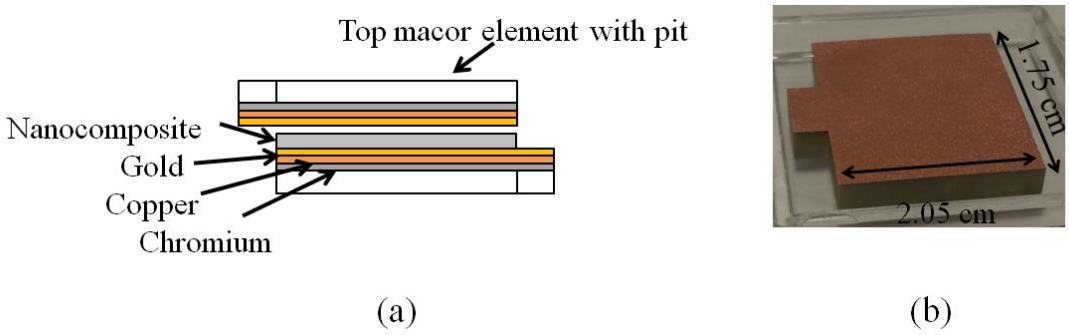

Figure 4.2. (a) A side view schematic illustration of the functional test device, not to scale. (b) An image of the electrode prior to the printing of the nanocomposite.

A four-probe method would involve utilising two contacts to apply a voltage and a further two contacts to measure the current passed through the ink. This particular setup allows contact resistance to be ignored since the voltage is applied through contacts separate from those used to measure the current. The geometry of the test device in this study, however, and the necessity to compress the sample uniformly, meant that a two-probe setup was a better choice for the electrical measurements, as long as the contact resistance was minimised as best possible. This is discussed further in section 4.6.1.

Copper was chosen as the bulk electrode layer due to its good electrical conductivity and low cost relative to other typical electrode materials, such as gold. A thin capping layer of gold was employed to prevent oxidation of the copper during the heating cycles and, as an added benefit, to further reduce the contact resistance. The inks were screen printed directly onto the electrodes and air dried in a furnace at 90 °C. A printed sample is shown in figure 4.3.

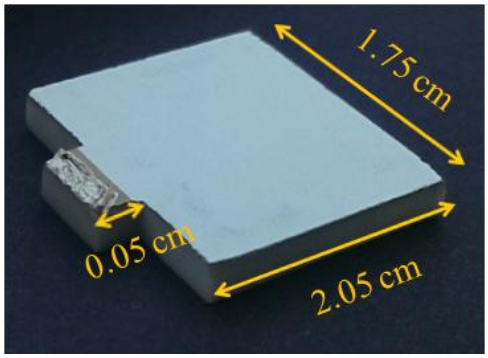

Figure 4.3. An image of a bottom macor element with a printed opaque ink layer.

4.3 Scanning electron microscopy

Understanding the structure of the complex nanocomposite inks in this study involved detailed high resolution electron microscopy. The relevant methods are described here.

4.3.1 Operation overview

Scanning Electron Microscopy (SEM) is a powerful technique for acquiring high resolution images of surfaces. A schematic illustration of an SEM is provided in figure 4.4 [131]. The images are created by the interaction of a highly focussed beam of electrons (produced through thermionic and/or field emission from a tungsten tip, detailed in Chapter 3, and focussed with electromagnetic lenses) with a sample surface; the scanning of this beam across the sample surface area in a raster pattern, and measuring the resulting electron intensity, affected by electron interactions with the atoms in the surface and the topography of the surface, at each pixel in order to form a grey-scale image [131] [132].

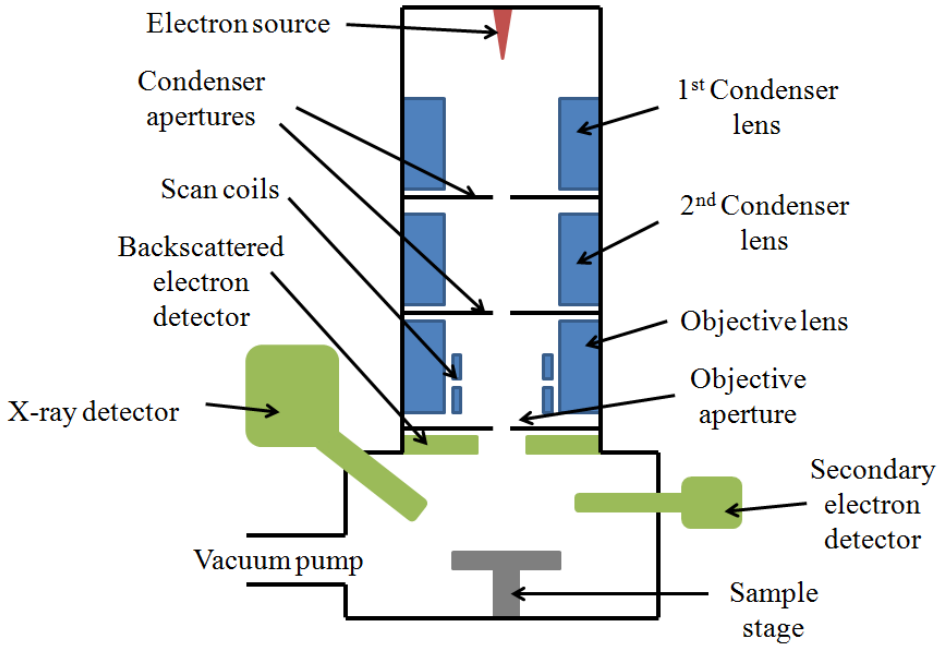

Figure 4.4. A schematic side view of the main components of a scanning electron microscope.

4.3.2 Electron Interactions

The incident electrons can interact with the sample surface either elastically or inelastically. Elastic collisions involve incident electrons penetrating the sample surface and impinging on orbital electrons in the sample atoms, resulting in their ionisation and, in some cases, damage to the sample surface. Ejected orbital electrons become low energy "secondary electrons" which may escape the sample and be detected to form an image. Additionally, this type of interaction may produce characteristic x-rays if core orbital electrons are ejected; outer electrons fall to fill the empty states, releasing energy as photons as they do so.

Inelastic collisions are incident electrons that are scattered (typically to high angles) by atoms in the sample surface, becoming "backscattered electrons", and have an energy comparable to the incident electron beam energy. During the

scattering interaction, the incident electrons decelerate, releasing Bremsstrahlung x-ray radiation. This scattering process is highly dependent on atomic number, so materials comprising high atomic number atoms produce more intense backscatter electron signals [131] [132].

The volume in which all of these interactions take place is called the generation volume. The size of the generation volume is dependent on the beam energy and the atomic number of the sample. If incident electron energy is increased, or if the atomic number of the sample is lower, the incident electrons are able to penetrate further into the sample surface, and so the generation volume becomes larger. This will eventually lead to a loss of image resolution, as the image signal acquired by the SEM will be weaker and will not be confined to the surface, it will be of a volume of material below and including the surface, making the image a complex integration of volume. [131].

4.3.3 Image formation

As previously discussed, secondary electrons and backscattered electrons are emitted from a surface under electron bombardment and these two signals have very different typical energies [131] [132]. As such, different detectors are used to measure the intensity of the secondary and backscattered electron signals. X-rays may be detected by using either wavelength dispersive or energy dispersive analysis. The latter (EDX) is a rapid technique and was used in this study.

Image artefacts, defined as unwanted distortions of the SEM image, are a common problem in microscopy, particularly in the imaging of insulating specimens. The most common are detailed in turn:

Edges, peaks and areas of high aspect ratio can appear bright in SEM images due to the "edge effect", where charge emission from the surface is enhanced at edges and peaks. While this effect helps to give definition to objects in SEM imaging, an incident electron beam with too high an energy will lead to very bright areas in the resulting image. This is remedied by reducing the accelerating voltage (as before, this determines the beam energy).

When an incident electron beam interacts with a surface, some of the energy of the electrons is inevitably transferred to the surface as heat. More delicate samples, such as polymers, can be damaged by this localised heating (and this can in turn spoil the vacuum of the SEM chamber). Limiting the incident electron energy can help alleviate this problem, as well as increasing the working distance, which increases the spot size (the area of surface highlighted by the incident electron beam) on the surface. The latter option will decrease the resolution, however.

It is also possible for electron beam deposition to occur during imaging. This manifests as dark, rectangular areas on a surface where an image at high magnification has been taken. This is reduced by careful and diligent maintenance of the SEM chamber, and by taking low magnification images before acquiring high magnification images [131] [132].

Finally, charging is a very common issue when imaging surfaces with low conductivity, or surfaces which are not sufficiently contacted with the sample stub holder (which provides an electrical ground for the sample). Charging, or the accumulation of charge, can lead to the formation of a large negative electric field at the point where the incident electron beam strikes the surface. This results in effects such as image shift, deformation and unusual contrast. Sudden emissions of

accumulated charge can cause bright flashes and dynamic “psychedelic” bright patterns on the surface being viewed, making stable imaging impossible. The sample can also become dislodged from the sample stub holder as a result of these discharging events. Reducing the incident electron beam energy, coating a surface in a conductive material (such as gold or platinum) and ensuring good electrical contact to ground are ways of alleviating these artefacts [131].

4.3.4 Facility and procedure

A Hitachi SU70 SEM in the Durham GJ Russell Microscopy Facility, shown in figure 4.5, was used extensively for structural and compositional analysis of ink samples in this study. This model uses a Schottky field-emission electron source (SFEG), which can produce probe currents of up to 100 nA. The system can achieve a maximum magnification of 8 x 10^5 and is capable of ultra-high resolutions of 1 nm at a beam energy of 15 keV. The SU70 can also use ultra-low landing voltages to slow beam electrons just prior to interaction with the sample surface, enabling the user to perform shallow surface studies. Additionally, the system is equipped with both EDX, wave dispersive x-ray analysis (WDX) and a load lock mechanism. Sample stubs are loaded onto a sample holder which sits inside a side chamber affixed to the main chamber. The load-lock and side chamber allow samples to be inserted into the microscope without ventilating the main chamber (the system used here typically maintains a vacuum of approximately 10^{-7} Torr). This drastically reduces the time taken to insert a sample into the microscope helps to reduce the maintenance required to keep the main chamber clean.

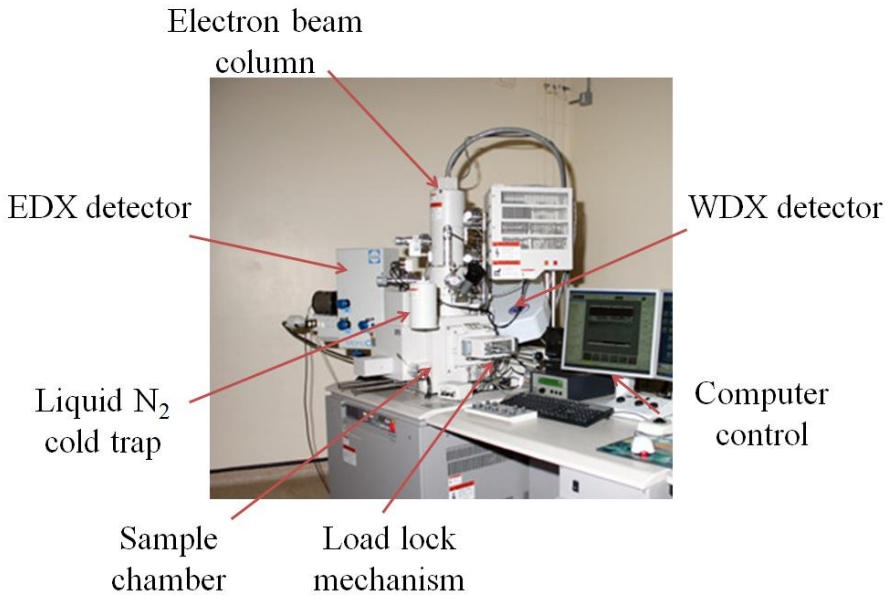

Figure 4.5. An image of the Hitachi SU70 scanning electron microscope in the Durham Microscopy Facility.

EDX and SEM imaging were undertaken as part of this study. Typically, a working distance (the distance between the sample surface and the pole piece of the final lens) between 2 and 7 mm was used. This range was determined empirically to be a range suitable for obtaining high resolution images of the ink surface.

Low accelerating voltages were used, normally between 5 and 10 kV. The lowest accelerating voltages were used for acquiring high resolution images of the ink sample surfaces and also to prevent damage to the surface of some of the ink samples; damage to the polymer layer did occur in the imaging of the transparent ink. This is detailed in Chapter 5. A 15 mm working distance was used for the EDX analysis, as a consequence of the detector set up within the microscope sample chamber.

4.4 Focussed ion beam milling

Ordinary SEM imaging is an excellent surface analysis tool, but in order to view and study the structure below the surface, a sample must be either broken to expose a cross-section using a technique such as cryo-fracture, or Focussed Ion Beam (FIB) milling can be utilised. The basic principles of FIB and its uses, in general as well as its application to this study, are detailed below.

4.4.1 Ion Interactions

Focussed Ion Beam (FIB) systems are used for micro- and nano-scale milling of materials for cross-sectioning, imaging and transmission electron microscope (TEM) sample preparation. This milling is achieved by locally sputtering material from a sample with a tightly focussed beam of gallium (Ga^+) ions. The ions are produced at a source comprising a hot tungsten tip coated in liquid gallium, exposed to a large electric field. The liquid gallium is ionised and the ions are emitted from the tip through field emission. The emitted ions accelerate away from the tip through a set of electromagnetic lenses in much the same way electrons are focussed in SEMs. The ion beam interacts with the surface of the material and atoms are sputtered from the surface. Ions become implanted in the surface of the sample during this process.

Cross-sections may appear uneven and rugged due to the “channelling effect”. Here, the milling of the sample is uneven and is a result of a variable milling rate. The variability arises from cutting into inhomogeneous samples that comprise many components, air gaps, or randomly orientated grains. This effect can be reduced with a polishing cut, where the face of the cross-section is smoothed by milling at a low ion

dose. The key interaction of the beam with the sample surface is illustrated in figure 4.6 [131].

4.4.2 Facility and procedure

A FEI Helios Nanolab DualBeam 600, shown in figure 4.7, in the Durham Microscopy facility was employed for milling to expose cross-sections of the as-printed ink for high resolution SEM imaging. As the name suggests, this system combines an electron beam column and an ion beam column, allowing nano-fabrication and SEM imaging in one facility. The two beam columns are oriented at an angle of 52° from each other and the sample stage can tilt to be perpendicular to either; the sample can be tilted and milled using the ion beam, then the resulting exposed cross-section imaged side on by the SEM. The electron beam column also uses a SFEG and is capable of imaging to a resolution of 0.8 nm at 15 keV beam energy. The gallium ion source was used to mill 5 to 10 µm deep trenches in ink sample surfaces for imaging cross-sections.

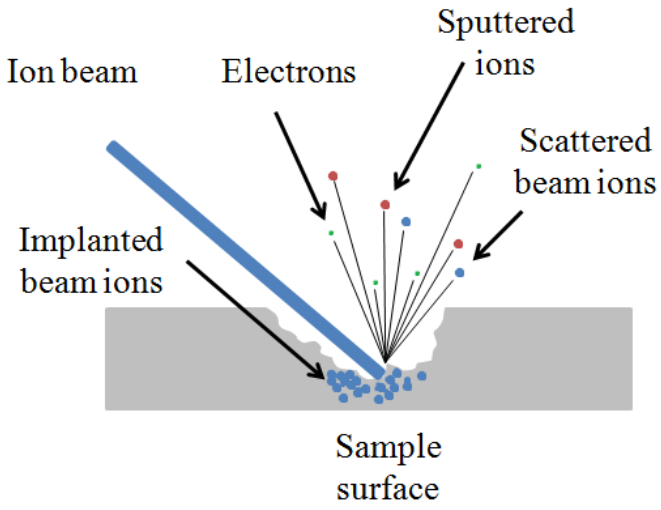

Figure 4.6. An illustration of ion/surface interactions in focussed ion beam milling.

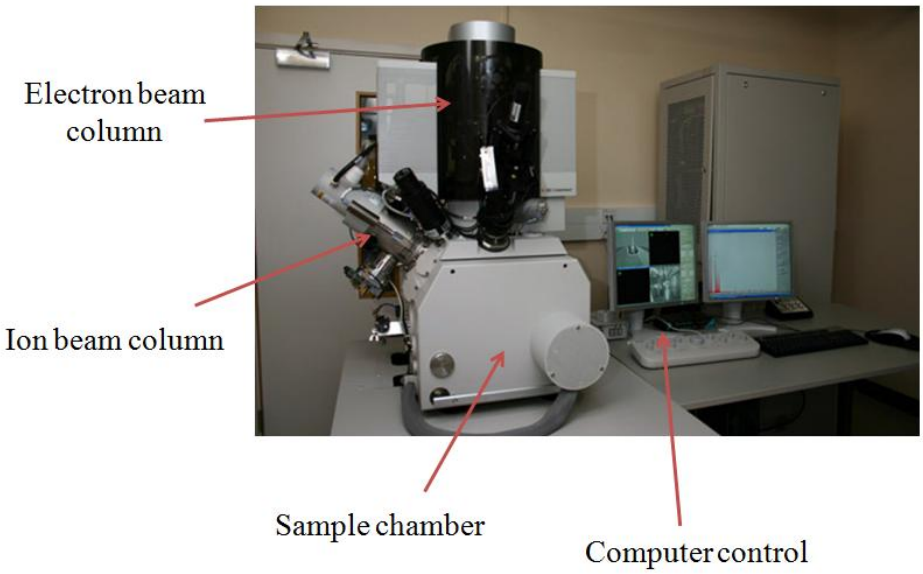

Figure 4.7. The FEI Helios Nanolab 600, with key components indicated. The EDX facility is situated behind the column

A platinum cap was deposited on the surface using electron beam- and ion beam-induced vapour deposition, prior to the milling, as a sacrificial protective layer. Incident ions can damage the face of the cross-section during the milling process; the platinum cap acts as a barrier, helping to protect the cross-section from undesirable sputtering. The trenches took approximately 15 minutes to mill and comprised of a rough cut, followed by a polishing cut at a lower dose.

4.5 Thermal properties analysis

4.5.1 Thermogravimetric analysis

To fully understand any temperature dependent behaviour of functional nanocomposite inks, both electrical and physical/chemical temperature dependent changes in the ink and its components must be considered. For physical/chemical changes, a combination of Thermogravimetric Analysis (TGA) and Differential

Scanning Calorimetry (DSC) has been used. These methods are described below, while temperature dependent electrical transport measurements are discussed in section 4.6.

4.5.1.1 Physical principles

Thermogravimetric analysis is a technique whereby a material is heated in a precision pan balance and its mass is constantly measured as a function of temperature or time [133] [134]. Changes in the mass of the material imply physical and/or chemical processes induced by the increase of temperature. The results from this analytical technique may be presented as either a thermogravimetric (TG) curve, which is mass change as a function of temperature or time, or as a derivative thermogravimetric curve (DTG), where the first derivative of the mass change is plotted as a function of temperature or time. An example of a typical TG curve and the corresponding DTG curve are shown in figure 4.8.

The shape of the TG curve is dependent on how the material behaves as temperature is increased. Sloping areas of a TG curve indicate a change in the mass of the sample material, while flat areas are representative of constant mass and no

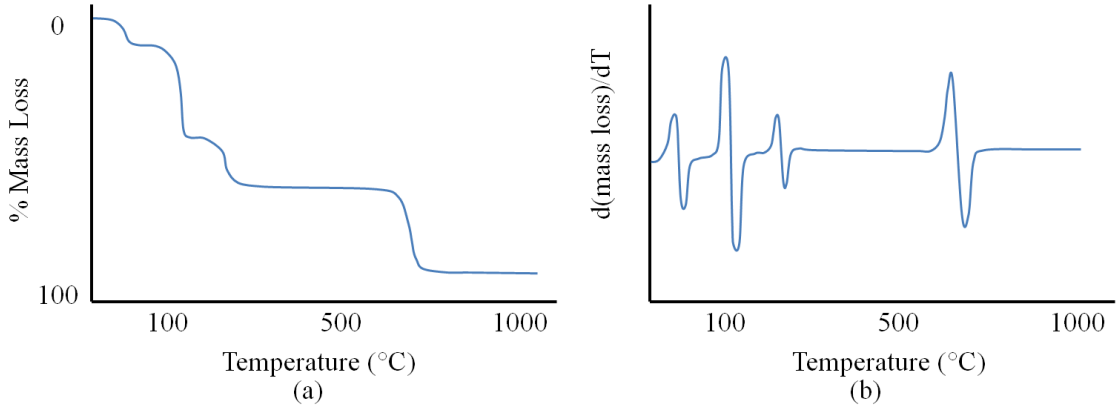

Figure 4.8. An illustrative example of (a) a TG curve, and (b) a DTG curve for the same material.

change [133] [134]. Similarly, peaks in a DTG curve indicate a point of maximum slope in the TG curve, and thus mass change. DTG is useful for analysing complex TG curves as even small changes in the slope manifest clearly in the DTG curve. Mass loss in a sample material may arise from chemical reactions, decomposition of the sample, and the release of adsorbed chemical species. The first of these three may be influenced by the atmosphere used for the TG experiment. Most TG analysers are capable of holding a custom atmosphere, for example air, oxygen, nitrogen, or even vacuum. Furthermore, the shape of a TG curve may be affected by the heating rate, the shape of the sample and by the crucible (where the sample sits) geometry.

Typically, if a sample is heated at a faster rate, it will decompose at a higher temperature as the heating rate affects how the sample will decompose and what chemical species/compounds it will break down into [134]. Faster heating rates also result in a poor distribution of heat energy; a sample may internally reach its decomposition temperature when the external temperature has already risen far above this point because not enough time has elapsed to allow thermal equilibrium to be reached. A flat, open crucible geometry (much like a plate) is preferred as this facilitates easier diffusion of gases produced in the sample during the heating process. A more confined crucible, such as one shaped as a cone, will limit the diffusion of gases and thus the TG curve will show a slower rate of mass change.

Finally, the sample material particle size and the overall size of the sample are important. Large samples do not heat as efficiently as smaller samples and so linear heating of a sample (if required) may not be possible. If a sample is composed of large particulates, mass change may be altered by the restricted diffusion of evolved gases, much akin to more confined crucible geometries. It is therefore more desirable

to use small sample sizes and to use powdered samples composed of small particulates [134].

4.5.1.2 Facility and procedure

A Perkin Elmer Pyris 1 TGA, shown in figure 4.9, in the Durham University Chemistry Department was utilised for this study. The system can record mass changes to a precision of ± 0.001 mg, and heat sample materials up to 800 °C at a maximum rate of 80 °C/min. 10 mg samples of the inks and their individual components, described in detail in the next chapter, were placed in the pan balance at room temperature. Fluid ink samples were allowed to dry before running the tests.

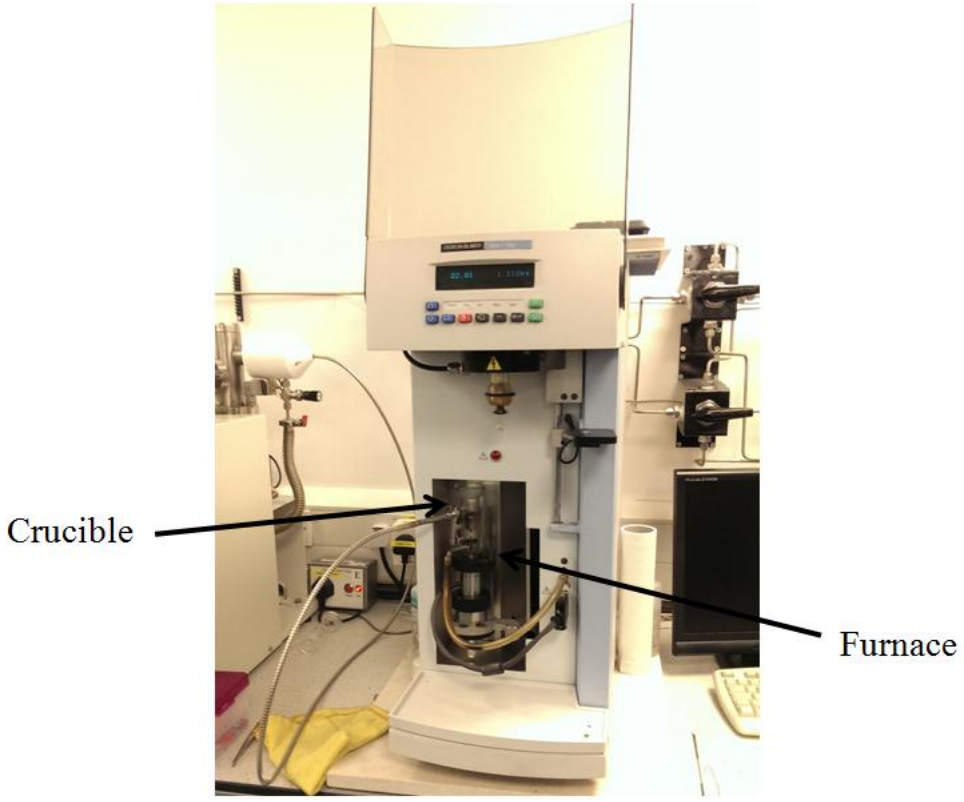

Figure 4.9. The Perkin Elmer Pyris 1 TGA system, with key components indicated.

The samples were heated to 130 °C at a rate of 0.5 °C/min (the same rate of heating used in the electrical transport measurements, detailed in Chapters 6 and 7), and then up to 800 °C at a rate of 20 °C/min.

4.5.2 Differential scanning calorimetry

Differential Scanning Calorimetry (DSC) was also utilised in this study to analyse the temperature dependent physical and chemical behaviour of both the opaque and transparent inks. While TGA is well suited for analysing decomposition behaviour, DSC is highly useful for the identification of a variety of chemical reactions and phase changes, such as melting points and glass transition temperatures [134].

4.5.2.1 Physical principles

Differential Scanning Calorimetry is a technique which involves heating the sample and a reference material, typically aluminium(III) oxide, at a linear rate in a furnace and measuring the differential energy required to keep them both at the same temperature during this heating process. For example, an increased energy input would be observed if the sample underwent an endothermic reaction of some kind, as energy would be required to maintain zero temperature difference between the sample and the reference. In contrast, less energy would be required during exothermic reactions. DSC enables calorimetric measurements of the quantities of energy involved in thermally induced chemical reactions and phase transitions as the energy input from the DSC furnace is balanced against the energy of reaction/transition [134]. An illustrative example of a DSC curve is shown in figure 4.10.

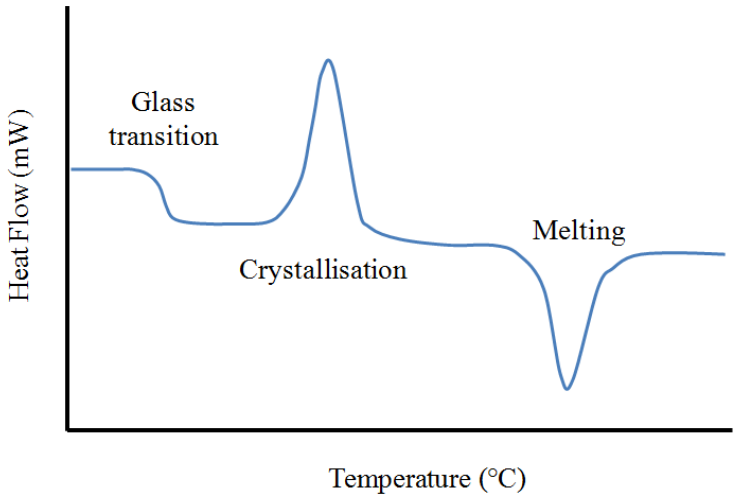

Figure 4.10. An illustrative example of a DSC curve, showing some common features DSC curves can be used to analyse.

4.5.2.2 Facility and procedure

A Perkin Elmer Pyris 1 DSC, shown in figure 4.11, in the Chemistry Department of Durham University was used to carry out DSC measurements on samples identical to those used for the TG analyses. The 10 mg samples were heated in the same way as those in the TG experiment, described above.

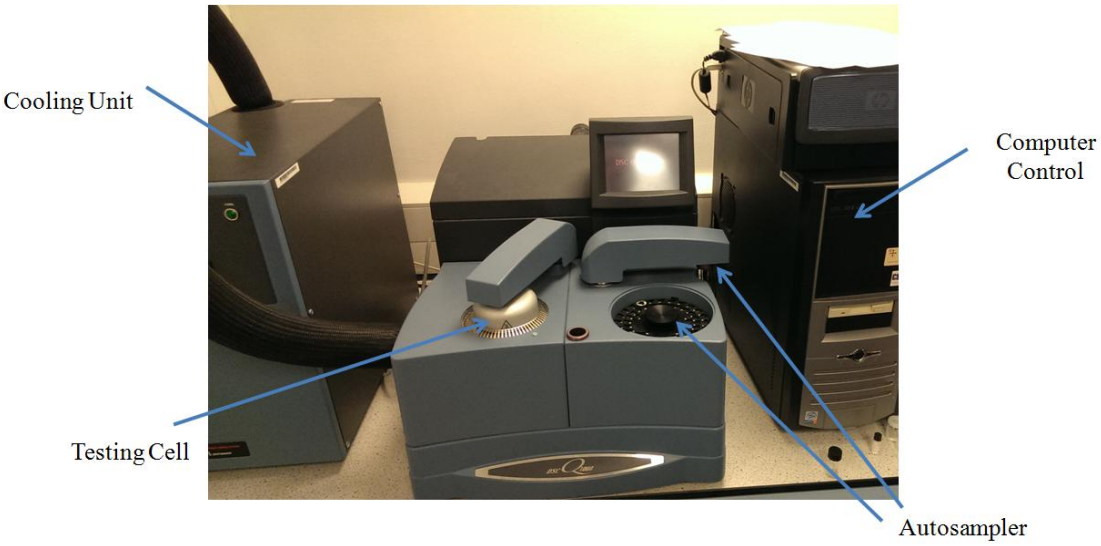

Figure 4.11. A TA Instruments Q1000 DSC system.

4.6 Electrical transport measurements

An understanding of the electrical properties of a material is not only of academic interest but, in the case of the inks studied here, commercial interest too. The touch-pressure sensitivity exhibited by the inks in this work is a result of the combination of their structure and electrical behaviour. Simple diagnostic electrical transport measurements are key to discerning the modes of electrical conduction within the inks. Measurements of current and voltage, and their relation to each other and to temperature, can reveal how charge is transported and also how it may be trapped. The measurements undertaken to achieve this goal are detailed in this subsection.

4.6.1 Physical principles

Electric transport measurements form the focus of this work on understanding electrical conduction mechanisms and charge trapping phenomena in the ink materials. A common route for electrical transport investigations is performing current-voltage (I-V) sweeps via a two- or four-probe method.

A two-probe technique was utilised in this work due to the difficulties involved in applying a four-probe method, as mentioned earlier. The geometry of the four-probe method would involve bonding or fixing wires/electrodes to either the surface of the ink, or to the sides of the ink. Since the ink is printed to a thickness of about 2-5 microns, and is uniformly compressed as part of these measurements, the four-probe method was deemed unsuitable for this work. Instead, two plane parallel contacts were used that facilitated easy compression of the ink samples, as described in section 4.2.2.

In current-voltage measurements a potential difference is applied across a sample and the current is measured. The potential difference is then incrementally increased and the current is measured at each increment. Electrical conduction via different mechanisms will produce a different I-V curve. For example, ohmic conduction is characterised by a linear I-V curve, while quantum tunnelling processes and conduction through insulators are uniquely non-linear, as described in Chapter 3. Electrical hysteresis may also be indicative of exotic charge transport mechanisms as well as charge trapping behaviour. A good example of this is the bulk composite called QTC™ which exhibits complex non-linear and hysteretic I-V behaviour attributed to a combination of Fowler-Nordheim tunnelling conduction, charge trapping, and a pinching effect; traps accumulate enough charge, creating a large local electric field, to "pinch off" and block nearby conduction pathways [135].

Conduction mechanisms may also exhibit intrinsic temperature dependencies. These dependencies may be used to identify certain mechanisms present in a material and how this temperature dependence physically originates. For example, ohmic conduction in metallic materials is reduced at higher temperatures because of the excitation of phonons which scatter conduction electrons, while thermionic conduction is increased with increasing temperature as charge carriers gain more energy to overcome the workfunction of their parent emitter. These mechanisms are covered in more detail in Chapter 3.

Other physical factors, such as compression, may also impact on electrical conduction behaviour. This is exemplified by percolative conduction and the narrowing of potential barriers in quantum tunnelling junctions, also discussed in Chapter 3.

4.6.2 Facility and procedure

In this investigation, I-V behaviour of touch-pressure sensitive inks was studied at a range of compressive loadings and temperatures. Opaque and transparent ink test structures, described at the beginning of this chapter in section 4.2, were placed in a custom compression rig inside an oven. This rig was designed using Autodesk Inventor Professional 2012, the design drawings are shown in figure 4.12.

The rig comprises a base plate in which the electrically functional test structures sit. A thermocouple was fixed into thermal contact with the test device to more accurately measure the ink temperature during the measurements. Mass loads, made of mild steel, were used to compress the device, and these were held in place with a scaffold. The scaffold was slotted onto a support structure comprising three cone-tipped rods, shaped as such so the scaffold would remain level in the case of any thermal expansion. In addition, a gap of 1 mm was allowed between the scaffold and

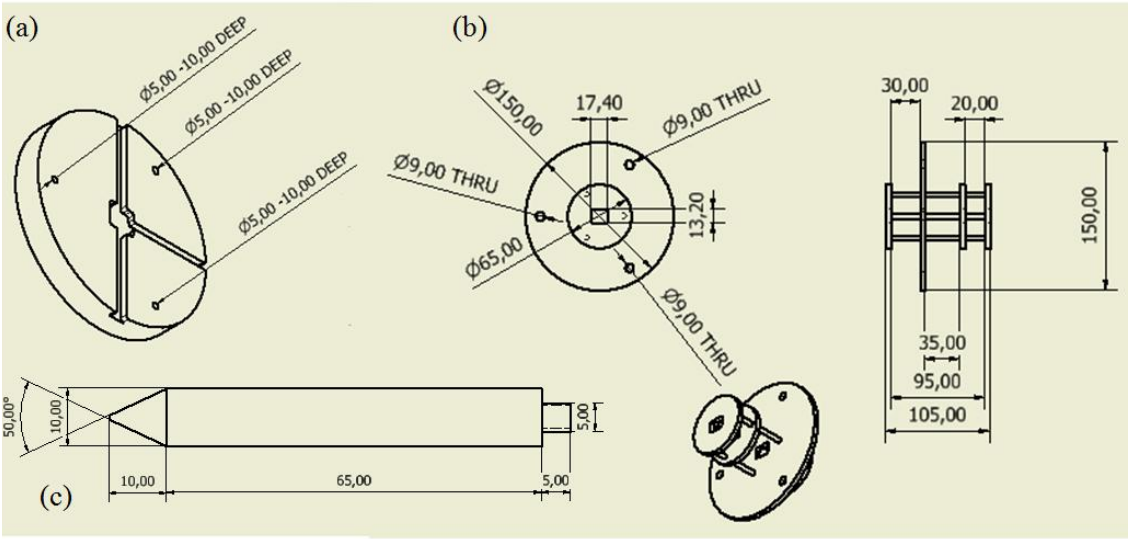

Figure 4.12. Autodesk design images of the component parts of the compression rig: (a) the base plate, (b) the scaffold to maintain a constant compression vector, and (c) the pegs which screw into the base plate to support the scaffold. All measurements are in *mm*.

the mass loads to allow for thermal expansion: if the mass loads and/or scaffold expanded and became wedged together, the magnitude of compression experienced by the test device would not remain constant through the entire temperature range of the experiment. The rig inside the oven is shown in figure 4.13.

The entire rig was placed inside an oven capable of heating to 250 °C. The temperature of the oven was manually controlled, as its own thermostat controlled the temperature to an insufficient degree of accuracy and precision (the temperature would fluctuate by approximately ± 10 °C around the set temperature). Manual control of the oven temperature, using in situ thermocouples, allowed the temperature to be set and controlled to ± 1 °C. The test device was connected to a computer controlled (using Labview software) Keithley 2420 Sourcemeter. The electrical set-up is shown in figure 4.14. An I-V sweep measurement consisted of

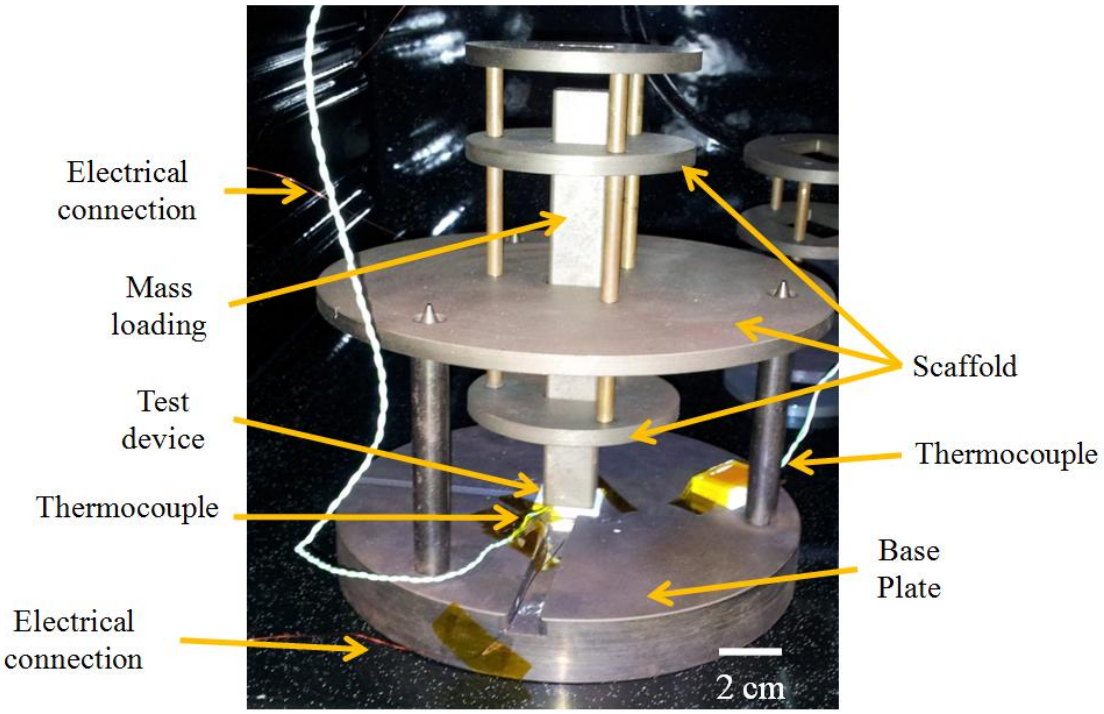

Figure 4.13. Image of the compression rig and test device set-up in the oven, with key components indicated.

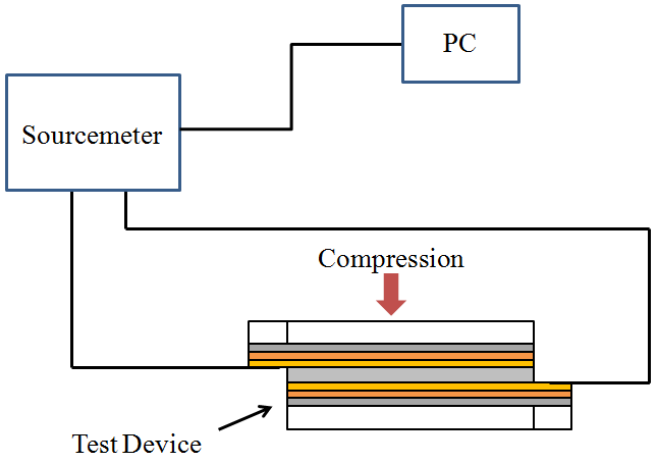

Figure 4.14. Schematic of the electrical set-up for the temperature and touch-pressure dependent current-voltage analysis.

loading a mass onto the device at room temperature and allowing the inks' electrical resistance to settle. The voltage across the device was then ramped up from 0 to 10 V in 0.1 V increments over 5 seconds, then back to 0 V at the same rate. A further 9 sweeps were taken for a total of 10 I-V sweeps at room temperature. The temperature was then increased by 10 °C and allowed to stabilise for twenty minutes before performing a further 10 I-V sweep measurements. This process was repeated until the ink was at 100 ° C. The oven was then switched off and left to cool to room temperature before increasing the mass loading and repeating the temperature dependent I-V measurement cycle.

5. Understanding the physical structure of nanocomposite ink

5.1 Introduction

In this chapter, the physical structuring and the physical response to temperature of the separate ink constituents, and of the as-printed ink samples, are detailed. Electron microscopy combined with focussed ion beam milling were used extensively to image the surface and cross-sectional morphology of the printed inks and their individual constituents, while thermal gravimetric analysis and differential scanning calorimetry were utilised to study the physical and chemical changes that occur in the inks and their constituents in response to temperature. Two distinct inks have been studied as part of this thesis: opaque ink and transparent ink.

5.2 Physical properties of the opaque ink

The opaque ink is so named because of it's solid white appearance when printed, the physical reasons are explained in the following section. The composition of the opaque ink, not only the choice of component materials but also the ratios of the components which make up its formulation, were chosen as part of a long iterative process with the aim of producing an ink with the best electrical functionality for touch-pressure sensitivity. This empirical optimisation process was undertaken elsewhere and does not form part of this work. It is this specific formulation that has been studied here.

5.2.1 Opaque ink constituent structure and thermal behaviour

Scanning electron microscopy was used to analyse the surface and cross-sectional structure of the opaque ink components and the as-printed ink layer. The individual components and printed ink thermal properties were investigated with thermal gravimetric analysis and differential scanning calorimetry.

5.2.1.1 Structural analysis

The opaque ink is comprised of acicular (needle-like) titanium dioxide particles with an antimony (Sb)-doped tin oxide surface coating (henceforth referred to as needles), and roughly spherical wide band-gap semiconductive (essentially insulating) titanium dioxide particles (referred to as TiO_2 particles from now on), dispersed in a flowing polymer binder (which itself is a solution containing some solvents in addition to the polymer). The presence of titanium dioxide, which has a high refractive index, gives the opaque ink its white colour.

An SEM image of the needles is shown in figure 5.1(a). While it is difficult to ascertain whether the needles truly lie at all angles due to the top-down perspective of the SEM image, it can be said that, in the x-y plane, the needles are randomly orientated. They have a tendency to clump and smaller needles are seen “stuck” to larger needles. This can be a result of electrostatic effects between separate needles. A closer view of the needles is shown in figure 5.1(b). The surface of the needles appears smooth overall with no distinctive features. The distributions of the measured needle length and width, calculated using the microscope control software, are given in the histograms in figure 5.2. Both the length and width distributions

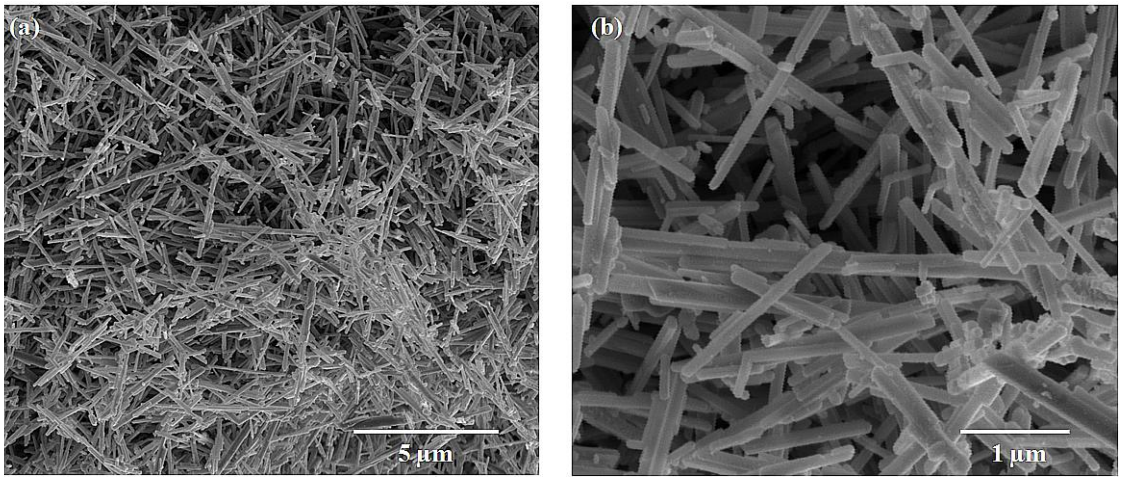

Figure 5.1. Scanning electron microscope (SEM) images of the opaque ink needles at (a) low magnification, and (b) high magnification.

exhibit a positive skew (a tail to the right), but the width distribution is narrower. They have an average length of 1.1 ± 0.1 µm and average width of 87 ± 1 nm. These dimensional aspects are controlled during the growth of the needles, which is an intricate and complex chemical process and outside the scope of this thesis. An energy dispersive x-ray (EDX) spectrum analysis of the needles is shown in figure 5.3, which confirms the needles comprise titanium dioxide with a doped tin oxide surface coating. The near-spherical TiO_2 particles are shown in figure 5.4. These particles tend to clump a lot and, although they appear to be bonded tightly together, in reality they are not. This, as well as the unusual contrast in some areas of the

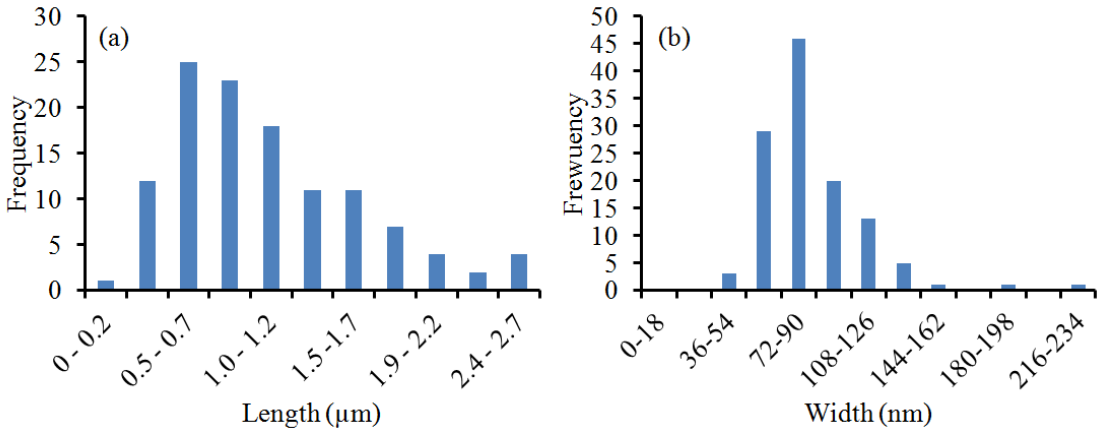

Figure 5.2. Histogram distributions of the opaque ink needle (a) length, and (b) width.

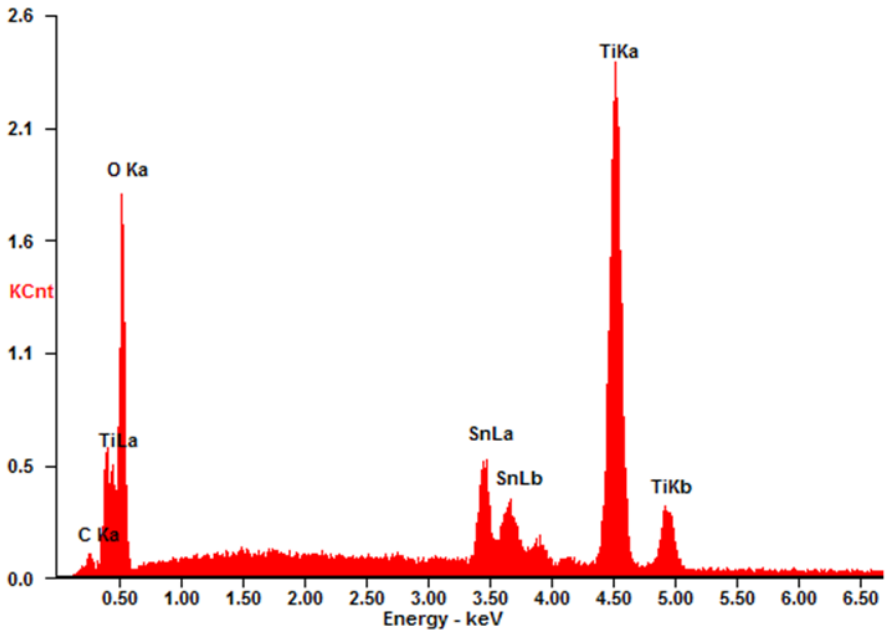

Figure 5.3. EDX elemental analysis of the opaque ink needles.

image and the over-saturated bright edges, are image artefacts as described in Chapter 4. The EDX analysis of the TiO_2 particles is given in figure 5.5. There is a strong signal for titanium dioxide and, in contrast to figure 5.3, no signal for tin oxide. The measured width/diameter distribution of the TiO_2 particles is given in figure 5.6.

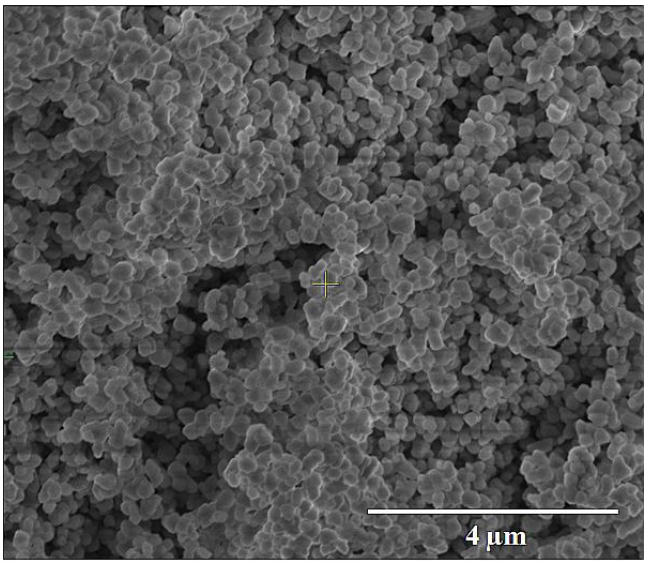

Figure 5.4. SEM image of the opaque ink TiO_2 particles.

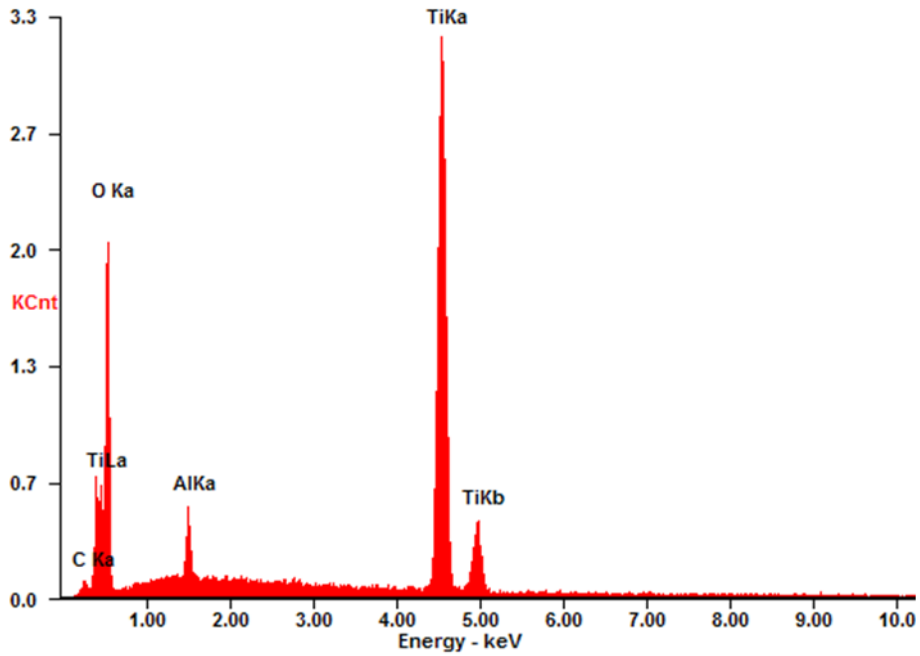

Figure 5.5. EDX elemental analysis of the opaque ink TiOx particles.

The TiO_2 particles have a near normal distribution of diameter, with an average diameter of 210 nm and a standard deviation of 54.

5.2.1.2 Thermal analysis

Titanium dioxide is physically stable over a wide range of temperature and pressure, as discussed in Chapter 2 with regard to gas sensing applications. In the temperature

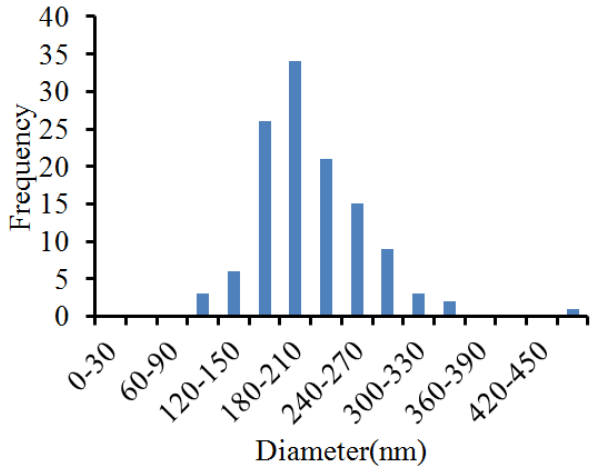

Figure 5.6. Histogram distribution of the opaque ink TiOx particle diameter.

range utilised in this study (approximately 300 K to 400 K), no transitions occur in titanium dioxide [136], so it was decided not to perform thermal analysis on the needles or the TiO_2 particles. The polymer binder used in the opaque ink is identical to that used in the transparent ink. It's TGA and DSC curves are presented in figure 5.7(a) and (b). In the TGA curve, a 70 % mass loss is observed up to 150 °C. The sample was left to dry before running the test but was not prepared in exactly the same way as the printed samples: the polymer was placed on the crucible/pan, not printed, and left to dry at room temperature, not in a furnace).

As a result of this preparation, it is highly possible that much solvent remained in the polymer, thus solvent being driven off is responsible for this large observed loss of mass from the sample. A decomposition event, completing at 400 °C, takes place afterwards. The DSC curve of the polymer features an anomaly shown in figure 5.7(b) at approximately 80 °C in the heating curve. The heating curve slopes upwards and reaches a maximum at just above 120 °C. It is unclear if this signifies a transition as the maximum temperature of 130 °C is reached and the cooling cycle begins.

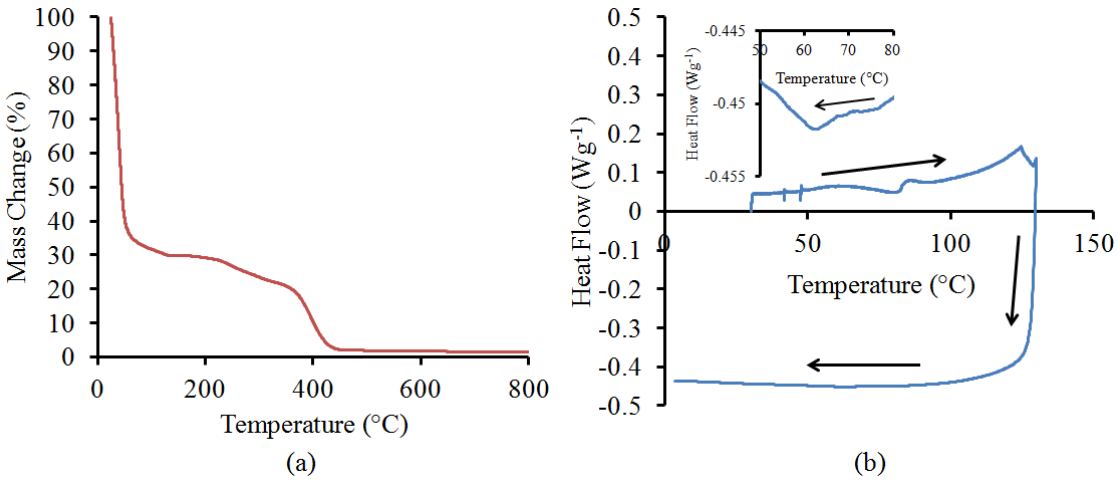

Figure 5.7. Thermal analysis of the opaque (and transparent) ink polymer binder: (a) thermogravimetric analysis (TGA) curve, and (b) differential scanning calorimetry (DSC) curve. Arrows indicate the direction of the curve.

During the cooling cycle, no feature occurs at 80 °C, which suggests the anomaly seen in the heating curve may be from either a contamination, a jolt to the system, or some other source of error. A very small feature occurs between ~58 and 73 °C however, shown in the insert. This could either be an exothermic reaction (unlikely as a corresponding event does not occur during the heating ramp), or an artefact, such as contamination, a change in the heat transfer to the sample (if the sample changes shape or crumbles, for example), or a change in heat flow between the sample pan and the sensor. The latter example occurs if the pan (which is hermetically sealed) changes shape due to the vapour pressure of the sample, or through thermal expansion.

5.2.2 As-printed opaque ink structure and thermal behaviour

The constituents described in 5.2.1.1 were blended according to the procedure outlined in Chapter 4. As-printed samples on *macor* substrate were examined using SEM and FIB, while the ink was applied to a flat crucible for TGA and DSC studies.

5.2.2.1 Structural analysis

The as-printed opaque ink has a complex surface structure, as shown in figure 5.8 (a). This image shows the needles are randomly oriented in the surface, but there do seem to be local areas of alignment and ordering, where the needles point in the same or similar direction. The TiO_2 particles are more uniformly distributed throughout the surface. A closer view in figure 5.8 (b) shows the clumping of both particle types has been greatly reduced, compared to the raw component images, with many gaps present between the particles in the as-printed layer. As this is a top-

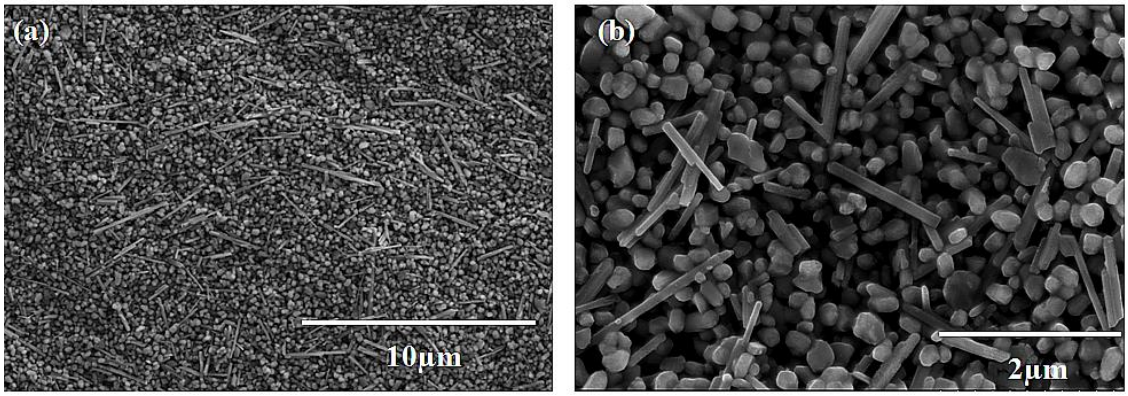

Figure 5.8. SEM image of the as-printed opaque ink surface at (a) low magnification, and (b) high magnification.

down image, it is difficult to accurately state the angles at which the needles lie. That said, it does appear that some of the needles penetrate into the body of the printed layer, but most tend to lie parallel to the plane of the surface.

High magnification images of the TiO_2 particles and needles are given in figure 5.9(a) and 5.9(b). These images more clearly reveal the gaps between the TiO_2 particles and needles. It is suggested here that these gaps in the ink may lend to the as-printed inks compressibility. A discontinuous surface coating is also evident on both the TiO_2 particles and needles. Indeed, most of the particles appear to have a thin surface coating, likely to be the polymer binder. In previous attempts to view cross-sections of the printed ink, a cryo-fracture technique was employed due to its

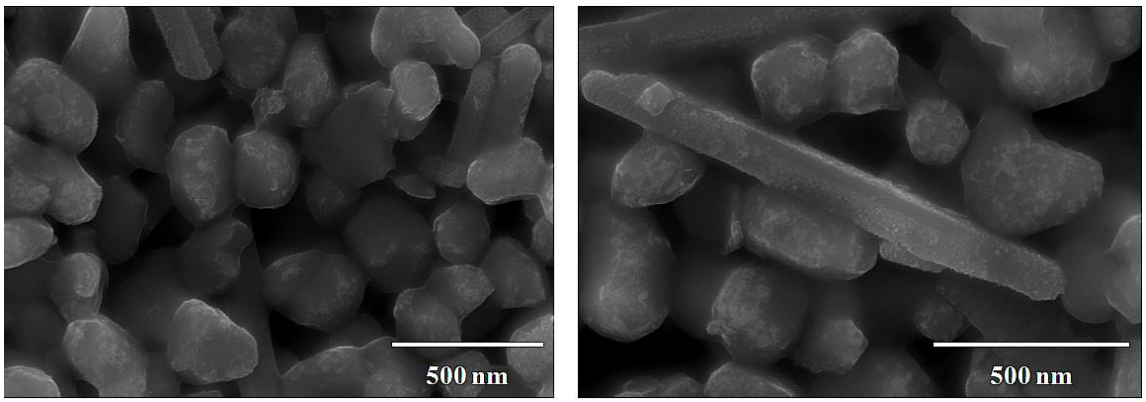

Figure 5.9. SEM images of (a) TiOx particles and some needles in the printed ink surface, and (b) a clearer view of a needle in the printed ink surface.

simplicity. The layers did not snap cleanly, however, which made focusing a problem in the microscope. Instead, FIB milling was used to mill trenches and image uniform cross-sections of the as-printed ink. An example of such a cross-section is shown in figure 5.10. At the top of the image a platinum cap can be seen, as well as residual damage to the top surface of the printed ink in the background. The platinum cap, deposited using electron- and ion-beam induced deposition, was used as a sacrificial layer to protect the cross-section face from undesired milling and damage from the ion beam. In the cross-section, air-gaps are visible throughout the whole depth of the printed layer and it is worth noting that the majority of the needles lie horizontally. Near the bottom of the trench, the *macor* ceramic and evaporated electrode layers can be seen. The striations in the trench face are the manifestation of what is termed the "curtaining" or "channelling" effect, as mentioned in Chapter 4. This milling artefact occurs when the surface is milled at variable rates in different places. This can happen because of air gaps in the surface, certain areas of the surface might be more difficult to mill than others (due to different materials being present or even

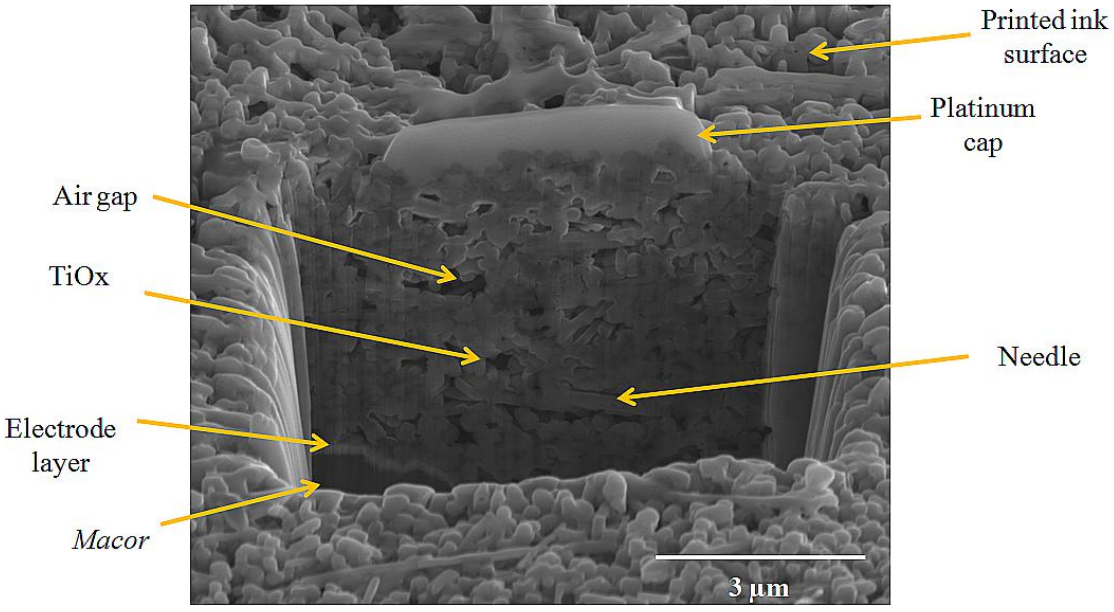

Figure 5.10. Focused ion beam (FIB) milled trench in an as-printed opaque ink sample.

varying crystal faces), and as a result of the surface's inhomogeneous topography. The FIB trench in figure 5.11 similarly shows the platinum cap, but, as this trench is larger (while the depth of the trench is approximately equal, the total area milled away is greater), the bottom of the trench can be seen; the pillars and structures jutting out of the bottom of the trench are formed from the channelling effect. This trench shows that the electrode layer is not completely flat, but has a topography that varies in height by 0.5 to 1 micron. This might be critical in the compressive force dependence of the electrical behaviour, as some regions of the ink are effectively thinner than in other areas and could therefore be easier to compress into a conducting state.

The opaque ink has a complex structure with the needles and TiO_2 particles well dispersed and intricately wetted with polymer binder, which could act as a potential barrier between adjacent conductive needles. Voids in the surface may lend to the compressibility of the ink rather than the pliability of the polymer. While

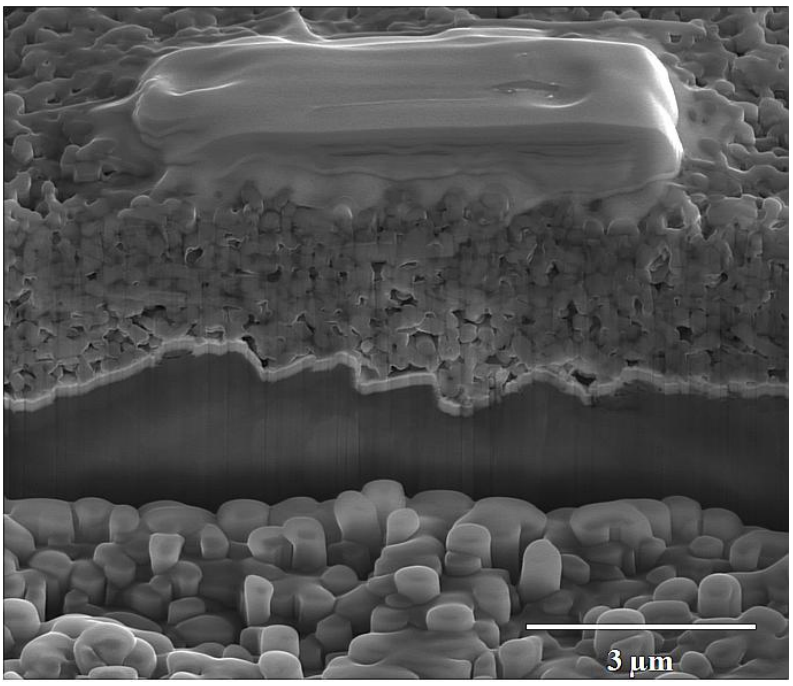

Figure 5.11. FIB milled trench in an as-printed opaque ink sample.

the thermal behaviour of the polymer exhibits a large change in mass, this transition is likely due to solvents evaporating. This feature will be absent from samples previously furnace dried at 90 °C, as were the samples used in the electrical transport measurements. It is unclear how it will behave during successive heating and cooling ramps from room temperature to circa 100 °C.

5.3 Physical properties of the transparent ink

The transparent ink, like the opaque ink, comprises of particles and polymer binder blended in ratios that were tailored by an iterative process. This study examines a particular blend of the ink with enhanced touch-pressure sensitive electrical behaviour and optimal transparency.

5.3.1 Transparent ink constituent structure and thermal behaviour

5.3.1.1 Structural analysis

The transparent ink is similarly comprised of needles and approximately spherical particles dispersed in a polymer binder but with an additional component: 6 μm diameter poly(methyl methacrylate) PMMA micro-beads, used as spacers. The difference is that in this case both particle types are conducting and are made of Sb-doped tin oxide, and the ratio of polymer binder to conducting particles is much greater in the transparent ink. From here, the transparent ink needles will be referred to as Sb-needles, while the more spherical particles will simply be referred to as Sb-particles. The topography of the Sb-needles is almost identical to that of the needles in the opaque ink, as shown in figure 5.12(a). The Sb-particles are also

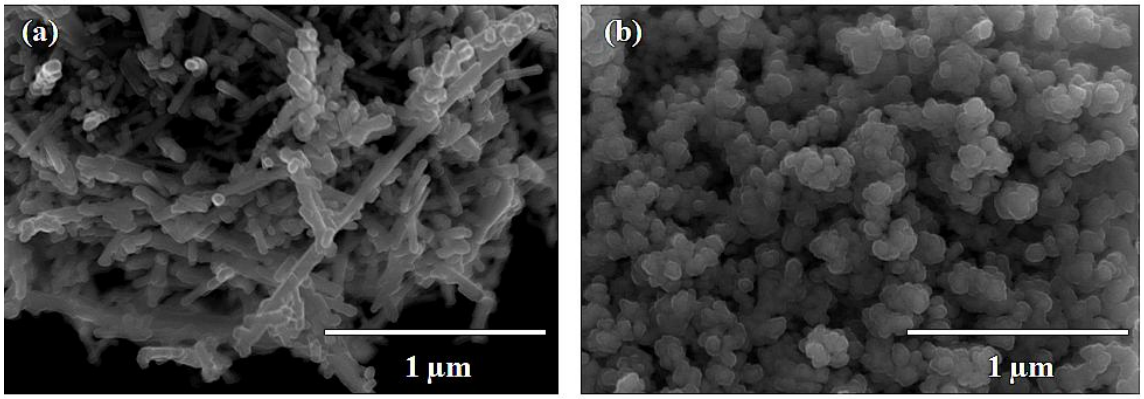

Figure 5.12. SEM image of the transparent inks (a) Sb-needles, and (b) Sb-particles.

similar to the TiO_2 particles in appearance, see figure 5.12(b). Once again, the Sb-needles and Sb-particles look as though they have been bonded together, but this is an image artefact likely to be the result of poor electrical connection to the sample holder (the Sb-needle and Sb-particle powders were dispersed onto a sticky carbon pad, which was grounded through the sample stub. As the samples are powders, the connections between agglomerated areas can be small and discontinuous, leading to charge accumulation. This causes image artefacts as discussed in Chapter 4.). The PMMA beads, shown in figure 5.13, appear to be near-spherical and are very consistently sized. The EDX elemental analysis of both the Sb-needles and Sb-particles, see figure 5.14, show that they exhibit a strong tin oxide signal. The

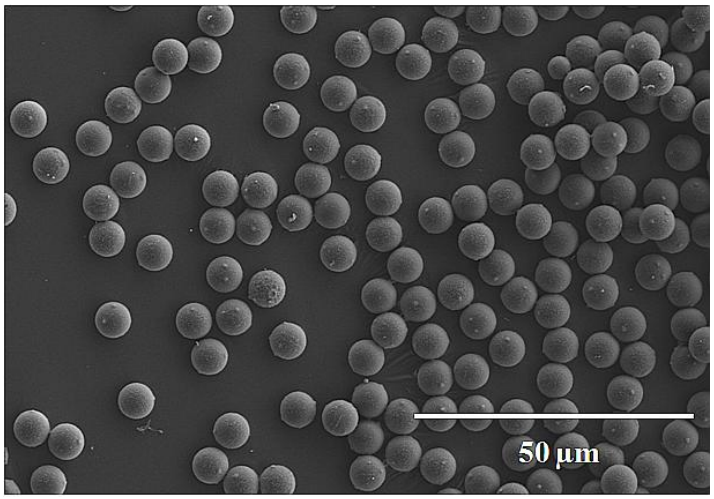

Figure 5.13. SEM image of PMMA microbeads.

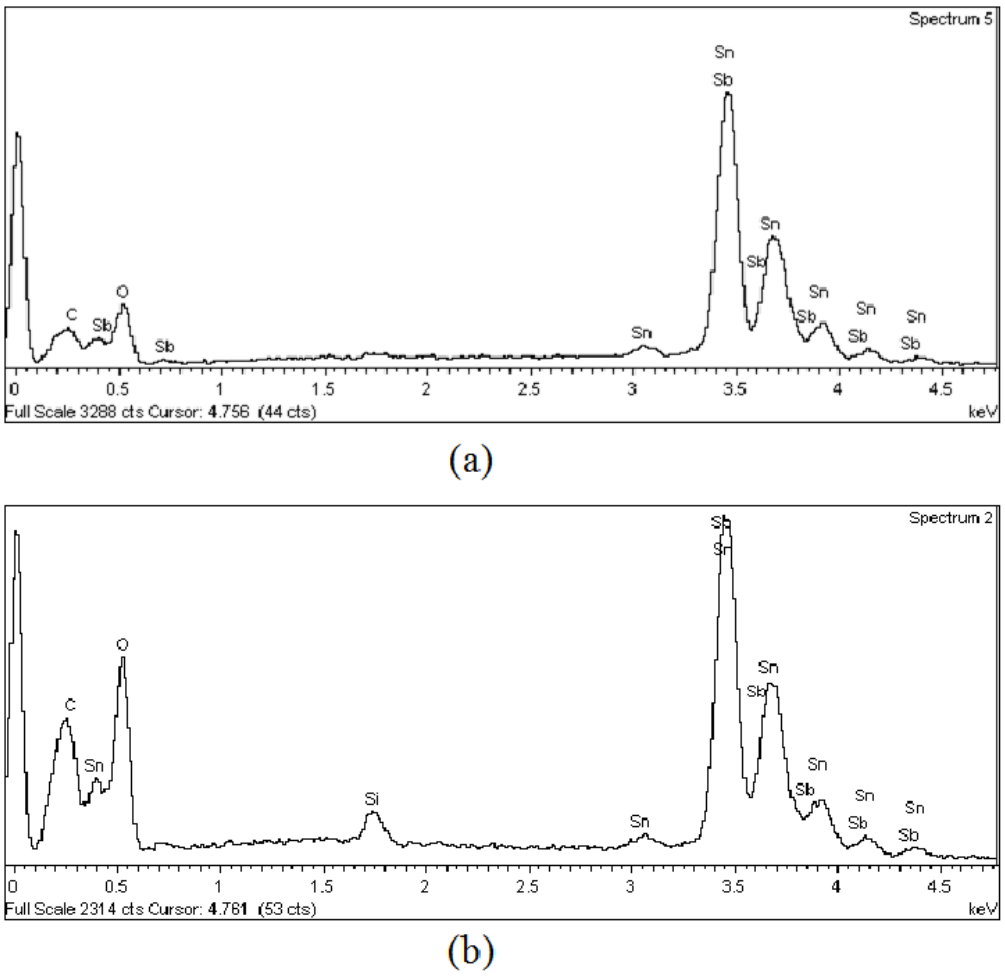

Figure 5.14. EDX elemental analysis of the Sb-needles and Sb-particles.

size distributions of the Sb-needles are shown in figure 5.15. The distributions share the characteristics of those for the needles in the opaque ink: the length of the Sb-

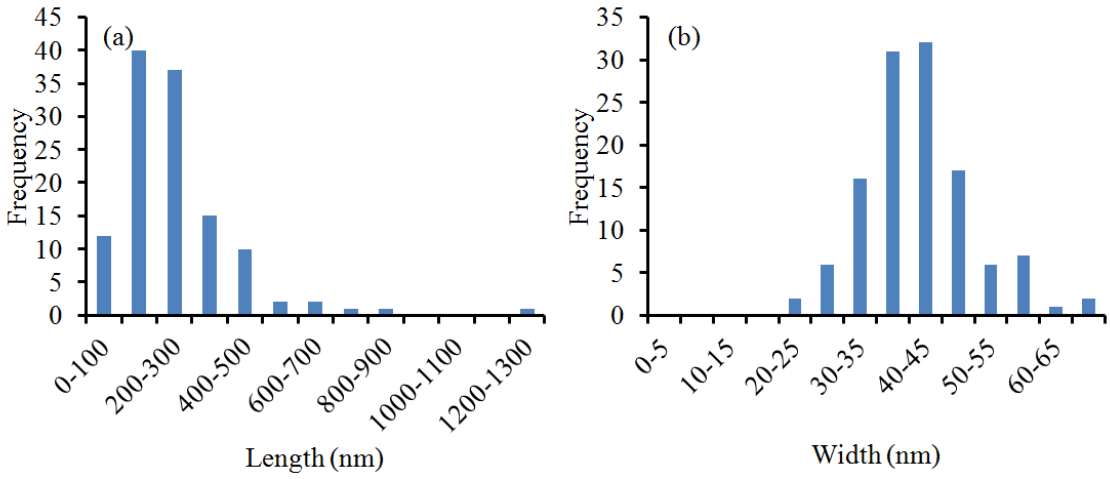

Figure 5.15. Histogram distributions of the Sb-needle (a) length, and (b) width.

needles have a positive skew, while the width distribution is more symmetrical. This may be because the needles are grown from seeds so the width is largely determined by the original seed width, while the length is more variable. Interestingly, the diameter distribution of the Sb-particles in figure 5.16 exhibits a negative skew. In both the case of the Sb-needles and Sb-particles, it is worth noting that these constituents have smaller dimensions than their opaque ink counterparts. The Sb-needles have an average length of 254 ± 1 nm and average width 41 ± 1 nm. Comparing these dimensions with those of the opaque ink needles, the Sb-needles are approximately one fifth the length and one half the width. The Sb-particles have an average diameter of 67 ± 1 nm, approximately one third of the diameter of the TiO_2 particles in the opaque ink. The reason for this difference in size becomes clear after analysing the topography of printed transparent ink layers, discussed below.

5.3.1.2 Thermal analysis

As with the opaque ink, all the separate ink constituents and the blended transparent ink were all studied with TGA and DSC individually.

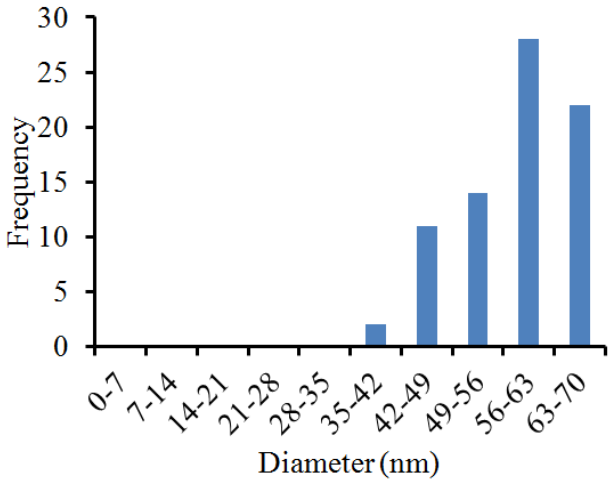

Figure 5.16. Histogram distribution of Sb-particle diameter.

The results for the individual components and the blended ink are discussed here in turn.

The TGA and DSC curves for the Sb-doped needles are shown in figure 5.17(a) and (b). The first aspect of this curve to consider is the total percentage mass loss over the whole temperature range. Between room temperature and 800 °C, the Sb-needle powder loses 1% of its total mass. This suggests that the Sb-needles are essentially inert when heated in air, with no significant chemical reactions or physical changes occurring during the process. Below 50 ° C, a steep decline in the curve is observed. This may be attributed to adsorbed gases/chemicals driven off by the initial heating. Circa 80/90 °C is a small trough in the curve, caused by a physical knock to the experiment. Above this, the curve exhibits a step before undergoing a decline.

While the shape of this decline looks like a decomposition process, the amount of mass lost suggests this curve is caused by gas escaping from within the powdered sample. The DSC curve in figure 5.17(b) shows a steadily declining heating curve with no visible transitions or reactions occurring between 30 and 130 °C. The

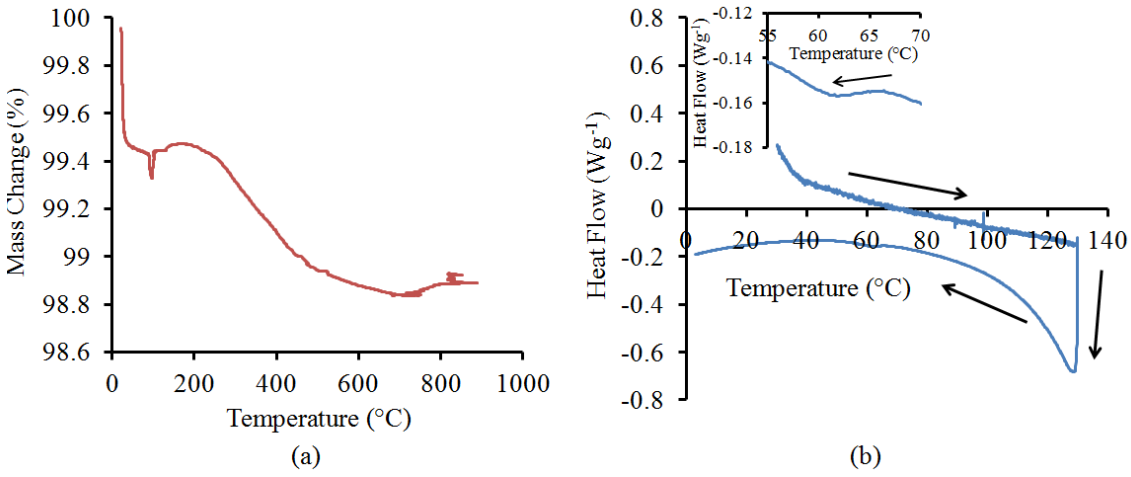

Figure 5.17. Thermal analysis of Sb-needles: (a) TGA curve, (b) DSC curve.

cooling curve is smooth, except for a small feature between 50 and 70 °C similar to that in figure 5.7(b), shown more clearly in the insert. The gentle slope of the DSC curve can be attributed to the action of desorption processes. The TGA and DSC curves for the Sb-particles are shown in figure 5.18. It is important to bear in mind that the Sb-needles and Sb-particles are made from the same material and differ only in shape and size. The TGA curve, figure 5.18(a), shows the same initial decline below 50 °C, indicating the start of desorption of adsorbed gases/molecules. The powder loses approximately 3 % of its total mass during this test up to 700 °C, again suggesting that desorption is the only significant process occurring here. The DSC curve, figure 5.18(b), confirms this, with the heating portion of the curve looking very similar to the heating curve of the Sb-needles. Interestingly, the same small feature between 50 and 70 °C occurs in the Sb-particle cooling curve, shown in the insert. This could be caused by desorption of specific molecules or compounds, some kind of exothermic reaction (unlikely given it does not occur during the initial heating curve), or an artefact as described above. The TGA curve of the PMMA microbeads, shown in figure 5.19(a), shows a mass loss event between approximately 60

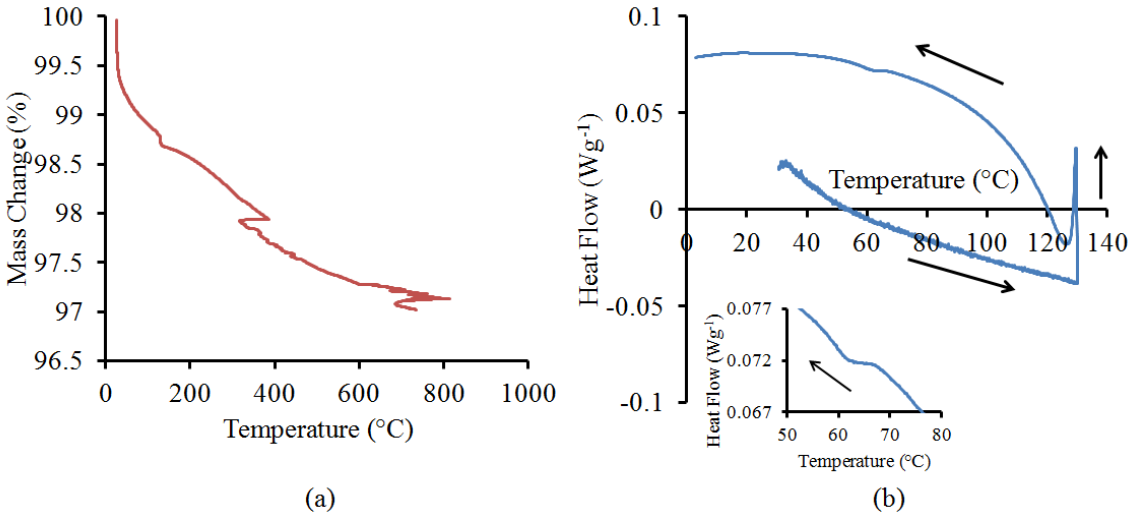

Figure 5.18. Thermal analysis of Sb-particles: (a) TGA curve, (b) DSC curve.

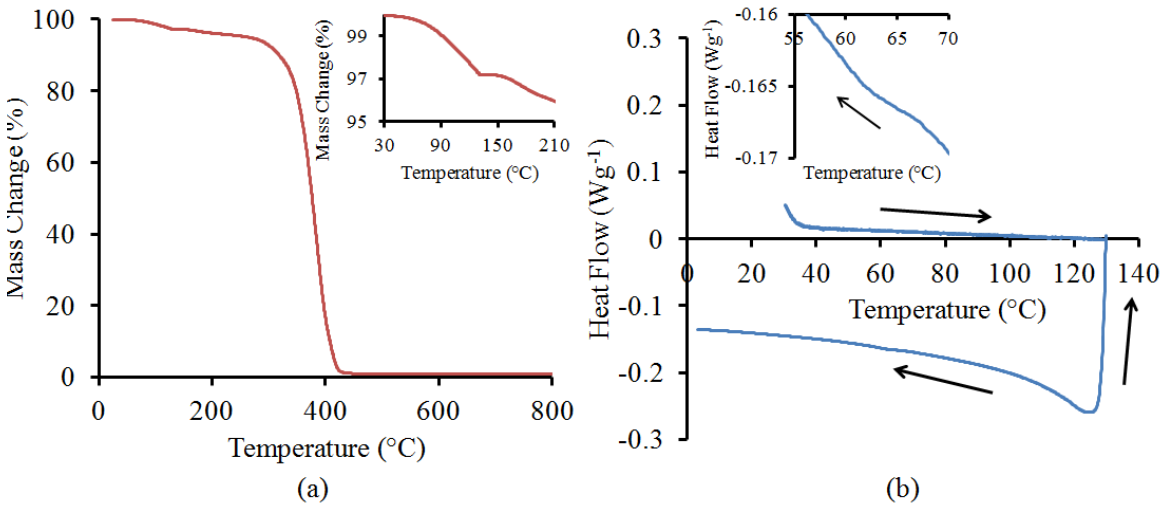

Figure 5.19. Thermal analysis of PMMA microbeads: (a) TGA curve, (b) DSC curve.

and 120 °C, with the sample decomposing between 350 to 400 °C. The first feature is again likely to be related to desorption processes. The corresponding DCS in figure 5.19(b) is, like the previous curves, featureless and smooth. It is worth noting that no feature is found which corresponds to that seen in figure 5.19(a) between 60 and 120 °C. Zooming into the cooling curve, a small anomaly is found between 60 and 70 °C. This has once again occurred in the same range as the previous anomalies. This suggests that, while this might be a glass transition, the possibility of it being an artefact cannot be ruled out.

5.3.2 As-printed transparent ink structure and thermal behaviour

5.3.2.1 Structural analysis

While the opaque ink was sufficiently conductive to image directly under a SEM, the as-printed transparent ink layer is less conductive and SEM analysis was extremely difficult due to significant charging effects leading to numerous image artefacts. To remedy this situation the printed transparent layers were coated with a 20 nm layer

of carbon, and this top coating was electrically connected to the grounded sample stub on to which the transparent ink samples were fixed. This coating was achieved using a Cressington Carbon Coater: it operates by passing a current through two conically sharpened carbon rods, in contact with each other via their sharpened tips. The current heats the carbon rod tips, the point of contact, and leads to the production of carbon.

An example of the SEM imaging of the printed transparent ink layer is shown in figure 5.20. The surface is not as complex as that for opaque ink, due to the fact that the ratio of polymer binder to conducting particles is much greater in order to obtain high transparency. The conducting particles clump into relatively large aggregates, with an average diameter of 7 μm, in the printed ink layer. These are highlighted in figure 5.20 and more clearly in figure 5.21, a collection of images, including those taken with a backscatter electron detector, where image contrast is associated with atomic number. The size of the conducting particles was reduced in the transparent ink to tailor the structure of these aggregates. The SEM images of the transparent inks were taken at low beam energies (5 kV or less) and at

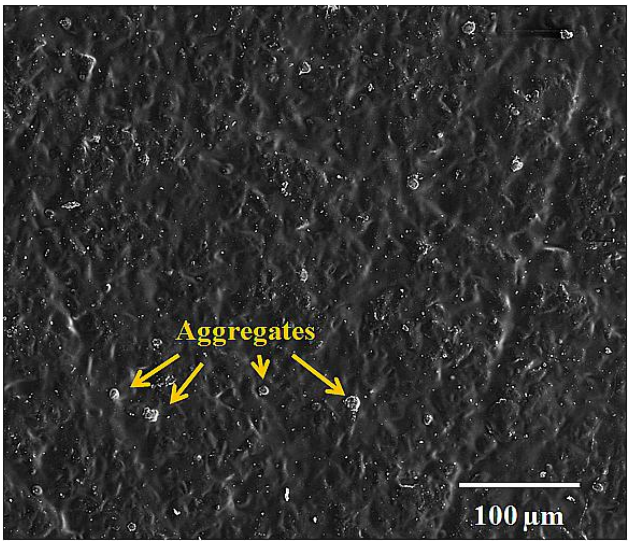

Figure 5.20. SEM image of the as-printed transparent ink surface.

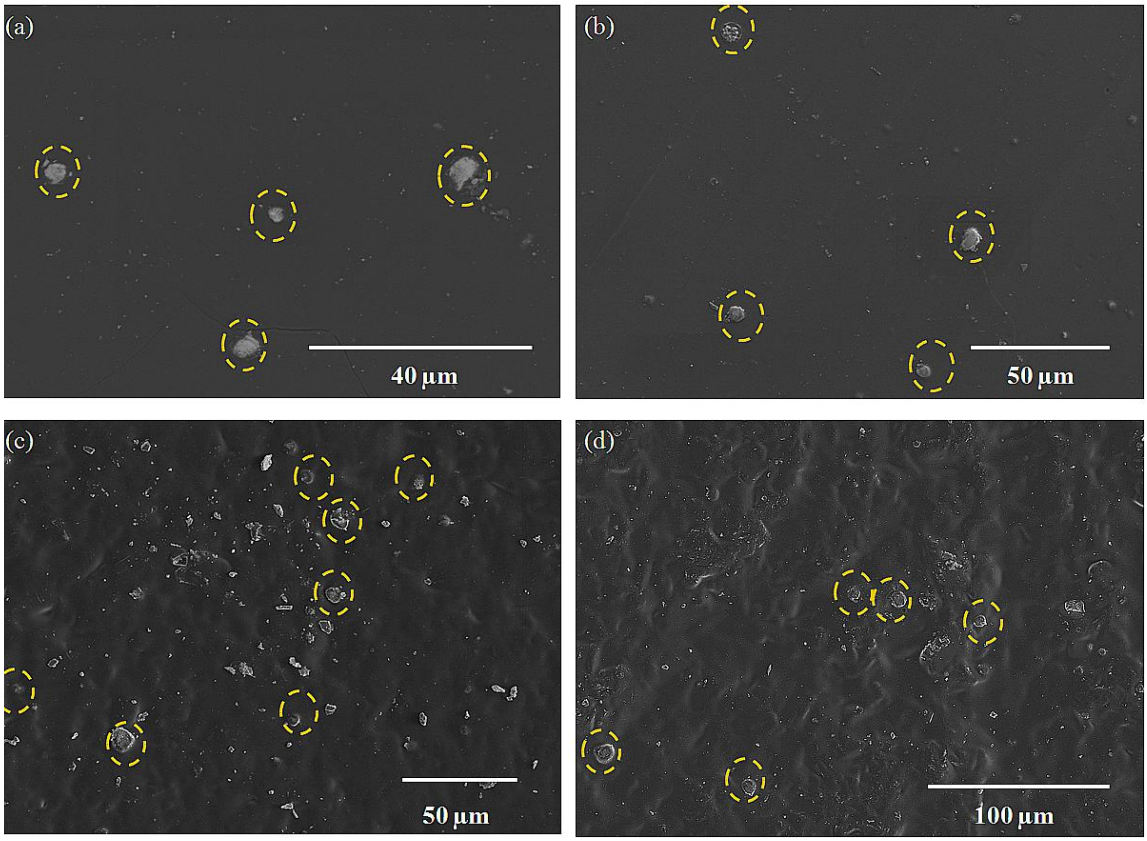

Figure 5.21. Example SEM images of the as-printed transparent ink surface using the backscattered electron detector in (a) and (b), and the secondary electron detector in (c) and (d). Aggregates are highlighted in the dashed yellow circles.

working distances greater than 4 mm because of the fragile nature of the polymer layer: higher beam energies or smaller working distances consistently resulted in local heating and irreversible physical damage to the polymer layer, which manifested as "bullet-holes" in the polymer surface. This is shown in figure 5.22.

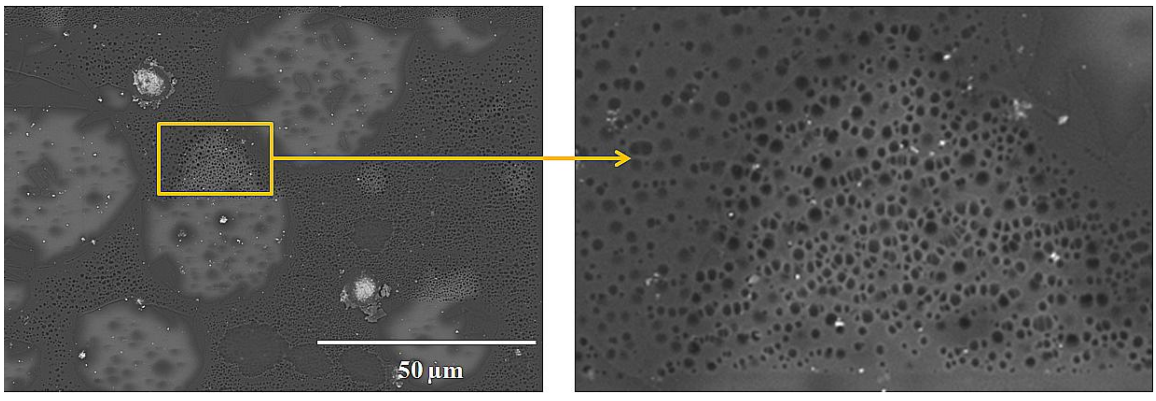

Figure 5.22. SEM backscatter image of a printed transparent ink layer showing "bullet-hole" damage to the polymer as a result of interactions between the polymer and the incident electrons.

Early forms of the transparent ink used larger conducting particles and as such featured larger aggregates with rough surfaces. These aggregates lead to undesirable electrical behaviour as a result of the aggregates piercing through the top layer of polymer binder (leading to short circuits under compression) and becoming squashed and flattened after cycles of compression, reducing the touch-pressure sensitivity of the electrical behaviour. Examples of these are shown in figure 5.23. The addition of the PMMA beads as spacers was also intended to reduce the likelihood of sample breakdown via these mechanisms.

The measured size distribution of the aggregates is presented in figure 5.24. The aggregates appear to have a bimodal Gaussian distribution. The reason for this bimodality is not yet known: it could be related to the blending process, the printing of the ink or even the drying process. Cross-sections, see figure 5.25, reveal the aggregates are more densely compacted near the top surface of the printed ink. Air gaps are observed throughout the aggregate, but these tend to increase in size towards the bottom of the aggregate structure. It is also worth noting that the

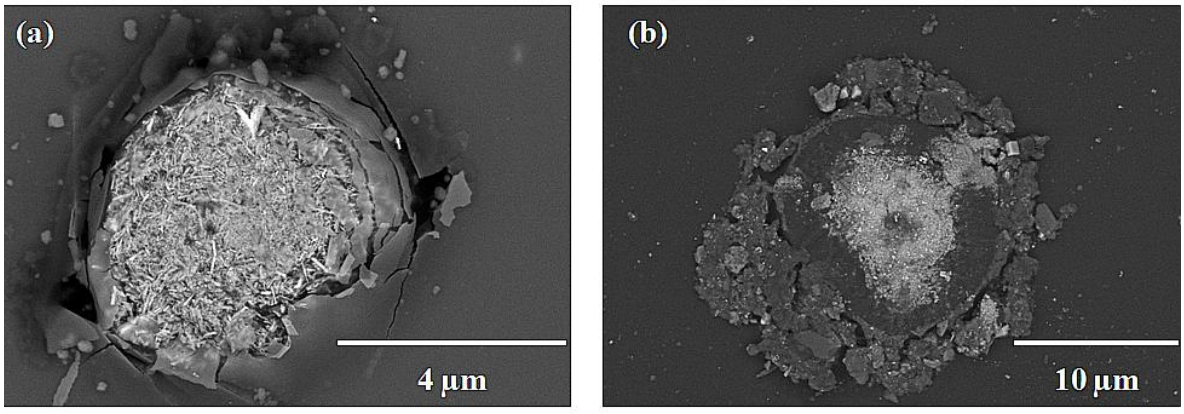

Figure 5.23. SEM image of (a) an aggregate bursting through the top surface of a printed transparent ink layer, and (b) an aggregate flattened by compressive force.

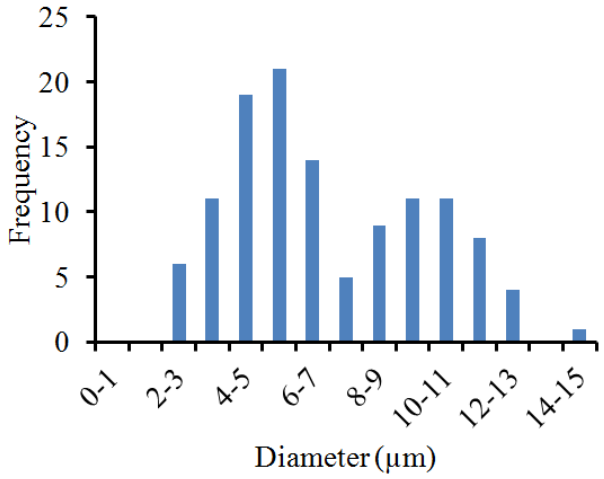

Figure 5.24. A histogram distribution of transparent ink aggregate measured diameter.

aggregates are approximately as deep as the printed layer. Once again, this cross-section shows that the *macor* electrodes are not always very flat, having an approximate RMS roughness of 1.0 µm.

5.3.2.2 Thermal analysis

The TGA of the blended transparent ink is shown in figure 5.26(a). This curve appears to be a superposition of all the previous curves but is dominated by the thermal response of the polymer binder, showing a ~70 % loss of mass below 100 °C and undergoing decomposition by 400 °C. The initial 70 % mass change is once again due to solvent loss as the sample was not furnace dried prior to testing. The DSC heating curve in figure 5.26(b) features a trough and hump at 40 and 90 °C, respectively. This pattern could be related to the drying of the ink. The cooling curve has a steady incline but once again contains an anomalous feature between 58 and 72 °C, shown in the insert. The fact that the anomaly between ~50 and 70 °C occurs in every sample suggest it is either a systematic error from the equipment, or more likely some kind of undetermined contamination rather than a chemical or physical change in any of the samples tested. The transparent ink surface structure is

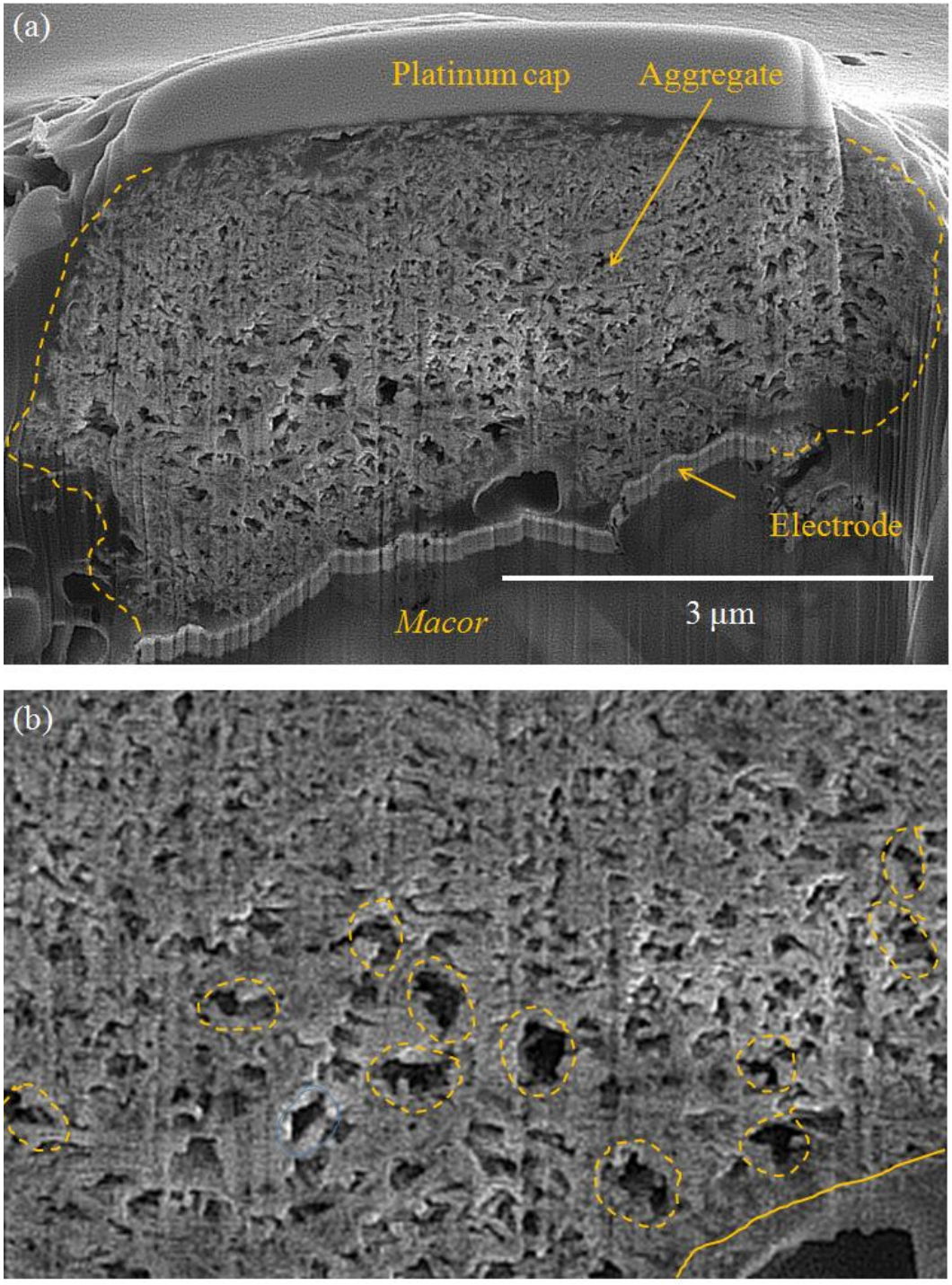

Figure 5.25. Example of (a) a FIB milled trench of an aggregate in a printed transparent ink layer – the edges of the aggregate are highlighted by the dashed yellow lines, (b) a closer view of the cross-section – air gaps/voids are highlighted by the dashed yellow circles, the bottom of the aggregate is indicated by the solid yellow line.

characterised by large aggregates sparsely dispersed in polymer binder. Conduction between isolated aggregates is unlikely due to their large (several microns) separation. The structure within the aggregates is similar to that of the opaque ink,

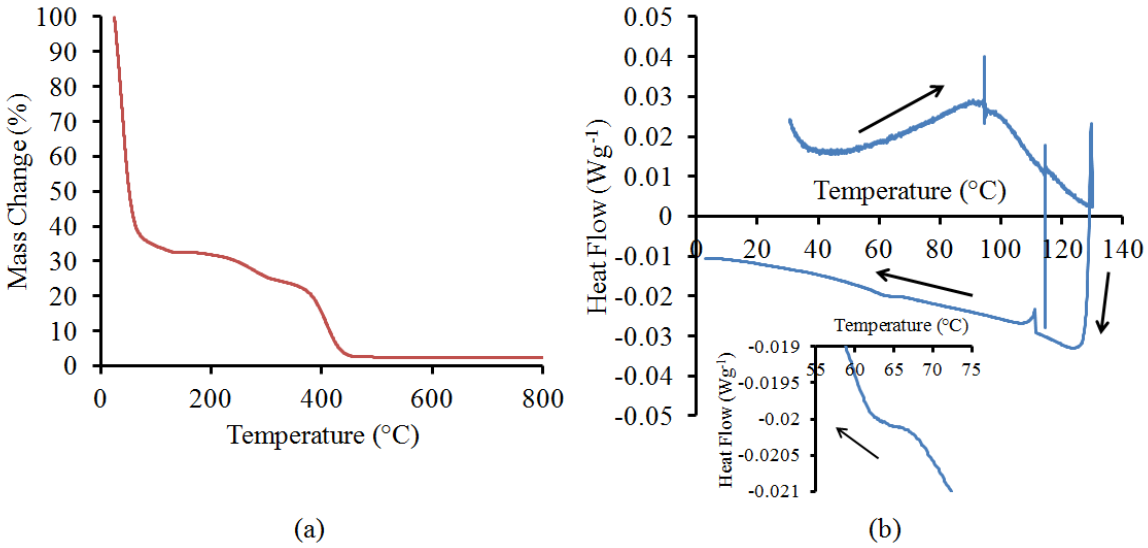

Figure 5.26. Thermal analysis of a transparent ink sample: (a) TGA curve, (b) DSC curve.

with the Sb-needles and Sb-particles randomly dispersed within the aggregate and small voids evident. The compressibility of the transparent ink will be attributed to these air gaps but also to the polymer binder, due to its more significant presence. The thermal analysis reveals the Sb-needles and Sb-particles are essentially chemically and physically inert in response to increasing temperature and that the thermal response of the ink is dominated by the thermal properties of the polymer binder. As with the opaque ink, it is unclear how the polymer binder and ink responds to successive heating/cooling ramps after being furnace dried prior to testing.

5.4 Summary

The opaque ink comprises nano-scale conducting needles and insulating near-spherical TiO_2 nanoparticles dispersed in an insulating polymer binder. The as-printed ink has a complex surface structure, and this surface structuring is also representative of the cross-section. Small areas of local ordering exist in the surface, where some of the needles “point” in the same direction, but generally both the

needles and the TiO_2 particles are well dispersed, with some air gaps present. Some needles project out of the plane of the ink surface but generally they tend to lie in the plane of the printed ink, both at the surface and within the bulk of the printed ink layer. The particles appear to be wetted with polymer binder. This thin coating of polymer may be acting as a potential barrier between many of the conductive needles, an important factor in quantum tunnelling mechanisms. That said, there will also likely be many direct electrical connections between the needles, forming a large percolative network.

The transparent ink is similarly comprised of nano-scale needles and near-spherical particles dispersed in insulating polymer binder, with the exception that both these smaller particle types are conducting in the transparent ink. The particles coalesce into large clusters/aggregates, presumably while the ink is wet prior to printing. These aggregates are randomly dispersed throughout the ink layer and are typically separated by several microns. Quantum mechanical tunnelling of charge between aggregates is unlikely due to this large average separation. Cross-sections of the aggregates, which are about as thick as the printed ink layer depth, show a structure similar to that of the opaque ink cross-section. It is more reasonable to suggest that, on the basis of this SEM analysis, much of the charge transport occurs within the individual aggregates.

Thermal analysis reveals the nanoparticles in both inks are very stable over a wide range of temperature. The TGA and DSC of the polymer binder shows an extensive drying and decomposition process, which reaches completion by 400 °C: this dominates the thermal analysis of the blended inks.

6. Electrical transport phenomena of opaque ink: results and discussion

6.1 Introduction

The electrical transport measurement results obtained for the opaque ink, and the analysis and physical interpretation, are presented in this chapter. The transport measurements were performed as described in Chapter 4, recording current-voltage (I-V) curves at a range of compressive loadings and at a range of temperature up to 100 °C. First, the compressive loading dependence of the electrical behaviour at fixed temperature is described and discussed, before the temperature dependence of the electrical behaviour is presented and discussed. A physical model describing the electrical behaviour is developed here. This consists of two distinct conduction contributions and is used in the analysis of the data as a function of temperature. Finally, the main findings and conclusions are summarised in the closing section.

6.2 Compressive force dependence of electrical transport

The I-V curves were obtained according to the method outlined in Chapter 4. An example I-V curve (1st sweep) and a repeat measurement, taken at 0.2 N compressive force, is shown in figure 6.1(a). Generally, the I-V curves are non-linear and there is some electrical hysteresis. This hysteresis shows as the down ramp of the voltage produces more current than the up ramp of voltage in the test device. The hysteresis is shown in more detail in figure 6.1(b). Subsequent I-V curves (4th, 7th, and 10th

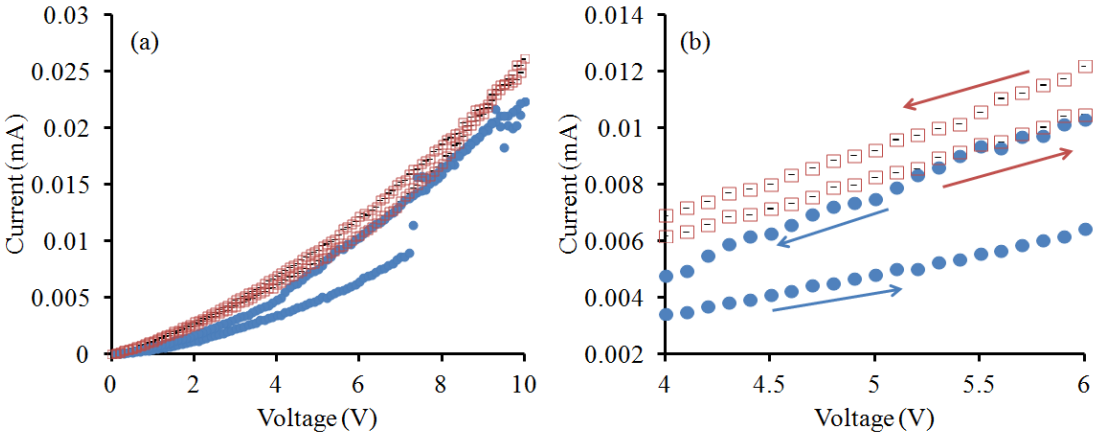

Figure 6.1. (a) 1st sweep of an I-V cycle (solid circles) and a repeat measurement (open squares) taken at 0.2 N compression and 20 °C. (b) A closer view of the electrical hysteresis. The arrows indicate the direction of the voltage sweep. Error bars are smaller than the data points.

sweeps) are compared to 1st sweep in figure 6.2. These data show that the hysteresis largely occurs during the 1st sweep, and it is less pronounced in the later I-V sweeps

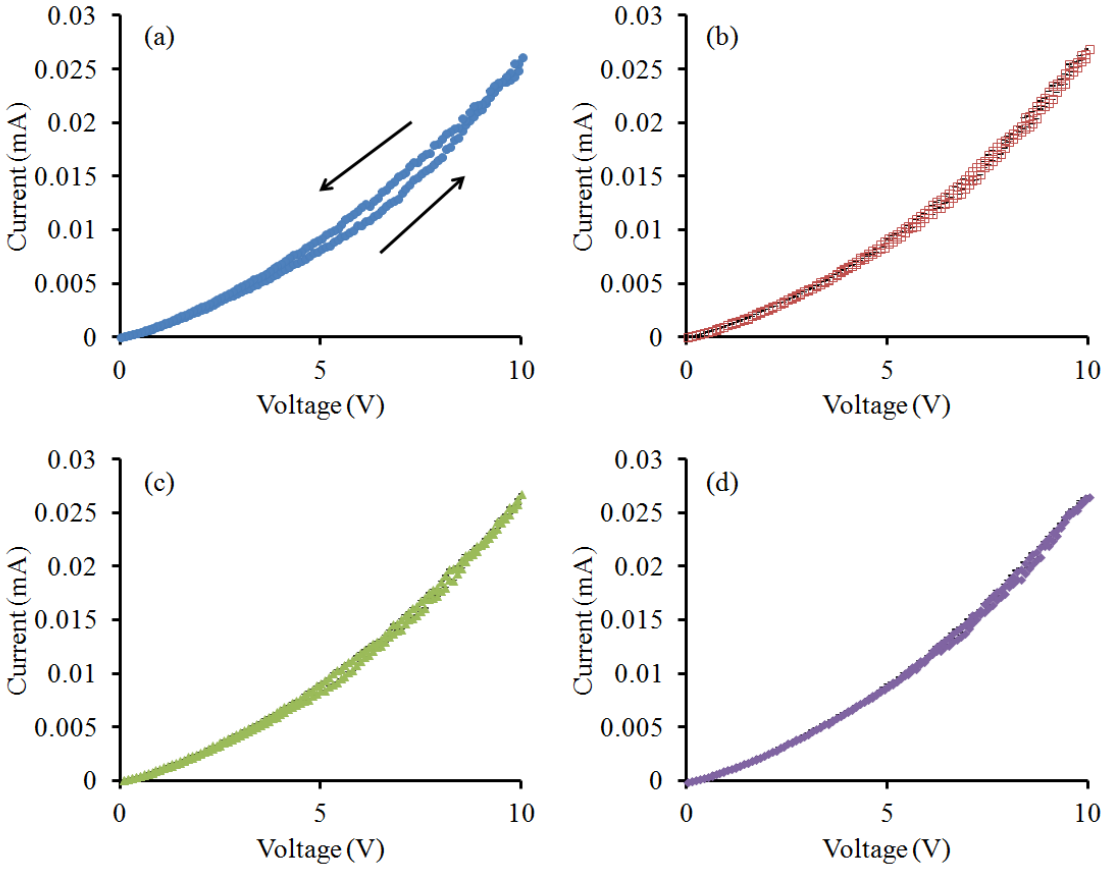

Figure 6.2. Examples of individual sweeps in series (a) 1st, (b) 4th, (c) 7th, (d) 10th of an I-V cycle taken at 0.2 N compression and at 20 °C.

in a cycle. Comparing figure 6.1 to the 1st sweep of an I-V cycle (and a repeat measurement), taken at a higher compressive loading of 0.8 N in figure 6.3(a), the behaviour has become more linear, and the current passed through the device has increased approximately 20-fold. Notice also that the hysteresis remains and is shown more clearly in figure 6.3(b). A series of I-V sweeps from a cycle at 0.8 N compression are shown in figure 6.4. As in the sweeps shown in figure 6.2, the hysteresis is largely observed in the first I-V sweep.

Figure 6.5 compares the averaged I-V curves taken at 0.2 and 1.0 N compression. With increasing compression, the I-V behaviour becomes more linear. Figure 6.6 shows the same I-V curves, up to 1.0 N, normalised to their peak current values. This figure shows the small increase in linearity as the compressive force increases from 0.2 N to 1.0 N compression. The shape and pressure sensitivity of the I-V behaviour suggest that complex conduction mechanisms may be present in the ink, and that these mechanisms are dependent on the compression of the ink layer. Higher compression causes the ink to behave in a more linear, ohmic fashion. Additionally, the electrical hysteresis implies a memory effect may be at work. This

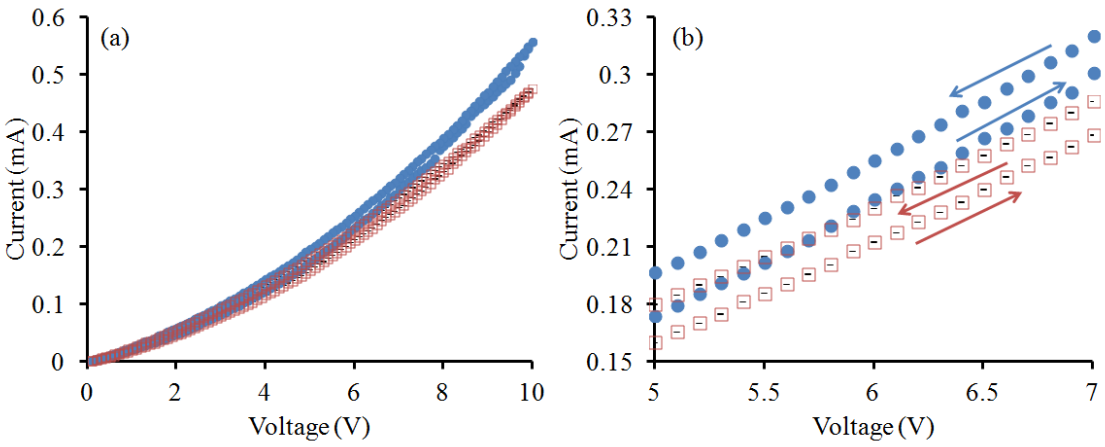

Figure 6.3. (a) The 1st sweep of an I-V curve (solid blue circles) and a repeat measurement (open squares) taken at 0.8 N compression and at 20 °C. (b) A closer view of the hysteresis. The arrows indicate the direction of the voltage sweep. Error bars are smaller than the data points.

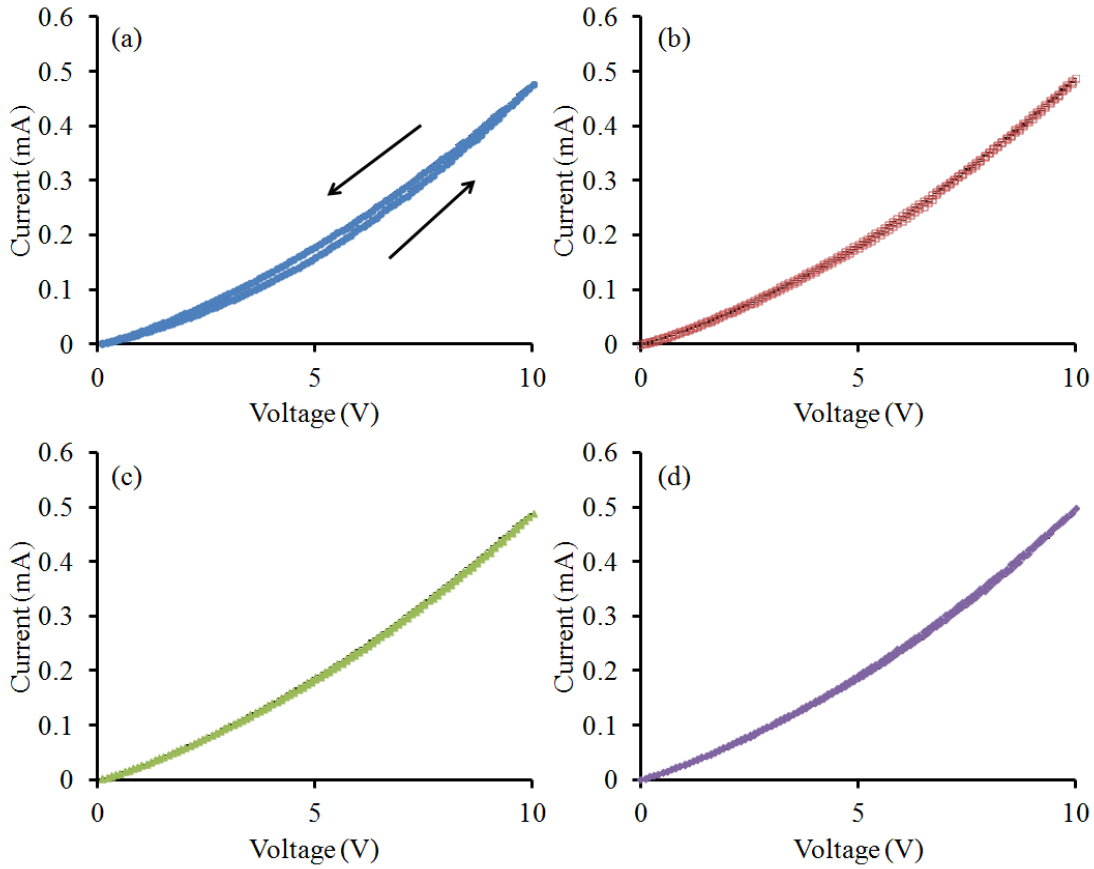

Figure 6.4. A series of sweeps in series (a) 1st, (b) 4th, (c) 7th, (d) 10th of an I-V cycle taken at 0.8 N compression and at 20 °C.

feature results in the ink having a lower overall electrical resistance on the down ramp of the voltage. The resistance response of the ink, calculated from the initial resistance from the 1st I-V sweep, to compressive force is summarised in figure 6.7.

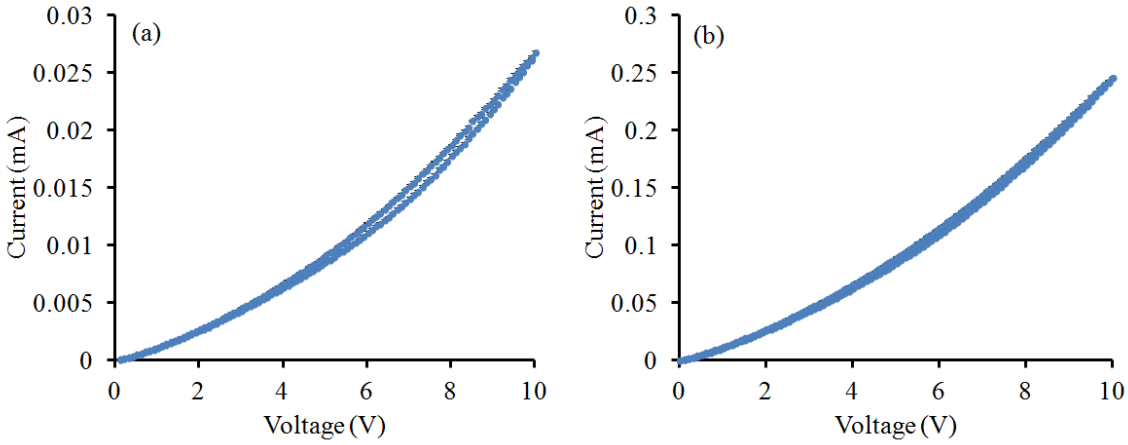

Figure 6.5. Averaged I-V curves measured at (a) 0.2 N and (b) 1.0 N compression. Note the magnitude of the current passed and the linearity of the behaviour are greater at higher compressions.

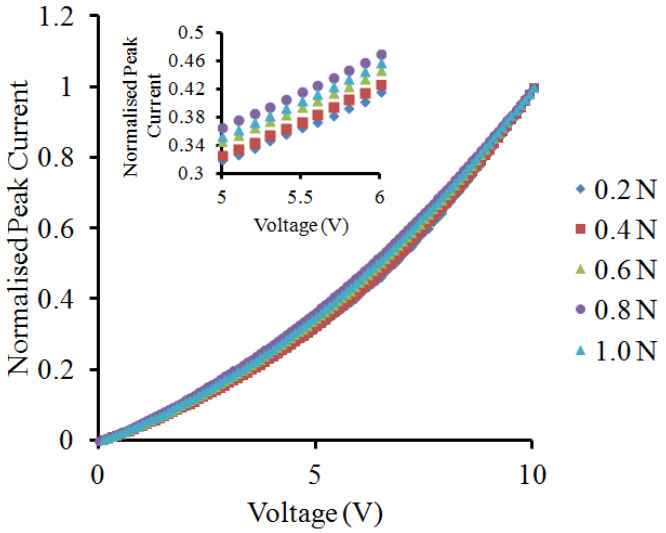

Figure 6.6. (a) I-V curves taken at 5 mass loads and normalised to their peak current values.

The data suggest that there are three regions of electrical resistance behaviour: first, there is an initial dramatic drop in the electrical resistance of the ink at the lowest compressions. The decrease of the resistance in response to force slows in the second region, between 0.5 and 1.0 N, before falling at a lower rate above 1.0 N compression.

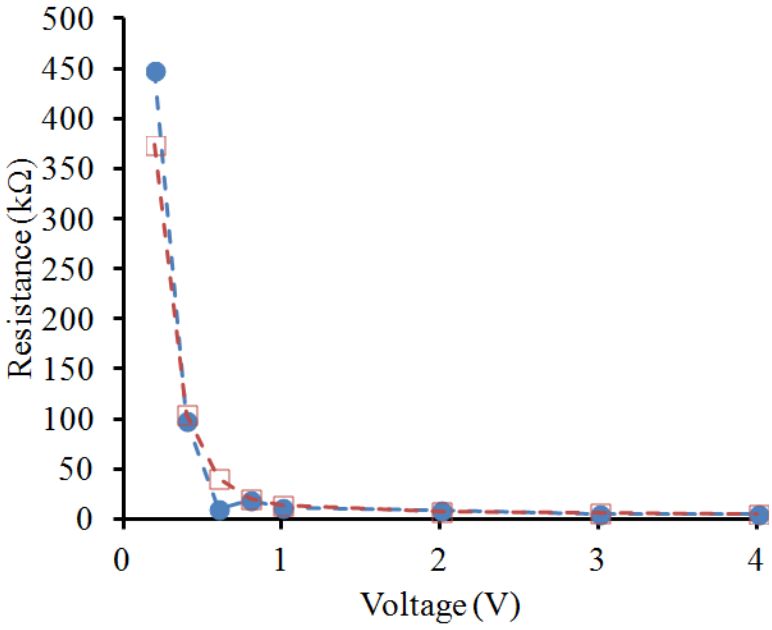

Figure 6.7. The electrical resistance response of the nanocomposite ink to compressive force. An initial measurement run (solid circles) is compared with a repeat measurement (open squares).

6.3 Temperature dependence of electrical transport

Electrical transport measurements were taken up to a maximum temperature of 100 °C. Preliminary work experimented with heating the ink sensors up to 120, 150 and 200 °C, but I-V sweeps taken at these temperatures resulted in the samples being destroyed after one use, preventing repeat measurements. Typical I-V curves taken at room temperature, 40, 60, 80 and 100 °C, at four compressions, are shown in figure 6.8. As the temperature is increased, the total current passed through the ink increases. This effect is thought to be a result of temperature increasing the efficacy of tunnelling mechanisms and conduction through the semiconducting material in the ink, mentioned in Chapter 3 and discussed in greater detail in section 6.4. Four sweeps of an I-V cycle taken at 50 °C are shown in figure 6.9. As in figures 6.3 and 6.6 the electrical hysteresis is more prominent in the first sweep of the cycle. These are compared to four sweeps of an I-V cycle taken at 80 °C in figure 6.10. As before,

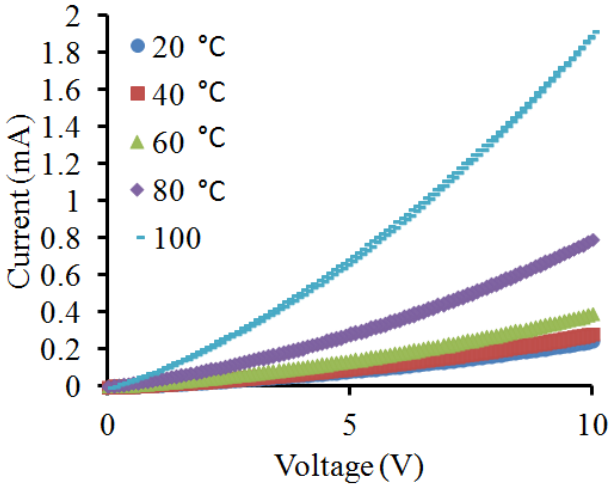

Figure 6.8. Averaged I-V curves measured at 5 temperatures: 20, 40, 60, 80 and 100 °C. All I-V curves were taken at a compression of 0.6 N.

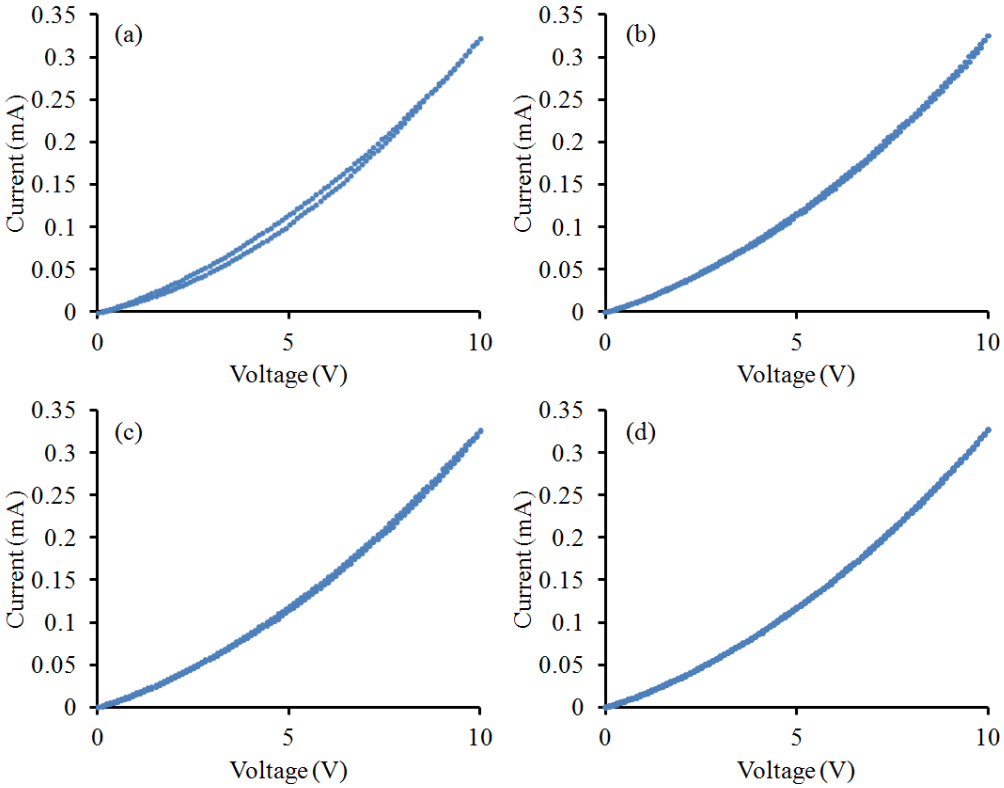

Figure 6.9. Example sweeps in series (a) 1st, (b) 4th, (c) 7th, (d) 10th of an I-V cycle taken at 0.6 N compression and at 50 °C.

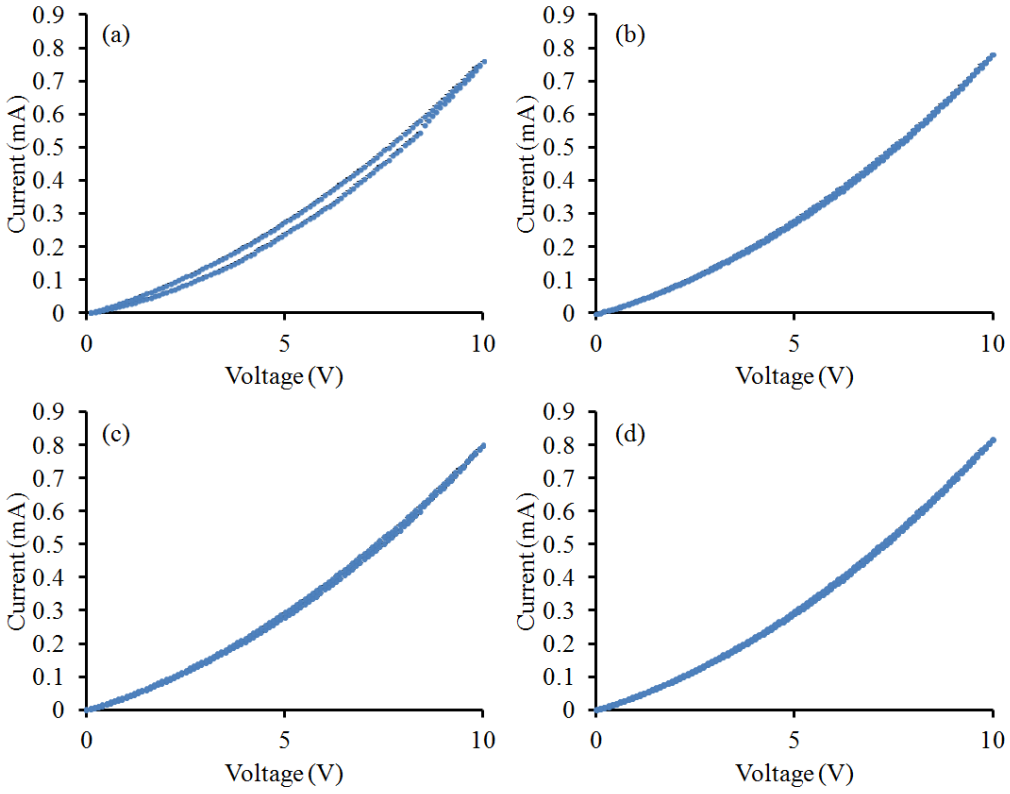

Figure 6.10. Example sweeps in series (a) 1st, (b) 4th, (c) 7th, (d) 10th of an I-V cycle taken at 0.6 N compression and at 80 °C.

the hysteresis is observed in the first sweep and is seen to a much lesser extent in subsequent sweeps. Figure 6.11 shows averaged I-V curves taken at five temperatures and normalised to their peak current values. While the curvature of the I-V behaviour decreases with increasing compression (higher compression leads to more linear I-V), it does not appear to significantly vary with temperature. This implies that temperature has an equal effect on all conduction mechanisms.

6.4 Modelling the conduction mechanisms

6.4.1 Electrical conduction behaviour in response to compressive force

As discussed in Chapter 3, an electrical conduction model comprising two components, linear conduction through direct contacts and non-linear field-assisted quantum tunnelling conduction, is developed as the theoretical basis for interpreting

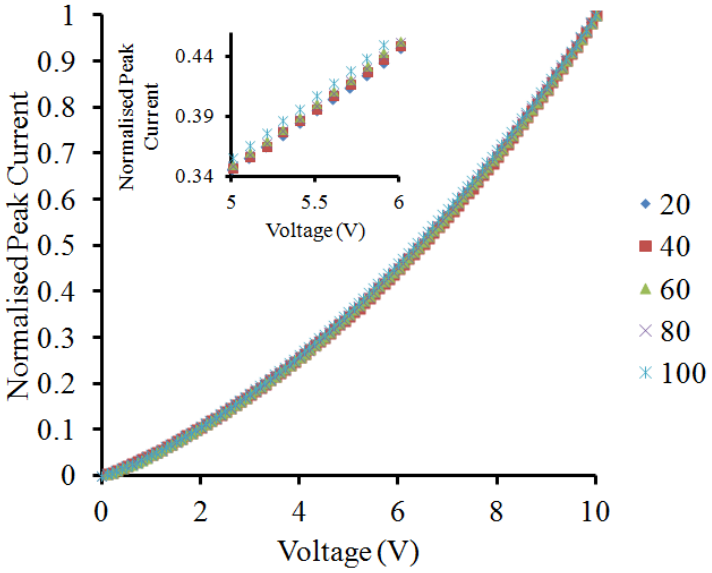

Figure 6.11. Averaged I-V curves measured at 5 temperatures and normalised to their peak current values.

and understanding the conduction behaviour in this nanocomposite ink. Equation 6.1 describes the relationship between the current density and electric field.

$$J = \sigma_0 E + AE^n exp\left(-{}^{C}/_{E}\right) \quad (6.1)$$

where σ_0 is the linear electrical conductivity; E is the electric field; parameter A is related to the frequency of tunnelling events (or the magnitude of tunnelling conduction) and comprises numerous physical factors, such as the field enhancement; n is an exponent that depends upon the tunnelling mechanisms present and can take a value between 1 and 3. In the special case of Fowler-Nordheim tunnelling n = 2. C is a constant associated with the height of the potential barrier.

This model utilises a simplified expression for the current density of field-assisted quantum tunnelling from Chapter 3, added in series to a linear, ohmic conduction contribution. The linear contribution is considered to originate from direct contacting between the conducting acicular particles in the ink. The non-linear contribution is attributed to quantum tunnelling between isolated needles and isolated clusters of needles. The fitting was performed using Origin® Pro 7 software, which automatically optimises the values of each parameter in the model using a Levenberg-Marquardt (damped least-squares method) algorithm [137]. The use of this model has allowed the extraction of values for the linear conductivity and parameter A as a function of both applied compressive force and ink temperature, as well as values for the exponent n.

An example of the fitting of the model to an increasing I-V curve measured under 0.2 N compression is shown in figure 6.12, along with the statistical residual

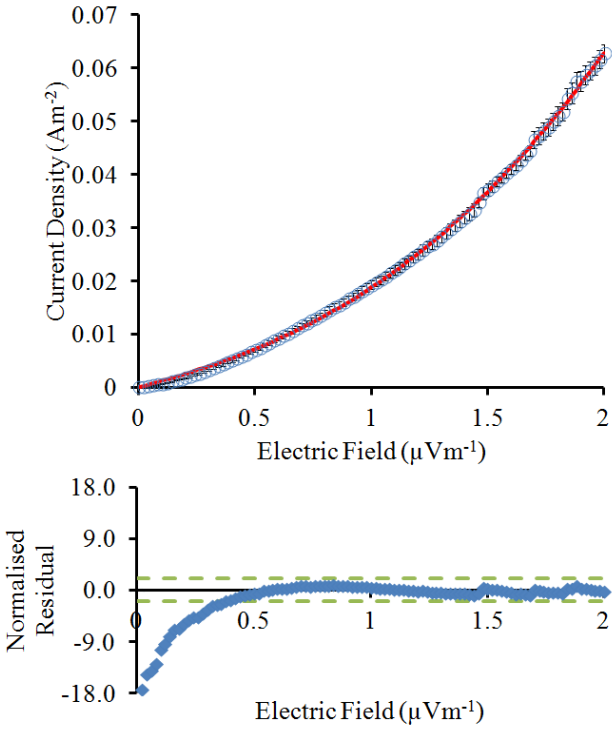

Figure 6.12. An example of the fit of a model comprising linear and non-linear conduction contributions to a 10 sweep average increasing I-V curve taken at 0.2 N compression and 20 °C. The model fit is shown as a solid red line. Below is a normalized residual analysis of the fit to the data. The dashed green lines represent the boundaries for an acceptable fit.

analysis. The normalised residual analysis involves taking the difference between the best fitting model data points and the corresponding observed data points, and dividing this difference by the error on the observed data points. A good fit is characterised by randomly distributed residuals which are nominally constrained between ±2. Upon first inspection, the fit appears to be very good but the residual analysis reveals some interesting details. Firstly, the model is a poor description of the electrical behaviour below 0.5 μVm^{-1}. Specifically, the model predicts a greater current density than that observed in practice. At higher electric field, while the residuals generally lie between 2 and -2, their distribution has some ordering which also suggests that the model is incomplete.

Figure 6.13(a) shows an example fit to increasing I-V data taken at 0.6 N compression. Again we see that the fit appears to be good, but the same patterns are

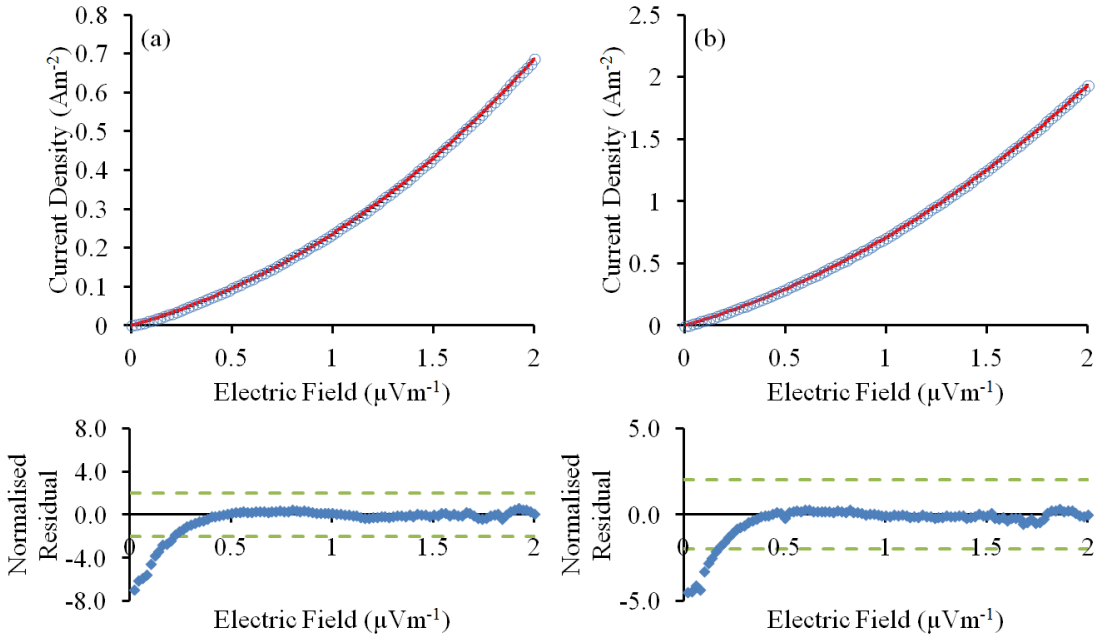

Figure 6.13. An example of the fit of a model comprising linear and non-linear conduction contributions to a 10 sweep average increasing I-V curve taken at 20 °C under (a) 0.6 N compression, and (b) 1.0 N compression. The model fit is shown as a solid red line. Below is a normalized residual analysis of the fit to the data. The dashed green lines represent the boundaries for an acceptable fit.

found in the residuals: the model performs poorly in the low electric field limit and the residuals show some order at higher electric field values. The same fitting behaviour is exhibited in figure 6.13(b), which is a fit of the model to the increasing I-V curve taken at 1.0 N compression. As the compression is increased, the residuals below 0.5 μVm^{-1} steadily improve from -18 in figure 6.12 to -4.5 in figure 6.13(b), but still suggest the model is not a good description of electric conduction at low voltages in the nanocomposite. Examples of fits to decreasing I-V data are shown in figure 6.14.

The model fit behaves in the same way here, being a more accurate description of conduction at higher electric field values. As mentioned previously, the use of this model allows the extraction of two parameters: the linear conductivity σ_0, and the non-linear parameter A which quantifies the conduction attributed to field-assisted tunnelling. Figure 6.15(a) shows the behaviour of the linear conductivity, σ_0, as a

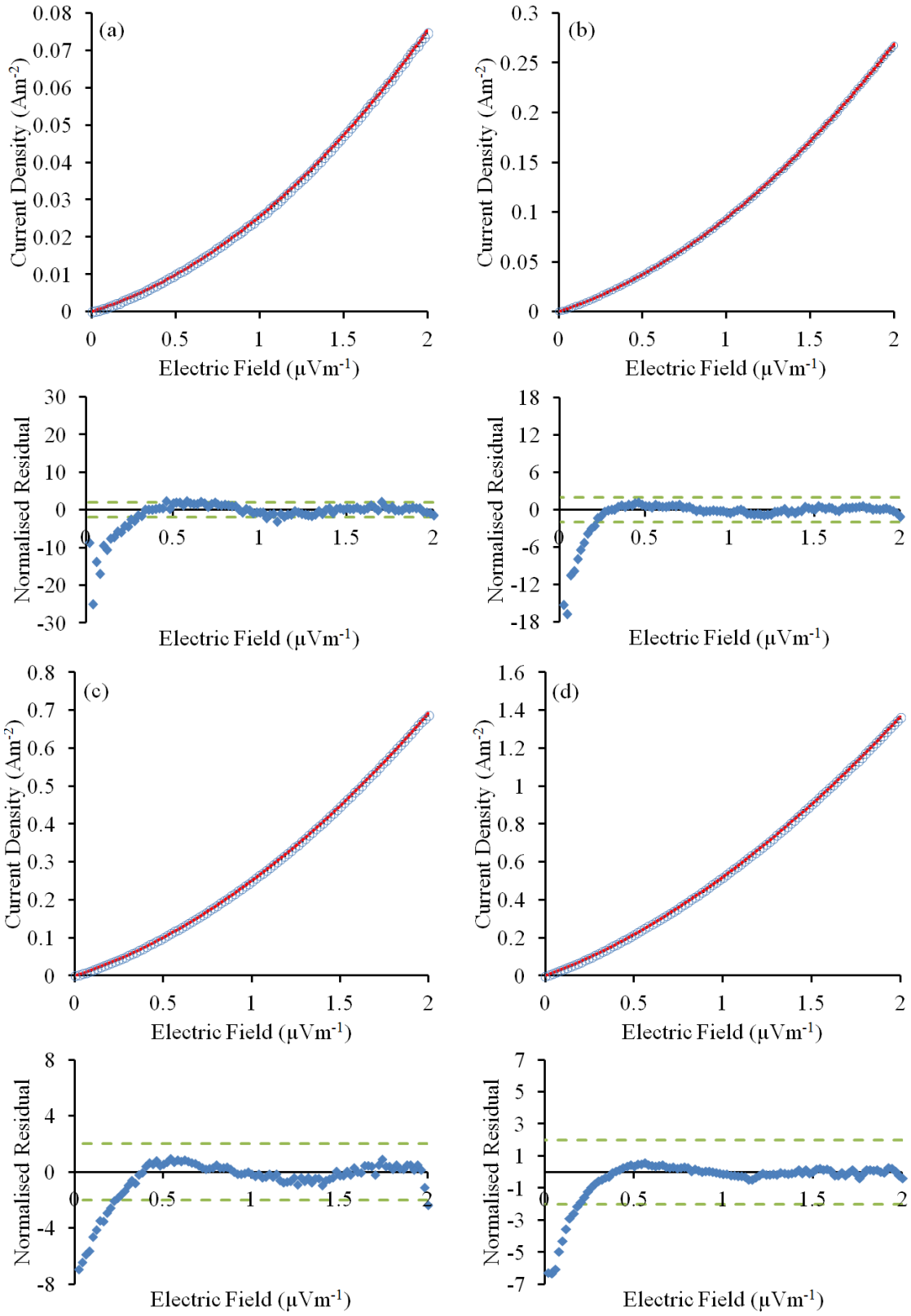

Figure 6.14. Example fits of a model comprising linear and non-linear conduction contributions to 10 sweep averages of decreasing I-V data at (a) 0.2 N, (b) 0.4 N, (c) 0.6 N and (d) 0.8 N compressive force, and at 20 °C. The solid red line is the model fit, the open blue circles are the observed data. The green dashed lines in the residual analysis plots are guides to the limits of an acceptable fit. Error bars are smaller than the data points.

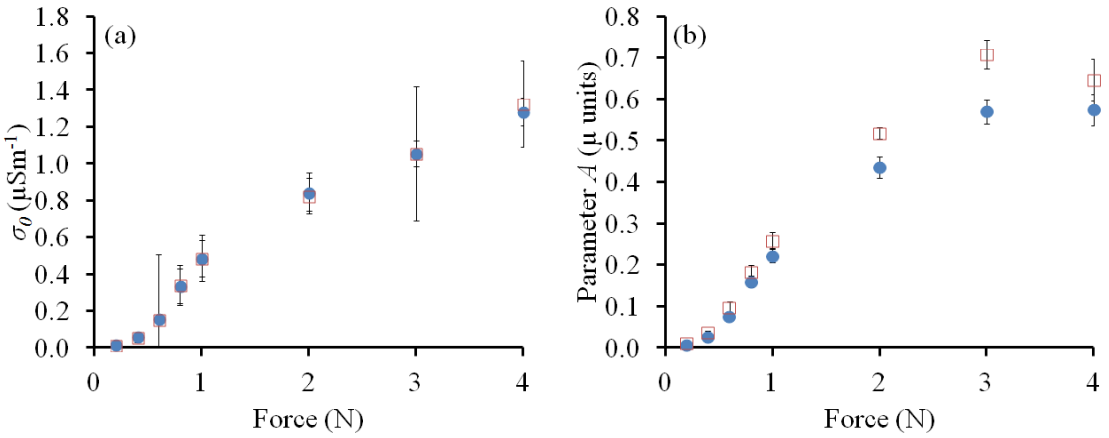

Figure 6.15. The force sensitive behaviour of the (a) linear conductivity σ_0, and (b) the A parameter as a function of compressive force. The solid circles show the increasing voltage values and the open squares show the decreasing voltage values.

function of compressive force from increasing and decreasing I-V curves at room temperature. Initially, the linear conductivity rises at an increasing rate. As the force increases beyond 1 N, the linear conductivity then increases more slowly. This suggests the ink is nearing complete compression and thus is approaching a maximum possible electrical conductivity under these given temperature and pressure conditions. The parameter A exhibits similar behaviour as a function of compressive force as shown in figure 6.15(b). Parameter A increases at an increasing rate up to 1 N, and between 3 -4 N compression it reaches a plateau, again indicating the nanocomposite is near maximum compression.

Figure 6.15 shows that the linear conductivity is similar for increasing and decreasing voltage ramps, but in contrast also shows that generally the non-linear conductivity is greater on the down-ramp than the up-ramp. Thus the non-linear component is the apparent cause of the electrical hysteresis. This may be related to charge trapping phenomena: charge becomes trapped during the up-ramp, thereby reducing the current flow. However, these traps fill up at higher voltage and by the time the maximum voltage has been reached are filled. Therefore they no longer

inhibit current flow. This issue has not been investigated in great detail however, and could be a focus for future work as discussed in Chapter 8.

The relative contributions to the linear and non-linear conductivity are compared in figure 6.16. This figure shows that, as the compressive force is increased, the contribution to the total electrical conduction from non-linear mechanisms increases, reaching a maximum above 0.4 N. Above this level of compression the total conduction is constituted of approximately 68 % linear and 32 % is attributed to non-linear mechanisms. The behaviour of the linear and non-linear terms suggest that, as compression is increased, the number of direct electrical connections between the conducting needles increases due to them being pushed together, allowing greater ohmic current flow. Simultaneously, isolated needles and clusters of needles are pushed into closer proximity. This results in narrowing of tunnelling barriers and hence more pronounced field-assisted quantum tunnelling conduction.

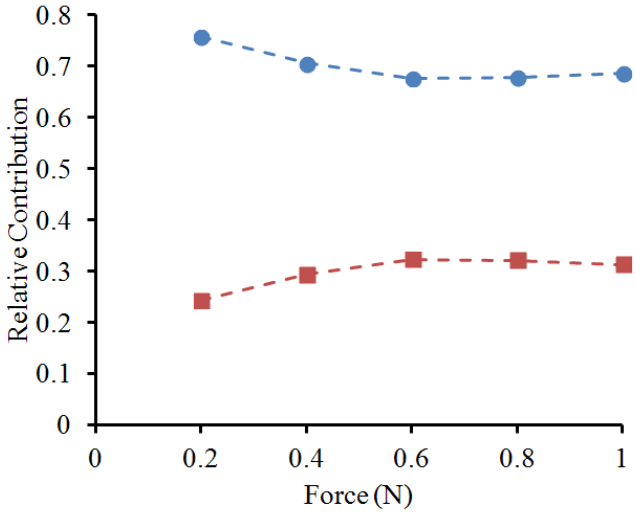

Figure 6.16. The relative contributions of the linear σ_0 (blue circles) and non-linear A (red squares) parameters to the total electrical conduction in the ink. The dashed lines are a guide to the eye.

Figure 6.17 shows the behaviour of the tunnelling exponent *n* as a function of compressive force at room temperature. It consistently takes a value close to 2, except below 0.5 N where the model is inaccurate, which suggests that Fowler-Nordheim-like tunnelling, as detailed in Chapter 3, may be a significant contributor to the non-linear electrical conduction in the nanocomposite. The exponent exhibits interesting behaviour below 1 N: the exponent decreases up until 1 N, whereby it increases its value. This pattern is more noticeable in the increasing I-V data. This may be a real effect or an artefact arising from the model poorly describing the conduction at low compression.

The poor performance of equation 6.1 in describing the low electric field I-V behaviour suggests that the electrical conduction in this region may be more complex than a series combination of linear and non-linear conductivities. Additional pathways, such as the electrodes and ink acting in unison as a leaky capacitor, must be considered if an improvement is to be made to the model. That said, too many variables will result in a model that can be fitted to any behaviour and it may

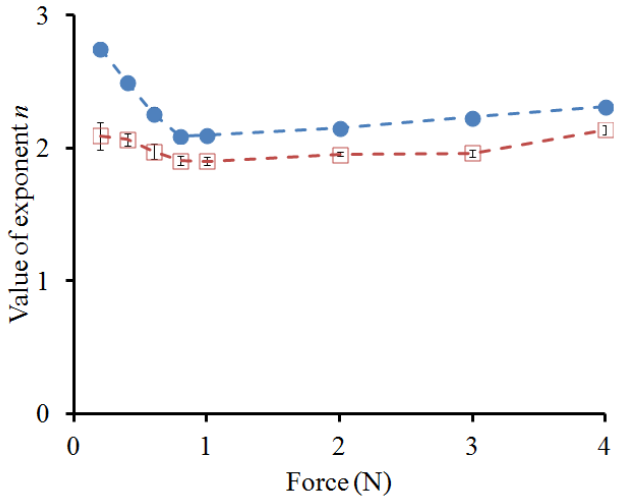

Figure 6.17. The value of the tunnelling exponent *n* as a function of compressive force. The solid circles are values from the increasing voltage sweep, while the open squares are values from the decreasing voltage sweep.

lose the ability to provide genuine insight and understanding of the charge transport behaviour. Generally the combination of linear and non-linear conductivities is a good fit at higher electric field values, so it is reasonable to suggest that conduction arising from direct connections and tunnelling processes become dominant in this region. It should also be noted from figure 6.17 that the up and down sweeps are different again indicating more complex behaviour perhaps associated with charge trapping.

6.4.2 Electrical conduction behaviour in response to temperature

The temperature dependence of the electrical transport behaviour of the opaque ink was studied to provide deeper insight into the conduction mechanisms. The temperature dependence of electrical conduction in metals, semiconductors, insulators and of quantum tunnelling mechanisms was described in Chapter 3. This information has been developed to test the model and fully understand the conduction mechanisms at play, namely linear ohmic conduction and non-linear quantum tunnelling conduction. The acicular particles in opaque ink are made of a titanium dioxide core, coated in antimony doped tin oxide. The titanium dioxide core is a wide band-gap semiconductor, while the surface coating is a doped semiconductor with good electrical conductivity. As discussed in Chapter 3, semiconductor materials generally display an increasing electrical conductivity with increasing temperature; electrons are thermally promoted into the conduction band. This behaviour follows the relation below in equation 6.2:

$$\sigma_0 = \sigma_i exp(-\alpha/T) \qquad (6.2)$$

where σ_0 is the conductivity, σ_i is the extrapolated initial conductivity, α is a constant equal to $E_g/2k_B$, and T is the temperature.

The linear component of the conductivity, σ_0, in equation 6.1 should obey this temperature dependence if there are direct electrical conduction pathways through the semiconducting needles in the ink. Figure 6.18 shows the variation of the linear conductivity with increasing temperature at 0.2 N compression. We see that the linear conductivity rises at an increasing rate as the temperature is increased. Figure 6.19 shows the linear conductivity as a function of temperature for compressions of 0.2, 0.6 and 1.0 N. All three show the same general behaviour: the linear conductivity increases at an increasing rate with temperature. It is worth noting that the amount by which the linear conductivity increases is greater for higher compressions and the value of the linear conductivity has increased approximately 10 fold between 0.2 and 1.0 N compression.

Figure 6.20 shows example fits of the semiconductor electrical conductivity temperature dependence, equation 6.2, to the derived linear conductivity as a function of temperature. The residual analysis reveals that the fitting improves

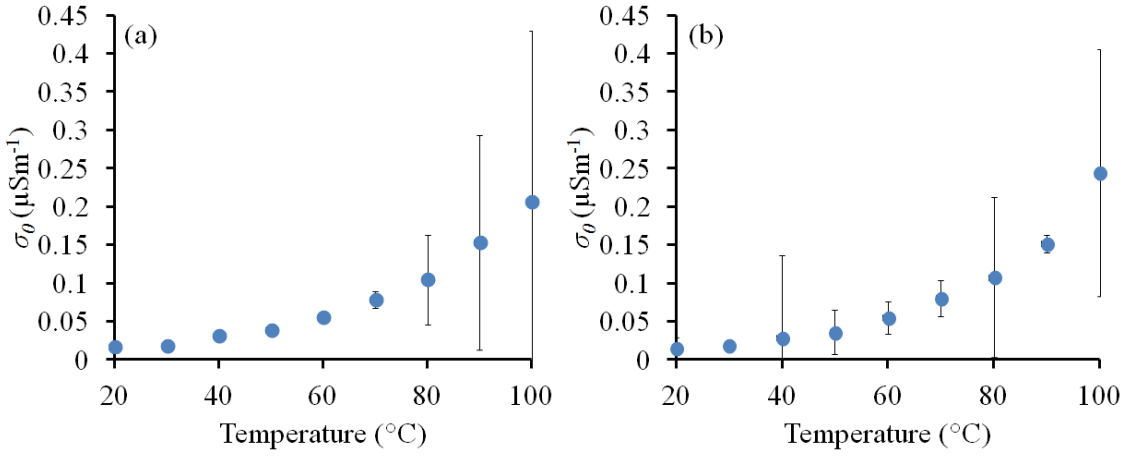

Figure 6.18. The behaviour of the linear conductivity, σ_0, as a function of temperature for (a) increasing voltage, and (b) decreasing voltage.

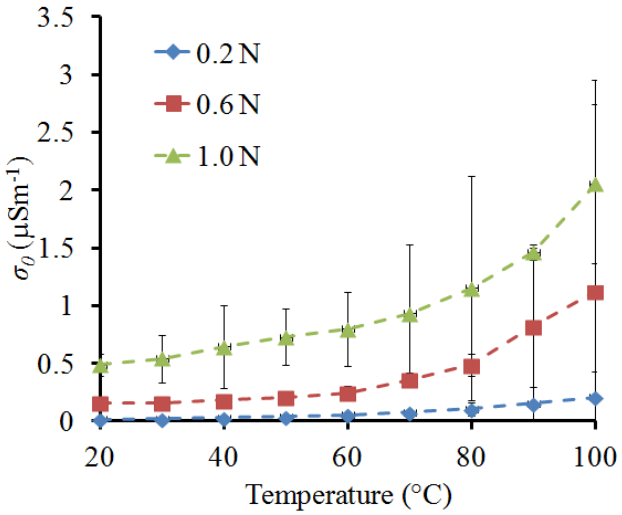

Figure 6.19. The behaviour of the linear conductivity, σ_0, as a function of temperature at three mass loadings: 0.2, 0.6 and 1.0 N.

with increasing temperature and that the model is a poor fit at the lowest compressions and temperatures. In fact, the residuals show that the model does not predict the correct current density below 40 °C (the observed current is greater than what the model predicts). This suggests that the model description does not fully encapsulate the electrical conduction near room temperature and that there may be other conduction mechanisms that have not been considered. It should be noted that the residuals form the same pattern here, though, with more current observed in practice than as predicted by the corresponding fitting. Above 40 °C, the model is a more accurate description of the linear conduction, with all residual points within the acceptance of fit region. On the basis of this fitting, it is reasonable to suggest that the linear conductivity term originates from electrical transport through direct contacts between the semiconducting material in the needles. Interestingly, if equation 6.2 is modified to include a linear offset added to the temperature dependence expression, $\sigma = \sigma_0 exp(-\alpha/T) + c$, the fits improve dramatically, with the residuals indicating a good fit in all but the lowest mass loading at room temperature. These can be seen in figure 6.21. A physical basis for c could be a residual conductivity associated with the

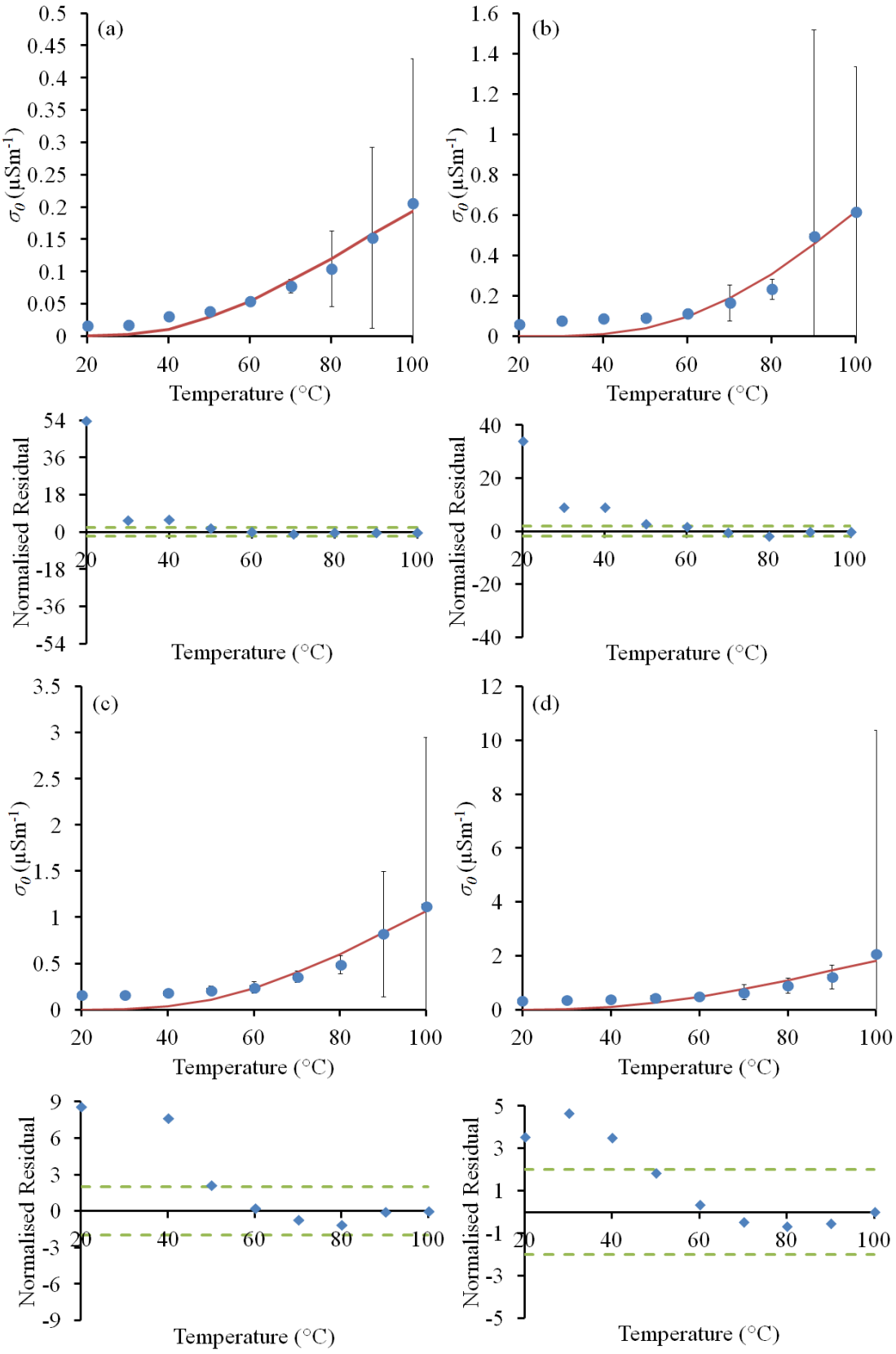

Figure 6.20. Example fits of semiconductor temperature dependence behaviour to the linear conductivity as a function of temperature at (a) 0.2 N, (b) 0.4 N, (c) 0.6 N, and (d) 0.8 N. The blue circles are the data and the solid red lines are the model fits. The green dashed lines in the residual analyses are guides to the limits of a good fit.

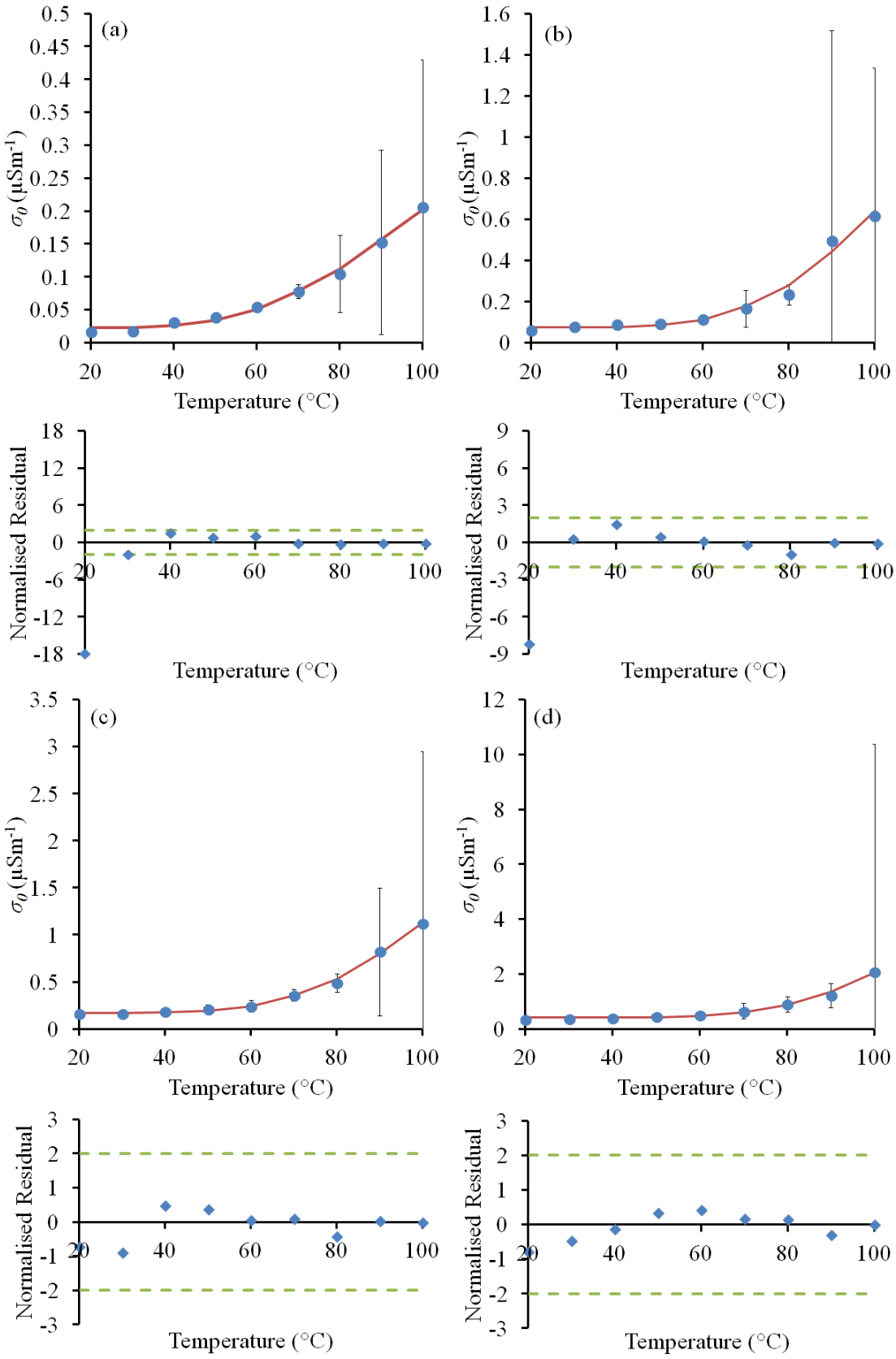

Figure 6.21. Example fits of semiconductor temperature dependence behaviour and a linear offset to the linear conductivity as a function of temperature at (a) 0.2 N, (b) 0.4 N, (c) 0.6 N, and (d) 0.8 N. The blue circles are the data and the solid red lines are the model fits. The green dashed lines in the residual analyses are guides to the limits of a good fit.

contact between the ink and the electrodes, but this has not yet been determined.

The behaviour of parameter A in response to increasing temperature at 0.2 and 0.4 N compression is shown in figure 6.22. A increases at a steady rate before 60 °C, after which point it increases more steeply. This change in the non-linear conduction could be linked to a physical change in the ink, or an artefact from not having enough data. Increasing the volume of data may improve the resolution of this apparent transition. The increase of parameter A with temperature becomes smoother at higher compressions, shown in figure 6.23. If the non-linear characteristic observed in the electrical transport behaviour of opaque ink is attributed to field-assisted quantum tunnelling, then the temperature dependence of the non-linear parameter A should follow the temperature dependence outlined in Chapter 3. It is repeated for convenience in equation 6.3.

$$A = D\left(\frac{\pi\zeta T}{\sin \pi\zeta T}\right) \tag{6.3}$$

where D is a constant encapsulating a collection of correction factors, ζ is a further constant including terms such as the workfunction, and T is the temperature.

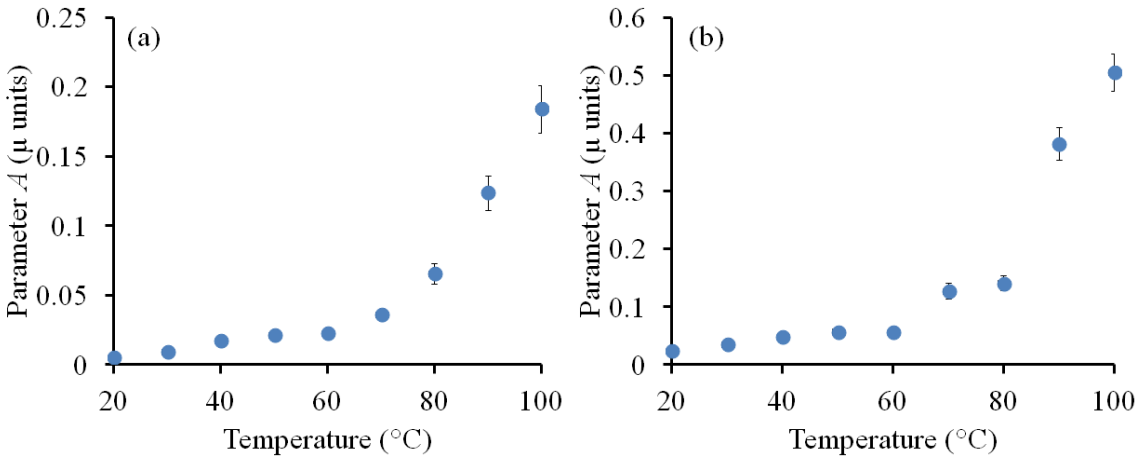

Figure 6.22. The behaviour of the non-linear conduction parameter A for the (a) increasing, and (b) decreasing voltage sweeps as a function of temperature.

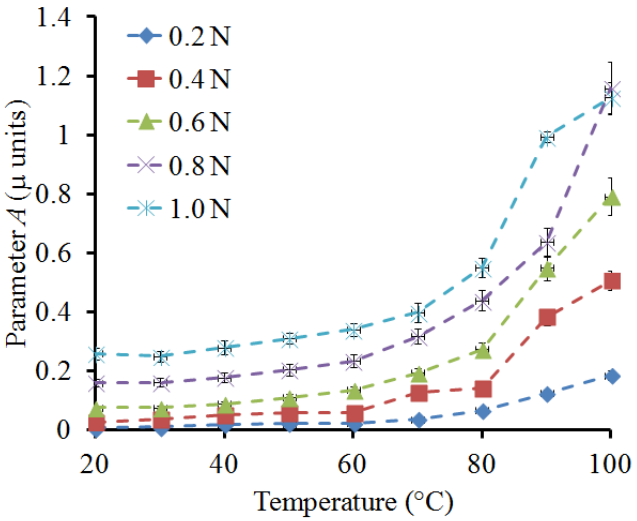

Figure 6.23. The behaviour of the non-linear parameter *A* as a function of temperature at five mass loadings: 0.2, 0.4, 0.6, 0.8, and 1.0 N.

Figure 6.24 shows an example fit of equation 6.3 to parameter *A* as a function of temperature at 0.2 N compression. The residual analysis shows that, at this low compression, the model is a poor description of the temperature dependence

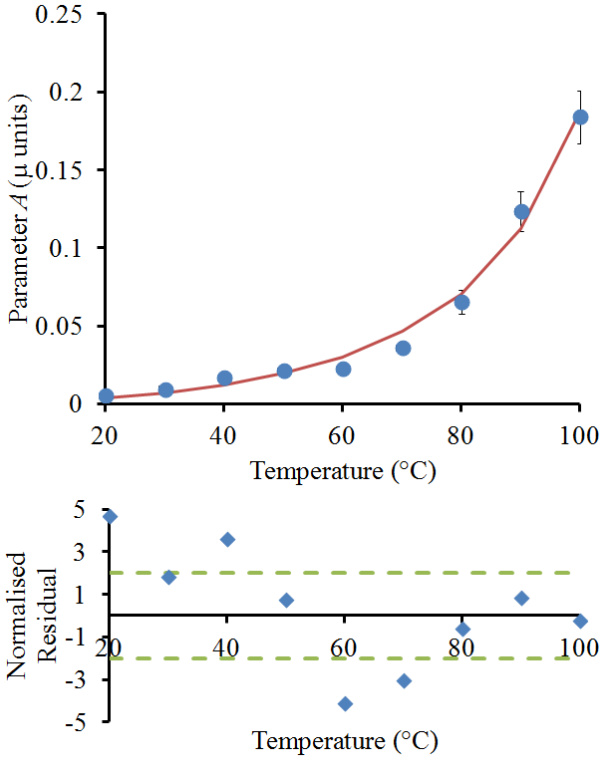

Figure 6.24. An example of the field-assisted tunnelling temperature dependence (solid red line) fitted to the non-linear parameter *A* at 0.2 N compressive force (blue circles). The green dashed lines in the residual analysis are guides to the limits of a good fit.

of parameter *A*. At 0.4, 0.6, 0.8 and 1.0 N compression, however, the fit becomes acceptable, as shown in figure 6.25. Overall, it appears that field-assisted tunnelling may be responsible for the non-linearity found in the electrical transport

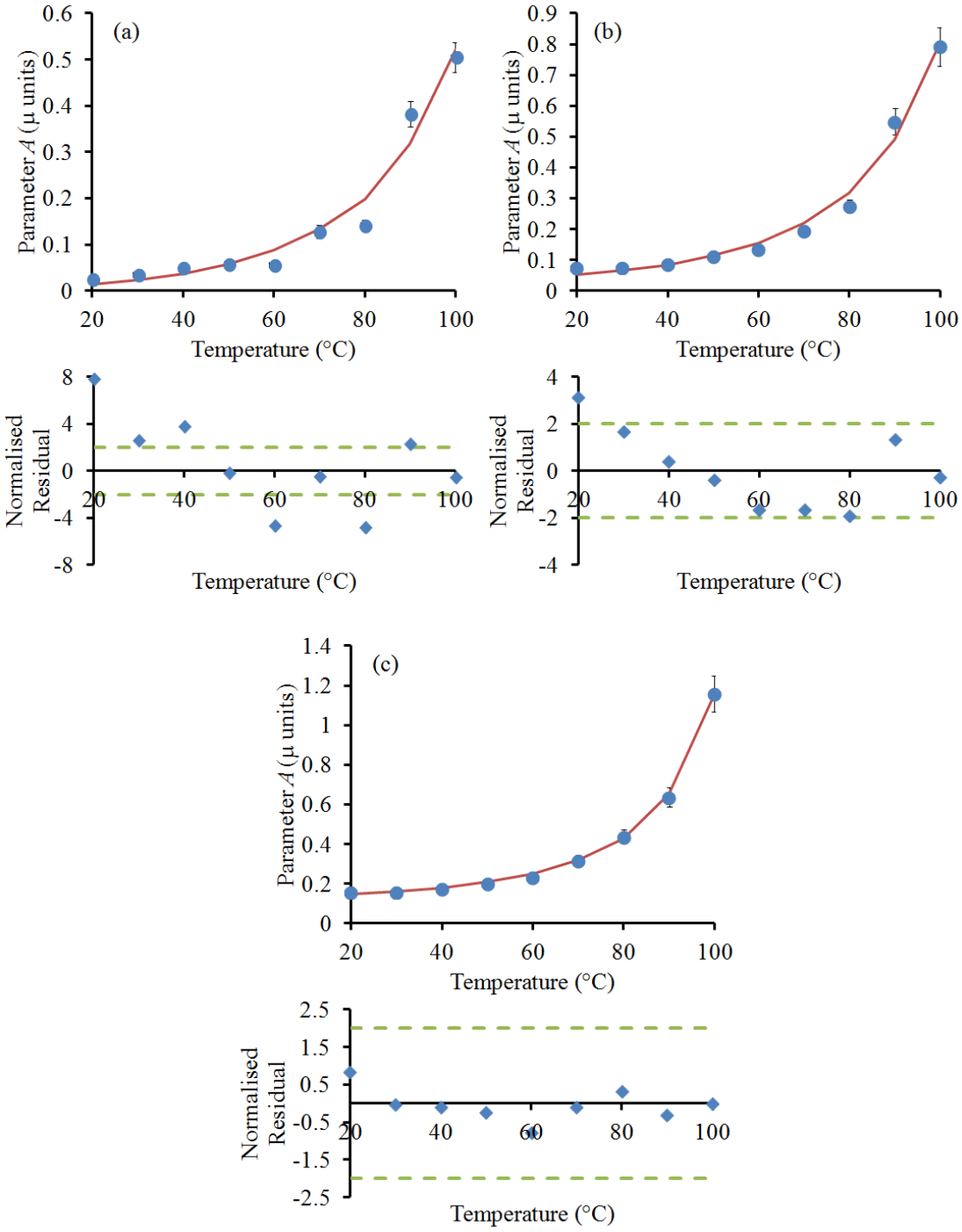

Figure 6.25. Example fits of equation 6.3 (solid red line) to the behaviour of parameter *A* as a function of temperature (blue circles) at (a) 0.4 N, (b) 0.6 N, and (c) 0.8 N compressive force. The green dashed lines in the residual analyses are guides to the limits of a good fit.

behaviour found in the opaque ink. It may not, however, be the only mechanisms at play. The poor fitting at low compression suggests that the model is lacking and this concurs with the poor fitting of model 6.1 to the raw I-V data at low electric field values; this may be due to additional conduction pathways not yet considered.

Figure 6.26 shows the relative contributions of the linear conductivity and the non-linear conductivity parameter *A* as a function of temperature, at four different levels of compression. At low compression, the increase of temperature has a large effect on the relative contributions from linear and non-linear conduction: the non-linear contribution increases from 24% to 47% share of the conduction as the temperature is increased to 100 °C. As the compressive loading is increased,

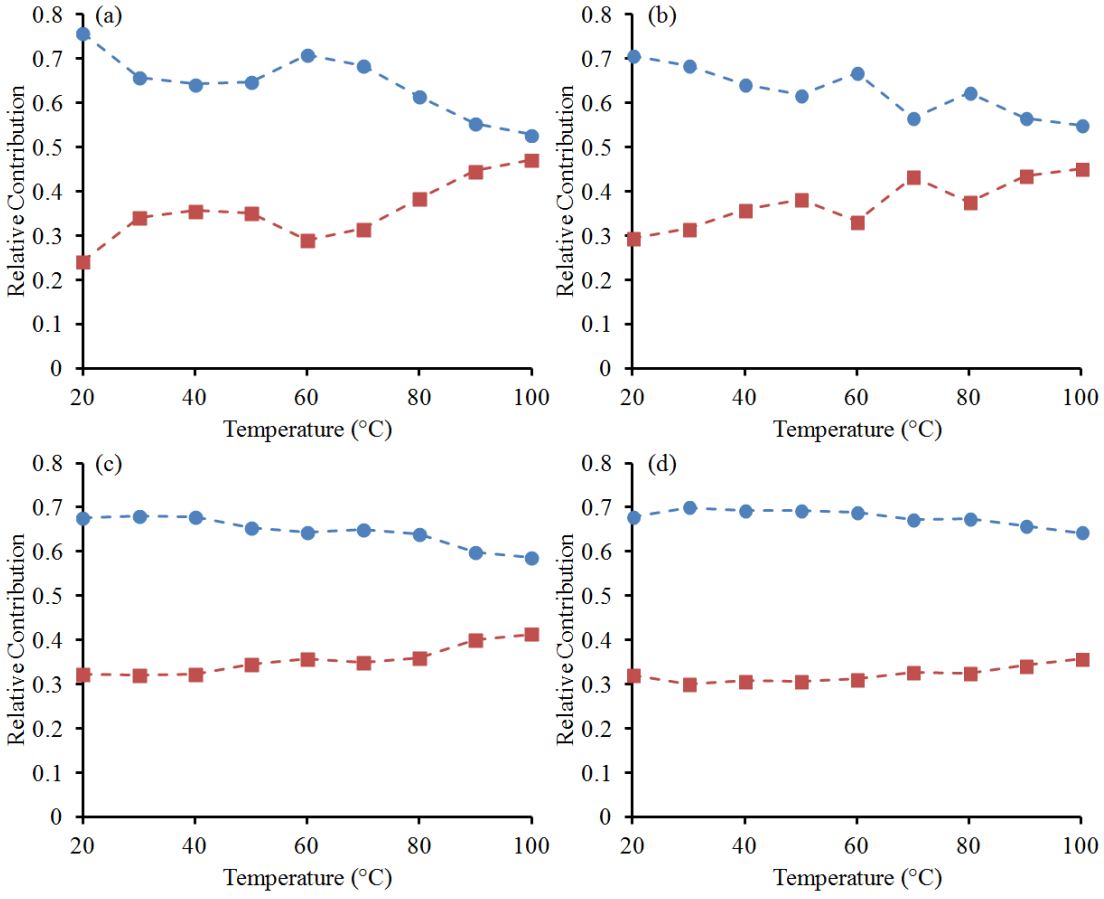

Figure 6.26. Relative contributions of the linear (blue circles) and non-linear (red squares) parameters as a function of temperature at (a) 0.2 N, (b) 0.4 N, (c) 0.6 N, and (d) 0.8 N. The dashed lines are a guide to the eye.

temperature changes have a reduced effect on the relative conduction contributions, with the contribution from the non-linear mechanisms remaining static at approximately 36%.

This behaviour suggests that, at higher compressions, many tunnelling junctions have been compressed into direct connections, so even changes in temperature cannot affect the tunnelling contribution too greatly. The poor fitting at low temperatures and compression, as well as the large error bars on the extrapolated linear conductivity term $\sigma_{0,}$ suggest that it may not only be direct connections and quantum tunnelling responsible for the electrical conduction, although these two mechanisms are significant contributors, particularly at higher compressions and temperatures.

6.5 Summary

The opaque ink exhibits complex non-linear electrical transport behaviour that is affected by compression and temperature. This conduction can be reasonably described as a summation of two conduction mechanisms; linear ohmic charge transport from direct connections between the semiconducting needles, and non-linear charge transport attributed to quantum tunnelling processes. Increasing the compression of the ink pushes the needles into closer proximity, creating new direct contacts and narrowing tunnelling barriers, resulting in an increase of both linear and non-linear conduction. Increasing the temperature of the ink similarly increases the linear and non-linear conduction: the former may arise from thermal excitation of charge carriers into the conduction band of the semiconducting material, while in the latter case, the increase in temperature provides charge carriers with extra

energy to either hop over or tunnel through potential barriers. Modelling of the temperature dependent behaviour provides further clear evidence for the quantum tunnelling conductivity of the electrical transport behaviour. The evidence of hysteresis indicates more complex mechanisms are also present that may be associated with space charge and trapping.

7. Electrical transport phenomena of transparent ink: results and discussion

7.1 Introduction

The transparent ink has been investigated in detail and the results and analysis of the electrical transport measurements are presented in this chapter. The measurements were taken according to the method detailed in Chapter 4. The I-V curves were obtained from room temperature up to 100 °C, the reason for which is identical to that stated in the previous chapter. The results are presented in the same fashion as those in Chapter 6: the behaviour of the electrical transport in response to compression at room temperature is first described, before moving on to describe the temperature dependence behaviour and a discussion of the conduction mechanisms. Again, a model comprising two conduction constituents was used to analyse and interpret the I-V characteristics and the temperature dependence of this behaviour.

7.2 Compressive force dependence of electrical transport

The I-V data were acquired using the method presented in Chapter 4. An example of the first sweep of an I-V cycle, under 0.2 N compressive force and at room temperature (20 °C), is shown in figure 7.1(a). The curve is highly non-linear and there is significant electrical hysteresis, where the current is much larger for a given voltage on the down ramp of the voltage, which indicates a lower ink resistance.

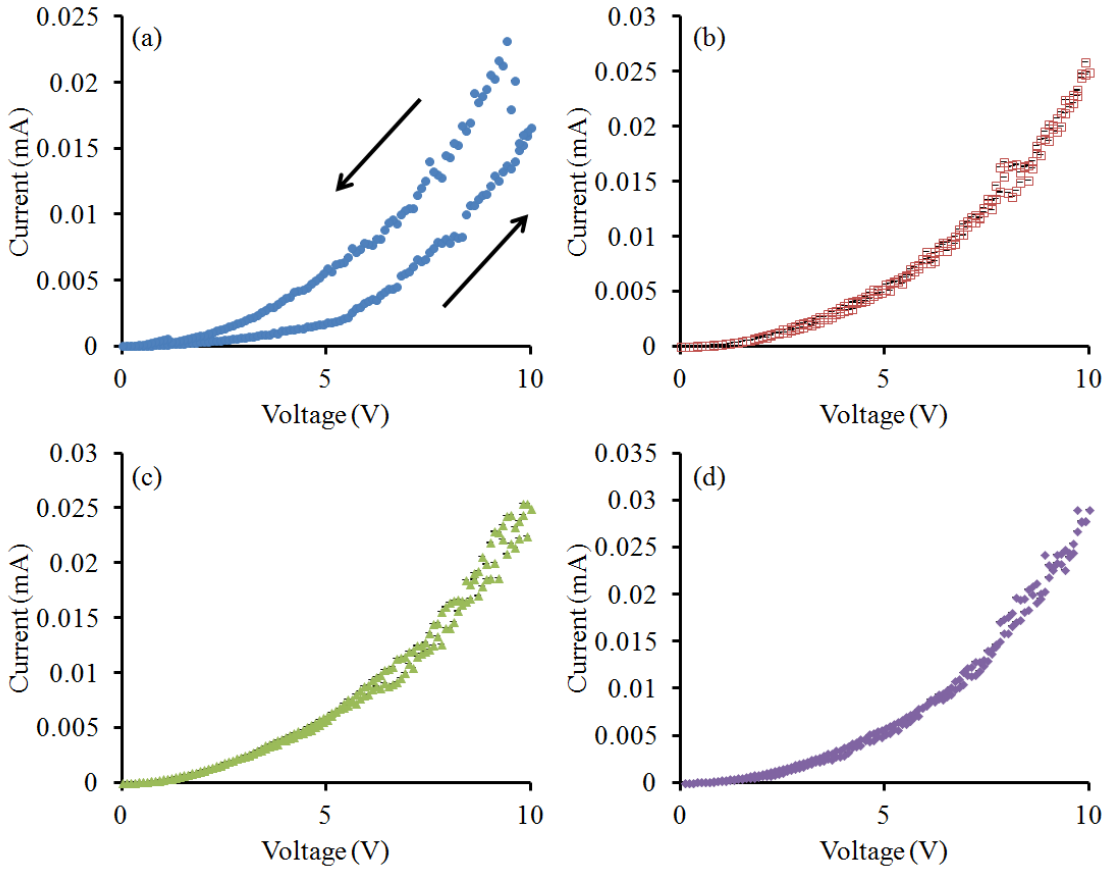

Figure 7.1. I-V sweeps (a) 1, (b) 4, (c) 7, (d) 10 of an I-V cycle taken at 0.2 N compression and at 20 °C. The error bars are smaller than the data points.

Subsequent I-V sweeps from the cycle are compared to the 1st sweep in figure 7.1(b), (c) and (d). As with the opaque ink, the electrical hysteresis is significantly larger in the 1st voltage sweep of the 10 sweep cycle. Comparing figure 7.1(a) to an I-V sweep taken at a higher compressive loading, for example at 0.8 N, see figure 7.2(a), it can be observed that the behaviour is still non-linear, but the current through the device has increased approximately 100-fold. Also, similar hysteretic behaviour was still observed, as shown in more detail in figure 7.2(b). Four I-V sweeps taken at 0.8 N compression are compared in figure 7.3. Comparing these to the sweeps in figure 7.1, the hysteresis is still predominantly in the first sweep of a cycle. Some of the I-V sweeps contain anomalous peaks, as seen in the insert of figure 7.3(a). Further examples of these peaks are shown in figure 7.4. These peaks typically occur during

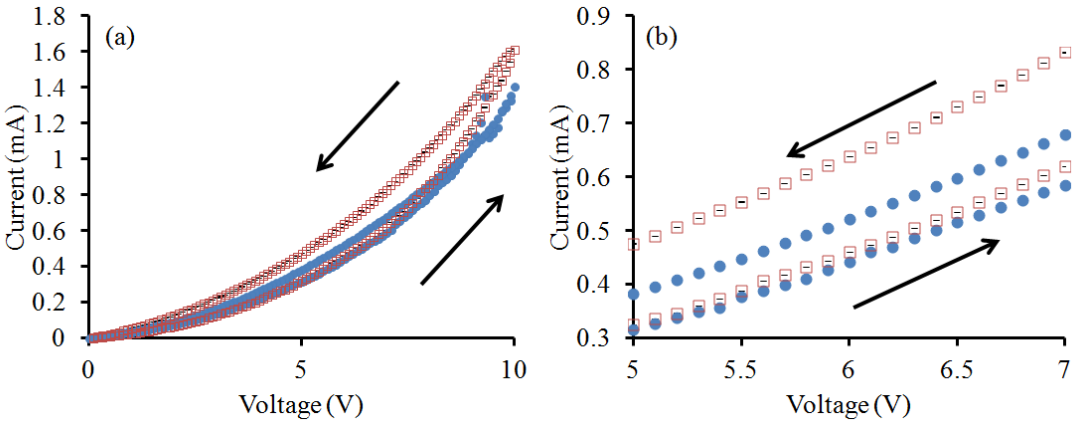

Figure 7.2. An example of (a) the first sweep of an I-V curve (solid blue circles) and a repeat measurement (open red squares) taken at 0.8 N compression and at 20 °C, and (b) a closer view of the hysteresis. The arrows indicate the direction of the voltage sweep. Error bars are smaller than the data points.

the increase of voltage in the first sweep in an I-V cycle, at random values of compression and temperature. The trapping of charge and a subsequent release of charge has resulted in similar observations in bulk QTC™ composites [6] [135].

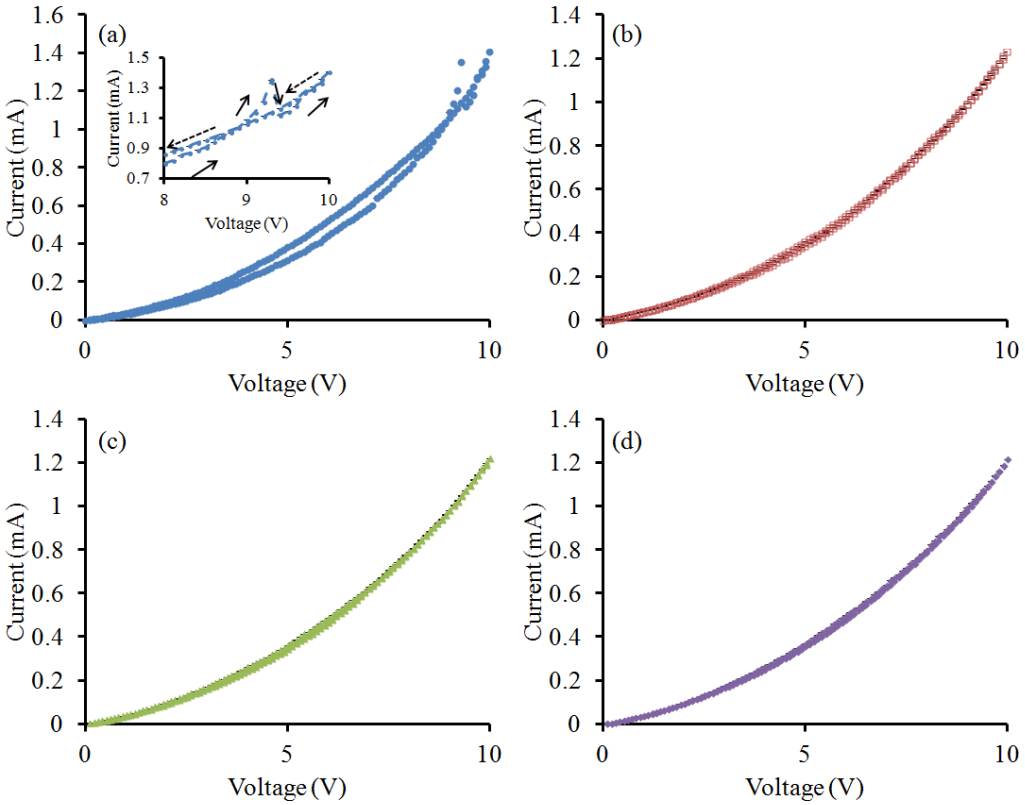

Figure 7.3. Sweeps (a) 1, (b) 4, (c) 7, (d) 10 of an I-V cycle taken at 0.8 N compression and at 20 °C. The insert shows in more detail an anomalous peak. The increasing voltage ramp is indicated by solid arrows, while the decreasing voltage ramp is indicated by dashed arrows. Error bars are smaller than the data points.

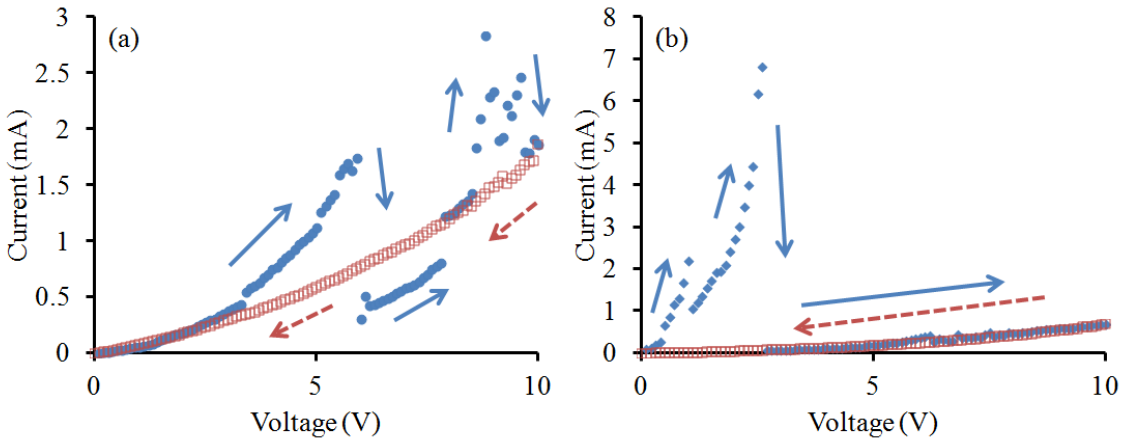

Figure 7.4. Examples of anomalous peaks in the I-V data at (a) 0.2 N compression, 90 °C, and (b) 3 N compression, 20 °C. The solid blue circles (and solid guide arrows) are the increasing voltage sweep, while the open red squares (and dashed guide arrows) are from the decreasing voltage sweep.

The structure of the transparent ink is somewhere between the opaque ink and bulk QTC™ composites, thus a similar physical basis for the anomalous I-V peaks may be plausible. Figure 7.5 compares mean average I-V curves (calculated from the full 10 sweeps in a cycle) taken at 0.2 and 1.0 N compressive loading. As compression increases, the I-V behaviour, at first inspection, does not exhibit a change in its linearity. Adopting the same strategy as presented in Chapter 6, normalization of the curves can reveal changes in the linearity of the data. Figure 7.6 shows the same I-V curves, along with those for 0.4, 0.6 and 0.8 N of compression, which have been normalised to their peak current values. It is found that the curves become more

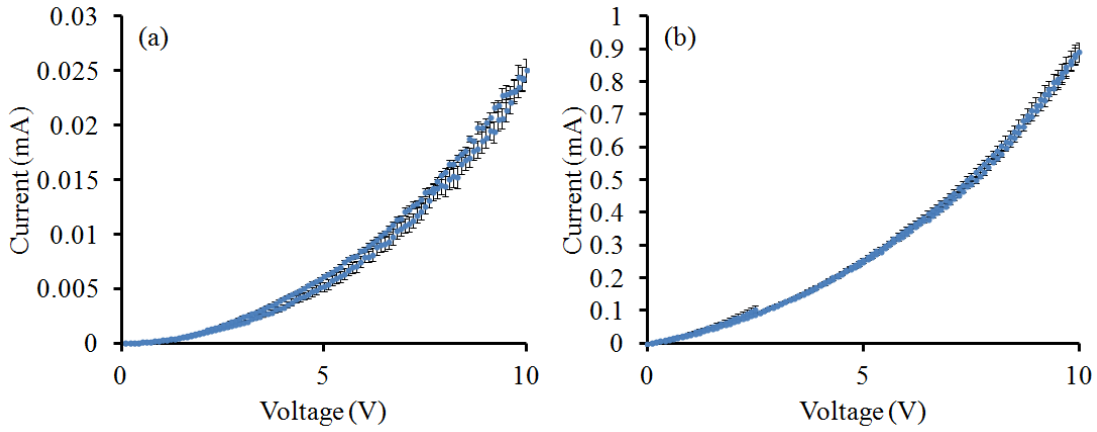

Figure 7.5. I-V curves (10 sweep average) taken at (a) 0.2 N and (b) 1.0 N compression.

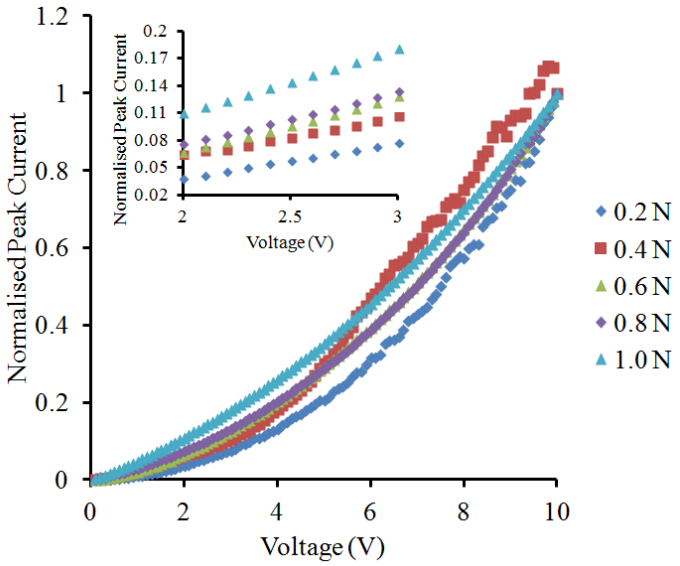

Figure 7.6. Average I-V curves taken at 5 mass loads and normalized to their peak values. The insert presents a closer view to show how the linearity of the I-V slowly increases with increasing compression.

linear as the compression is increased and this is covered in more detail in later model fitting. The non-linearity of the I-V curves suggests complex conduction with some compression dependence that is best shown in figure 7.6. The response of the electrical resistance to compressive force, calculated using the initial ink resistance from the first sweep I-V data and a repeat I-V measurement, is shown in figure 7.7. There is a large initial drop in the resistance between 0.2 and 0.6 N, after which the resistance decreases much more slowly up to 1 N of compression.

Overall, compression appears to act on the transparent ink in a similar manner as it does on the opaque ink. As compression is increased, the total current passing through the ink increases, while the curvature of the I-V behaviour decreases. Anomalous peaks in I-V curves at random compressions and temperatures are observed. These are possibly a result of trapping and subsequent release of charge. In contrast, the anomalous peaks are absent in the opaque ink's electrical behaviour.

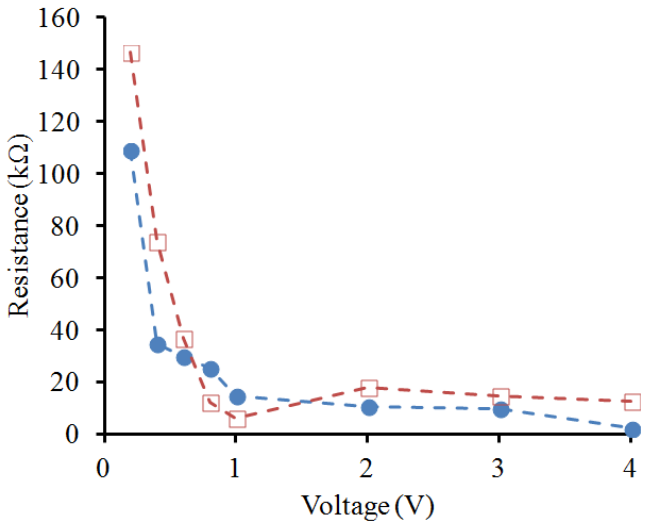

Figure 7.7. The electrical resistance response of the nanocomposite ink to compressive force. An initial measurement run (solid blue circles) is compared with a repeat measurement (open red squares). The dashed lines are a guide to the eye.

7.3 Temperature dependence of electrical transport

Electrical transport measurements were taken as a function of temperature up to a maximum of 100 °C, while some samples were tested only up to 70 °C. Samples that were heated above 100 °C, and in some cases above 70 °C, became unusable (short circuiting) after a single measurement run, preventing testing of the sample under different compressive loadings or repeat measurements. Typical I-V curves taken at 20, 40, 60, 80 and 100 °C, and under 0.8 N of compression, are shown in figure 7.8. As the temperature is increased, the current passed by the test device also increases. Four sweeps of an I-V cycle taken at 50 °C, 0.6 N, are shown in figure 7.9. In this I-V cycle, the hysteresis is observed in all of the sweeps to approximately the same

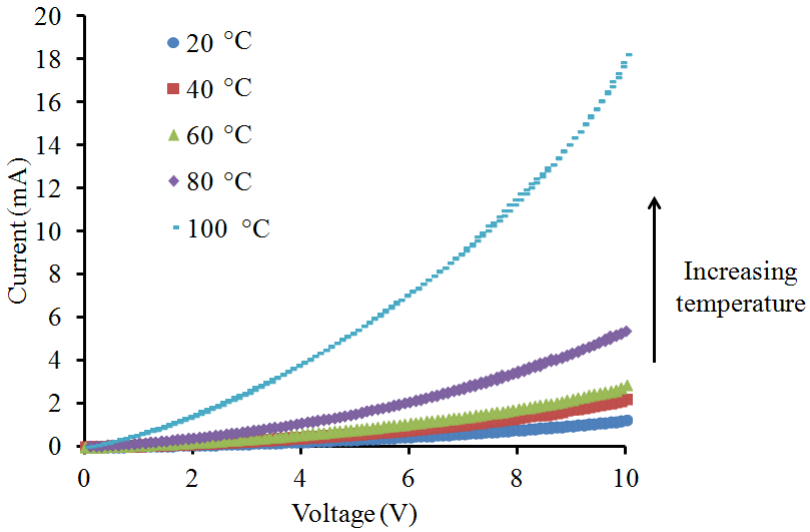

Figure 7.8. I-V curves (each a 10 sweep average) at 5 temperatures: 20, 40, 60, 80 and 100 °C. All I-V curves were measured with the sample under a compression of 0.8 N. The error bars are smaller than the data points.

degree. Figures 7.10 and 7.11 show the first four sweeps of I-V cycles taken at 60 and 80 °C, under 0.6N, respectively. These demonstrate the same overall features seen in

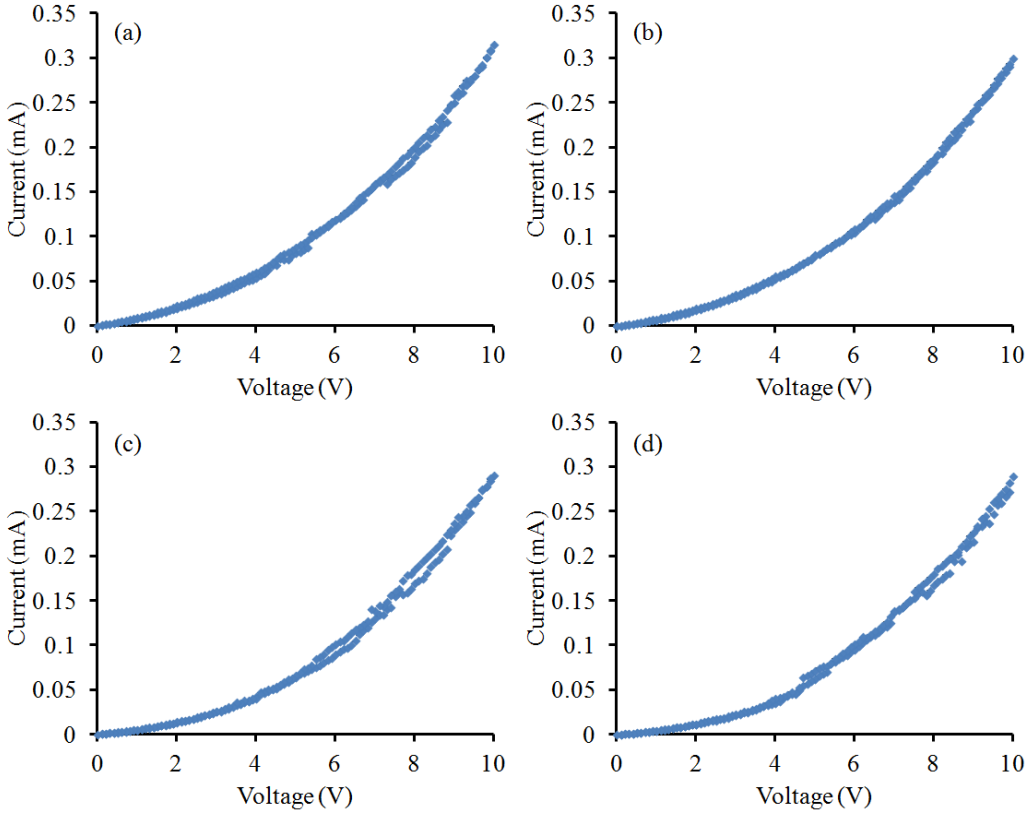

Figure 7.9. Example sweeps in series (a) 1st, (b) 4th, (c) 7th, (d) 10th of an I-V cycle under 0.6 N of compression at 50 °C. Error bars are smaller than the data points.

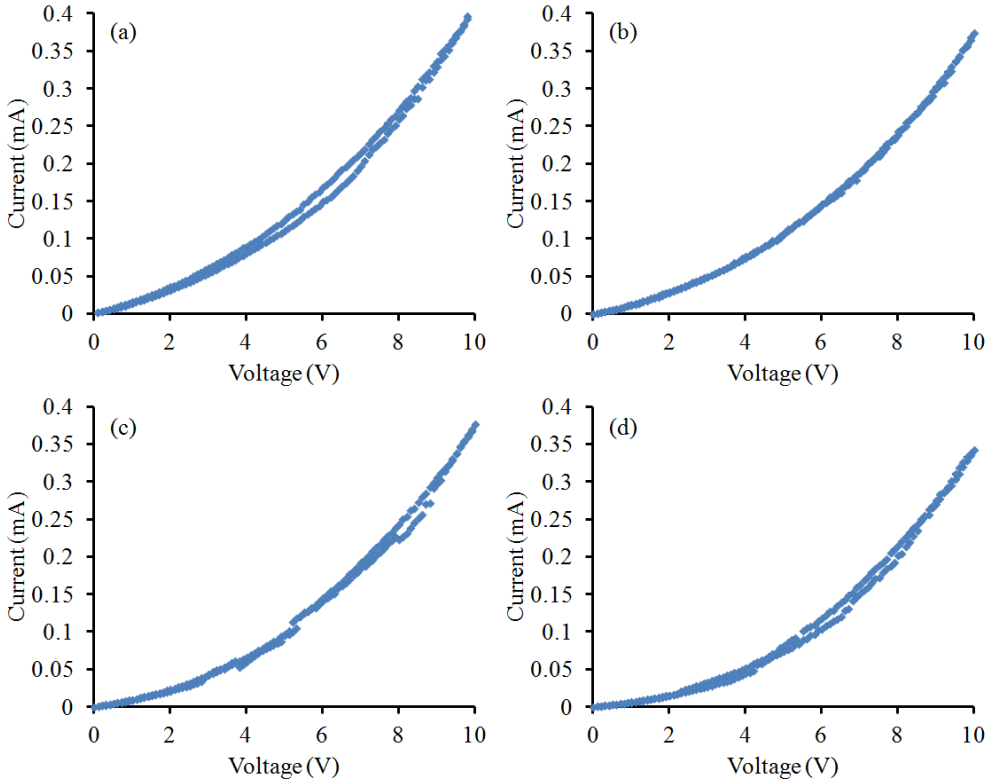

Figure 7.10. Example sweeps in series (a) 1st, (b) 4th, (c) 7th, (d) 10th of an I-V cycle under 0.6 N of compression at 60 °C. Error bars are smaller than the data points.

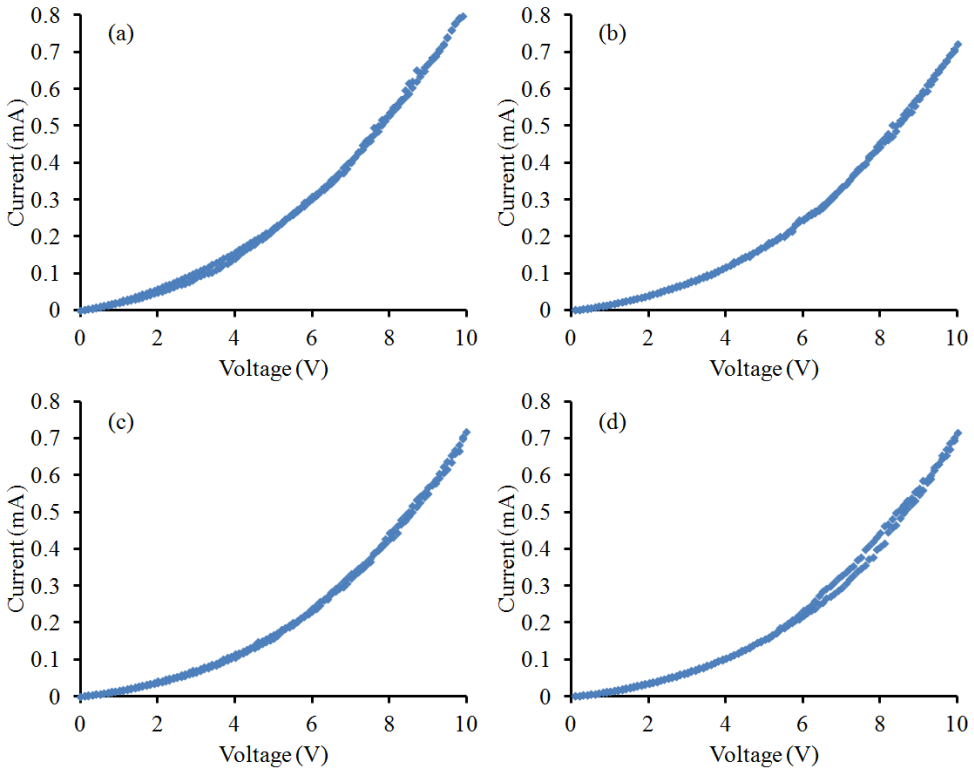

Figure 7.11. Example sweeps in series (a) 1st, (b) 4th, (c) 7th, (d) 10th of an I-V cycle under 0.6 N of compression at 80 °C. Error bars are smaller than the data points.

figures 7.1, 7.3, and 7.9. The first sweep has significant hysteresis while subsequent sweeps show little hysteresis. This is the case for most of the I-V cycles at all compressions and temperatures, but there are occasional exceptions such as those presented in figure 7.9. Note that the peak current in figures 7.9 to 7.11 increases as the temperature of the system is raised.

It is difficult to tell much about whether the curvature of the I-V behaviour varies with temperature from these graphs, so 5 averaged I-V curves have been normalised to their peak current values and are shown in figure 7.12. Much like the opaque ink, the curvature of the I-V behaviour does not vary significantly or in any specific pattern with increasing temperature, implying temperature affects the conduction mechanisms within the ink equally. While temperature affects the electrical behaviour uniformly (meaning the I-V curvature is unchanged), the electrical behaviour is more sensitive to compression; the peak current increases

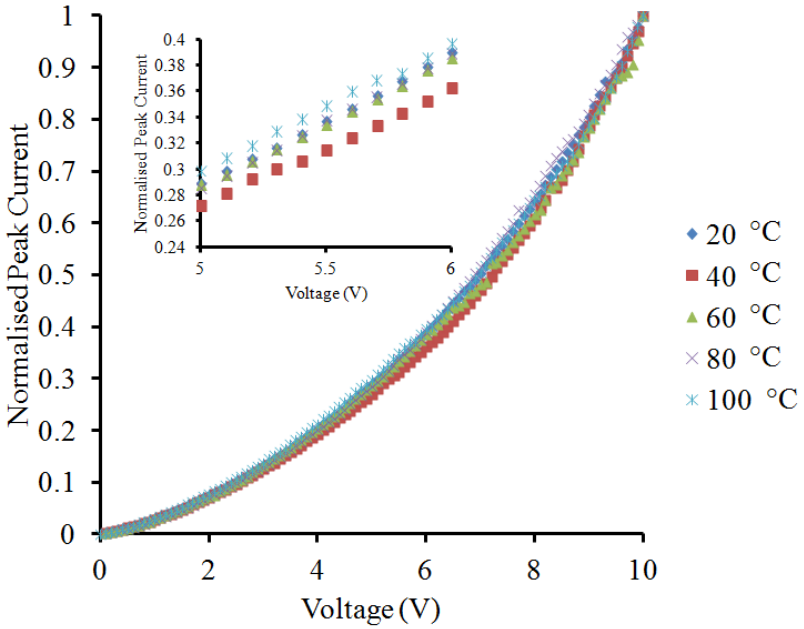

Figure 7.12. I-V cycles at five temperatures normalized to their peak current values. The insert highlights the variation of the I-V curvature with temperature.

100-fold between 0.2 and 0.8 N compression, while increasing only 20-fold between 20 and 100 °C.

7.4 Modelling the conduction mechanisms

7.4.1 Electrical conduction behaviour in response to compressive force

In order to understand the conduction behaviour the electrical transport data was modelled with a system containing linear (ohmic) and non-linear conduction contributions. The conduction model combining linear conduction that was attributed to direct contact percolative conduction, and a non-linear term presumed to be associated with field-assisted quantum tunnelling conduction. The model introduced in Chapter 6 was used here for fitting to the I-V data.

Similarly to its application to the opaque ink in Chapter 6, the linear contribution was considered to originate from direct contact between the conducting particles in the printed ink, while the non-linear contribution is attributed to some form of quantum tunnelling between isolated conducting particles and isolated clusters of conducting particles. As before, the modelling was used to determine values for the linear conductivity σ_0 and the non-linear contribution, via the parameter A, as a function of both compressive force and temperature. Values for the tunnelling exponent n were also obtained to gain some insight into the tunnelling mechanism. An example of the model fitted to an increasing voltage I-V curve, measured under 0.2 N compression, is shown in figure 7.13 along with the statistical normalised residuals. As with the case of the opaque ink, the model used here

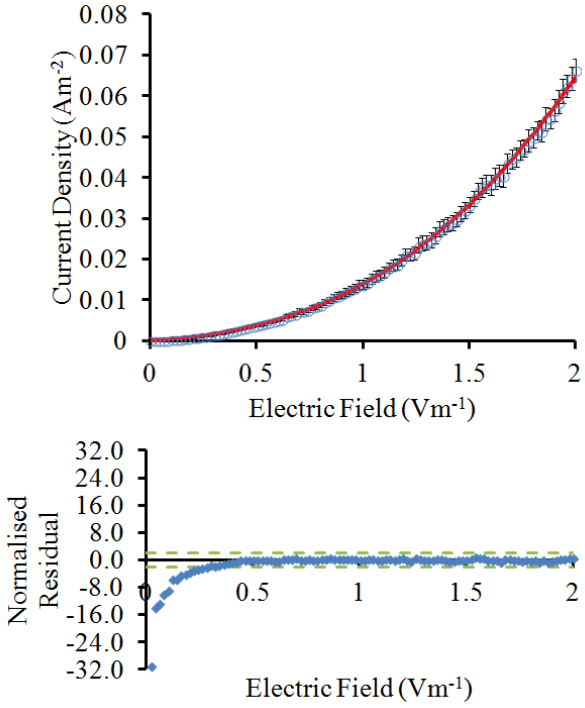

Figure 7.13. An example of the fit of a model, comprising linear and non-linear conductivity terms, to a 10 sweep average increasing voltage I-V curve taken at 20 °C under 0.2 N compression. The model fit is shown as a solid red line. Below is a normalised residual analysis of the fit to the data. The dashed green lines represent the boundaries for an acceptable fit.

provides a poor description of the electrical behaviour below a value of 0.5 μVm^{-1}, where the model predicts a higher current density than that observed. At higher electric fields, the statistical residuals lie within the ±2 limits, indicating a good fit of the data to the two component model. The residuals, however, show non-random variation which suggests the physics is more complex on the fine scale.

Figure 7.14(a) shows an example of a fit to an increasing voltage I-V curve taken at a compression of 0.6 N. The fitting below 0.5 μVm^{-1} is slightly better, but still lies outside the limits for a statistically reasonable fit. Similar small scale non-random variations of the residuals are also observed at higher electric field. Similar behaviour is observed up to 1.0 N of force, where there are further improvements of the fitting at low electric field, see figure 7.14(b). As the compression increases, the residuals below 0.5 μVm^{-1} improve, which is encouraging, but ultimately show the model is a

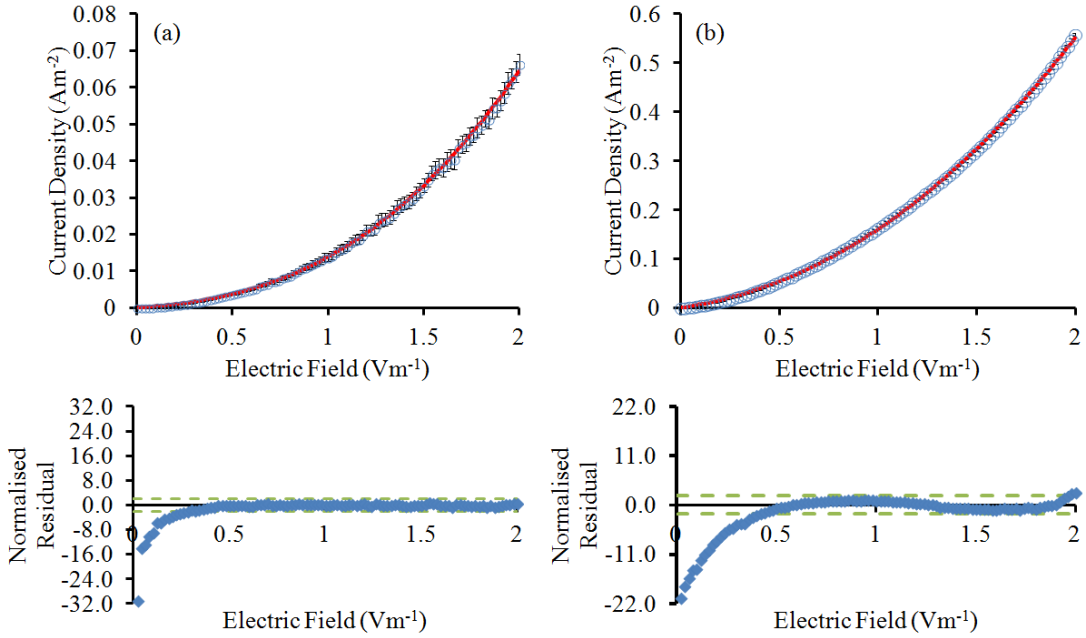

Figure 7.14. An example of the fit of a model, comprising linear and non-linear conductivity terms, to a 10 sweep average increasing voltage I-V curve taken at 20 °C under (a) 0.6 N compression, and (b) 1.0 N compression. The model fit is shown as a solid red line. Below is a normalised residual analysis of the fit to the data. The dashed green lines represent the boundaries for an acceptable fit.

poor description of the electrical conduction processes at the very low electric field values. As stated before, the model predicts a higher current than that observed, so perhaps charge transport occurs via an alternate, less efficient mechanism, or is inhibited, at these low electric fields. The ordering and structure of the residuals at higher electric field values suggest that, while the model provides a gross description, some details of the conduction processes are not represented in the model. Examples of fits to I-V sweeps with decreasing voltage are shown in figure 7.15. The model fits the data in the same way, with the fitting being a more precise description of the electrical conduction at higher electric field values. Using the best fits of the model to the experimental dataset allows the extraction of the linear conductivity σ_0, and the non-linear parameter A (attributed to field-assisted tunnelling conduction).

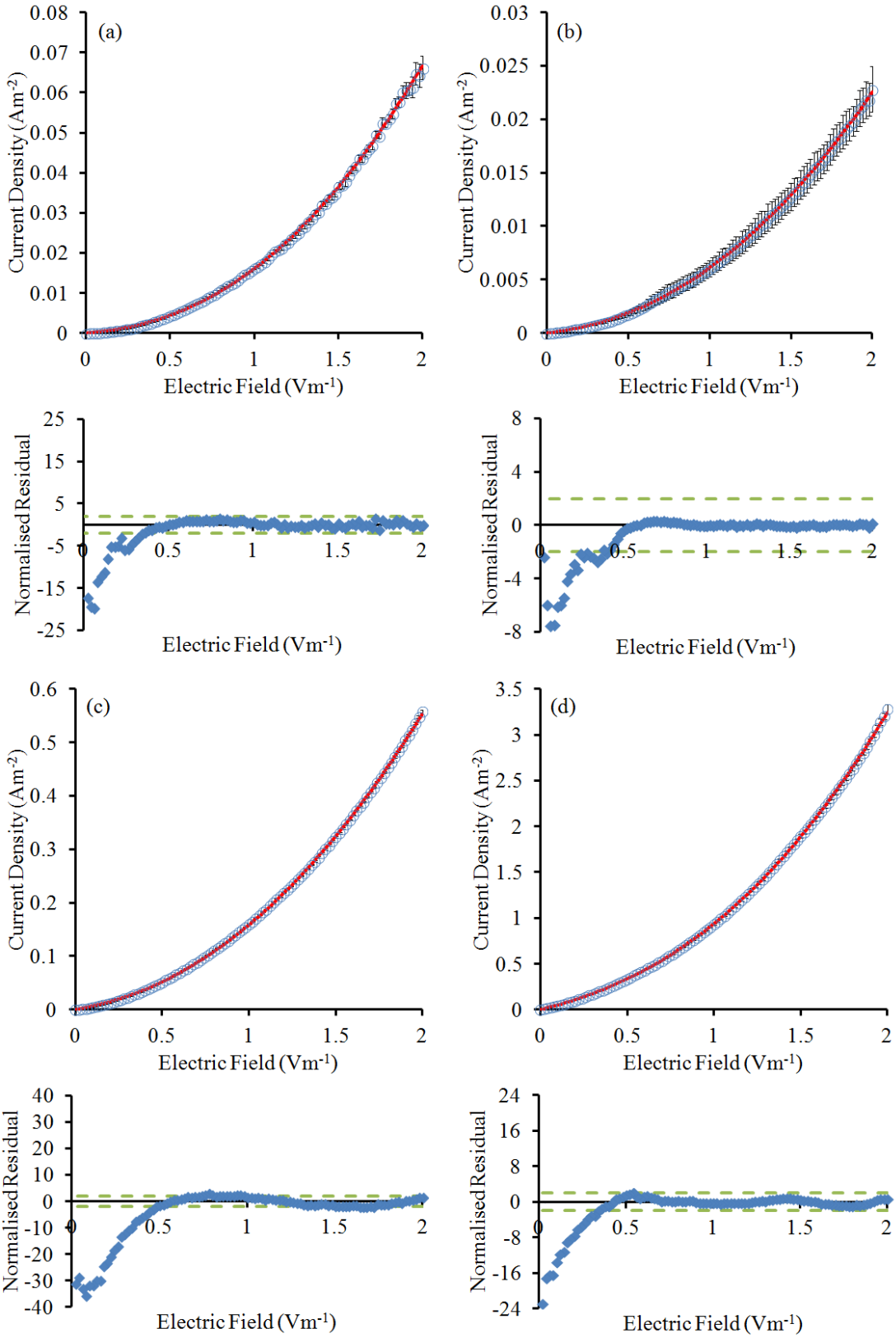

Figure 7.15. Example fits of a model comprising linear and non-linear conduction contributions to 10 sweep average decreasing voltage I-V curves at (a) 0.2 N, (b) 0.4 N, (c) 0.6 N and (d) 0.8 N compressive force, and at 20 °C. The solid red line is the model fit, the blue diamonds are the observed data. The green dashed lines in the residual analysis plots are guides to the limits of an acceptable fit.

Figure 7.16(a) shows the behaviour of the linear conductivity, σ_0, as a function of compressive force from increasing and decreasing voltage sweeps at room temperature. Similar to the opaque ink, the linear conductivity increases with increasing force. The A parameter from the fits exhibits similar behaviour as a function of compressive force as shown in figure 7.16(b), although its variation with increasing compression appears more linear. Interestingly, disparities between the up- and down-voltage ramp measurements are observed for both the linear conduction at high forces and non-linear conduction parameters, suggesting that both conduction mechanisms are affected and contribute to the electrical hysteresis in the I-V data. There is also no clear pattern to the disparities.

This observation contrasts with the trends observed in the opaque ink in Chapter 6, where it appeared only the non-linear conduction varied between the increasing and decreasing voltage ramps. The errors on the linear conductivity of the opaque ink were quite large, however, so this is still not certain and requires further study.

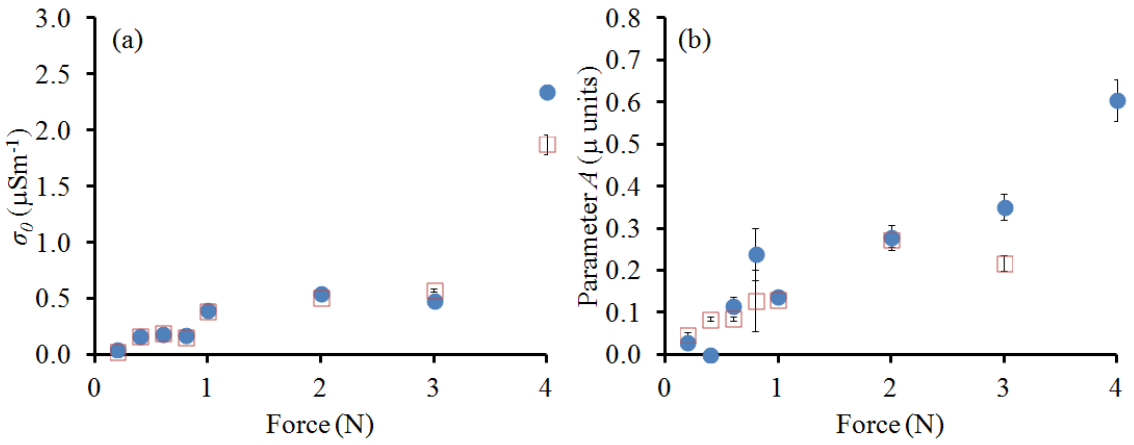

Figure 7.16. The behaviour of (a) the linear conductivity, σ_0, and (b) the non-linear conduction parameter, A, as a function of compressive force. The blue circles show the increasing voltage sweep values and the open red squares show the decreasing voltage values.

In figure 7.17 relative contributions of the linear and non-linear conductivity parameters are compared. This figure shows that as the compressive force is increased the non-linear conduction is initially the main contributor to the total conduction, but its relative contribution steadily decreases while the linear conduction grows to become the larger contributor by 1 N. The behaviour of the linear and non-linear parameters suggest that as compression is increased the number of direct electrical connections between the conducting particles in the aggregates increases due to them being pushed together, allowing more percolative current paths. At the same time, isolated conducting particles and clusters of conducting particles are also pushed into closer proximity resulting in narrower tunnelling barriers and enhancing field-assisted quantum tunnelling conduction. This effect appears to be limited, however, with the relative non-linear contribution decreasing above 1 N.

Figure 7.18 shows the behaviour of the tunnelling exponent, *n*, as a function of compressive force at room temperature. The value of this exponent can inform upon

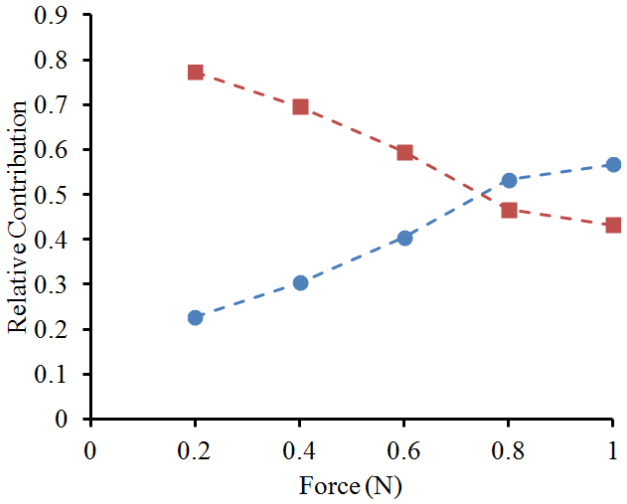

Figure 7.17. The relative contributions of the linear (blue circles) and non-linear (red squares) parameters to the total electrical conduction in the ink. The dashed lines are a guide to the eye.

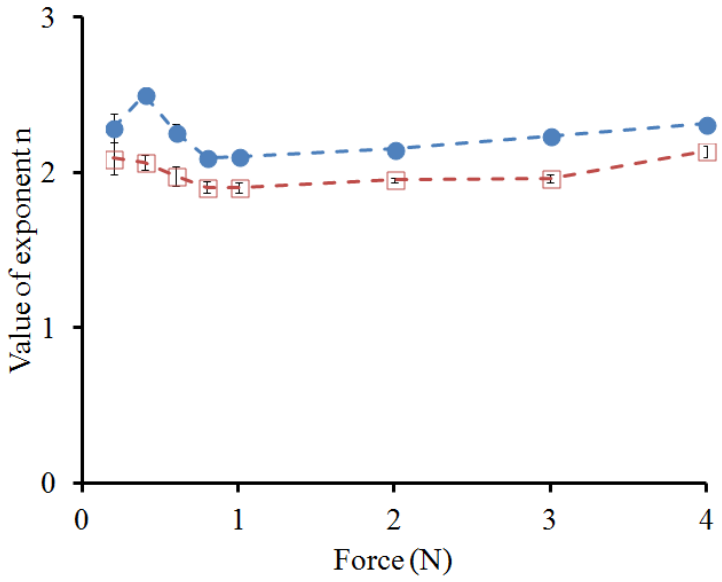

Figure 7.18. The behaviour of exponent *n* as a function of compressive force. The solid blue circles are values from the increasing voltage sweep, while the open red squares are values from the decreasing voltage sweep. The dashed lines are a guide to the eye.

the tunnelling mechanism [138]. Anomalous results were obtained at 0.4, 2, 3, and 4 N from the fitting of I-V data with increasing voltage, caused by difficulties arising from modelling with the anomalous peaks in the I-V data mentioned previously. These anomalous peaks lead to largely varying calculated values, with large errors, for the linear and non-linear conduction parameters and the tunnelling exponent, as the model does not account for such phenomena but the fitting algorithm attempts to entirely reproduce the anomalies.

Despite these issues, the parameter consistently takes a value close to 2, suggesting that field assisted Fowler-Nordheim-like tunnelling may be the main mechanism for the non-linear electrical conduction in this nanocomposite ink. This was also the case for the opaque ink analysed in Chapter 6.

7.4.2 Electrical conduction behaviour in response to temperature

The temperature dependence of the electrical transport behaviour of the transparent ink was studied to provide deeper insight into the conduction mechanisms. The conducting particles in the transparent ink are antimony-doped tin oxide, which is a doped semi-conductor with high conductivity. As mentioned in Chapter 3, semiconductor materials generally display an increasing electrical conductivity with increasing temperature; electrons are thermally promoted to the conduction band. This behaviour follows the relation below in equation 7.1.

$$\sigma_0 = \sigma_i exp(-\alpha/T) \tag{7.1}$$

where σ_0 is the conductivity, σ_i is the extrapolated intrinsic conductivity, α is a constant equal to $E_g/2k_B$, and T is the temperature.

The linear conductivity, σ_0, obtained from the model fits should follow this temperature dependence if the physical basis is associated with direct electrical connections between the semiconducting particles. Figure 7.19 shows the variation

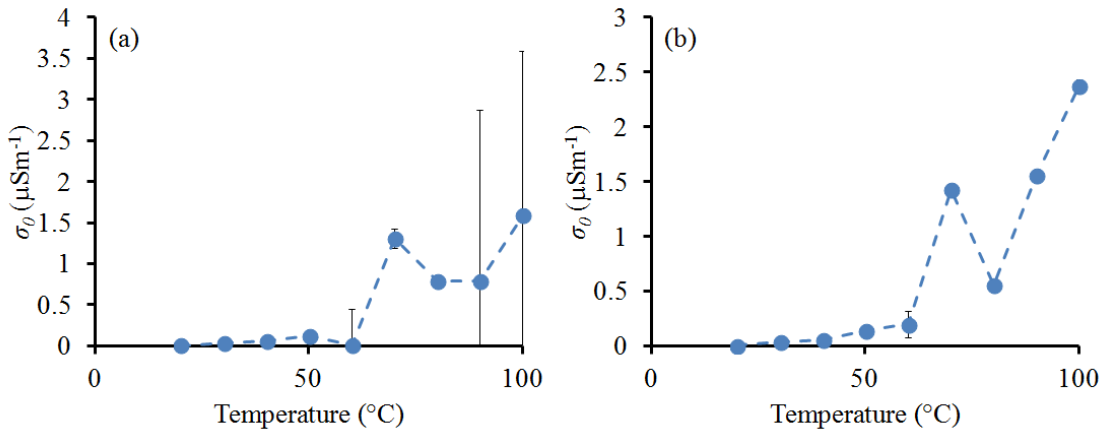

Figure 7.19. The behaviour of the linear conductivity, σ_0, as a function of temperature during the (a) increasing voltage sweep, and (b) decreasing voltage sweep under 0.2 N compression.

of the linear conductivity with increasing temperature at 0.2 N compression for both increasing and decreasing voltage. The linear conductivity behaves in a similar way to the linear conductivity of the opaque ink, increasing with increasing temperature. An anomalous point in both the linear and non-linear terms is observed in figure 7.19 at 70 °C. Points such as these, which significantly deviate from average behaviour of the ink, correlate with anomalous peaks in the I-V and are a result of how the fitting algorithm attempts to replicate the peaks using the model in equation 6.1. Figure 7.20 shows the linear conductivity as a function of temperature for compressions of 0.2, 0.6 and 1.0 N. All three datasets show the same general behaviour: the linear conductivity increases with increasing temperature. It is to be noted that data points are missing at 90 and 100 °C for the 1.0 N dataset due to sample degradation. The increase of the linear conductivity is larger at higher compressions and the maximum value of the linear conductivity increases approximately 10 fold between 0.2 N and 1.0 N compression. Figure 7.21 shows example fits of the semiconductor electrical conductivity temperature dependence, using equation 7.1, to the experimentally derived linear conductivity as a function of temperature. The residual analysis reveals that the fitting is generally not good and that the model is worst

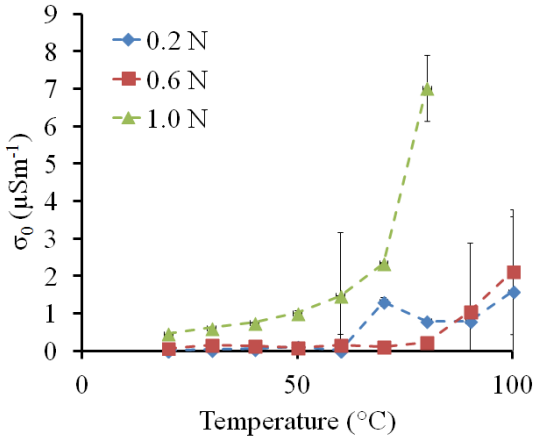

Figure 7.20. The behaviour of the linear conductivity, σ_0, as a function of temperature at three mass loadings: 0.2, 0.6 and 1.0 N. Data at 90 and 100 °C for 1.0 N does not exist due to sample failure.

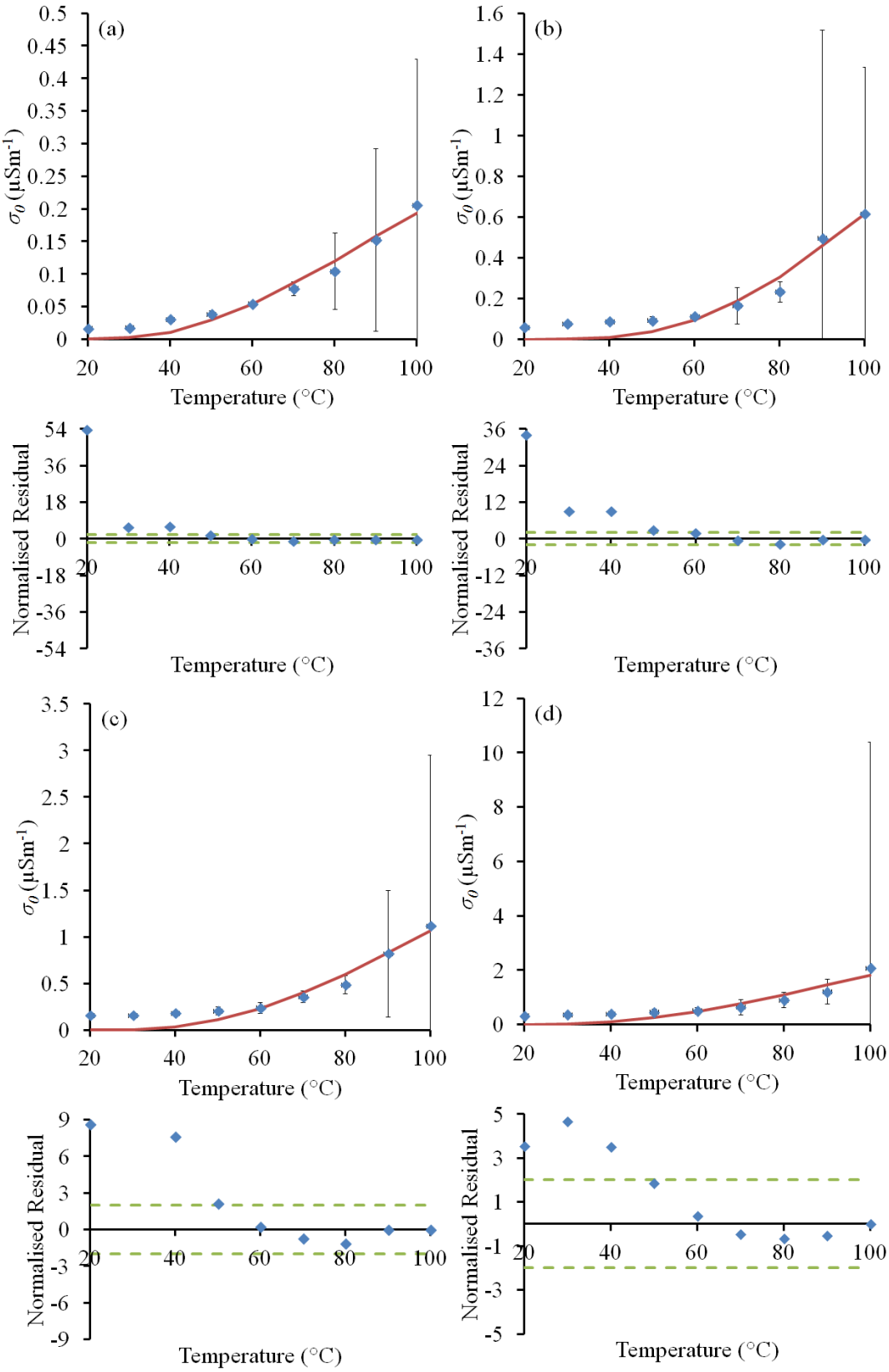

Figure 7.21. Example fits of a model of semiconductor temperature dependence of conductivity to the linear conductivity as a function of temperature at (a) 0.2 N, (b) 0.4 N, (c) 0.6 N, and (d) 0.8 N. The blue diamonds are the data and the solid red lines are the model fits. The green dashed lines in the residual analyses are guides to the limits of a good fit.

at temperatures below approximately 70 °C. The semiconductor model fit also appears to get worse as the compression increases. Addition of a linear offset, as was done in Chapter 6 ($\sigma = \sigma_0 exp[-\alpha/T] + c$), improves the fitting, particularly at high temperatures and compressions, seen in figure 7.22. On the basis of this fitting, it seems that the temperature dependence of the linear conductivity does not originate in the intrinsic temperature dependence of conduction in the semi-conducting material. The non-linear component of the conductivity increases very slowly with temperature until approximately 60 - 70 °C, where it rises with a larger gradient, see figure 7.23. While the non-linear conduction rises rapidly, the associated errors also increase with increasing temperature. As with the opaque ink, this change seems to be sudden and could be linked to a physical change in the ink.

Figure 7.24 shows the non-linear conduction parameter A as a function of temperature at five compressions. No clear pattern is observed between the temperature dependence of parameter A and the compressive loading, unlike the case for opaque Ink. As before, the behaviour of the non-linear conduction parameter, A, as a function of temperature, has been modelled using the temperature dependence of field-assisted quantum tunnelling, described in Chapter 3. It is repeated below on the following page for convenience.

$$A = D\left(\frac{\pi\zeta T}{\sin \pi\zeta T}\right) \tag{7.2}$$

where D is a constant and collection of physical factors, ζ is a constant that encapsulates several factors such as the workfunction, and T is the temperature. Figure 7.25 shows an example of the fitting of equation 7.2 to the non-linear

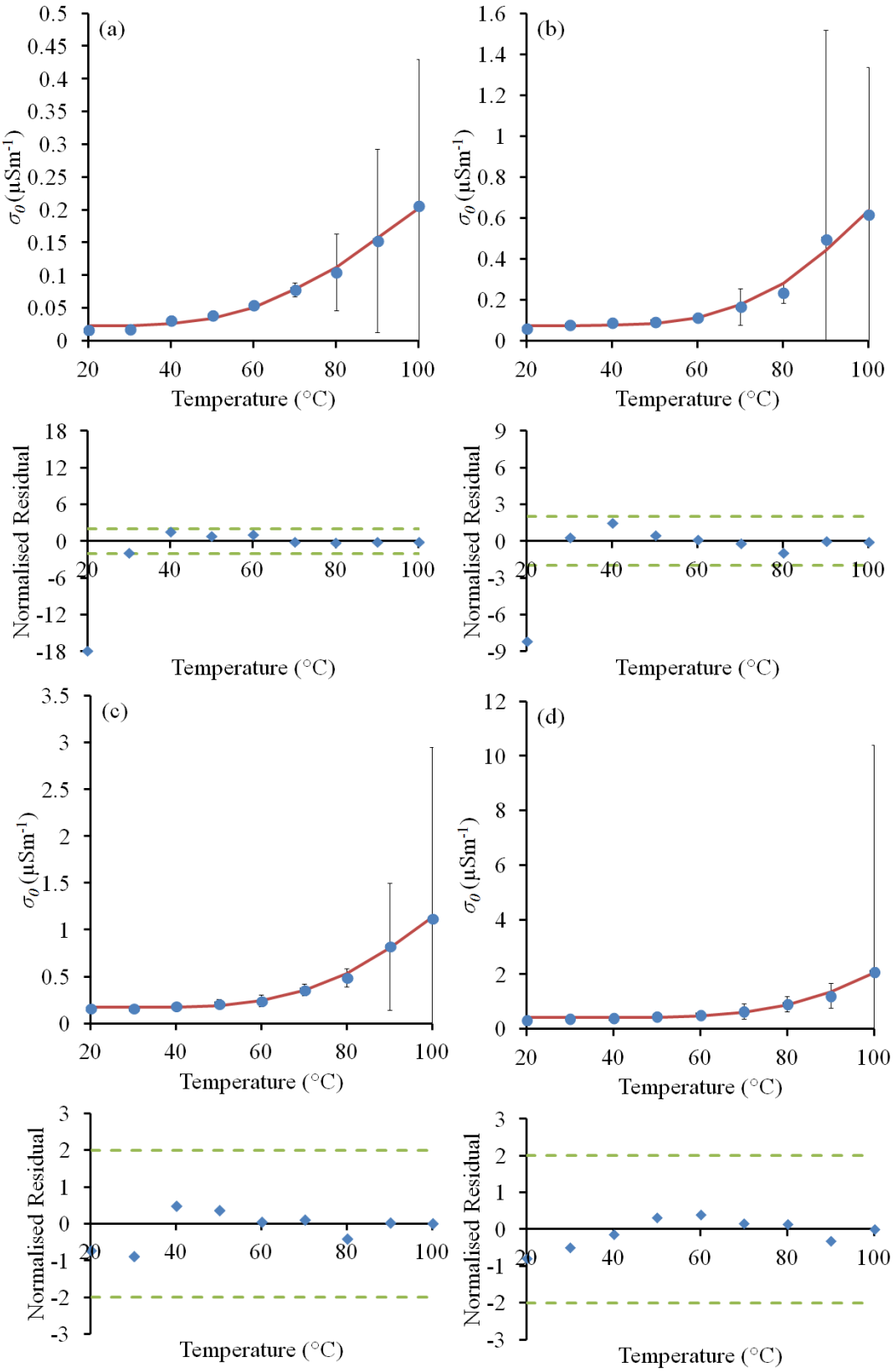

Figure 7.22. Example fits of a model of semiconductor temperature dependence of conductivity, with an offset *c*, to the linear conductivity as a function of temperature at (a) 0.2 N, (b) 0.4 N, (c) 0.6 N, and (d) 0.8 N. The blue diamonds are the data and the solid red lines are the model fits. The green dashed lines in the residual analyses are guides to the limits of a good fit.

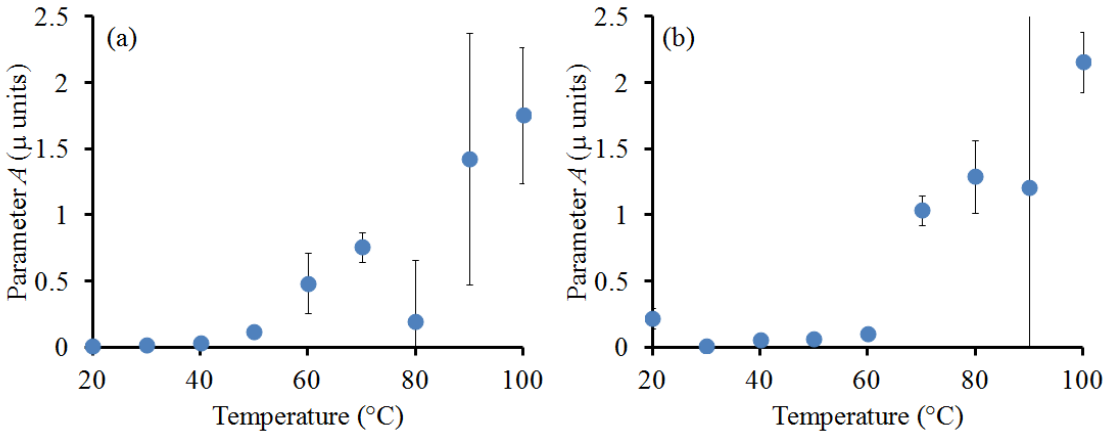

Figure 7.23. The behaviour of the non-linear parameter *A* during the (a) increasing voltage sweep, and (b) decreasing voltage sweep, as a function of temperature.

conduction parameter *A* data as a function of temperature under 0.2 N of compression. The residual analysis shows that at low compression the model is a poor description of the temperature dependence of parameter *A*.

At higher compressions (0.4 – 1.0 N), however, the fit does not improve greatly, as shown in figure 7.26. The anomalous peaks in the increasing voltage I-V data prevent fitting, while the fitting for the decreasing voltage I-V data was better.

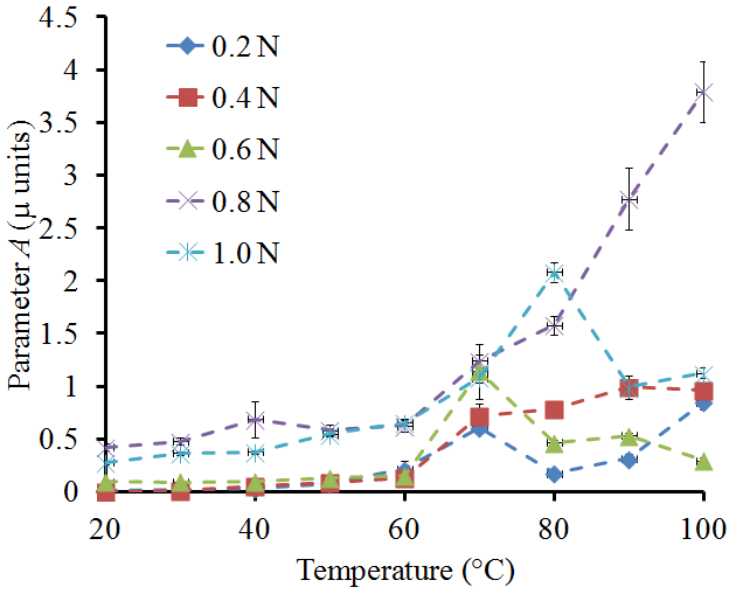

Figure 7.24. The behaviour of the non-linear parameter *A* as a function of temperature at five mass loadings: 0.2, 0.4, 0.6, 0.8, and 1.0 N.

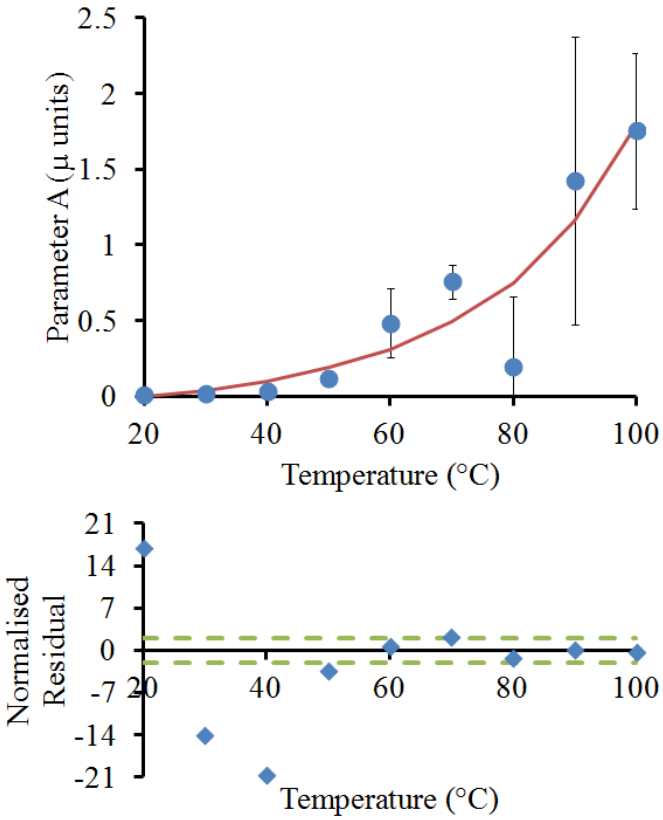

Figure 7.25. An example fit of equation 7.3 (solid red line) to the non-linear parameter *A* at 0.2 N compressive force (blue circles). The green dashed lines in the residual analysis are guides to the limits of a good fit.

Overall, the comparison with the temperature dependent model does not shed significant light on the details of the conduction mechanisms at play in the transparent ink. At low compression, however, there may be some other, more significant effect causing the change in the non-linear parameter, possibly softening of the polymer binder material which accounts for a larger percentage of the printed transparent ink than it does in opaque ink (though this is only true macroscopically. Within the aggregates of the transparent ink, the polymer binder wetting appears to be similar to that in the opaque ink), or the process of establishing full contact with the upper electrode.

Figure 7.27 shows the relative contributions of the linear conductivity and parameter *A* as a function of the temperature, at four different compressive loadings.

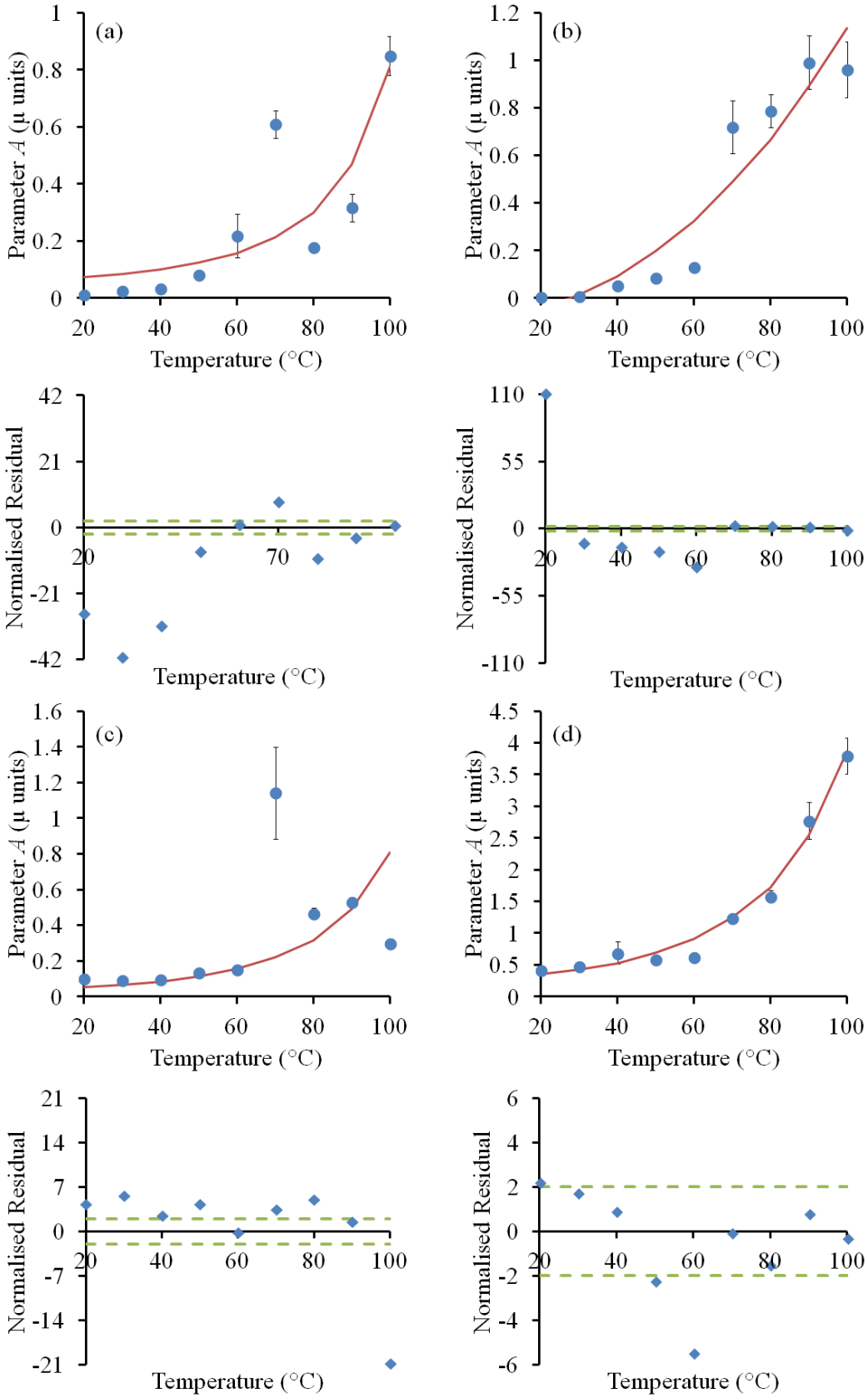

Figure 7.26. Example fits of equation 6.3 (solid red line) to the behaviour of parameter *A* as a function of temperature (blue diamonds) at (a) 0.2 N, (b) 0.4 N, (c) 0.6 N, and (d) 0.8 N compressive force. The green dashed lines in the residual analyses are guides to the limits of a good fit.

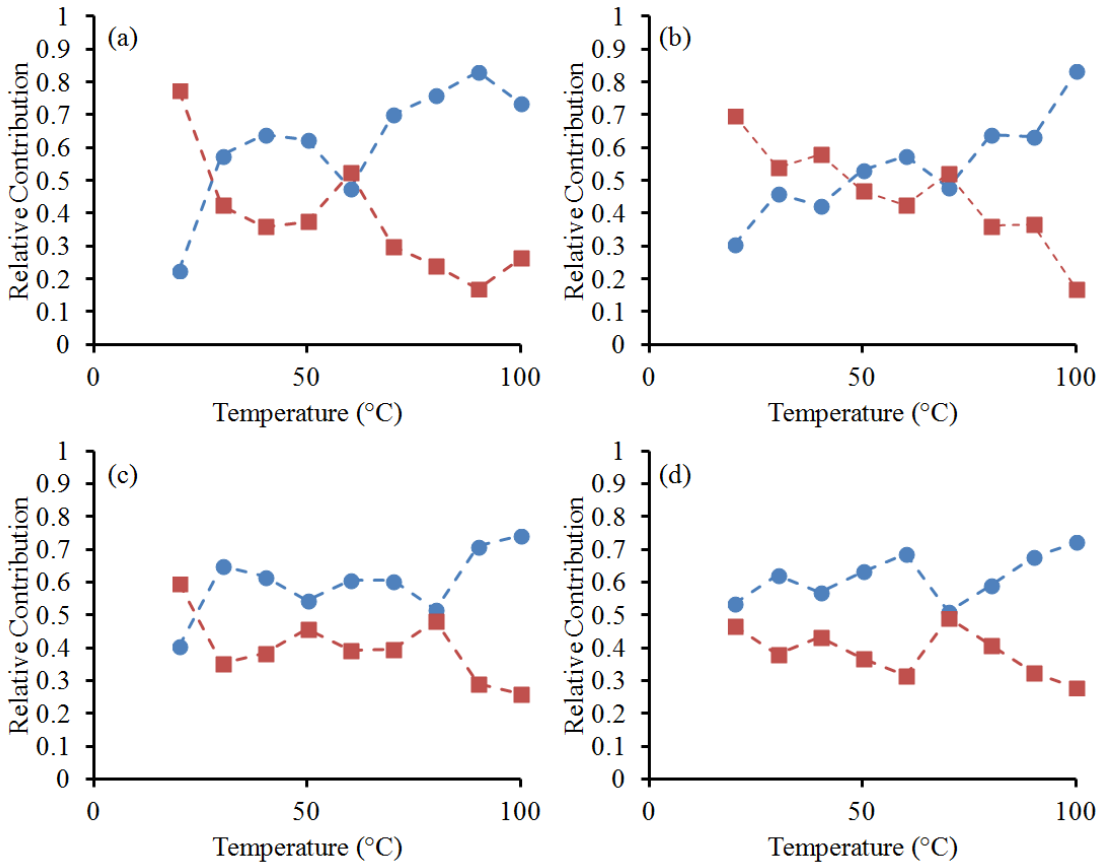

Figure 7.27. Relative contributions of the linear (blue circles) and non-linear (red squares) parameters as a function of temperature at (a) 0.2 N, (b) 0.4 N, (c) 0.6 N, and (d) 0.8 N.

At low compression, figure 7.27(a), the non-linear term is the dominant contribution to the total electrical conduction, but this changes as the temperature increases. In fact, the linear and non-linear contributions cross between 30 and 60 °C, before the linear term becomes the dominant conduction contribution. The behaviour of the relative contributions is not linear and is variable, particularly in the 30 to 60°C range. This pattern is repeated at higher compressions, but the linear term is more significant at each higher compression. This suggests that tunnelling processes in the transparent ink are only significant contributors to the current at low compression and temperature. The variability of the contributions, which causes the linear and non-linear conduction to cross over, twice in figure 7.27(a) and (b), may be a result of the poor fitting caused by the anomalous current peaks in the I-V data, or a complex

behaviour that is dependent on both the compression and ink temperature. For example expansion and, at the higher temperatures, softening of the polymer layer could be competing with the thermal and compression dependencies of the linear and non-linear conduction contributions.

7.5 Summary

The transparent ink displays complex non-linear electrical transport behaviour which is affected by both compressive loading and temperature. The electrical conduction has been modelled as a combination of two mechanisms: linear ohmic, percolative conduction and non-linear conduction attributed to field-assisted quantum tunnelling processes. An increase of compression leads to more conducting particles being pushed into close proximity, narrowing tunnelling barriers, and/or into direct contact, increasing electrical conduction directly through the needles. Increasing the temperature of the ink similarly increases the linear and non-linear conduction: thermal excitation of charge carriers in the semiconducting particles and extra thermal energy input to tunnelling charges may increase the linear and non-linear conduction contributions.

The modelling of the transparent ink I-V data suggests that this two component conduction regime is not the most reasonable physical basis upon which to describe the conduction behaviour. The extracted linear and non-linear conduction parameters are more variable than in the case of the opaque ink and have larger associated errors. It is likely that the model is lacking finer details in the description of the conduction. Physical effects, such as the softening of the polymer binder with

temperature, and establishing contact with the upper electrode, may have large roles in the conduction behaviour and these are not represented in the model as it is.

8. Conclusions and further work

8.1 Physical structure and thermal behaviour

In this chapter, the key findings of the research from Chapters 5, 6, and 7 are summarised, discussed further and final conclusions are presented. Suggestions for extending this research work are also detailed at the end of the chapter.

8.2 Electrical transport behaviour as a function of compression and temperature

Studies of the physical composition and structure of the inks considered in this work have revealed insights into how the composite ink's behaviour is a function of the ways in which its constituent parts interact. The opaque ink comprises acicular titanium dioxide needles with a conductive antimony-doped tin oxide surface coating (average measured length 1 μm, average measured width 87 nm) and insulating near-spherical titanium dioxide nanoparticles (average measured diameter 210 nm), dispersed in an insulating polymer binder. This work has shown that the constituent nanoparticles, prior to being blended in the polymer, have a tendency to excessively clump together, which may be attributed to electrostatic forces between the particles.

Microscopy analysis has shown that the screen printed ink has a complex surface structure, with the needles generally well dispersed throughout the surface, occasionally forming clumps of 2 to 4 needles. However there appeared to be areas of local ordering of the needles. The cause of this arrangement has not been fully

explained in the course of this work but may be a result of the screen printing process described in Chapter 2. The TiO_2 particles, on the other hand, were more uniformly distributed throughout the surface, in between the needles and small clumps of needles. At high magnification, a surface coating not shown to be present in the scanning microscopy analysis of the individual ink constituents was observed when imaging the printed ink. This coating comprises the residual polymer binder. Across the whole surface air gaps, or voids, were observed. These voids are a likely result of residual air bubbles present in the ink prior to printing, and are not a deliberate feature. Indeed, bubbles or voids are often detrimental to device functionality where uniform and homogeneous printed layers are required. In the case of the opaque ink, however, these voids may lend the ink its compressibility in what is otherwise a rigid surface structure.

Focussed ion beam milling, as detailed in Chapter 4, was used to expose cross-sections in the printed ink and these revealed a cross-sectional structure similar to that of the printed ink surface. The printed layers were approximately 2 to 5 μm thick. The majority of the needles tended to lie in the plane of the surface of the ink, although some were seen lying out of the plane. The distribution of the needles, TiO_2 particles and voids appeared to be similar to that observed at the printed ink surface. The cross-sections also revealed that the *macor* ceramic electrodes were not flat, having an approximate surface roughness of 1.0 μm. This reflects inconsistent or incomplete polishing of the *macor* tiles prior to electrode deposition.

The transparent ink comprised conductive antimony-doped tin oxide needles and near-spherical nanoparticles, and PMMA microbeads (diameter: 6 μm) dispersed within an insulating polymer binder. A greater ratio of polymer binder to conductive

filler particles was used in this ink to maintain a high optical transparency. The individual filler particles were very similar to those used in the opaque ink but were smaller: the Sb-needles have an average measured length of 252 nm and average measured width of 41 nm, while the Sb-particles have an average measured diameter of 67 nm.

The surface structure of the as-printed transparent ink differed significantly from that of the opaque ink, consisting primarily of polymer binder, with self-assembled aggregates of the filler particles that were distributed randomly throughout the whole printed layer. The filler particle size was reduced for the transparent ink to help limit the average size of the aggregates formed, as large aggregates protrude well above the surface of the printed ink and become easily damaged after successive compressions. Also, the large aggregates act as optical scattering centres, reducing transparency. The aggregates had an average measured diameter of 7 μm and were typically separated from each other by several micrometres. FIB cross-sectional imaging revealed that the aggregates had an internal structure similar to that of the original opaque ink: they were more tightly packed, but voids between the constituent filler particles were observed and it was clear that some sedimentation process may have taken place when the ink was drying, as larger filler particles were observed towards the bottom of the aggregates. The acicular particles in the aggregates appeared to be randomly spatially orientated within the aggregates of the transparent ink, more than those in the surface of the opaque ink, which tended to lie in the plane of the printed surface. While further high resolution cross-sectional imaging is required to confirm this, the distribution of orientations suggest that the aggregates form in suspension while the ink is wet,

prior to printing. Typically, the aggregates bridged the thickness of the entire printed ink layer. From the obtained images, it was not clear if the particles in the aggregates were fully wetted (i.e. coated) by the polymer.

The response of the composite inks to temperature was important in an academic sense and for applications purposes, providing further insight into conduction processes and revealing limitations in potential applications. Thermal analysis of the opaque and transparent ink constituents revealed that the filler particles for both inks were invariant over a wide range of temperatures but that the PMMA microbeads and polymer binder both underwent decomposition at approximately 400 °C. A potential glass transition was detected in the TGA of the PMMA microbeads between 60 and 120 °C, but this was not verified by the corresponding DSC analysis. The TGA of the polymer revealed a ~70% mass change when heating from room temperature to 100 °C: this was attributed to solvents being driven off as the polymer and ink samples for the TGA and DSC analyses were not furnace dried (the ink samples used for the electrical transport measurements were furnace dried at 90 °C for up to 30 minutes) prior to the testing.

8.3 Electrical transport behaviour as a function of compression and temperature

The opaque ink exhibited non-linear I-V electrical behaviour at low compressions. Upon further compression, the total current passed through the ink increased and the I-V curvature was reduced. Some hysteresis was observed and was consistently more pronounced in the first sweep of the ten sweep I-V cycles. A model of the ink conduction comprising a linear ohmic term, attributed to direct contact percolative

conduction between the conductive particles, and a non-linear contribution associated with field-assisted quantum tunnelling (see Chapter 3 for discussions of conduction mechanisms) was used successfully to describe this compression dependent I-V behaviour.

The model suggests that direct contact, ohmic conduction was largely responsible for the conduction through the ink but, as compression increased, the relative contribution from quantum tunnelling processes increased. This was attributed to the conductive needles and clusters of needles being pushed into closer proximity, together with compression of the thin polymer coating of the needles (which acted as a potential barrier for tunnelling conduction), increasing the efficiency of quantum tunnelling. The electrical conduction model, however, performed poorly at the lowest electric fields where it overestimated the conductivity of the ink and therefore did not fully encapsulate the conduction in the low electric field regime. Other less efficient conduction mechanisms, which become overwhelmed as the electric field is increased, could be responsible for this poor agreement. The poor fitting at low electric field improved with increasing compression, however. At room temperature, the linear conductivity term accounted for approximately 80 % of the conduction and increasing compression reduced its relative contribution to ~70 % by 0.6 N.

As the temperature of the ink was raised, the overall conductivity of the ink increased. However, the curvature of the I-V behaviour was still observed, which suggested that temperature affected the conduction contributions uniformly. The temperature dependence of intrinsic percolative semiconductor conductivity was fitted to the extrapolated linear conductivity parameter and provided a reasonable fit

above 40 °C and at mid to high compressions. Adding a constant offset to the model improved the fitting dramatically: this offset could be attributed to a currently unconsidered conduction mechanism or pathway through the ink, such as an interaction related to the ink contacting the electrodes. Meanwhile the behaviour of the extrapolated non-linear parameter *A*, as a function of temperature, was modelled with an expression associated with the temperature dependence of field-assisted quantum tunnelling conduction. This model gave a good fit, suggesting that field-assisted tunnelling mechanisms formed a significant part of the non-linear conduction in the opaque ink.

At low compression, as the temperature was increased, an increase in the relative contribution of non-linear conduction (from ~25 % to ~50 % between 20 and 100 °C under 0.2 N compression) in the opaque ink was observed. As compression increased temperature had a less significant effect on the conduction contributions, with the linear and non-linear terms showing little variation with temperature (remaining at ~30 % between 20 and 100 °C). At low compression increases in temperature provide energy to charge carriers, increasing the tunnelling efficiency, but at the highest compressions it is possible that many tunnelling junctions have become compressed into direct contacts, countering the effect temperature has on increasing the tunnelling current contribution.

The transparent inks electrical behaviour was macroscopically very similar to that of the opaque ink. Both exhibited similar non-linear behaviour at room temperature which became more linear as the compression was increased. In the transparent I-V data, however, anomalous peaks were observed. These occurred at random compressions and temperatures but tended to occur most during the first

sweep of a 10 sweep I-V cycle. It is possible that this behaviour was associated with charge trapping, particularly trap sites becoming filled or emptying, as similar behaviour arising from charge trapping phenomena has been observed in the bulk QTC™ composite material. A model comprising linear and non-linear conduction contributions was also fitted to the I-V behaviour of the transparent ink. The presence of the anomalous peaks made the modelling more challenging but overall the model fitted the data well. The model, as in the case of the opaque ink, was a poor fit at the lowest electric fields and compressions, again overestimating the current passing through the ink, possibly for similar reasons. The derived linear ohmic and non-linear tunnelling conduction parameters were also more variable as a function of loading than the corresponding parameters for the opaque ink, largely due to the difficulty in fitting the model to the data with the anomalous peaks.

The temperature dependent behaviour of the transparent ink I-V data was also similar to that of the opaque ink. The total current passed through the transparent ink was seen to increase with increasing temperature, and the curvature of the I-V sweeps was similar with increasing temperature. Fitting of the temperature dependence of semiconductor conductivity to the linear conduction term was generally poor, only becoming a reasonable description of the conduction at high compression and above ~70 °C, indicating the linear component of the conduction was not wholly attributed to charge transport through semiconducting material. The temperature dependence of the non-linear parameter was also not well described by the temperature dependence of conduction attributed to field-assisted quantum tunnelling at low temperature or compression, but the agreement with the model improved as both the compression and temperature increased.

Overall, the model developed provides a simple but appropriate method for describing the conduction behaviour of the opaque ink. However, the model did not describe the finer details of the conduction within the transparent ink. In this case, other factors, such as softening of the polymer with temperature and interactions between the top surface of the ink and the electrode may have affected the conduction behaviour. The model was generally less successful in describing the conduction behaviour of the transparent ink: the behaviour here was more complex and a further study of the effects of compression and temperature on the polymer binder, aggregates and aggregate-electrode contacts is needed to refine the model. These results are discussed and links between the structural and thermal properties of the composite inks and their electrical behaviour are suggested in the following section.

8.4 Links between the structure, thermal properties and electrical behaviour of the composite inks

The structures of the opaque and transparent inks differ greatly and this may be critical in explaining why the model, combining linear and non-linear conduction terms, works well for the opaque ink but not so well for the transparent ink. Quantum tunnelling requires adjacent conductors to be in very close proximity and this was largely the case for the opaque ink throughout the entire surface and cross-section. The conductive needles were well distributed through the ink and appeared to be wetted with a thin layer of polymer binder, which acted as a sufficiently thin barrier to facilitate quantum tunnelling conduction. As the compression was

increased, these conductive needles were pushed into closer proximity, increasing the efficacy of field-assisted tunnelling processes. Simultaneously, some of the needles were pushed into direct contact, increasing the ohmic conduction. Additionally, the temperature dependence of the linear and non-linear contributions agrees well with the behaviour of semiconductor and field-assisted tunnelling conductivity as a function of temperature, indicating the model provides a reasonable description of the electrical transport behaviour in the opaque ink.

In contrast, the conductive particles in the transparent ink formed large aggregates randomly dispersed with a spacing of several micrometres. Conduction between the aggregates via tunnelling processes is very unlikely. Instead, conduction will occur through each aggregate individually. It is unclear as to whether the conductive filler particles in the transparent ink were all wetted with polymer binder. Higher resolution imaging from scanning electron microscopy is required to determine this. If the polymer wetting of the filler particles was incomplete then the aggregate might be largely conductive, by percolative means, due to the fact that all of the filler particles are conductive and generally in direct contact, unlike the case of the opaque ink where the TiO_2 nanoparticles were insulating. The transparent ink was formulated with proportionally more polymer binder than in the opaque ink, so it will have a more significant effect on the ink properties. It is possible that the polymer binder underwent significant softening as the temperature was increased.

The thermal analysis showed a 70 % mass change, associated with the evaporation of solvent. This effect could have masked more subtle physical changes, such as a glass transition. If the polymer did soften with increasing temperature then this would affect how the ink layer was compressed and how the aggregates were

contacted with the upper electrode. On the other hand, the polymer could have expanded and swelled with increasing temperature, changing the compressibility of the ink layer. It is therefore possible that the complex non-linear behaviour observed in the transparent ink, while similar to that seen in the opaque ink, arises from the interaction of the aggregates and polymer contacting the electrode, or from complex physical changes within the polymer affecting the physical properties of the printed ink layer as a whole.

Both these inks are very well suited to touch-pressure sensing applications as they both exhibit not only the ability to detect location, but also how hard a press is on a touch input. Early variations of the transparent ink were not as durable as the opaque ink due to large aggregates becoming deformed and perforating the printed ink layers after successive compression cycles, but this has been largely remedied by reducing the filler particle size and thus limiting the size of the aggregates. The opaque ink was also durable in response to exposure to heat, with some samples tested above 100 °C. This is above the average operating temperature of touch inputs found in phones and laptop touch pads.

The same cannot be said of the transparent ink however. Much of the temperature and compression dependent I-V work had to be limited to a maximum temperature of 70 °C. Above this temperature, the inks exhibited a dramatic increase of conductivity, experiencing significant joule heating and subsequent damage. This could be problematic if the ink is used in devices which tend to get hot with use, or even if such a device is left in a car on the dashboard on a sunny day, for example.

8.5 Further work

This research has ultimately provided a deeper understanding of the conduction in the opaque and transparent inks. This knowledge will facilitate the continued development of the inks: insights into the physical operation of the inks allows informed decisions to be made on how to improve the performance and durability through the selection of filler particle materials and geometries, insulating matrix materials and printing techniques. However, there are still numerous areas in which this work could be expanded.

Firstly, the thermal analysis of the inks could be expanded to include multiple sequential heating and cooling curves on samples that are identical to those used for electrical testing (i.e. screen printed and furnace dried). In particular, not much is known about the polymer binder and the PMMA microbeads. These may or may not play a significant role in determining the compression and temperature dependence of electrical behaviour in the transparent ink and should be studied further. This could be followed up with a study of alternative solutions for the polymer binder and spacer beads in an attempt to improve the temperature durability of the transparent ink.

Secondly, direct imaging of the conduction network was intended to be part of this research but facilities and time constraints led to the experiment being unavoidably dropped. This experiment would involve the use of the electron beam induced current (EBIC) technique. An unearthed sample connected in a circuit would be placed under a scanning electron microscope and a beam of electrons would be scanned over the sample surface. At each pixel, the incident beam interacts with the

surface and charge is injected into the sample. The injected electrons then dissipate through the percolative conduction network within the composite sample and are detected as pulses of current. An intensity map, where image brightness corresponds to the magnitude of electric current detected, can thus be generated with bright areas indicating the conduction network. A combination of cross-sectional and top-down approaches could be used and the sample could be flexed to simulate compression. Such an experiment would provide valuable insight into the conduction processes and, to the best of the author's knowledge at the time of writing, would be the first instance of EBIC being used to image a percolation network within a composite material.

Thirdly, this research focussed on describing the temperature and compression dependence of the electrical behaviour but work could also be undertaken to investigate the vapour sensing characteristics of the inks. Both inks already contain materials (titanium dioxide and tin oxide nanoparticles) that are used in gas and vapour sensors, and can additionally sense gas through interactions between the vapour and the polymer binder. Basic characterisation of the sensing ability of the inks could be undertaken, such as response time, recovery time and gas selectivity, before progressing to attempts to model the chemical and physical basis of the vapour sensing characteristic. A future project could also include the development of a functional sensor.

References

[1] J.-P. Won, B.-T. Hong, T.-J. Choi, S.-J. Lee and J.-W. Kang, "Flexural Behaviour of Amoprhous Micro-Steel Fibre-Reinforced Cement Composites," *Composite Structures,* vol. 94, pp. 1443-1449, 2012.

[2] T. A. Kim, H. S. Kim, S. S. Lee and M. Park, "Single-Walled Carbon Nanotube/Silicone Rubber Composites for Compliant Electrodes," *Carbon,* vol. 50, pp. 444-449, 2012.

[3] B. Wang, J. Yin and L. Wang, "Structure and Properties of Aeronautical Composites using Carbon Nanotubes/Epoxy Dispersion as Nanocomposite Matrix," *Polymer Composites,* vol. 34, pp. 1690-1697, 2013.

[4] W. Zhao, M. Li and H.-X. Peng, "Functionalized MWNT-Doped Thermoplastic Polyurethane Nanocomposites for Aerospace Coating Applications," *Macromol. Mater. Eng.,* vol. 295, pp. 838-845, 2010.

[5] M. Rosso, "Ceramic and Metal Matrix Composites: Routes and Properties," *J. Mater. Process. Tech.,* vol. 175, pp. 364-375, 2006.

[6] D. Bloor, K. Donnelly, P. J. Hands, P. Laughlin and D. Lussey, "A Metal-Polymer Composite with Unusual Properties," *J. Phys. D.: Appl. Phys.,* vol. 38, pp. 2851-2860, 2005.

[7] A. J. Webb, M. Szablewski, D. Bloor, D. Atkinson, A. Graham, P. Laughlin and D. Lussey, "A Multi-Component Nanocomposite Screen-Printed Ink with Non-Linear Touch Sensitive Electrical Conductivity," *Nanotechnology,* vol. 24, p. 165501, 2013.

[8] IDTechEx, "IDTechEx," [Online]. Available: http://www.idtechex.com/research/reports/printed-organic-and-flexible-electronics-forecasts-players-and-opportunities-2013-2023-000350.asp?viewopt=showall. [Accessed 2 May 2013].

[9] C. Brunetti and R. Curtis, "Printed-Circuit Techniques," *Proceedings of the IRE,* vol. 36, pp. 121-161, 1948.

[10] Y. Mitake and T. Fujimoto, "Screen Printing Machine". Patent US 2014/0109779 A1, 24 April 2014.

[11] N. A. Skow, "Laminates for Printed Circuits," *Electrical Engineering,* vol. 74, pp. 1092-1093, 1955.

[12] W. Yin, D.-H. Lee, J. Choi, C. Park and S. M. Cho, "Screen Printing of Silver Nanoparticle Suspension for Metal Interconnects," *Korean J. Chem. Eng.,* vol. 25, pp. 1358-1361, 2008.

[13] J. Perelaer, P. Smith, D. Mager, D. Soltman, S. K. Volkman, V. Subramanian, J. G. Korvink and U. Schubert, "Printed Electronics: The Challenges Involved in Printing Devices, Interconnects, and Contacts based on Inorganic Materials," *J. Mater. Chem.,* vol. 20, pp. 8446-8453, 2010.

[14] J. Perelaer, A. de Laat, C. E. Hendriks and U. S. Schubert, "Injet-Printed Silver Tracks: Low Temperature Curing and Thermal Stability Investigation," *J. Mater. Chem,* vol. 18, pp. 3209-3215, 2008.

[15] A. Bonea, A. Brodeala, M. Vladescu and P. Svasta, "Electrical Conductivity of Inkjet Printed Silver Tracks," in *35th Int.l Spring Seminar on Electronics Technology*, 2012.

[16] H.-H. Lee, K.-S. Chou and K.-C. Huang, "Inkjet Printing of Nanosized Silver Colloids," *Nanotechnology,* vol. 16, pp. 2436-2441, 2005.

[17] E. Tekin, P. J. Smith and U. S. Schubert, "Inkjet Printing as a Deposition and Patterning Tool for Polymers and Inorganic Particles," *Soft Matter,* vol. 4, pp. 703-713, 2008.

[18] M. Mionic, K. Pataky, R. M. A. Gaal, J. Brugger and L. Forro, "Carbon Nanotubes-SU8 Composite for Flexible Conductive Inkjet Printable Applications," *J. Mater. Chem.,* vol. 22, pp. 14030-14034, 2012.

[19] A. L. Dearden, P. J. Smith, D.-Y. Shin, N. Reis, B. Derby and P. O'Brien, "A Low Curing Temperature Silver Ink for Use in Ink-Jet Printing and Subsequent Production of Conductive Tracks," *Macromol. Rapid. Commun.,* vol. 26, pp. 315-318, 2005.

[20] M. L. Allen, M. Aronniemi, T. Mattila, A. Alastalo, K. Ojanpera, M. Suhonen and H. Seppa, "Electrical Sintering of Nanoparticle Structures," *Nanotechnology,* vol. 19, p. 175201, 2008.

[21] D.-G. Lee, D. K. Kim, Y.-J. Moon and S.-J. Moon, "Effect of Temperature on Electrical Conductance of Inkjet-Printed Silver Nanoparticle Ink during Continuous Wave Laser Sintering," *Thin Solid Films,* vol. 546, pp. 443-447, 2013.

[22] J. Niittynen, R. Abbel, M. Mantysalo, J. Perelaer, U. S. Schubert and D. Lupo, "Alternative Sintering Methods Compared to Conventional Thermal Sintering for Inkjet Printed Silver Nanoparticle Ink," *Thin Solid Films,* vol. 556, pp. 452-459, 2014.

[23] X. Nie, H. Wang and J. Zou, "Inkjet Printing of Silver Citrate Conductive Ink on PET Substrate," *Applied Surface Science,* vol. 261, pp. 554-560, 2012.

[24] R. P. Tortorich, E. Song and J.-W. Choi, "Inkjet-Printed Carbon Nanotube Electrodes with Low Sheet Resistance for Electrochemical Sensor Applications," *J. Electrochem. Soc.,* vol. 161, pp. 3044-3048, 2014.

[25] O.-S. Kwon, H. Kim, H. Ko, J. Lee, B. Lee, C.-H. Jung, J.-H. Choi and K. Shin, "Fabrication and Characterisation of Inkjet-Printed Carbon Nanotube Electrode Patterns on Paper," *Carbon,* vol. 58, pp. 116-127, 2013.

[26] W. Jillek and W. K. C. Yung, "Embedded Components in Printed Circuit Boards: A Processing Technology Review," *Int. J. Adv. Manuf. Technol.,* vol. 25, pp. 350-360, 2005.

[27] R. Ulrich, "Integrated and Embedded Passives," in *Wiley Encyclopedia of Electrical and Electronics Engineering*, John Wiley & Sons, 2013, pp. 1-16.

[28] H.-S. Kao, "Carbon-Conductive Ink Resistor Printed Circuit Board and its Fabrication Method". Patent US 6713399 B1, 30 March 2004.

[29] C. A. Neugebauer, "Resistivity of Cermet Films containing Oxides of Silicon," *Thin Solid Films,* vol. 6, pp. 443-447, 1970.

[30] B. Morten, A. Masoero, M. Prudenziati and T. Manfredini, "Evolution of Ruthenate-Based Thick Film Cermet Resistors," *J. Phys. D: Appl. Phys.,* vol. 27, pp. 2227-2235, 1994.

[31] D. Dees, T. D. Claar, T. E. Easler, D. C. Fee and F. C. Mrazek, "Conductivity of Porous Ni / ZrO2 - Y2 O3 Cermets," *J. Electrochem. Soc.,* vol. 134, pp. 2141-2146, 1987.

[32] A. C. Antes, J. R. Drehle and B. H. Harrison, "Fabrication of Thick Film Resistors". Patent

US 3998980 A, 21 December 1976.

[33] F. Windrich, "Carbon Contacts and Resistors in Printed Circuit Boards - a Practical Overview," in *Electronics Systemintegration Technology Conference*, 2006.

[34] P. R. Desmarais and A. J. DiTroia, "Methods of and Apparatus for Trimming Film Resistors". Patent US 4381441 A, 26 April 1983.

[35] K. R. Bube, "Laser-Trimmed Resistor". Patent US 3947801 A, 30 March 1976.

[36] A. K. Gupta and A. K. Sen, "Nonlinear DC Response in Composites: A Percolative Study," *Phys. Rev. B,* vol. 57, pp. 3375-3388, 1998.

[37] V. I. Roldughin and V. V. Vysotskii, "Percolation Properties of Metal-Filled Polymer Films, Structure and Mechanisms of Conductivity," *Progress in Oganic Coatings,* vol. 39, pp. 81-100, 2000.

[38] R. Strumpler and J. Gltaz-Reichenbach, "Conducting Polymer Composites," *J. Electroceram.,* vol. 3, pp. 329-346, 1999.

[39] T. Hassinen, B. Ahn and S. Ko, "Printed Polymer and Carbon Nanotube Thin Film Resistors with High-K Barium Titanate Insulator," *J. J. Appl. Phys.,* vol. 53, p. 05HB14, 2014.

[40] S. H. Eom, S. Senthilarasu, P. Uthirakumar, S. C. Yoon, J. Lim, C. Lee, H. S. Lim, J. Lee and S.-H. Lee, "Polymer Solar Cells Based on Inkjet-Printed PEDOT:PSS Layer," *Org. Elec.,* vol. 10, pp. 536-542, 2009.

[41] M. Hilder, B. Winther-Jenson and N. B. Clark, "Paper-Based, Printed Zinc-Air Battery," *J. Power Sources,* vol. 194, pp. 1135-1141, 2009.

[42] F. Villani, P. Vacca, G. Nenna, O. Vantino, G. Burrasca, T. Fasolino, C. Minarini and D. della Sala, "Inkjet Printed Polymer Layer on Flexible Substrate for OLED Applications," *J. Phys. Chem. C,* vol. 113, pp. 13398-13402, 2009.

[43] B. P. J. de Lacy Costello, R. J. Ewen, N. Guernion and N. M. Ratcliffe, "Highly Sensitive Mixed Oxide Sensors for the Detection of Ethanol," *Sensors and Actuators,* vol. 87, pp. 207-210, 2002.

[44] K. Arshak and I. Gaidan, "Development of a Novel Gas Sensor based on Oxide Thick Films," *Mater. Sci. Eng. B.,* vol. 118, pp. 44-49, 2005.

[45] M. F. Mabrook, C. Pearson and M. C. Petty, "Inkjet-Printed Polypyrrole Thin Films for Vapour Sensing," *Sensors and Actuators B,* vol. 115, pp. 547-551, 2006.

[46] M. Castro, J. Lu, S. Bruzaud, B. Kumar and J.-F. Feller, "Carbon Nanotubes/Poly(e-caprolactone) Composite," *Carbon,* vol. 47, pp. 1940-1942, 2009.

[47] J. Watson, K. Ihokura and G. S. V. Coles, "The Tin Dioxide Gas Sensor," *Meas. Sci. Technol.,* vol. 4, pp. 711-719, 1993.

[48] N. O. Savage, S. A. Akbar and P. K. Dutta, "Titanium Dioxide based High Temperature Carbon Monoxide Selective Sensor," *Sensors and Actuators B,* vol. 72, pp. 239-248, 2001.

[49] N. Barsan and U. Weimar, "Understanding the Fundamental Principles of Metal Oxide based Gas Sensors; the example of CO Sensing with SnO2 Sensors in the Presence of Humidity," *J. Phys.: Condens. Matter,* vol. 15, pp. R813-R839, 2003.

[50] H. Bai and G. Shi, "Gas Sensors Based on Conducting Polymers," *Sensors,* vol. 7, pp.

267-307, 2007.

[51] G. Barrett and R. Omote, "Projected Capacitive Touch Screen Technology," *Information Display,* vol. 26, pp. 16-21, 2010.

[52] M. R. Bhalla and B. A. V., "Comparative Study of Various Touchscreen Technologies," *Int. J. Comput. Appl.,* vol. 6, pp. 12-18, 2010.

[53] T. Chelidze and Y. Gueguen, "Pressure-Induced Percolation Transitions in Composites," *J. Phs. D.: Appl. Phys.,* vol. 31, pp. 2877-2885, 1998.

[54] W.-Y. Chang, T.-H. Fang, Y.-T. Shen and Y.-C. Lin, "Flexible Electronics Sensors for Tactile Multisensing," *Rev. Sci. Instrum.,* vol. 80, p. 084701, 2009.

[55] D.-K. Kim, J.-H. Kim, H.-J. Kwon and Y.-H. Kwon, "A Touchpad for Force and Location Sensing," *ETRI Journal,* vol. 32, pp. 722-728, 2010.

[56] V. Subramanian, J. B. Chang, A. de la Fuente Vornbrock, D. C. Huang, L. Jagannathan, F. Liao, B. Mattis, S. Molesa, D. R. Redinger, D. Soltman, S. K. Volkman and Q. Zhang, "Printed Electronics for Low-Cost Electronic Systems: Technology Status and Application Development," in *European Solid-State Circuits Conference*, 2008.

[57] J. I. Biegeleisen, The Complete Book of Silk Screen Printing Production, Dover, 1963.

[58] H. Kipphan, Handbook of Print Media, Springer, 2001.

[59] A. Hobby, "Fundamentals of Screens for Electronics Screen Printing," *Circuit World,* vol. 16, pp. 16-28, 1990.

[60] F. C. Krebs, "Fabrication and Processing of Polymer Solar Cells: A Review of Printing and Coating Techniques," *Solar Energy Materials & Solar Cells,* vol. 93, pp. 394-

412, 2009.

[61] D. S. Tsoukleris, I. M. Arabatzis, E. Chatzivasiloglou, A. I. Kontos, V. Belessi, M. C. Bernard and P. Falaras, "2-Ethyl-1-Hexanol Based Screen-Printed Titania Thin Films For Dye-Sensitized Solar Cells," *Solar Energy,* vol. 79, pp. 422-430, 2005.

[62] M. Manceau, D. Angmo, M. Jorgenson and F. C. Krebs, "ITO-Free Flexible Polymer Solar Cells: From Small Model Devices to Roll-to-Roll Processed Large Modules," *Organic Electronics,* vol. 12, pp. 566-574, 2011.

[63] J. P. Metters, R. O. Kadara and C. E. Banks, "Fabrication of Co-Planar Screen Printed Microband Electrodes," *Analyst,* vol. 138, pp. 2516-2521, 2013.

[64] I. M. Hutchings and G. D. Martin, Inkjet Technology for Digital Fabrication, John Wiley & Sons, 2013.

[65] K. Rahman, J.-B. Ko, S. Khan, D.-S. Kim and K.-H. Choi, "Simulation of Droplet Generation through Electrostatic Forces," *J. Mech. Sci. Tech.,* vol. 24, pp. 307-310, 2010.

[66] J.-S. Chang, A. J. Kelly and J. M. Crowley, "Printers," in *Handbook of Electrostatic Processes*, Marcel Dekker, 1995, pp. 304-305.

[67] D. Kim, J. H. Yoo, Y. Lee, W. Choi, K. Yoo and J.-B. Lee, "Gallium-Based Liquid Metal Inkjet Printing," in *MEMS*, 2014.

[68] R. P. Tortorich and J.-W. Choi, "Inkjet Printing of Carbon Nanotubes," *Nanomaterials,* vol. 3, pp. 453-468, 2013.

[69] R. D. Deegan, O. Bakajin, T. F. Dupont, G. Huber, S. R. Nagel and T. A. Witten,

"Capilliary Flow as the Cause of Ring Stains from Dried Liquid Drops," *Nature,* vol. 389, pp. 827-829, 1997.

[70] H. Hu and R. G. Larson, "Marangoni Effect Reverses Coffee-Ring Dispersions," *J. Phys. Chem. B.,* vol. 110, pp. 7090-7094, 2006.

[71] C. McIlroy, O. G. Harlen and N. F. Morrison, "Modelling the Jetting of Dilute Polymer Solutions in Drop-On-Demand Inkjet Printing," *J. Non-Newtonian Fluid Mechanics,* vol. 201, pp. 17-28, 2013.

[72] S. D. Hoath, S. Jung and I. M. Hutchings, "A Simple Criterion for Filament Break-Up in Drop-On-Demand Inkjet Printing," *Phys. Fluids,* vol. 25, p. 021701, 2013.

[73] H. Kang, R. Kitsomboonloha, J. Jang and V. Subramanian, "High-Performance Printed Transistors Realized Using Femtoliter Gravure-Printed Sub-10um Metallic Nanoparticle Patterns and Highly Uniform Polymer Dielectric and Semiconductor Layers," *Adv. Mater.,* vol. 24, pp. 3065-3069, 2012.

[74] M. Allen, C. Lee, B. Ahn, T. Kololuoma, K. Shin and S. Ko, "R2R Gravure and Inkjet Printed RF Resonant Tag," *Microelec. Eng.,* vol. 88, pp. 3293-3299, 2011.

[75] A. K. Sankaran and J. P. Rothstein, "Effect of Viscoelasticity on Liquid Transfer During Gravure Printing," *J. Non-Newtonian Fluid Mechanics,* Vols. 175-176, pp. 64-75, 2012.

[76] L. W. Schwartz, "Numerical Modeling of Liquid Withdrawal from Gravure Cavities in Coating Operations; the Effect of Cell Pattern," *J. Eng. Maths.,* vol. 42, pp. 243-253, 2002.

[77] R. H. Norman, Conductive Rubbers and Plastics: Their Production, Application and Test Methods, Elsevier, 1957.

[78] D. E. El-Nashar, S. H. Mansour and E. Girgis, "Nickel and Iron Nano-Particles in Natural Rubber Composites," *J. Mat. Sci.,* vol. 41, pp. 5359-5364, 2006.

[79] D. P. Skinner, R. E. Newnham and L. E. Cross, "Flexible Composite Transducers," *Materials Research Bulletin,* vol. 13, pp. 599-607, 1978.

[80] P. Pramanik, D. Khastgir, S. K. De and T. N. Saha, "Pressure-Sensitive Electrically Conductive Nitrile Rubber Composites Filled with Particulate Carbon Black and Short Carbon Fibre," *J. Mat. Sci.,* vol. 25, pp. 3848-3853, 1990.

[81] Y. A. Kim, T. Hayashi, M. Endo, Y. Gotoh, N. Wada and J. Seiyama, "Fabrication of Aligned Carbon Nanotube-Filled Rubber Composite," *Scripta Materialia,* vol. 54, pp. 31-35, 2006.

[82] T. Kuilla, S. Bhadra, D. Yao, N. H. Kim, S. Bose and J. H. Lee, "Recent Advances in Graphene Based Polymer Composites," *Prog. Poly. Sci.,* vol. 35, pp. 1350-1375, 2010.

[83] G. A. Somorjai and J. Y. Park, "Colloid Science of Metal Nanoparticle Catalysts in 2D and 3D Structures. Challenges of Nucleation, Growth, Composition, Particle Shape, Size Control and Their Influence on Activity and Selectivity," *Top. Catal.,* vol. 49, pp. 126-135, 2008.

[84] A. R. Tao, S. Habas and P. Tang, "Shape Control of Colloidal Metal Nanocrystals," *Small,* vol. 4, pp. 310-325, 2008.

[85] B. D. Busbee, S. O. Obare and C. J. Murphy, "An Improved Synthesis of High-Aspect-Ratio Gold Nanorods," *Adv. Mater.,* vol. 15, pp. 414-416, 2003.

[86] D. Wang, C. Song, Z. Hu and X. Zhou, "Synthesis of Silver Nanoparticles with Flake-Like Shapes," *Mater. Lett.,* vol. 59, pp. 1760-1763, 2005.

[87] P. Xie, P. Gu and J. J. Beaudoin, "Electrical Percolation Phenomena in Cement Composites Containing Conductive Fibres," *J. Mat. Sci.,* vol. 31, pp. 4093-4097, 1996.

[88] I. Krupa, I. Novak and I. Chodak, "Electrically and Thermally Conductive Polythylene/Graphite Composites and their Mechanical Properties," *Synth. Met.,* vol. 145, pp. 245-252, 2004.

[89] H.-B. Zhang, W.-G. Zheng, Q. Yan, Y. Yang, J.-W. Wang, Z.-H. Lu, G.-J. Ji and Z.-Z. Yu, "Electrically Conductive Polyethylene Terephthalate /Graphene Nanocomposites Prepared by Melt Compounding," *Polymer,* vol. 51, pp. 1191-1196, 2010.

[90] A. Allaoui, S. Bai, H. M. Cheng and J. B. Bai, "Mechanical and Electrical Properties of a MWNT/Epoxy Composite," *Compos. Sci. Tech.,* vol. 62, pp. 1993-1998, 2002.

[91] W. A. J., M. Szablewski, D. Bloor, D. Atkinson, A. Graham, P. Laughlin and D. Lussey, "A Multi-Component Nanocomposite Screen-Printed Ink with Non-Linear Touch Sensitive Electrical Conductivity," *Nanotechnology,* vol. 24, p. 165501, 2013.

[92] H. Scher and R. Zallen, "Critical Density in Percolation Processes," *J. Chem. Phys.,* vol. 53, p. 3759, 1970.

[93] R. Zallen, The Physics of Amorphous Solids, Wiley, 1998, pp. 183-191.

[94] X. Jing, W. Zhao and L. Lan, "The Effect of Particle Size on Electric Conducting Percolation Threshold in Polymer/Conducting Particle Composites," *J. Mater. Sci. Lett.,* vol. 19, pp. 377-379, 2000.

[95] S. R. Broadbent and J. M. Hammersley, "Percolation Processes," *Proc. Camb. Phil. Soc.,* vol. 53, pp. 629-641, 1957.

[96] F. Lux, "Models Proposed to Explain the Electrical Conductivity of Mixtures made of Conductive and Insulating Materials," *J. Mater. Sci.,* vol. 28, pp. 285-301, 1993.

[97] I. J. Youngs, "Exploring the Universal Nature of Electrical Percolation Exponents by Genetic Algorithm Fitting with General Effective Medium Theory," *J. Phys. D.: Appl. Phys.,* vol. 35, pp. 3127-3137, 2002.

[98] I. Krupa and I. Chodak, "Physical Properties of Thermoplastic/Graphite Composites," *European Polymer Journal,* vol. 37, pp. 2159-2168, 2001.

[99] D. A. G. Bruggeman, "Calculation of Various Physical Constants of Heterogeneous Substances. I. Dielectric Constants and Conductivities of Mixed Bodies from Isotropic Substances," *Ann. Phys.,* vol. 416, pp. 636-664, 1935.

[100] R. Landauer, "Electrical Conductivity in Inhomogeneous Media," in *AIP. Conf. Proc.*, 1977.

[101] A. Graham, Electrical Properties and Vapour Sensing Characteristics of a Novel Metal-Polymer Composite, Durham University, 2008.

[102] D. S. McLachlan, "An Equation for the Conductivity of Binary Mixtures with Anisotropic Grain Structures," *J. Phys. C.; Solid State Phys.,* vol. 20, pp. 865-877, 1987.

[103] D. S. McLachlan, A. Priou, I. Chenerie, E. Isaac and F. Henry, "Modelling the Permittivity of Composite Materials with a General Medium Equation," *J. Electromag. Wav. Appl.,* vol. 6, pp. 1099-1131, 1992.

[104] C. Kittel, Introduction to Solid State Physics, John Wiley & Sons, 2005.

[105] D. Cvijovic, "The Bloch-Gruneissen Function of Arbitrary Order and its Series Representations," *Theoret. Mathemat. Phys.,* vol. 166, pp. 37-42, 2011.

[106] G. D. Mahan, Condesned Matter in a Nutshell, Princeton University Press, 2011.

[107] P. A. Tipler and G. Mosca, Physics for Scientists and Engineers, Volume 2: Electricity, Magnetism, Light, and Elementary Modern Physics, W. H. Freeman, 2004.

[108] R. J. Singh, "Band Theory of Insulators and Semiconductors," in *Solid State Physics*, Dorling Kindersley, 2012, p. 333.

[109] J. R. Hook and H. E. Hall, Solid State Physics, John Wiley & Sons, 2001.

[110] D. C. Child, "Discharge from Hot CaO," *Phys. Rev. Series I,* vol. 32, pp. 492-511, 1911.

[111] N. F. Mott and R. W. Gurney, Electronic Processes in Ionic Crystals, Oxford University Press, 1940.

[112] P. N. Murgatroyd, "Theory of Spcae-Charge Limited Current Enahnced by Frenkel Effect," *J. Phys. D.: Appl. Phys.,* vol. 3, pp. 151-156, 1970.

[113] M. A. Lampert, Current Injection in Solids, Academic Press, 1970.

[114] N. F. Mott, "Conduction in Non-Crystalline Materials," *Phil. Mag.,* vol. 19, pp. 835-852, 1969.

[115] S. M. Sze and K. K. Ng, "Metal-Insulator-Semiconductor Capacitors," in *Physics of Semiconductor Devices*, John Wiley & Sons, 2007, pp. 227-229.

[116] C. Crowell, "The Richardson Constant for Thermionic Emission in Schottky Barrier Diodes," *Solid-State Electronics ,* vol. 8, pp. 395-399, 1965.

[117] I. S. Grant and W. R. Phillips, "Electrostatic Field Calculations," in *Electro-Magnetism*, John Wiley & Sons, 2004, pp. 93-97.

[118] J. G. Simmons, "Poole-Frenkel Effect and Schottky Effect in Metal-Insulator-Metal Systems," *Phys. Rev.,* vol. 155, pp. 657-660, 1967.

[119] L. Solymar, D. Walsh and R. R. A. Syms, Electrical Properties of Materials, Oxford University Press, 2014.

[120] A. F. J. Levi, Applied Quantum Mechanics, Cambridge University Press, 2006.

[121] C. B. Duke, Tunnelling in Solids, Academic Press, 1969.

[122] R. H. Fowler and L. Nordheim, "Electron Emission in Intense Electric Fields," *Proc. R. Soc. A.,* vol. 119, pp. 173-181, 1928.

[123] E. L. Murphy and R. H. Good Jr, "Thermionic Emission, Field Emission, and the Transition Region," *Phys. Rev.,* vol. 102, pp. 1464-1473, 1956.

[124] D. Lussey, D. Bloor, P. Laughlin, A. Graham and C. Hilsum, (Peratech Ltd.) "Electrically Responsive Composite Material for Transducers". Great Britain Patent GB2462920 A, 3 March 2010.

[125] R. Gruber, (Kronos International, Inc.) "Method for Manufacturing Titanium Dioxide".

United States of America Patent US20130058860 A1, 7 March 2013.

[126] H. Okuda, H. Takahashi and E. Yamada, (Ishihara Sangyo Kaisha, Ltd.) "Acicular Titanium Dioxide Particles and Method of the Production Thereof". Europe Patent EP 0341703 A2, 15 November 1989.

[127] V. Jeurgens, A. Breyder, F. Mersch, S. Bluemel and V. Schmitt, (Kronos International, Inc.) "Method for the Surface Treatment of Inorganic Pigment Particles". United States of America Patent US20140000483 A1, 2 January 2014.

[128] C. J. Lussey, P. Laughlin, A. Graham, D. Bloor and D. Lussey, (Peratech Ltd.) "Composite Material". United States of America Patent US20140109698 A1, 24 April 2014.

[129] H. Okuda, H. Futamata, H. Takahashi and N. Sanefuji, (Ishihara Sangyo Kaisha, Ltd.) "Acicular Electroconductive Tin Oxide Fine Particles and Process for Producing the Same.". United States of America Patent US5575957 A, 19 November 1996.

[130] Corning, "Macor Product Information Sheet," 2014. [Online]. Available: http://www.corning.com/docs/specialtymaterials/pisheets/Macor.pdf. [Accessed 21 May 2014].

[131] J. Goldstein, D. E. Newbury, D. C. Joy, C. E. Lyman, P. Echlin, E. Lifshin, L. Sawyer and J. R. Michael, Scanning Electron Microscopy and X-ray Microanalysis, 3 ed., Springer, 2003.

[132] W. Zhou and Z. L. Wang, Scanning Microscopy for Nanotechnology, Springer, 2007.

[133] A. W. Coats and J. P. Redfern, "Thermogravimetric Analysis," *Analyst,* vol. 88, pp. 906-924, 1963.

[134] A. I. Vogel, "Thermal Methods," in *A Textbook of Quantitative Inorganic Analysis including Elementary Instrumental Analysis*, Longman, 1978, pp. 849-862.

[135] D. Bloor, A. Graham, E. J. Williams, P. J. Laughlin and D. Lussey, "Metal-Polymer Composite with Nanostructured Filler Particles and Amplified Physical Properties," *App. Phys. Lett.,* vol. 88, p. 102103, 2006.

[136] X. Chen and S. S. Mao, "Titanium Dioxide Nanomaterials: Synthesis, Properties, Modifications, and Applications," *Chem, Rev.,* vol. 107, pp. 2891-2959, 2007.

[137] K. Levenberg, "A Method for the Solution of Certain Non-Linear Problems in Least Squares," *Q. Appl. Math.,* vol. 2, pp. 164-168, 1944.

[138] L. He and S.-C. Tjong, "Nonlinear Electrical Conduction in Percolating Systems Induced by Internal Field Emission," *Synth. Met.,* vol. 161, pp. 540-543, 2011.